Robert Hammann

Probing the Invisible

From Dark Matter and Neutrinos in XENONnT to Infrared Scintillation for Future Xenon Detectors

Dissertation

submitted to the

Combined Faculty of Mathematics, Engineering and Natural Sciences
of Heidelberg University, Germany

for the degree of

Doctor of Natural Sciences

Put forward by

Robert Hammann

born in: Kaiserslautern, Germany
Oral examination: November 27, 2025

Probing the Invisible

From Dark Matter and Neutrinos in XENONnT to Infrared Scintillation for Future Xenon Detectors

Referees:
Prof. Dr. Teresa Marrodán Undagoitia
Prof. Dr. Belina von Krosigk

Abstract – The fundamental nature of dark matter remains one of the most profound mysteries in modern physics. Liquid xenon (LXe) time projection chambers (TPCs) are at the frontier of sensitivity to search for weakly interacting massive particle (WIMP) candidates. This thesis presents contributions to both current dark matter searches with the XENONnT experiment and foundational studies of infrared (IR) scintillation in xenon with the potential to enhance the sensitivity of next-generation detectors like XLZD.

The combined analysis of XENONnT's first two science runs, with a total exposure of 3.1 tonne-years, found no evidence for dark matter. Consequently, it placed competitive upper limits on the WIMP-nucleon cross section as low as 1.7×10^{-47} cm^2 for a WIMP mass of 30 GeV/c^2. Through a dedicated analysis optimized to achieve an even lower energy threshold, XENONnT achieved the first measurement of ^{8}B solar neutrinos in a ton-scale detector via coherent elastic neutrino-nucleus scattering (CEνNS), observing 10.6 excess events above background with 2.73 σ significance. The statistical methods, sensitivity studies, and robustness assessments developed in this thesis were central to these results.

Furthermore, this thesis investigates IR scintillation in xenon, showing promising results for future detector applications. Systematic measurements in gaseous xenon revealed a substantial IR light yield of approximately 6000 photons/MeV, which is similar in magnitude to ultraviolet (UV) scintillation commonly used in current detectors. The time response was characterized for the first time, finding a dominant microsecond-scale component that challenges previous understanding of xenon de-excitation pathways. Additionally, a dual-phase xenon TPC was operated with broad wavelength sensitivity spanning UV to IR, observing signals consistent with IR scintillation in both liquid and gaseous phases.

Zusammenfassung – Die grundlegende Natur der Dunklen Materie gehört zu den größten Rätseln der modernen Physik, wobei Flüssigxenon-Spurendriftkammern (engl. TPCs) an der Empfindlichkeitsgrenze für die Suche nach schwach wechselwirkenden massiven Teilchen (engl. WIMPs) stehen. Diese Arbeit leistet Beiträge sowohl zur aktuellen Dunkle-Materie-Suche mit dem XENONnT-Experiment als auch zu grundlegenden Untersuchungen der IR-Szintillation in Xenon mit dem Potenzial die Empfindlichkeit von Detektoren der nächsten Generation wie XLZD zu verbessern.

Die kombinierte Analyse der ersten beiden Messperioden von XENONnT mit einer Gesamtexposition von 3.1 Tonnenjahren fand keine Hinweise auf Dunkle Materie und setzte daher kompetitive Obergrenzen für den WIMP-Nukleon-Wirkungsquerschnitt von bis zu 1.7×10^{-47} cm^2 bei einer WIMP-Masse von 30 GeV/c^2. Durch eine speziell optimierte Analyse zur Erreichung einer noch niedrigeren Energieschwelle gelang XENONnT die erste Messung von ^{8}B-Sonnenneutrinos in einem Tonnenskala-Detektor mittels kohärenter elastischer Neutrino-Nucleus-Streuung (engl. CEνNS), wobei 10.6 Überschussereignisse über dem Untergrund mit einer Signifikanz von 2.73 σ beobachtet wurden. Diese in dieser Arbeit entwickelten statistischen Methoden, Sensitivitätsstudien und Robustheitsbewertungen waren für diese Ergebnisse zentral.

Darüber hinaus wurde in dieser Arbeit die IR-Szintillation in Xenon mit vielversprechenden Ergebnissen für zukünftige Detektoranwendungen untersucht. Systematische Messungen in gasförmigem Xenon zeigten eine beträchtliche IR-Lichtausbeute von etwa 6000 Photonen/MeV, was in der Größenordnung ähnlich der UV-Szintillation ist, die in aktuellen Detektoren üblicherweise verwendet wird. Das Zeitverhalten wurde erstmalig charakterisiert und zeigte eine dominante Komponente im Mikrosekundenbereich, die das bisherige Verständnis der Xenon-Relaxationsprozesse in Frage stellt. Zusätzlich wurde eine Zweiphasen-Xenon-TPC mit breiter Wellenlängenempfindlichkeit von UV bis IR betrieben, die Signale beobachtete, welche mit IR-Szintillation sowohl in der flüssigen als auch in der gasförmigen Phase konsistent sind.

Author's Contributions and List of Publications

This work comprises the statistical analysis of two major results of the XENONnT experiment and studies on xenon scintillation properties in laboratory setups. The XENONnT analyses represent a great collaborative effort with many people contributing. My main contributions to these analyses were the development of the statistical inference framework now used for all analyses of XENONnT and beyond, along with comprehensive sensitivity studies performed with this framework. These studies build on excellent foundational work by many other collaborators. In addition to the analyses presented in this work, my role as co-chair of XENONnT's simulations, modeling, and statistical inference team involved coordinating high-level analysis efforts including signal and background modeling, crucial for the two major analyses presented here. The long-term sensitivity study presented in Section 5.5 was conducted by the author, with inputs on signal and background distributions and rates provided by the collaboration. Additionally, this thesis describes major contributions to work published in six publications, which will be referenced by Roman numerals in the following chapters:

Paper I (corresponding author)
XENON collaboration (Aprile et al.), **XENONnT WIMP Search: Signal & Background Modeling and Statistical Inference**, *Phys. Rev. D 111, 103040 (2025)*

- This paper summarizes the high-level analysis procedure of XENONnT. My primary contribution was writing the statistical inference chapter, while also participating in the broader manuscript editing process.
- Studies on the suitability of various goodness-of-fit tests for typical XENONnT data, highlighted in this paper, were performed as part of my Master's thesis.

Paper II (corresponding author)
XENON collaboration (Aprile et al.), **WIMP Dark Matter Search in a 3.1 tonne $\times$ year Exposure of the XENONnT Experiment**, *arXiv.2502.18005 (2025)*, accepted for publication in *Phys. Rev. Lett.*

- My contributions included developing the statistical model based on inputs from collaborators and conducting sensitivity and mismodeling studies to guide analysis decisions, with particular emphasis on the statistical treatment of double electron capture background.
- I carried out the inference, including computing hypothesis test results and deriving limits.
- Significant contributions were made to writing and editing the manuscript as part of the paper writing team.

Paper III (major contributor)

XENON collaboration (Aprile et al.), **First Indication of Solar ^{8}B Neutrinos via Coherent Elastic Neutrino-Nucleus Scattering with XENONnT**, *Phys. Rev. Lett. 133, 191002 (2024)*

- My work included collecting inputs to develop the statistical model, assessing robustness of results against mismodeling, and performing sensitivity studies to guide analysis decisions.
- I performed part of the inference, including computing the discovery significance.
- As internal referee, I contributed to the development of the manuscript.

Paper IV (corresponding author)

Piotter er al., **First time-resolved measurement of infrared scintillation light in gaseous xenon**, *Eur. Phys. J. C 83, 482 (2023)*

- My work included extending the already existing setup by commissioning a gas purification system to reduce impurities.
- I acquired the datasets presented in this publication and developed a pipeline to analyze and model the results.
- I contributed substantially to the writing of the manuscript and the interpretation of the results.

Paper V (corresponding author)

Hammann et al., **Investigating the slow component of the infrared scintillation time response in gaseous xenon**, *JINST 19, C02080 (2024)*

- My work included conceptualizing and performing the measurements presented in this paper, as well as analyzing and modeling the results.
- I wrote the majority of the manuscript.

Paper VI (corresponding author)

Hammann et al., **Operation of a dual-phase xenon detector with wavelength sensitivity from ultraviolet to infrared**, *Front. Detect. Sci. Technol. 3, 1638362 (2025)*

- Together with the Heidelberg Xenon (HeXe) team, I acquired the datasets for this work.
- I analyzed and modeled the time responses of the signals, which forms the main result presented in the publication.
- I contributed substantially to the writing of the manuscript and the interpretation of the results.

Contents

Acronyms

AC accidental coincidence.

ADC analog-to-digital converter.

BDT boosted decision tree.

CDM cold dark matter.

CEνNS coherent elastic neutrino-nucleus scattering.

CL confidence level.

CMB Cosmic Microwave Background.

CSDA continuous slowing-down approximation.

DAQ data acquisition.

DEC double electron capture.

DSNB diffuse supernova neutrino background.

EC electron capture.

ER electronic recoil.

FDC field distortion correction.

FV fiducial volume.

FWHM full width at half maximum.

GOF goodness of fit.

GXe gaseous xenon.

HeXe Heidelberg Xenon.

IR infrared.

LCE light collection efficiency.

LED light emitting diode.

LNGS Laboratori Nazionali del Gran Sasso.

LXe liquid xenon.

LZ LUX-ZEPLIN.

MC Monte Carlo.

MFC mass flow controller.

MFP mean free path.

MMF mismodeling fraction.

MPIK Max-Planck-Institut für Kernphysik.

MV muon veto.

NEST "Noble Element Simulation Technique".

NR nuclear recoil.

NV neutron veto.

PBH primordial black hole.

PCA principal component analysis.

PCL power-constrained limits.

PDF probability density function.

PE photoelectron.

PMT photomultiplier tube.

PTFE polytetrafluoroethylene.

QE quantum efficiency.

ROI region of interest.

SD spin-dependent.

SHM standard halo model.

SI spin-independent.

SM Standard Model.

SNO Sudbury Neutrino Observatory.

SNS Spallation Neutron Source.

SPE single photoelectron.

SR science run.

TED tritium-enhanced dataset.

toyMC Toy Monte-Carlo.

TPC time projection chamber.

UL upper limit.

UV ultraviolet.

VUV vacuum ultraviolet.

WIMP weakly interacting massive particle.

1

The Search for Dark Matter

Various astrophysical and cosmological observations provide compelling evidence for the existence of dark matter. From its gravitational fingerprints, it is evident that the familiar baryonic matter, defined in astronomy as all ordinary atomic matter, accounts for approximately 5 % of the Universe's total mass-energy content today.[1] The remainder is made up of dark matter (26 %) and dark energy (68 %) [1] according to the Standard Model (SM) of cosmology, known as Λ cold dark matter (CDM), where Λ is the cosmological constant. While the existence of dark matter is well established, its form remains elusive. So far, no experiment has been able to measure a signal from dark matter interactions in a laboratory,[2] which constitutes one of the biggest open questions in fundamental physics [5, 6]. Numerous candidates for dark matter constituents have been proposed [7–9]. Among particle physicists' favorites is the broad class of WIMPs, which arise naturally in various extensions to the SM of particle physics and constitute the primary science target of the XENONnT experiment introduced in Section 3.3.

While the ΛCDM model successfully explains a wide range of astrophysical and cosmological observations, recent data have revealed tensions challenging its completeness [10, 11]. It should be acknowledged that some observations traditionally attributed to dark matter could alternatively be explained by modifications to gravity on large scales [12], though such theories do currently not provide a comprehensive replacement [7]. Ultimately, conclusive confirmation of the existence of dark matter requires direct measurements of its constituents.

This chapter briefly summarizes the evidence for dark matter (Section 1.1) before reviewing a few popular dark matter candidates (Section 1.2). Finally, experimental considerations for the direct detection of WIMPs are discussed in Section 1.3. For more detailed coverage, comprehensive reviews are available [5, 7].

[1] The term "baryonic matter" is often employed with notable flexibility. For the purposes of cosmology, it typically includes not only true baryons, such as protons and neutrons, but also electrons and atomic nuclei.

[2] One exception is the long-standing claim from the DAMA/LIBRA experiment, which measured an annually modulating signal for over 20 years [2]. The mass and cross section when interpreted as originating from a dark matter interaction are, however, strongly excluded by several orders of magnitude by other experiments, including those using the same target material [3, 4].

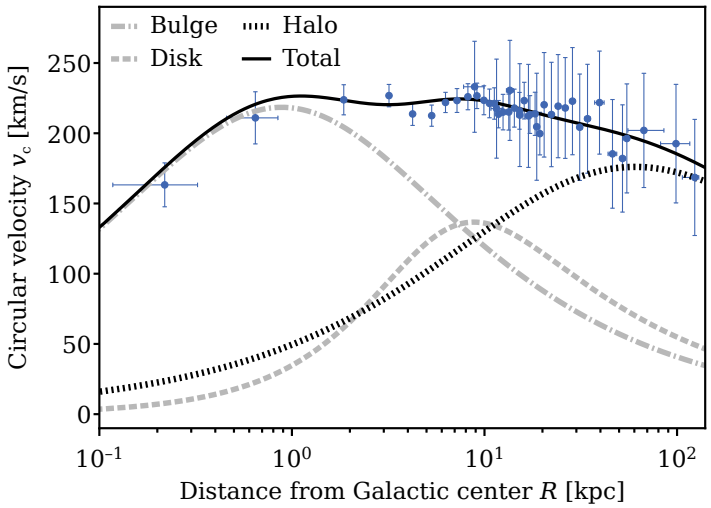

Figure 1.1.: Rotation curve of the Andromeda Galaxy (M31). The velocity remains flat up to a radius of ∼25 kpc before gradually decreasing. Contributions from bulge, disk, and dark matter halo are shown separately. Adapted from [18].

1.1 Indications of Dark Matter

Astronomical and cosmological observations provide strong evidence for the existence of dark matter across different cosmic scales. On the scale of individual galaxies, this evidence primarily arises from the radial velocity profiles of stars and gas, known as rotation curves. Vera Rubin and Kent Ford pioneered precision measurements of these rotation curves, using Doppler shifts of hydrogen emission lines to trace velocities into the outer regions of galaxies. Beginning with our neighboring Andromeda Galaxy (M31), their observations confirmed earlier hints that rotation curves remain flat at large radii [13, 14]. This behavior contrasts with Keplerian dynamics, which predicts that orbital velocities in the outer regions of galaxies should decrease with the square root of the radius. If only luminous mass were present in galaxies, stars in the outer regions should fly off into space. This discrepancy can be resolved by proposing that galaxies are embedded within much larger spheres of non-luminous matter, now known as dark matter halos [15]. The rotation curve of the Andromeda Galaxy, shown in Figure 1.1, demonstrates the characteristic flat profile where high rotational velocities persist even at large galactic radii. Figure 1.2 shows how Andromeda's extensive dark matter halo would appear in our night sky if it were visible. Precise measurements of hundreds of spiral galaxy rotation curves have now established robust evidence that galaxies are typically embedded within massive dark matter halos [16, 17].

The earliest compelling evidence for dark matter, however, came from observations on larger scales, specifically galaxy clusters. In 1933, Fritz Zwicky studied the Coma cluster and found that the galaxies' velocities were too high to be gravitationally bound by the visible matter alone, indicating a large amount of unseen mass [19]. Using the virial theorem, he concluded the cluster's total mass must be much greater than that inferred from its luminous matter, coining this missing component "dark matter". Today, gravitational lensing provides a precise method for measuring the total mass of galaxy clusters by observing how they bend light from background objects [20]. Colliding galaxy clusters provide an ideal laboratory for this technique. The Bullet Cluster (1E 0657-56), shown in Figure 1.3, is an iconic example. The

Figure 1.2.: Visualization of Andromeda's dark matter halo as it would appear on the night sky if it were visible. The photograph captures the night sky over La Palma at dawn, shortly after the Moon has risen. Overlaid in purple is a representation of Andromeda's dark matter halo, with a virial radius of approximately ∼220 kpc [18]. This corresponds to an angular diameter of about 32° on the night sky (dotted line), making it roughly 60 times larger than the apparent size of the Moon. Inspired by an artwork from J. DePasquale, E. Wheatley, and Z. Levay.

optical image in the background shows the locations of galaxies, while the overlaid blue map indicates the total gravitational mass measured via weak lensing. The pink overlay represents X-ray emission from hot intra-cluster gas, which constitutes most of the cluster's baryonic mass. Two key conclusions can be drawn: first, the gravitational mass is spatially offset from the gas, indicating that most gravitating matter is dark matter; second, unlike the baryonic gas, the dark matter halos passed through each other without strong interaction, placing limits on dark matter self-interaction [21, 22]. Studies of 72 similar colliding clusters found a remarkable $7.6\,\sigma$ significance for dark matter's existence [23].

Further evidence for dark matter comes from the largest observable scales. The Cosmic Microwave Background (CMB) is relic radiation from the epoch of recombination – about 380 000 years after the Big Bang – when the Universe cooled to roughly 3000 K and electrons combined with protons to form neutral hydrogen [25]. Since then, cosmic expansion has redshifted this primordial thermal spectrum to a temperature of $T \simeq 2.725\,\mathrm{K}$ with wavelengths now in the microwave range [26]. The CMB spectrum measured today is the closest to a perfect blackbody ever observed, and it is nearly isotropic. Yet, what makes it most interesting are its tiny deviations from perfection. Temperature anisotropies on the order of $\sim 10^{-5}$ ($30\,\mu\mathrm{K}$) encode valuable information about the early Universe, which the Planck satellite mapped in exceptional detail [27] (see Figure 1.4). The anisotropies can be decomposed into spherical harmonics, yielding a power spectrum of temperature fluctuations as a function of multipole moment l, where larger l correspond to smaller angular scales. The power spectrum exhibits a prominent peak at approximately one degree angular scale, followed by a series of peaks at

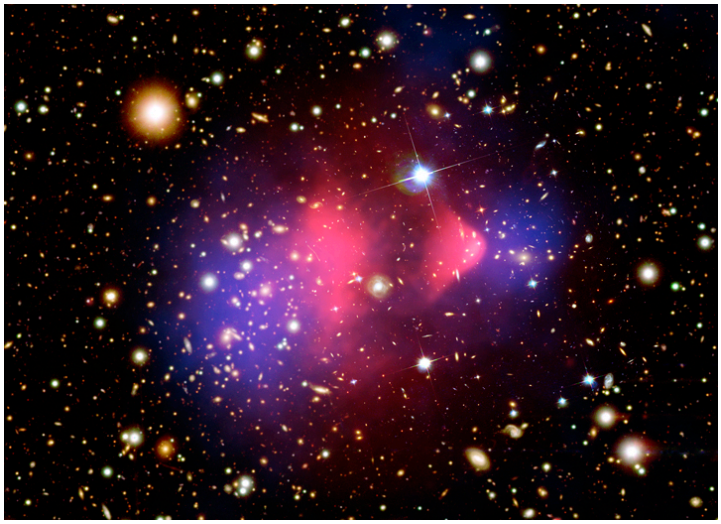

Figure 1.3.: Composite image of the Bullet Cluster. The optical image in the background was used to map the cluster's total gravitational mass, overlaid in blue. The pink overlay corresponds to X-ray emission from hot intra-cluster gas, which makes up most of the cluster's baryonic mass. Reproduced from [24].

smaller scales. These peaks represent a snapshot of acoustic oscillations in the photon-baryon fluid "frozen" at the time of photon decoupling. Their precise locations and amplitudes depend sensitively on the Universe's composition, particularly the dark matter density, as illustrated in Figure 1.4. The six-parameter ΛCDM model fits the data excellently, but only when including dark matter. The best-fit cosmological parameters split the mass-energy content of today's Universe into ∼68.5 % dark energy, ∼26.4 % dark matter, ∼and 4.9 % baryonic matter [1].

Another line of robust cosmological evidence for dark matter comes from large-scale structure formation [30]. Extensive astronomical surveys reveal that galaxies are not uniformly distributed, but instead form a "cosmic web" of filaments, clusters, and voids. N-body simulations successfully reproduce the evolution from primordial density fluctuations to today's large-scale structure, but only when they include a dominant CDM component present since the early Universe.

1.2 Dark Matter Candidates

The astronomical and cosmological observations that provide evidence for dark matter also constrain its fundamental properties. For a particle to be a viable dark matter candidate, it must satisfy several requirements [5, 7]:

- **Dark:** If it is a particle, it must be electrically neutral or have, at most, a very small electric charge (millicharge), to avoid interactions with photons and thus remain invisible ("dark") in astronomical observations.
- **Massive:** It must possess mass to account for the observed gravitational effects attributed to dark matter.
- **Collisionless:** Interactions with baryonic matter and self-interactions must be sufficiently weak to remain negligible, as observed in cluster collisions and necessary to avoid excessive energy dissipation. This is crucial for dark matter's distinct behavior com-

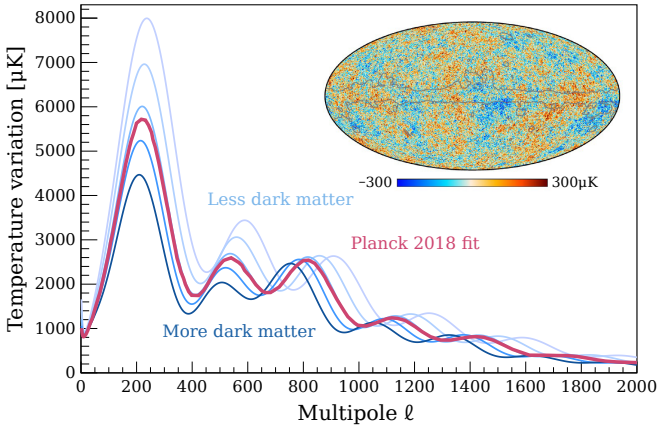

Figure 1.4.: Temperature variations of the Cosmic Microwave Background (CMB) measured by the Planck satellite [28], from which the angular power spectrum is extracted. The best-fit cosmological model [1] is shown in red. Spectra with increased and decreased dark matter content relative to the best fit illustrate the strong constraining power of CMB observations on the dark matter abundance of the Universe. Adapted from [29].

pared to baryonic matter during cosmic evolution. While gravity is the only interaction strictly required between dark matter and baryonic matter, most models for dark matter production in the early Universe involve additional, non-gravitational couplings.

- **Cold or warm:** The candidate must be non-relativistic ("cold") at the onset of structure formation (about 50 000 years after the Big Bang) to preserve the small-scale density perturbations that seed galaxy formation. Particles that remain relativistic ("hot") suppress small-scale structure formation through their large free-streaming lengths.
- **Stable or long-lived:** The lifetime of the candidate must be at least comparable to the age of the Universe, as dark matter signatures are seen in systems spanning all cosmic epochs.

Dark matter candidates meeting these criteria exist across an astonishing 90 orders of magnitude in mass [7], as illustrated in Figure 1.5. This includes both new fundamental particles [8] (described as fields below $\mathcal{O}(\mathrm{eV})$) and macroscopic objects for masses above the Planck scale of $\sim 10^{-8}\,\mathrm{kg}$. A selection of the most discussed dark matter candidates is provided below.

- **Primordial black holes (PBHs):** Black holes formed from primordial density fluctuations represent a compelling non-particle dark matter candidate. Large PBHs face tight observational constraints from microlensing surveys and other probes, and ultralight PBHs would have evaporated through Hawking radiation by now. However, asteroid-mass PBHs could still account for all dark matter [7, 31].
- **WIMPs:** This broad class encompasses hypothetical particles with masses from a few GeV/c^2 up to around $10^5\,\mathrm{GeV}/c^2$, interacting with SM particles via weak-scale or weaker couplings [9]. In the early Universe, WIMPs would have been in thermal equilibrium with the primordial plasma. During cosmic expansion and cooling, WIMPs would "freeze out" of thermal equilibrium once their annihilation rate fell below the expansion rate, preserving a relic abundance. Remarkably, for a particle with weak-scale mass and couplings similar to those of the weak interaction, the thermal freeze-out mechanism naturally yields the observed relic abundance, a coincidence known as the "WIMP miracle" [7]. Many extensions of the SM, such as supersymmetry, naturally predict stable WIMP candidates

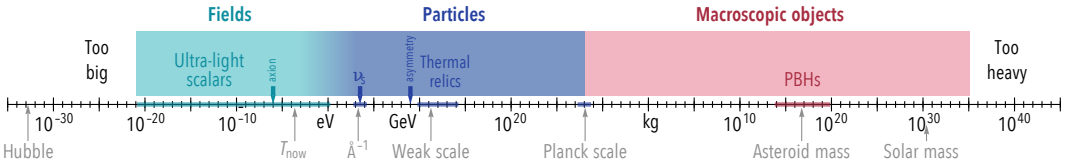

Figure 1.5.: Mass range of dark matter candidates, highlighting a few candidates. Adapted from [7].

like the lightest neutralino [7, 9]. Although a significant portion of the parameter space for minimal WIMP models has been ruled out by direct detection experiments (see Figure 1.8) and no new particles were discovered at colliders so far, variants with lower interaction cross sections or different masses remain viable candidates for dark matter [32].

- **Sterile neutrinos (ν_s):** Many of the properties required of dark matter candidates are met by SM neutrinos. However, at the onset of structure formation, SM neutrinos are relativistic and their abundance is too low to account for the dark matter density observed in galactic halos, ruling them out as main candidates. Beyond the three known active neutrino flavors, additional "sterile" neutrinos could exist that are right-handed and thus do not interact via the weak force. If these sterile neutrinos have masses in the keV range, they can be non-relativistic (cold or warm) by the time structure formation begins, making them viable candidates for dark matter [7, 33].
- **Axions and axion-like particles:** These are light bosonic candidates with typical masses below the meV scale, associated with scalar or pseudo-scalar fields [34]. Originally proposed to solve the strong CP problem in quantum chromodynamics [35], axions remain viable dark matter candidates even in broader theoretical contexts, independent of their connection to CP violation. Despite their very low masses, they would behave as CDM because they could be produced non-thermally via the misalignment mechanism [34].

1.3 Experimental Particle Dark Matter Searches

To resolve the long-standing mystery of dark matter, a wide array of experimental efforts aims to detect at least one of these candidates [7]. For particle dark matter, three complementary search strategies are employed:

- **Collider searches**, where experiments look for the production of dark matter particles or associated mediators in high-energy collisions [36, 37],
- **Indirect detection**, which searches for signals from dark matter annihilation or decay into SM particles in regions of high dark matter density with dedicated observatories [38],
- **Direct detection**, where dark matter particles interacting with SM particles in ultra-sensitive Earth-bound detectors are searched for [29, 39].

A thorough characterization of a dark matter candidate will ultimately require consistent signals from all three methods to disentangle degeneracies and confirm the particle's identity [32, 40]. As it is most relevant for the content of this thesis, in the following, we discuss a few considerations for the direct detection of WIMPs. Detectors for this search need to meet the following demanding requirements [29, 39]:

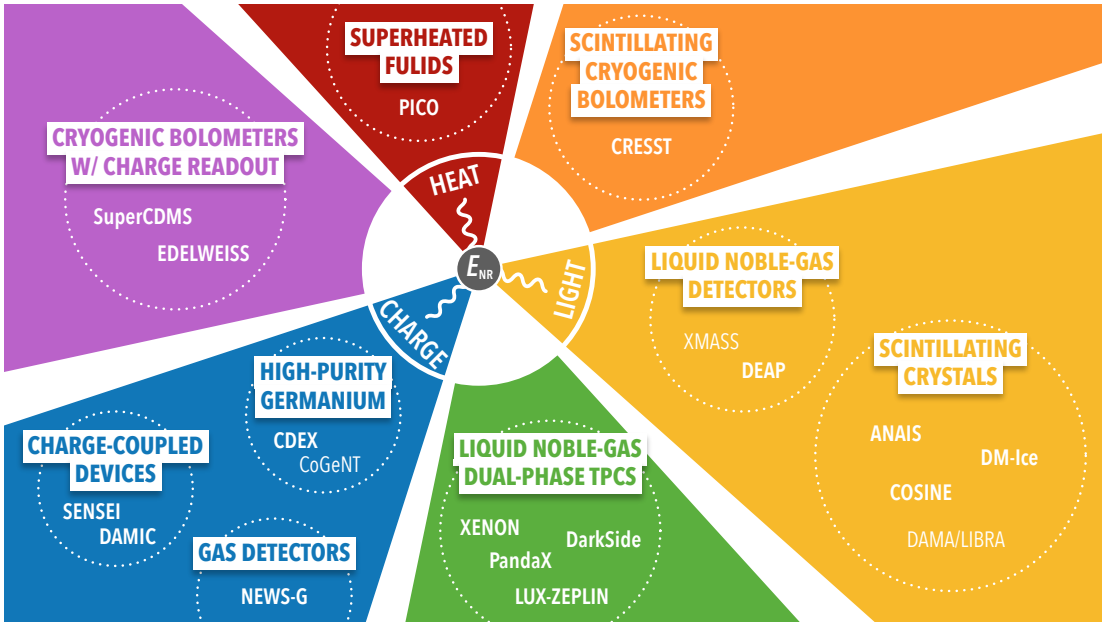

Figure 1.6.: Overview of detector technologies for direct dark matter detection via nuclear recoil (NR). Detection methods are categorized by their primary signal type: heat, ionization, scintillation, or combinations thereof. Representative active experiments are shown for each category, with three historic experiments displayed in regular font. Only experiments that have published dark matter constraints as of 2025 are included.

- **Exceptionally low background levels**, achieved through underground operation, material screening, veto systems, and analysis,
- **Low energy threshold** to detect the tiny recoil energies expected from dark matter interactions,
- **High target mass** to maximize exposure.

Particle detectors can register interactions through signals from liberated charge carriers, scintillation light, or heat (e.g., as phonons). While detecting one of them can suffice, combining multiple detection channels can be used to distinguish potential dark matter signals from backgrounds. An overview of detection concepts, grouped by their signal readout, is shown in Figure 1.6.

Elastic scattering of WIMPs on nuclei would produce nuclear recoils (NRs), which are experimentally detectable. The Solar System orbits the Galactic Center at approximately 220 km/s, inducing a relative velocity between the Earth and the dark matter halo. The expected nuclear recoil energy E_{NR} resulting from a WIMP of mass m_χ elastically scattering off a nucleus of mass m_A (mass number A) can be calculated using classical kinematics:

$$E_{\mathrm{NR}} = \frac{\mu^2 v^2}{m_A}(1 - \cos\theta), \tag{1.1}$$

where θ is the scattering angle in the center of mass frame and μ is the reduced mass of the WIMP-nucleus system. The maximum recoil energy occurs for $\cos\theta = -1$:

$$E_{\mathrm{NR}}^{\mathrm{max}} = 2\frac{\mu^2 v^2}{m_A}. \tag{1.2}$$

For a WIMP of mass $m_\chi = 100\,\mathrm{GeV}/c^2$ and velocity $v = 220\,\mathrm{km/s} \simeq 7.5 \times 10^{-4}\,c$ colliding with a xenon nucleus, this yields a maximum recoil energy of approximately 30 keV.

The expected differential recoil rate in a detector can be written as [7]:

$$\frac{\mathrm{d}R}{\mathrm{d}E_{\mathrm{NR}}} = N_{\mathrm{t}} \frac{\rho_\oplus}{m_\chi} \int_{v_{\mathrm{min}}} v f_\oplus(v) \frac{\mathrm{d}\sigma_A}{\mathrm{d}E_{\mathrm{NR}}} \mathrm{d}v, \tag{1.3}$$

which depends on astrophysical, detector, and particle physics parameters. Explicitly, the local dark matter density $\rho_\oplus$ as well as the dark matter velocity distribution $f_\oplus(v)$ in the detector's rest frame are astrophysical inputs. The detector with target mass m_{t} defines the number of target nuclei $N_{\mathrm{t}} = m_{\mathrm{t}}/m_A$. Finally, the particle physics properties, which we aim to measure, are the WIMP mass m_χ and the differential WIMP-nucleus scattering cross section $\mathrm{d}\sigma_A/\mathrm{d}E_{\mathrm{NR}}$. The minimum velocity required to induce a recoil with energy E_{NR} is $v_{\mathrm{min}} = \sqrt{m_A\,E_{\mathrm{NR}}/(2\mu^2)}$, which is obtained from rearranging Equation (1.2). Equation (1.3) can be approximated by a featureless, exponentially falling spectrum [41].

The precise spatial and velocity distribution of dark matter in the Milky Way remains uncertain. For direct detection experiments, the commonly adopted reference is the standard halo model (SHM): an isotropic, isothermal sphere whose velocity distribution in the Galactic rest frame is modeled as a Maxwell-Boltzmann truncated at the Galactic escape velocity of $v_{\mathrm{esc}} = 544\,\mathrm{km/s}$ [42]. This common benchmark model facilitates comparison between experimental results and allows straightforward rescaling should revised models predict strongly different local densities or velocity distributions [43]. While the exact form of $\rho(r)$ becomes increasingly uncertain toward the Galactic Center – critical for indirect searches – most halo models yield similar values at the Solar radius. The local dark matter density can be inferred from the Milky Way's rotation curve and the kinematics of nearby stars [44–46]. The canonical value used in direct detection is $0.3\,\mathrm{GeV}\,c^{-2}\,\mathrm{cm}^{-3}$, even though recent analyses favor somewhat higher values around $0.4\,\mathrm{GeV}\,c^{-2}\,\mathrm{cm}^{-3}$ [7]. To obtain the velocity distribution in the detector's rest frame $f_\oplus(v)$, we need to account for the Sun's motion around the Galactic Center, with a circular velocity of about 220 km/s. Additionally, the Earth's orbit around the Sun induces a periodic modulation of $f_\oplus(v)$ with higher average velocities (and thus higher expected rates) when Earth moves with the Sun's motion (summer), and lower when it moves against it (winter). This produces a detectable few-percent annual modulation in direct detection rates [47]. Furthermore, the apparent "wind" of dark matter always arrives from the same Galactic direction. This directionality is another compelling signature, in particular as it differs from the directionality of neutrino backgrounds [48] (see also Section 2.2).

Finally, we need to make an assumption about the type of interaction to obtain the differential cross section for Equation (1.3). The simplest WIMP-nucleus interactions are categorized as spin-dependent (SD) or spin-independent (SI), depending on whether they do or do not depend on the nuclear spin. For the SI case, WIMPs scatter coherently off the entire nucleus, resulting in A^2 enhancement of the cross section. The differential SI WIMP-*nucleus* cross section can be written in good approximation as [7]:

$$\frac{\mathrm{d}\sigma_A^{\mathrm{SI}}}{\mathrm{d}E_{\mathrm{NR}}} = \frac{m_A}{2v^2\mu_N^2}\,A^2\,\sigma^{\mathrm{SI}}\,F^2(q). \tag{1.4}$$

Here, σ^{SI} is the average SI WIMP-*nucleon* cross section,[3] μ_N the WIMP-nucleon reduced mass,

[3] The parameter for which direct detection experiments typically report bounds.

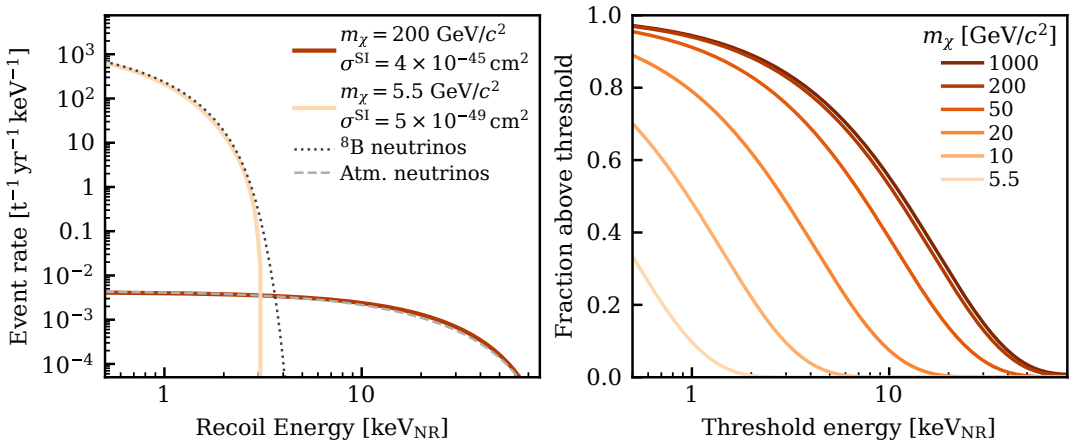

Figure 1.7.: *Left:* Recoil energy spectra for WIMP signals with spin-independent (SI) coupling compared to nuclear recoils (NRs) from solar ^{8}B and atmospheric neutrinos (see Chapter 2). *Right:* Fraction of WIMP recoils above threshold energy as a function of WIMP mass. Spectra were calculated using code from [49].

and $F(q)$ the nuclear form factor accounting for coherence loss at large momentum transfer. The expected SI recoil energy spectra for different WIMP masses, along with the fraction of detectable events above experimental thresholds, are presented in Figure 1.7. In contrast, SD interactions arise from WIMPs coupling to the spin content of protons and neutrons, yielding a differential cross section [50]:

$$\frac{d\sigma^{SD}}{dE_{NR}} = \frac{16\, m_A\, G_F^2}{\pi\, v^2} \left[a_p \langle S_p \rangle + a_n \langle S_n \rangle\right]^2 \frac{J+1}{J} \frac{S(q)}{S(0)}. \tag{1.5}$$

Here, G_F is the Fermi constant, $a_{p,n}$ are the effective WIMP couplings to protons and neutrons, $\langle S_{p,n} \rangle$ the respective spin expectation values in the nucleus, J the the total nuclear spin, and $S(q)$ the spin-structure function describing momentum dependence. A nonzero SD cross section requires nuclei with unpaired nucleons, i.e. $\langle S_{p,n} \rangle \neq 0$. For xenon, only ^{129}Xe ($\langle S_p \rangle = 0.010$, $\langle S_n \rangle = 0.329$ [51]) and ^{131}Xe ($\langle S_p \rangle = -0.009$, $\langle S_n \rangle = -0.272$ [51]) contribute (see Table 3.1).

The total expected number of WIMP events in a detector, for a given cross section and WIMP mass, is obtained by integrating the differential event rate over recoil energies above the detection threshold and multiplying it by the exposure time. When an experiment observes no WIMP-like signals, it can place exclusion limits on the WIMP parameter space.[4] Details of the statistical analysis are discussed in Section 4.5. Figure 1.8 shows the current status of direct WIMP searches as well as the "neutrino fog", which is discussed in Section 2.2. To date, no credible dark matter signal has been detected, resulting in stringent constraints on the WIMP parameter space.

[4] The logic is: "If WIMPs had these properties, we should have observed n events; since we observed none, we can exclude WIMPs with these properties."

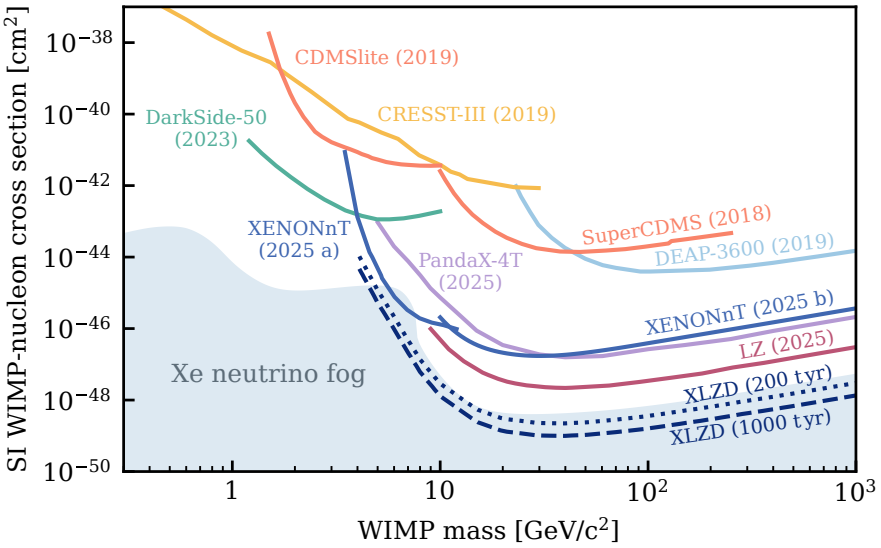

Figure 1.8.: Current upper limits (90 % CL) on the spin-independent (SI) WIMP-nucleon cross section from direct detection experiments. Results include CRESST-III [52], CDMSlite [53], SuperCDMS [54], DEAP-3600 [55], DarkSide-50 [56], PandaX-4T [57], LUX-ZEPLIN (LZ) [58], and XENONnT [59] (a) and [Paper II] (b). Dashed and dotted lines show projected exclusion sensitivities for XLZD [60]. The xenon "neutrino fog" region ($n > 2$, see Section 2.2) from [49] is also shown.

2

Coherent Elastic Neutrino-Nucleus Scattering

To explain missing energy in β-decay, Pauli proposed in 1930 the existence of a new fundamental particle [61]. Fermi built on this, naming it the "neutrino", and incorporating it in his theory of weak interactions [62]. This theory predicted tiny scattering cross sections for neutrinos, making their experimental confirmation challenging. However, 25 years later, Cowan and Reines succeeded in the first direct detection [63]. It took another 40 years to uncover that neutrinos have a small but nonzero mass, causing neutrino oscillations [64]. By now, neutrino physics is a rich field studying these elusive particles and their sources on various scales.

A variety of neutrino sources exist [65]. We focus on those shown in Figure 2.1. The largest flux at Earth, about $7 \times 10^{10}\,\mathrm{cm}^{-2}\,\mathrm{s}^{-1}$, comes from nuclear fusion processes in the Sun [65]. Most solar neutrinos are produced in the fusion of two protons into a deuterium nucleus (*pp* neutrinos). Due to the low energies of *pp* neutrinos, the dominant detected neutrino flux in many experiments comes from ^{8}B neutrinos, which originate from the β-decay

$$^8\mathrm{B} \rightarrow {}^8\mathrm{Be}^* + e^+ + \nu_e \tag{2.1}$$

with an endpoint energy around 15 MeV. At higher energies but with lower flux, atmospheric neutrinos arise from cosmic ray interactions in the Earth's atmosphere. In between are neutrinos from all past core-collapse supernovae, known as diffuse supernova neutrino background (DSNB), which have yet to be detected.

2.1 "Large" Neutrino Cross Sections

In 1974, the coherent elastic neutrino-nucleus scattering (CEνNS) process was theoretically predicted [66, 67]. It is an elastic, neutral-current Standard Model (SM) process mediated by the Z^0 boson:

$$\nu_\alpha + {}^A_Z\mathcal{N} \rightarrow \nu_\alpha + {}^A_Z\mathcal{N}, \tag{2.2}$$

where ν_α is a neutrino of flavor $\alpha = e, \mu, \tau$, and ${}^A_Z\mathcal{N}$ is a nucleus with a number of A nucleons (Z protons and $N = A - Z$ neutrons). The nature of scattering depends on the relationship

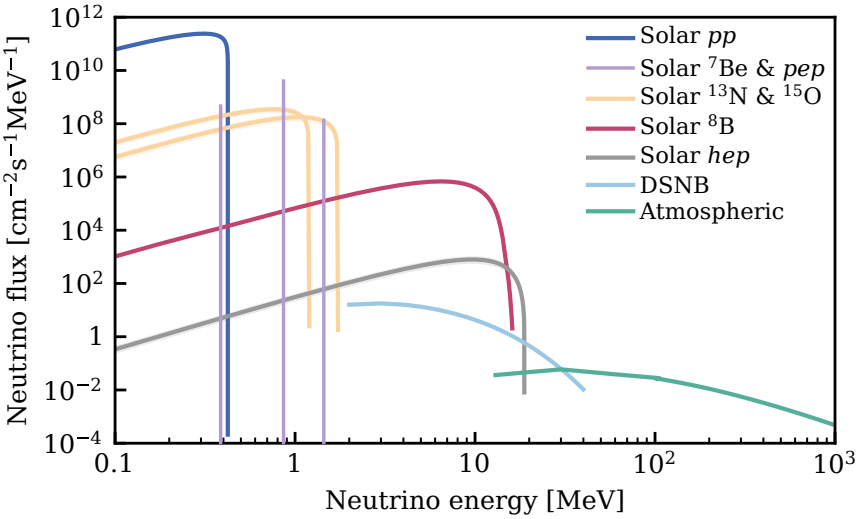

Figure 2.1.: Spectra of neutrinos from the Sun, the diffuse supernova neutrino background (DSNB), and the atmosphere. For the DSNB and atmospheric spectra, both neutrino and antineutrino fluxes are summed. Data from [65].

between the de Broglie wavelength of the exchanged Z^0 boson, $\lambda_{Z^0} = h/q$ (with h as Planck's constant and $q = |\vec{q}|$ the momentum transfer), and the nuclear radius R. Different regimes are illustrated in Figure 2.2. For large momentum transfer ($\lambda_{Z^0} \ll R$), the scattering is predominantly off individual nucleons, generally resulting in their ejection. For $\lambda_{Z^0} \lesssim R$, the interaction occurs with groups of nucleons, exciting the nucleus $\mathcal{N}^*$. Coherent scattering occurs when the wavelength exceeds the nuclear radius ($\lambda_{Z^0} \gtrsim R$). In this regime, the neutrino interacts with the nucleus as a whole, resulting in nuclear recoils (NRs) of energy E_{NR}. The momentum transfer is then approximated as $q \simeq \sqrt{2 m_A E_{\mathrm{NR}}}$, with nuclear mass m_A. For a xenon nucleus,[1] the coherence criterion is fulfilled for $q \lesssim 40\,\mathrm{MeV}/c$, restricting coherent scattering to recoil energies $E_{\mathrm{NR}} \lesssim 7\,\mathrm{keV}$. Since the average momentum transfer scales with neutrino energy, the CEνNS process is only observable for low-energy neutrinos with $E_\nu \lesssim 30\,\mathrm{MeV}$ [68]. For $E_{\mathrm{NR}} \ll m_A$, the differential CEνNS cross section can be written in good approximation [69] as

$$\frac{\mathrm{d}\sigma}{\mathrm{d}E_{\mathrm{NR}}} = \frac{G_{\mathrm{F}}^2}{2\pi}\frac{Q_{\mathrm{W}}^2}{4} F^2(q)\, m_A \left(2 - \frac{m_A E_{\mathrm{NR}}}{E_\nu^2}\right) \simeq \frac{G_{\mathrm{F}}^2}{2\pi}\frac{N^2}{4} F^2(q)\, m_A \left(2 - \frac{m_A E_{\mathrm{NR}}}{E_\nu^2}\right), \qquad (2.3)$$

where G_{F} is the Fermi constant and $Q_{\mathrm{W}} = [N - (1 - 4\sin^2\theta_{\mathrm{W}})Z]$ the weak nuclear charge with the weak mixing angle θ_{W}. Since $\sin^2\theta_{\mathrm{W}} \simeq 0.239$, the term proportional to Z nearly vanishes, yielding $\mathrm{d}\sigma/\mathrm{d}E_{\mathrm{NR}} \propto N^2$. The nuclear form factor $F(q)$ accounts for the loss of coherence at higher momentum transfer, and is the Fourier transform of the nucleon spatial distribution.

While the coherent enhancement factor $\sim N^2$ makes the cross section for this process quite sizeable for neutrino standards, the resulting recoil energies are so small that a detection is challenging. It took over 40 years for the experimental confirmation of this process by the COHERENT collaboration [70]. They measured neutrinos produced from pion decay at rest from the Spallation Neutron Source (SNS) with a CsI(Na) detector. With the same neutrino source, the COHERENT collaboration has subsequently also measured the process in liquid

[1] $A = 131$, $m_A = 122\,\mathrm{GeV}/c^2$, $R = 4.8\,\mathrm{fm}$

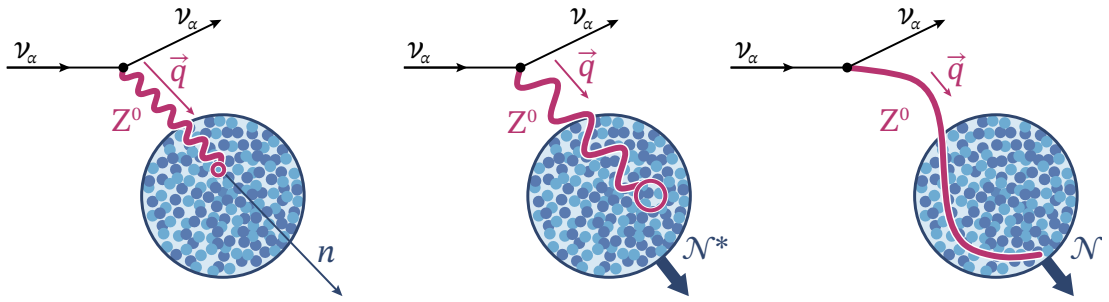

Figure 2.2.: Illustration of the coherence criterion for CEνNS. At high momentum transfer q, the Z^0 boson's De Broglie wavelength λ_{Z^0} becomes much smaller than the nuclear radius R, enabling interactions with individual nucleons and resulting in inelastic scattering. When $\lambda_{Z^0} \gtrsim R$, the neutrino scatters coherently off the entire nucleus in an elastic process. At intermediate momentum transfers, elastic but incoherent scattering occurs. Concept adapted from [68].

argon [71] and germanium targets [72]. More recently, the CEνNS process has been measured from reactor neutrinos by the CONUS collaboration [73] and solar neutrinos by PandaX-4T [74] and XENONnT [Paper III], which is discussed in Section 7.2.

2.2 CEνNS as a Background: The Neutrino Fog

Neutrinos scattering in dark matter detector targets produce low-energy, single-scatter NR events that mimic the expected signature of weakly interacting massive particle (WIMP) interactions. Figure 1.7 (left) shows that solar and atmospheric neutrino recoil spectra resemble the spectra expected from 5.5 GeV/c^2 and 200 GeV/c^2 WIMPs, respectively. Since Earth is constantly bombarded by a high flux of astrophysical neutrinos that cannot be shielded,[2] astrophysical neutrinos eventually limit the discovery potential of classical WIMP detectors [75].

The transition to neutrino-limited sensitivity is gradual, motivating the term "neutrino fog" rather than the previously used "neutrino floor". The neutrino fog, defined in [49], quantifies how additional exposure improves the median $3\,\sigma$ WIMP discovery potential[3] through its gradient with exposure. This concept is illustrated in Figure 2.3. The discovery potential σ improves with increasing exposure, which is proportional to the expected number of CEνNS events N. The scaling follows $\sigma \propto N^{-1/n}$, where n is the "opacity" index characterizing three distinct regimes:

- **Background-free regime ($n = 1$):** With $N < 1$ expected CEνNS events, sensitivity scales linearly with exposure (no backgrounds other than CEνNS assumed here).
- **Statistical regime ($n = 2$):** Neutrinos become a sizeable background, but Poisson uncertainty $\propto 1/\sqrt{N}$ of this background dominates.
- **Systematic regime ($n > 2$):** Discovery potential plateaus as systematic uncertainties in neutrino flux outgrow potential WIMP signals.

[2] Assuming a cross section of 10^{-43} cm^2, the mean free path in lead is approximately 3 ly – roughly the distance to Proxima Centauri. Understandably, shielding solar neutrinos is not an active research area for future dark matter detectors.

[3] The WIMP-nucleon cross section for which 50 % of experiments would yield at least $3\,\sigma$ discovery significance.

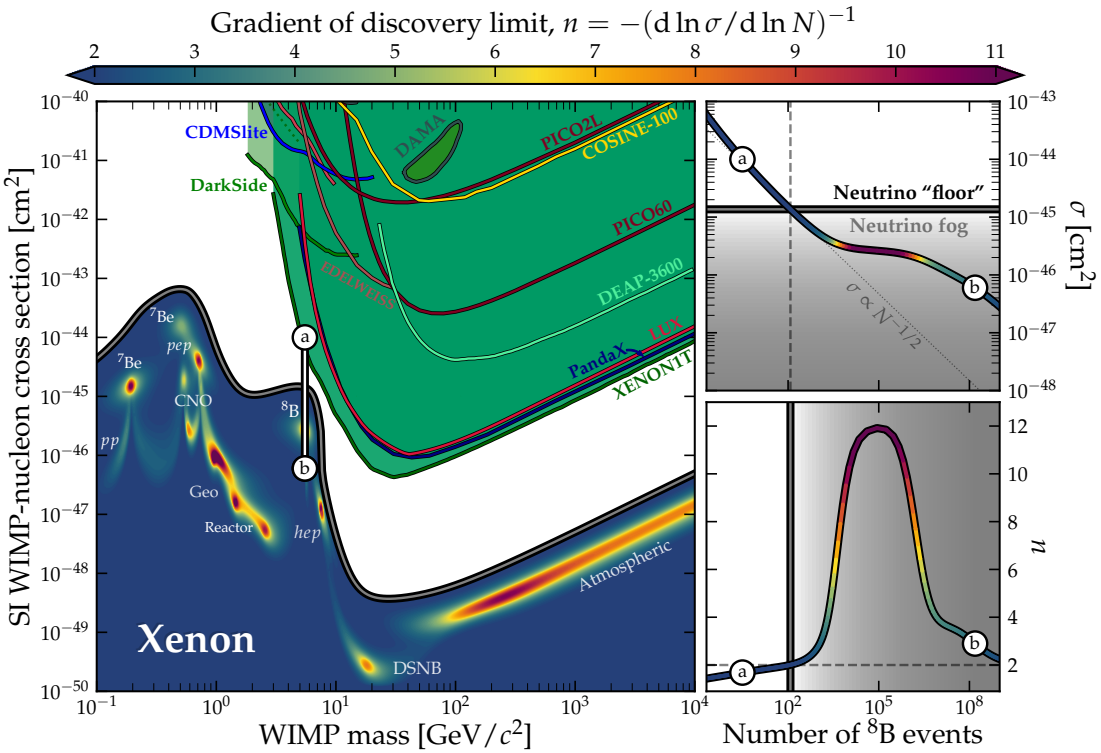

Figure 2.3.: Illustration of the "neutrino fog" definition. *Left:* Spin-independent (SI) WIMP-nucleon cross section versus mass showing exclusion regions (green) and the opacity index n on the color axis. *Top right:* WIMP discovery potential σ for a 5.5 GeV/c^2 WIMP versus number of ^{8}B CEνNS events (proportional to exposure). *Bottom right:* Opacity index n how flat σ evolves with increasing exposure. Reproduced from [49].

Crucially, the onset of the systematic regime and thus the severity of the neutrino fog depend on neutrino flux uncertainties. Tighter constraints shift the neutrino fog to lower cross sections. One intriguing feature visible in Figure 2.3 is that experiments boldly pushing through the neutrino fog can eventually emerge on the other side. While CEνNS and WIMP recoil spectra are remarkably similar, subtle spectral differences exist. Once a detector – originally designed as a low-background experiment – has accumulated hundreds of millions of neutrino events, it could use these differences to distinguish WIMP signals and return to the favorable $\sigma \propto 1/\sqrt{N}$ scaling. Of course, this approach would require scaling current detectors by over six orders of magnitude, a proposal that might face some skepticism during funding reviews. A more practical solution for surpassing the neutrino fog are detectors capable of measuring NR directionality [48]. Such detectors could distinguish between neutrino backgrounds (solar-directed or isotropic atmospheric) and potential WIMP interactions, which should preferentially point toward "dark matter wind" direction (see Section 1.3). Current liquid xenon (LXe) detectors are beginning to encounter the solar ^{8}B neutrino fog at WIMP masses around 6 GeV/c^2 (see Section 7.2). The atmospheric neutrino fog, relevant for higher masses, remains approximately two orders of magnitude away – a target for next-generation LXe observatories (see Section 3.4).

2.3 CEνNS as a Signal

While coherent neutrino scattering eventually presents a challenging background for direct dark matter searches, the same interactions also enable a rich physics program. In Equation (2.3) we approximated the weak nuclear charge as $Q_{\mathrm{W}} \simeq N$, neglecting the small contribution from proton couplings. This contribution, however, depends sensitively on the value of the weak mixing angle θ_{W}. Measurements of CEνNS thus allow constraining θ_{W} at low energies, where experimental data is scarce [68]. Deviations from the SM prediction of the CEνNS cross section would be a clear indication for new physics [68, 76]. In the SM, the process of Equation (2.2) is mediated by the Z^0 boson. However, many extensions of the SM predict additional mediators, such as a massive vector boson Z'. Alternatively, if neutrinos possess anomalous electromagnetic properties, such as a magnetic moment larger than the SM expectation or a nonzero electric millicharge, the process could even be mediated by photons. Precision measurements of the CEνNS cross section therefore provide a sensitive probe for such beyond-SM scenarios. Beyond particle physics, CEνNS measurements in the partially coherent regime (e.g., at the SNS) allow determining the nuclear form factor $F(q)$, yielding information on the largely unknown neutron distribution within nuclei [68]. Finally, because the CEνNS process is flavor-independent, it offers a complementary method to study astrophysical neutrino sources. Measurements using this channel can probe solar, atmospheric, or supernova neutrinos with different systematics than traditional neutrino experiments [76–78].

3

The XENON Project

Beginning in 2006, the XENON dark matter project has demonstrated the power of liquid xenon (LXe) time projection chambers (TPCs) for direct detection experiments. XENON10, featuring an active target of only 15 kg of LXe [79], marked the start of this successful program. Even with a modest exposure of 0.9 kg yr, it quickly surpassed other technologies [80]. Successive detectors increased the target mass: XENON100 (62 kg) [81], XENON1T (2 t) [82], and the current XENONnT (5.9 t) [83]. Over less than two decades, the exposure – and with it the exclusion limits on the weakly interacting massive particle (WIMP)-nucleon cross section – has improved by more than three orders of magnitude, following an approximately linear scaling,[1] as shown in Figure 3.1. This remarkable progress was enabled by simultaneously reducing backgrounds by four orders of magnitude. The next-generation XLZD experiment, now in planning, aims to extend sensitivity by another three orders of magnitude, reaching the 50 GeV/c^2 "neutrino fog" at $\sigma^{\mathrm{SI}} \simeq 10^{-49}\,\mathrm{cm}^2$ [60].

This chapter provides an overview of the properties that make LXe an exceptional target material (Section 3.1), describes the working principle of dual-phase TPCs (Section 3.2), introduces the XENONnT experiment (Section 3.3), and outlines plans for the next-generation XLZD detector (Section 3.4).

3.1 Xenon as a Detector Medium

LXe is the target material of choice for the leading dark matter experiments due to its excellent physical and chemical properties, such as a high atomic number, high density, and large scintillation and ionization yields. Currently, three major dark matter experiments employ LXe targets: XENONnT, LUX-ZEPLIN (LZ) [91], and PandaX-4T [92]. Beyond dark matter searches, LXe detectors have important applications in particle physics including searches for processes beyond the Standard Model (SM) such as neutrinoless double-beta decay [93, 94] and charged lepton flavor violation in muon decay [95, 96]. Additionally, LXe-based detectors aim to measure coherent elastic neutrino-nucleus scattering (CEνNS) from reactor neutrinos [97, 98]. The material's prompt and substantial scintillation response also make it compelling for medical imaging applications [99–102].

[1] This means that the limit on the absolute number of WIMP events stayed roughly constant.

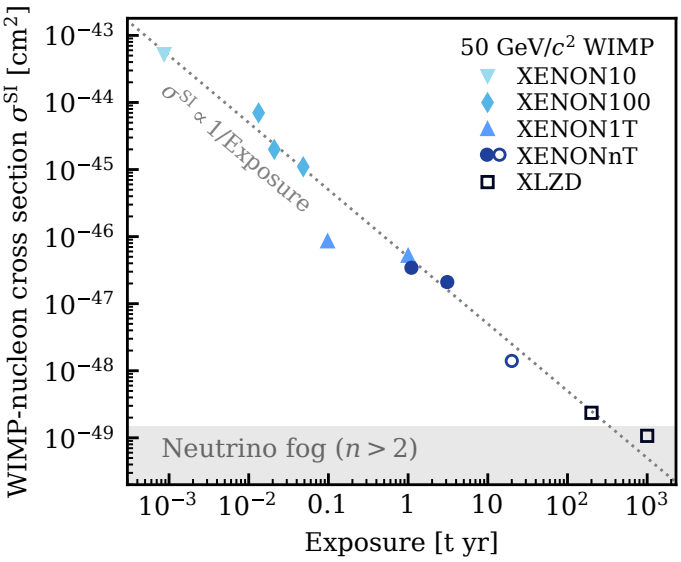

Figure 3.1.: Evolution of 90 % confidence level (CL) upper limits on the spin-independent (SI) WIMP-nucleon cross section for a 50 GeV/c^2 WIMP as a function of exposure. Filled markers show results from XENON10 [80], XENON100 [84–86], XENON1T [87, 88], and XENONnT [89] [Paper II]. Open markers indicate design sensitivities for XENONnT and XLZD [60, 90]. The dotted gray line corresponds to linear scaling with exposure, while the gray band represents the neutrino fog from [60] (see Section 2.2 for definition of n).

3.1.1 Properties of xenon

Xenon offers several advantages for rare-event searches [103, 104]. As the heaviest stable noble gas ($A \sim 131$), it enhances the SI WIMP-nucleon interaction rate, which roughly scales with A^2 (Equation (1.4)). Xenon is chemically inert, making it straightforward to handle and purify in large quantities. The noble gas liquefies at temperatures between 165 and 180 K and pressures of 1.5 to 2 bar, achievable with modest cryogenic systems. Its density in liquid form ($\sim 2.9\,\text{g/cm}^3$ [105]) allows for large target masses in compact, scalable detectors. Combined with its high atomic number ($Z = 54$), xenon provides strong self-shielding against external radioactivity. This leads to an inner volume with particularly low background levels.

Typical length scales for various particles in LXe are shown in Figure 3.2, with mean free path (MFP) plotted for neutrons and photons and continuous slowing-down approximation (CSDA) range for charged particles. Neutrons do not interact electromagnetically and instead loose their energy via collisions with xenon nuclei, resulting in MFPs of 10 to 20 cm for energies between 10 keV and 10 MeV. Few-MeV γ-rays exhibit a MFP of ~ 10 cm, interacting primarily via Compton scattering. At lower energies, photoelectric absorption dominates, causing the MFP to decrease rapidly. Low-energy charged particles lose their energy primarily through ionization and excitation. Electrons exhibit ranges spanning from one centimeter at few-MeV energies down to below 100 µm for energies below 100 keV, while α-particles with typical few-MeV energies have even shorter ranges between 10 and 100 µm.

Natural xenon comprises nine isotopes, which are listed in Table 3.1. Only ^{124}Xe and ^{136}Xe undergo radioactive decay,[2] both via second-order weak processes. Their exceptionally long

[2] For ^{126}Xe and ^{134}Xe, radioactive decays are also predicted but rates are so low that this has never been measured so far.

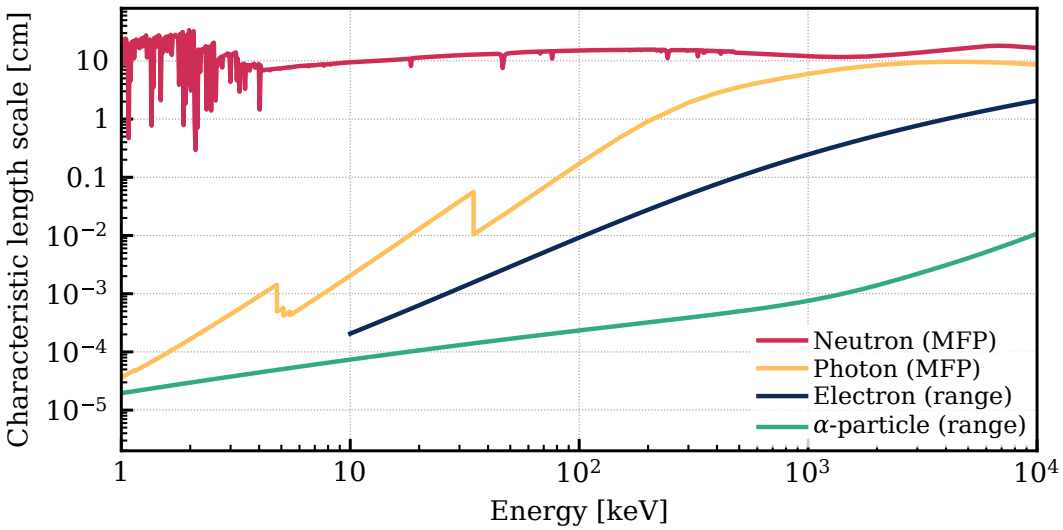

Figure 3.2.: Characteristic length scales of particles in LXe as a function of energy. The mean free path (MFP) is shown for neutrons and photons, while the continuous slowing-down approximation (CSDA) range is plotted for charged particles. Neutron data represent abundance-weighted averages over all stable xenon isotopes (see Table 3.1). Data from [106–108].

half-lives – most notably ^{124}Xe at 1.1×10^{22} yr, the longest half-life ever measured [109, 110] – result in small intrinsic backgrounds. These isotopes also allow for sensitive searches for neutrinoless double-weak decay processes [94, 111, 112]. With ^{129}Xe and ^{131}Xe, xenon also contains two isotopes with nonzero nuclear spin and significant abundance, allowing sensitivity to spin-dependent (SD) WIMP-nucleon interactions.

Table 3.1.: Properties of naturally occurring xenon isotopes. Isotopic composition from [113].

Isotope	**Abundance** [%]	**Half-life** [yr]	**Decay mode**	**Spin**
^{124}Xe	0.10	1.1×10^{22} [110]	DEC	0
^{126}Xe	0.09	$> 1.9 \times 10^{22}$ [114]	DEC†	0
^{128}Xe	1.91	stable	–	0
^{129}Xe	26.40	stable	–	$1/2$
^{130}Xe	4.07	stable	–	0
^{131}Xe	21.23	stable	–	$3/2$
^{132}Xe	26.91	stable	–	0
^{134}Xe	10.44	$> 2.8 \times 10^{22}$ [115]	$\beta\beta^\dagger$	0
^{136}Xe	8.86	2.23×10^{21} [116]	$\beta\beta$	0

† Theoretically predicted but not yet observed.

A further key advantage of LXe is its excellent ionization and scintillation properties, which is discussed in the following. The dominant emission mechanism is excimer decay (see also Section 8.1), which produces photons with energies too low to be absorbed by xenon atoms. As a result, LXe remains transparent to its own scintillation light.

3.1.2 Signal generation in xenon

When a particle traverses LXe, it deposits energy via interactions with xenon atoms. Particles interacting with the electron shell (charged particles, photons, neutrinos) produce electronic recoil (ER) events, while those interacting with the nucleus (neutrons, neutrinos via CEνNS, WIMPs if they exist) produce nuclear recoil (NR) events. In both cases, energy deposition leads to excitation and ionization, producing scintillation photons and free electrons that serve as detectable quanta. For NRs, approximately 80 % of the deposited energy is lost as unobservable heat [117–119]. A schematic of quanta generation is shown in Figure 3.3.

Most scintillation light in LXe originates from the de-excitation of the lowest-lying excimer state, which emits vacuum ultraviolet (VUV) photons at $\sim 175\,\mathrm{nm}$ [120, 121]:

$$\mathrm{Xe}_2^* \;\rightarrow\; 2\mathrm{Xe} + h\nu. \tag{3.1}$$

This process exhibits both a fast and a slow decay component with time constants of $\sim$4 ns and 20–40 ns, respectively [122–124]. Excimers form through two pathways. The first involves three-body collisions of directly excited atoms with ground-state atoms:

$$\mathrm{Xe}^* + \mathrm{Xe} + \mathrm{Xe} \;\rightarrow\; \mathrm{Xe}_2^* + \mathrm{Xe}. \tag{3.2}$$

The second pathway proceeds through electron-ion recombination. Following ionization, xenon ions rapidly form molecular ions:

$$\mathrm{Xe}^+ + \mathrm{Xe} + \mathrm{Xe} \;\rightarrow\; \mathrm{Xe}_2^+ + \mathrm{Xe}. \tag{3.3}$$

Electrons lose kinetic energy through collisions[3] and thermalize on a timescale of $\sim$10 ns [125, 126], then recombine with molecular ions:

$$\mathrm{Xe}_2^+ + e^- \;\rightarrow\; \mathrm{Xe}^{**} + \mathrm{Xe}. \tag{3.4}$$

The resulting highly excited atom de-excites via intermediate dimer formation:

$$\mathrm{Xe}^{**} + \mathrm{Xe} + \mathrm{Xe} \;\rightarrow\; \mathrm{Xe}_2^{**} + \mathrm{Xe} \;\rightarrow\; \mathrm{Xe}^* + \mathrm{Xe} + \mathrm{Xe}. \tag{3.5}$$

The resulting excited atom then forms an excimer via Equation (3.2). For NRs, the ionization density is so high that bi-excitonic quenching ("Penning ionization") can occur:

$$\mathrm{Xe}^* + \mathrm{Xe}^* \rightarrow \mathrm{Xe}^+ + \mathrm{Xe} + e^-. \tag{3.6}$$

This process converts two excited atoms into a single ion, effectively reducing the number of observable quanta.

For reasons detailed below, it is advantageous to detect scintillation and charge signals separately. Applying an electric drift field separates electrons and ions and thus suppresses recombination. Some electrons escape recombination even without an applied field if they travel sufficiently far before thermalizing [128]. The light yield (LY) and charge yield (QY) quantify the number of observable quanta per unit energy deposited. Figure 3.4 shows these yields for

[3] If their energy is high enough, they can excite or ionize xenon atoms (see Figure 3.3). Sub-excitation electrons, on the other hand, can only scatter elastically.

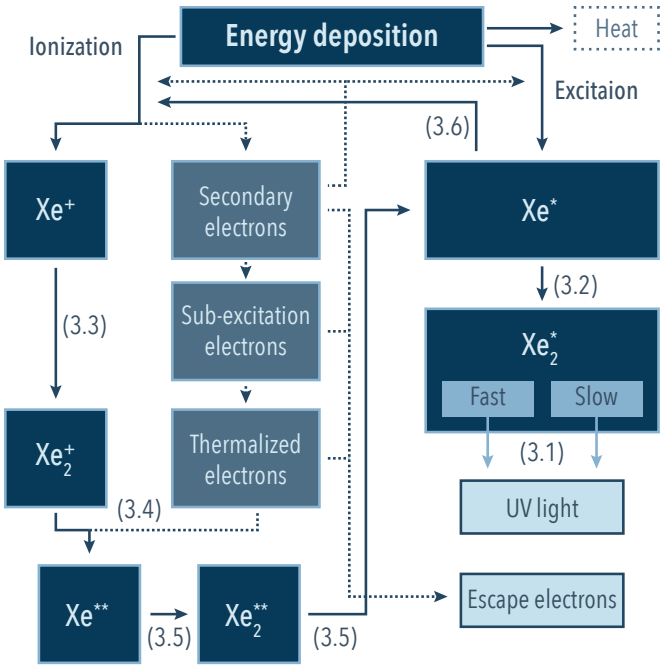

Figure 3.3.: Schematic of the xenon scintillation process. Numbers in parentheses refer to equations in the text. Adapted from [127].

ER and NR at electric fields between 20 and 200 V/cm. ERs achieve excellent light yields exceeding 50 ph/keV, while NRs still produce sizeable yields above 10 ph/keV. The field dependence of light and charge yields is anti-correlated: higher fields extract more electrons, reducing scintillation through decreased recombination. For NRs, this field dependence is less pronounced due to the higher ionization density, making recombination nearly inevitable regardless of field strength. Since no complete theoretical model exists for the microphysics processes involved in signal generation, the semi-empirical "Noble Element Simulation Technique" (NEST) model [129, 130] is used in LXe experiments to predict yields as a function of particle type, energy, and electric field.

3.2 Working Principle of Dual-Phase TPCs

A dual-phase TPC measures both prompt scintillation photons and ionization electrons from energy depositions in LXe, as illustrated in Figure 3.5. The detector consists of a LXe target with a thin layer of gaseous xenon (GXe) at the top. Photosensor arrays at the top and bottom detect prompt scintillation photons (**S1 signal**). A homogeneous electric field applied across the LXe target between cathode and gate electrodes (typically a few hundred V/cm) suppresses electron-ion recombination and drifts the ionization electrons upward at constant velocity [131]. Upon reaching the gate electrode positioned just below the liquid-gas interface, electrons encounter a much stronger extraction field between the gate and anode (several kV/cm). This field extracts electrons into the gas phase, where they accelerate above xenon's excitation threshold and produce proportional secondary scintillation through electroluminescence (**S2 signal**). Since the VUV emission spectra in gas and liquid phases are similar, both S1 and S2 signals can be detected by the same photosensor arrays.

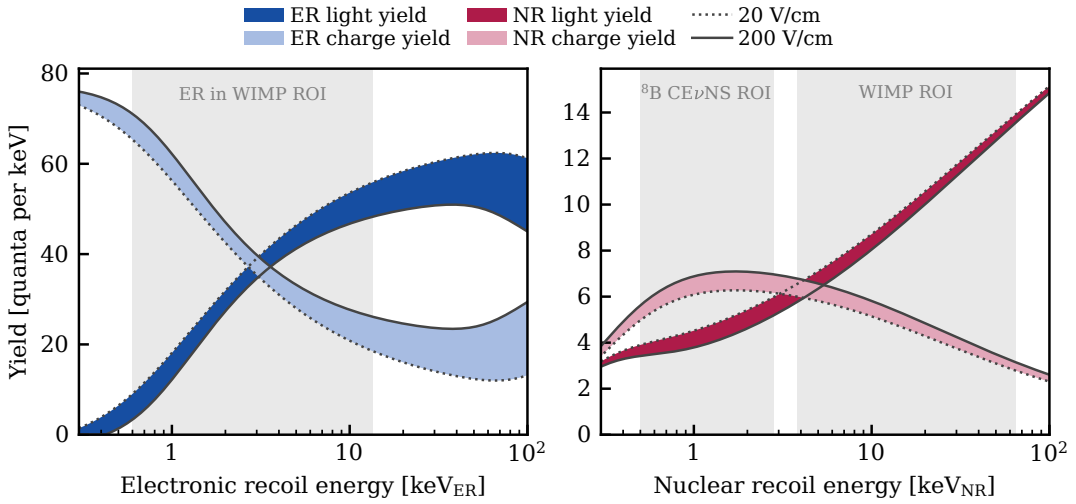

Figure 3.4.: Light and charge yields of LXe as a function of deposited energy for electronic recoil (ER) (left) and nuclear recoil (NR) (right). Bands show variation with drift field from 20 V/cm (dotted) to 200 V/cm (solid). Note the fivefold difference in yield scale between ER and NR. The region of interest (ROI) for ^{8}B CEνNS and WIMP searches, and the relevant ER background range, are indicated in gray.

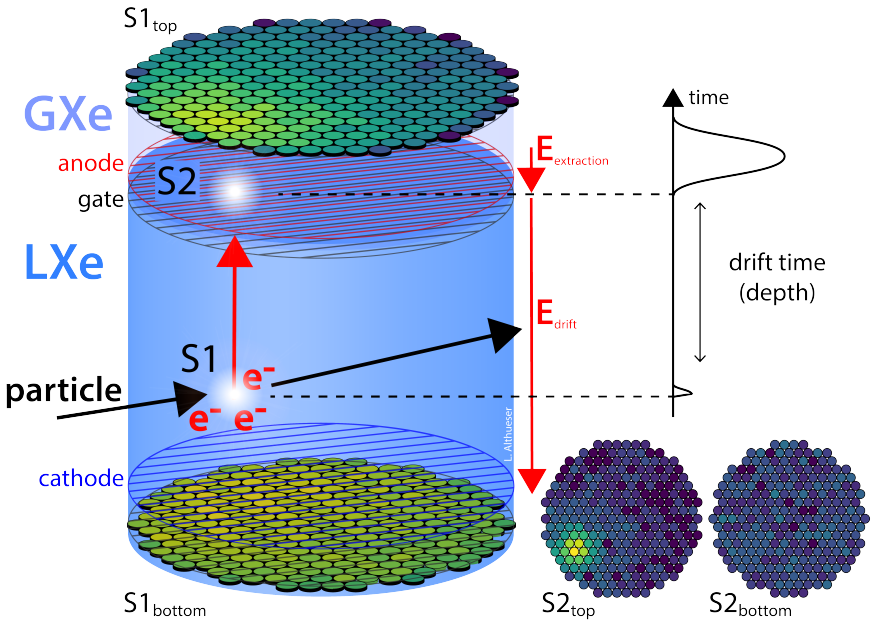

Figure 3.5.: Illustration of a dual-phase time projection chamber (TPC). See text for details. Courtesy of Lutz Althüser.

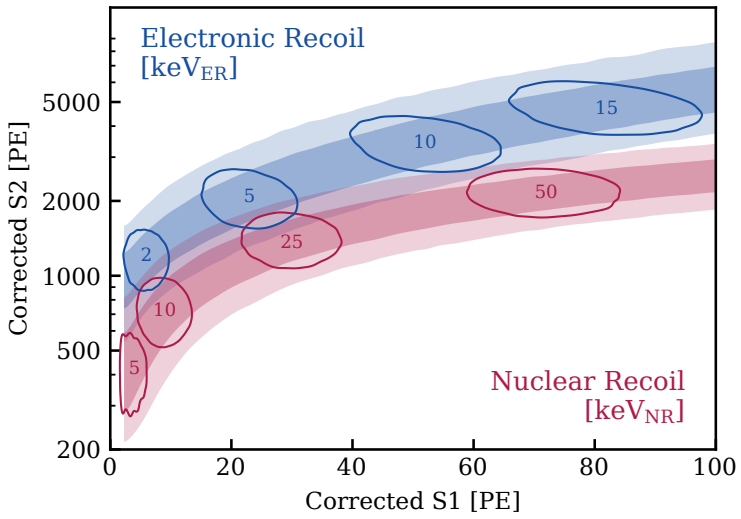

Figure 3.6.: Bands formed by electronic recoil (ER) (blue) and nuclear recoil (NR) events in corrected S1–S2 space for flat energy spectra. Dark (light) shading indicates bands containing 68 % (95 %) of events. In addition, 68 % contours are shown for selected mono-energetic peaks. Distributions are simulated with `nestpy` [138] using typical detector parameters.

The interaction position of an event is reconstructed using the S1 and S2 signals. The time difference between S1 and S2 gives the depth (Z) via the constant electron drift velocity. The horizontal position (X, Y), which defines the radial coordinate $\mathrm{R} = \sqrt{\mathrm{X}^2 + \mathrm{Y}^2}$, is determined from the S2 hit pattern in the top sensor array. This three-dimensional reconstruction enables selection of a low-background fiducial volume (FV) and informs signal and background modeling.

The deposited energy is reconstructed from combining both signal strengths:

$$E = \frac{W}{L}(n_{\mathrm{ph}} + n_{\mathrm{e}}) = \frac{W}{L}\left(\frac{\mathrm{S1}}{g_1} + \frac{\mathrm{S2}}{g_2}\right), \tag{3.7}$$

where n_{ph} and n_{e} are the number of scintillation photons and ionization electrons after recombination, $W = (13.7 \pm 0.2)\,\mathrm{eV/quantum}$ [132] is the average energy to produce a quantum, and $g_1 \equiv \mathrm{S1}/n_{\mathrm{ph}}$, $g_2 \equiv \mathrm{S2}/n_{\mathrm{e}}$ are detector-dependent parameters (typical values are $g_1 \sim 0.1\,\mathrm{photoelectron(PE)/ph}$, $g_2 \sim 20\,\mathrm{PE}/e$). The quenching factor L quantifies the fraction of deposited energy that produces detectable signals, accounting for energy lost as unobservable heat. For ERs, heat losses are negligible and thus $L = 1$, while for NRs, $L < 1$ and varies with energy. The different energy scales for ER and NR are given in units of $\mathrm{keV_{ER}}$ and $\mathrm{keV_{NR}}$, respectively. This is illustrated in Figure 3.6, which shows mono-energetic NR and ER peaks in S1–S2 space. Because light and charge signals are strongly anti-correlated, combining them improves energy resolution [133, 134].

Figure 3.6 also demonstrates that ER and NR events form distinct bands in S1–S2 space [135]. The ratio of initially excited to ionized atoms is between 1:5 and 1:17 for ER [136, 137] and 1:1 for NR [119], which results in a lower charge-to-light ratio for NR events compared to ER events.[4]

[4] The exact separation also depends on the recombination fraction, which depends on energy, particle-type, and electric field.

3.3 The XENONnT Dark Matter Experiment

The XENONnT experiment aims to directly detect signals from WIMPs using a dual-phase TPC with a 5.9 t of ultra-pure LXe target [83]. Located at the INFN Laboratori Nazionali del Gran Sasso (LNGS), it benefits from a rock overburden equivalent to 3600 m of water, reducing the cosmic muon flux by about six orders of magnitude. The experiment consists of three nested detectors, illustrated in Figure 3.7: at its core is the LXe TPC housed within a double-walled cryostat. Surrounding the TPC is the neutron veto (NV), and beyond that the muon veto (MV), both optically separated and immersed in a 700 t demineralized water tank.

Achieving ultra-low background levels is critical for detecting rare interactions. Consequently, all materials used in the detector construction, especially those directly interfacing with the xenon in the TPC, were carefully selected for their low radioactivity [140, 141].

3.3.1 The XENONnT TPC

At the heart of the experiment is the dual-phase TPC, shown in a cutaway view in Figure 3.8. The detector features an active cylindrical volume with 1.33 m diameter and a maximum electron drift length of 1.49 m. The cryostat holds a total of 8.5 t of LXe, with 5.9 t in the active target volume. At the top and bottom of the detector are two arrays with a total of 494 ultraviolet (UV)-sensitive 3-inch photomultiplier tubes (PMTs) [142–144]. The TPC walls are made of polytetrafluoroethylene (PTFE), which features high reflectivity for xenon scintillation light [145]. Temperature and pressure are maintained at ~ 177 K and ~ 1.9 bar and the liquid level is kept at approximately 5 mm above the gate electrode.

Electric fields are established by parallel-wire electrodes: a cathode at the bottom, a gate, and an anode above the liquid-gas interface. A drift field of 23 V/cm spans the active LXe volume between cathode and gate electrodes. An electric field between gate and anode (2.9 kV/cm in liquid) extracts electrons with an efficiency of $\sim 53\,\%$ into the gas phase [146]. Two (four) transverse support wires are installed to avert sagging of the gate (anode) electrode wires. Additional wire electrodes are placed in front of the PMT arrays to screen them from electric fields. A field cage made of two sets of concentric field shaping rings ("field shaping wires" and "guard rings" in Figure 3.8), connected via a resistor chain, ensures a homogeneous drift field in the active target [147].

3.3.2 Neutron and muon veto systems

The 700 t water tank provides passive shielding against external radiation and radiogenic neutrons while serving as the medium for two active Cherenkov veto detectors. The inner NV directly surrounds the TPC within a cage constructed from expanded PTFE panels that is equipped with 120 8-inch PMTs facing the cryostat. Radiogenic neutrons escaping the cryostat are moderated and captured by hydrogen, emitting 2.2 MeV γ-rays that produce detectable Cherenkov light via secondary electrons. In the initial operating condition, the neutron tagging efficiency was $(53 \pm 3)\,\%$ [148]. After the first two data-taking campaigns of XENONnT, the water tank was gradually loaded with Gd, which has the highest neutron capture cross section among stable elements and releases multiple γ-rays upon capture. As a result, the neutron tagging efficiency is expected to increase to $\sim 75\,\%$ at a Gd mass concentration of $0.05\,\%$ [148].

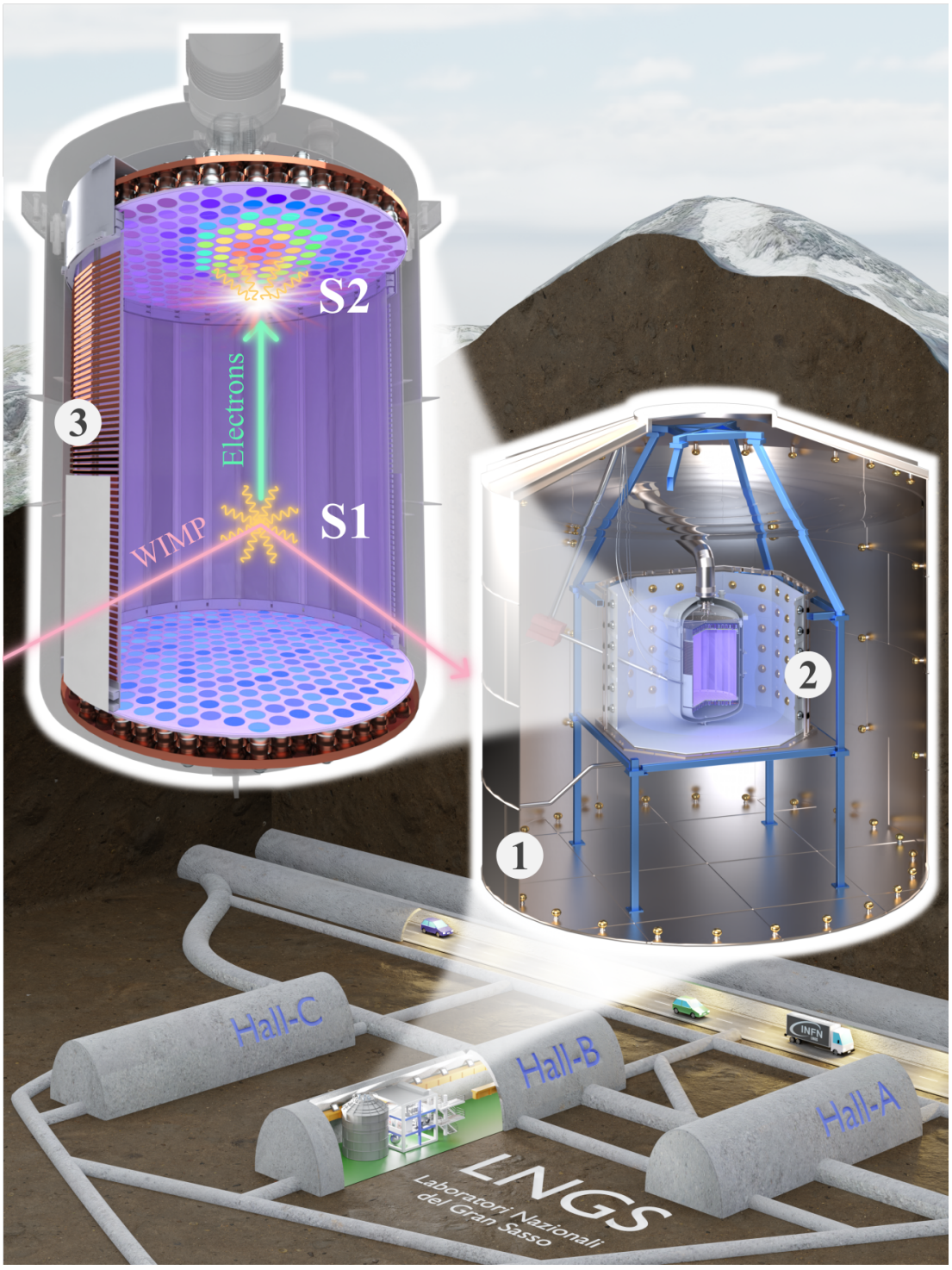

Figure 3.7.: Illustration of the nested XENONnT detector at Hall B of LNGS. Inside the 700 t water tank are the muon veto (MV) (1), neutron veto (NV) (2), and the time projection chamber (TPC) (3) housed in a double-walled cryostat. Reproduced from [139].

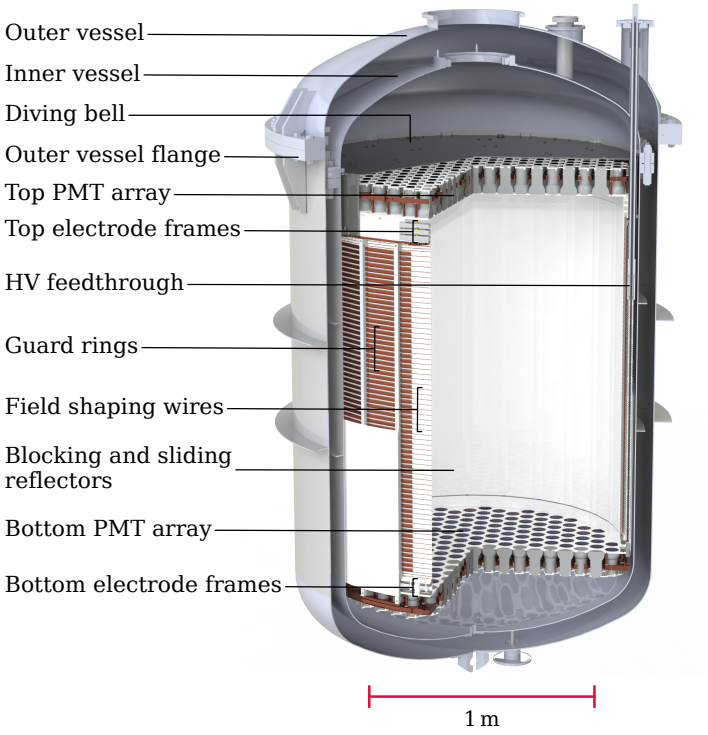

Figure 3.8.: Cutaway view of the XENONnT time projection chamber (TPC) inside its double-walled cryostat. Important components are labeled. Reproduced from [90].

The outer MV, inherited from XENON1T [149], is instrumented with 84 8-inch PMTs mounted on the reflective walls of the water tank. It detects Cherenkov light produced by cosmic muons and their secondary showers in the water and surrounding rock, enabling efficient tagging and rejection of muon-induced backgrounds.

3.3.3 Auxiliary systems

The nested detectors are supported by auxiliary systems housed in a three-story service building adjacent to the water tank (see Figure 3.9). In addition to the electronics, slow control, and data acquisition (DAQ), these subsystems are primarily dedicated to xenon handling. To maintain a cold, clean, and radiopure detector target, xenon is constantly recirculated between the cryostat and these auxiliary systems.

Cooling is provided by two pulse tube refrigerators in the service building that deliver cold xenon to the detector via a 6-meter-long cryogenic pipe [82]. Efficient collection of light and charge signals is crucial for the dual-phase TPC concept. Impurities in LXe can absorb photons and trap drifting electrons, causing exponential signal loss with drift time. Minimizing impurities is therefore essential (see also Section 4.2). This is achieved using both gaseous and liquid purification systems that continuously cycle xenon through getter materials. While the former was already used in XENON1T, the latter is a new addition for XENONnT, enabling purification in the 300-times denser liquid phase [150]. Xenon purity is commonly quantified by the "electron lifetime", the time over which the charge signal reduces by a factor of e. In XENONnT, lifetimes of up to 30 ms have been achieved, far exceeding the maximum drift time

Figure 3.9.: Photograph of the XENONnT water tank and service building photobombed by a shifter on duty.

of 2.25 ms, thus ensuring minimal charge loss. This represents a significant improvement over the ∼650 µs lifetime in XENON1T [88], largely due to the higher purification rates possible with liquid-phase purification [151].

Unlike electronegative impurities, noble gases such as radon and krypton cannot be removed by getters and, being homogeneously distributed, cannot be suppressed by fiducialization. Without mitigation, β-decays from ^{85}Kr and the ^{222}Rn daughter ^{214}Pb would dominate the ER background in the WIMP signal region. The experiment's success therefore hinges on reducing these contaminants. This is accomplished using two dedicated distillation columns that separate xenon from krypton and radon by leveraging their different vapor pressures (krypton accumulates in GXe, radon in LXe). Krypton distillation, already employed in XENON1T, reduces natural krypton levels by several orders of magnitude to $\mathcal{O}(10)$ ppq ($^{\mathrm{nat}}$Kr/Xe $\sim 10^{-14}$ mol/mol with ^{85}Kr/$^{\mathrm{nat}}$Kr $\sim 10^{-11}$ mol/mol) [152]. Xenon is processed through the column in campaigns conducted between and during data-taking periods (see Figure 4.1). Krypton concentrations are monitored via regular measurements using the highly-sensitive rare gas mass spectrometer (RGMS) at Max-Planck-Institut für Kernphysik (MPIK) [153]. Radon distillation was newly added for XENONnT [154]. Since radon is continuously emanated from detector surfaces, the column operates continuously during data-taking. This achieved an unprecedentedly low ^{222}Rn activity of $(0.90 \pm 0.01_{\,\mathrm{stat}} \pm 0.07_{\,\mathrm{syst}})\,\mu\mathrm{Bq\,kg^{-1}}$ [139], comparable to the irreducible neutrino-induced ER background.

Additionally, various calibration sources can be introduced into the xenon target or water tank from the service building to characterize the response of the three nested detectors. The most important calibrations for the analysis of XENONnT data are summarized in Section 4.1. The

facility also includes two storage units that enable rapid recovery of the experiment's entire xenon inventory when needed.

3.4 Into the Neutrino Fog: The XLZD Project

The XLZD collaboration – formed in 2024 from members of the XENON, LZ, and DARWIN collaborations – aims to build a next-generation LXe rare-event observatory. With excellent sensitivity, this detector will enable searches across a plethora of science channels [78], including the search for WIMP dark matter down to the neutrino fog (see Figure 3.1 and Section 2.2), probing neutrinoless double-beta decay [111, 155], and neutrino astrophysics. The baseline design features an active LXe target of 60 to 80 t, combining proven technologies from its successful predecessors [60].

Beyond this baseline, several innovative approaches are being investigated to advance the xenon technology further. Efforts to reduce radon backgrounds focus on lowering emanation rates, for instance through the application of surface coatings [156], employing a solid xenon target [157, 158], or constructing a TPCs with hermetically sealed LXe targets [159–161]. The development of single-phase TPCs is also being explored to overcome limitations of electron extraction into the gas phase [162–164]. Additionally, doping xenon with hydrogen is being studied to enhance sensitivity to light dark matter [165, 166]. Finally, new techniques are under investigation to improve discrimination between ER backgrounds and NR signals. One approach tries to exploit subtle differences in scintillation timing and directionality [167]. Another approach aims to improve separation by additionally detecting infrared (IR) scintillation light, which is discussed in detail in Chapters 8 and 9.

4

From Light to Limit: The XENONnT Analysis Chain

This chapter gives a brief overview of the analysis procedure from the light signals detected by the photomultiplier tubes (PMTs) to the final science result in XENONnT. The science and calibration campaigns relevant for this thesis are discussed in Section 4.1. The signal reconstruction and data selection, which are briefly summarized in Sections 4.2 and 4.3 are discussed in detail in [168]. The signal and background modeling (Section 4.4) as well as the statistical inference (Section 4.5) are discussed for the weakly interacting massive particle (WIMP) search in [Paper I]. Analysis-specific details for the WIMP and ^{8}B coherent elastic neutrino-nucleus scattering (CEνNS) searches are provided in Chapters 5 and 6, respectively.

4.1 Science- and Calibration Data

Data-taking in XENONnT is organized into periods of stable detector conditions, termed science runs (SRs). This thesis analyzes data from the first two SRs. The accumulated livetime over calendar time is shown in Figure 4.1. Key features of these runs are:

- **SR0:** May 1 – December 12, 2021. Achieved record-low electronic recoil (ER) background [146]. At the end, a two-week tritium-enhanced dataset (TED) was collected with the getter bypassed to test for ^{3}H, as motivated by the XENON1T excess [169], though no significant ^{3}H-like excess was found [146]. Since the TED was used for background validation in the WIMP search, it was excluded from the analysis dataset.
- **SR1:** May 19, 2022 – August 8, 2023. An unintentional introduction of commercial-grade xenon before the beginning of the SR increased backgrounds from ^{85}Kr and ^{37}Ar. A dedicated cryogenic distillation campaign (Oct 20 – Nov 30) reduced these again to subdominant levels [Paper II]. The initial high-background phase is called SR1$_{\mathrm{a}}$; the post-distillation phase is SR1$_{\mathrm{b}}$. The radon distillation column was operated in a more efficient mode compared to SR0, reducing ^{214}Pb β-decay backgrounds by factors of 1.9 (SR1$_{\mathrm{a}}$) and 1.7 (SR1$_{\mathrm{b}}$) relative to SR0 [Paper II]. Within SR1$_{\mathrm{a}}$, the liquid level was lowered from 5 mm to 4.8 mm and the anode voltage increased by 50 V ("SR1 detector condition" in Figure 4.1) to mitigate localized intermittent bursts of single-electron emission, referred

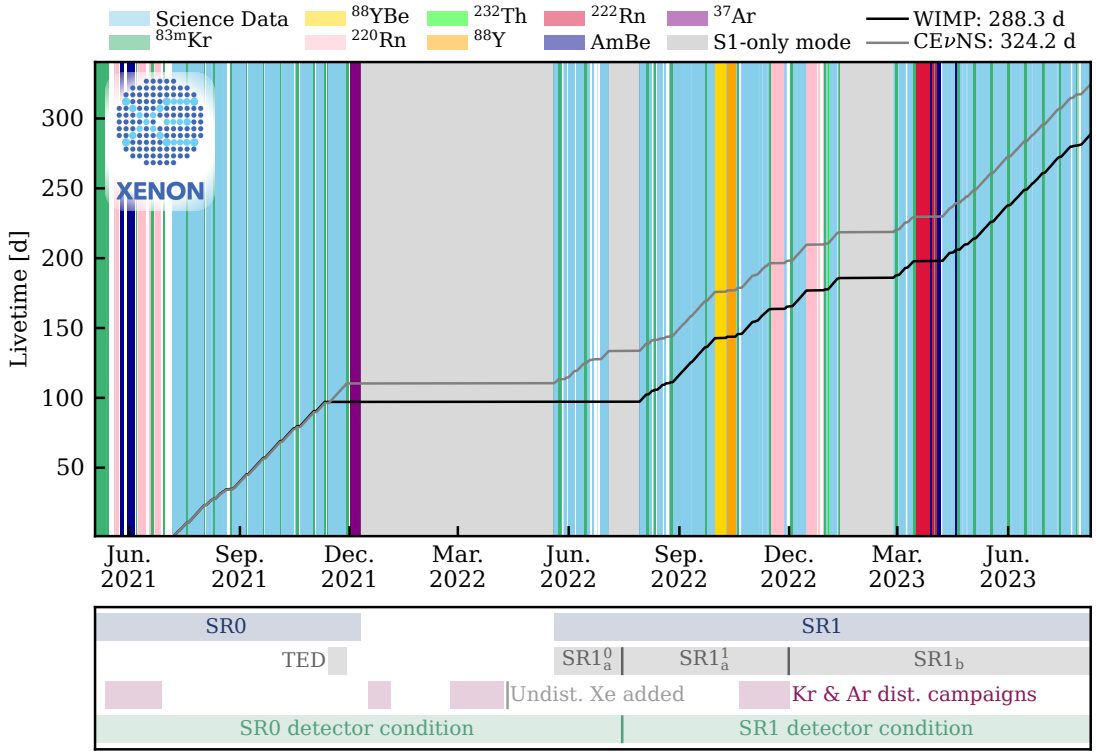

Figure 4.1.: Accumulated livetime for the SR0 + SR1 analyses versus calendar time. Science and calibration periods are indicated, with sub-run names and conditions labeled below. Adapted from the XENON collaboration.

to as "hot spots" while maintaining a comparable extraction field strength [Paper III]. This change of detector conditions splits $SR1_a$ into phase 0 (excluded from the WIMP search, see Section 5.3) and phase 1. In addition, a tenfold increase in delayed electron signals after high-energy events was observed, attributed to photoionization of dissolved impurities [Paper III], possibly from a gasket outgassing non-methane hydrocarbons. A new background resembling ^{3}H β-decay was also observed in SR1, which might have the same origin.

The selected livetimes for SR0 and SR1 are 288.3 d for the WIMP search and 324.2 d for the ^{8}B CEνNS search.

In addition to science search data, several calibration datasets were collected during these SRs. The most important calibration sources are:

- **^{83m}Kr** [170–172]: Bi-weekly calibration for monitoring and correcting spatial and temporal variations of the detector response. Uniformly distributed in the time projection chamber (TPC) after injection. Decays via two monoenergetic conversion electrons (32.1 and 9.4 keV) separated by a 157 ns half-life.
- **^{220}Rn** [173]: Used to calibrate the ER band and define selection criteria. Uniformly distributed after injection. Produces low-energy β-decays from ^{212}Pb, similar to the dominant ^{214}Pb background from the ^{222}Rn chain. Unlike ^{222}Rn, it has no long-lived daughters; the longest is ^{212}Pb (11 h), so rates drop quickly after calibration.
- **^{37}Ar** [174]: Used to model ERs near threshold in SR0. Electron capture (EC) source

yielding 2.82 keV (K-shell) and 0.27 keV (L-shell) ER peaks with a half-life of 35 d. To accelerate removal, a distillation campaign succeeded the calibration.

- **AmBe** [175]: Used to calibrate the nuclear recoil (NR) band and determine the neutron veto (NV) tagging efficiency. ^{241}Am emits α-particles that are captured on ^{9}Be, ejecting neutrons with a continuous spectrum (mean 4.5 MeV). The source was placed at different positions around the outer cryostat.
- **YBe** [176, 177]: Used to calibrate the low-energy NR response in SR1. ^{88}Y emits γ-rays that disintegrate ^{9}Be, producing quasi-monoenergetic 152 keV neutrons. The source was placed externally at one position.

4.2 Signal Reconstruction

When a particle interacts in the TPC, it produces a prompt scintillation signal (S1) and a delayed electroluminescence signal (S2) from ionization electrons extracted into the gas phase, as described in Chapter 3. A scintillation photon is detected when it strikes a PMT photocathode, releasing a single photoelectron (PE) into the vacuum tube. This electron is amplified by an electron cascade, yielding $\mathcal{O}(10^6)$ electrons per PE, resulting in a measurable anode current, which is read out as a voltage signal across a load resistor. Each PMT channel has a specific digitization threshold, typically 15 analog-to-digital converter (ADC) counts, above the average signal size of a single photoelectron (SPE) of ∼30 ADC counts, leading to an SPE acceptance $> 90\,\%$ [168]. If the threshold is exceeded, the PMT pulse is digitized by the data acquisition (DAQ) at a sampling rate of 100 MS/s (MegaSamples per second) [178].

The voltage signal from each PMT is proportional to the number of ejected PE. The conversion factor between voltage and PE is monitored in weekly light emitting diode (LED) calibrations [83, 179]. Time-dependent gain variations are smoothed and applied to the recorded signals to yield signals in units of PE.

Event reconstruction is performed entirely in software, without the use of a hardware trigger, utilizing the open-source frameworks `strax` and `straxen` [180, 181]. The reconstruction chain is illustrated in Figure 4.2:

- A **PMT pulse** above threshold is extended by 30 ns to the left and 200 ns to the right to form a PMT **hit**.
- Hits from the same or other PMTs are clustered if they occur within 700 ns. An iterative splitting algorithm then produces **peaklets**.
- Peaklets are classified as S1 or S2 peaklets based on the summed waveform's shape, area,[1] and area fraction in the top PMT array. For S2 peaklets, a further re-clustering step merges nearby few-electron signals. The result are S1 and S2 **peaks**.
- S1 and S2 peaks are then combined to form an **event**. An event is built around a sufficiently large, isolated S2 peak. The largest S1 peak preceding the S2 within 2.45 ms is assigned as the event's main S1. "Alternative" S1 and S2 signals are defined as the second largest respective peaks.

[1] Integrated signal amplitude.

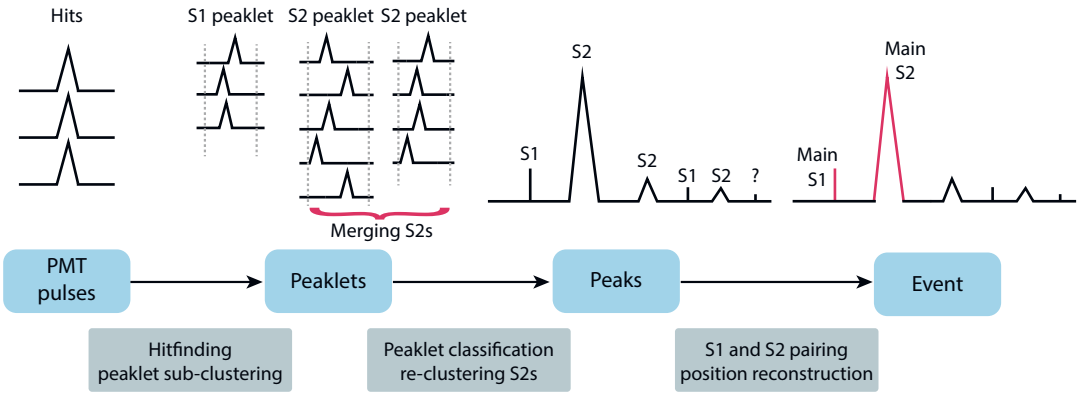

Figure 4.2.: Schematic overview of the XENONnT event reconstruction process. Starting from PMT pulses, events consisting of S1 and S2 signals are reconstructed through a sequence of intermediate objects (blue tiles). Peaklets that do not meet S1 or S2 criteria are marked with a question mark. Key processing steps are indicated in gray. Reproduced from [168].

To suppress misidentified S1 peaks from randomly coincident photon signals, a minimum "tight coincidence level" is required: the number of distinct PMTs with a hit within ±50 ns of the peaklet's maximum amplitude. A higher tight coincidence level reduces false S1s but increases the energy threshold. For the WIMP search, a level of 3 is required; for the ^{8}B CEνNS search, it is lowered to 2 ("3-fold" and "2-fold" coincidence). The peak reconstruction and classification efficiency as a function of signal size is determined using a data-driven method and validated with simulated waveforms [182] (S1 reconstruction efficiency shown in Figure 6.1, left). A small reconstruction bias is quantified as the relative deviation between the simulated truth and the reconstructed signal area. Both efficiency and bias corrections are incorporated into signal and background modeling.

Once an event is reconstructed, its three-dimensional position in the TPC is determined. The vertical position (Z) is calculated from the time difference between S1 and S2, multiplied by the drift velocity of $(0.675 \pm 0.006)\,\mathrm{mm/\mu s}$. $\mathrm{Z} = 0\,\mathrm{cm}$ is defined at the gate electrode, $\mathrm{Z} = -148.65\,\mathrm{cm}$ at the cathode. The horizontal position (X, Y) is inferred using machine-learning models from the S2 PMT hit pattern in the top array. Imperfect electric fields cause field lines to deviate from the vertical axis, leading to position reconstruction biases, especially near the detector wall [147]. In SR0, a data-driven field distortion correction (FDC) assumes ^{83m}Kr calibration events are uniformly distributed up to the wall [168]. In SR1, a more refined FDC method accounts for a charge-insensitive region near the wall. This region arises from distortions in the drift field lines at the edge of the TPC, causing electrons to terminate on the polytetrafluoroethylene (PTFE) wall rather than reaching the liquid xenon (LXe) surface [147].

Spatial and temporal detector effects can alter the reconstructed S1 and S2 signal sizes. Corrections are applied to ensure a uniform detector response across the TPC and over time. The S1 response is affected by the position-dependent light collection efficiency (LCE), and PMT quantum and collection efficiencies. Time-dependent variations arise from changing detector conditions and PMTs being cycled at the beginning of ^{220}Rn calibrations. The S2 signal for a given energy deposition depends strongly on the interaction position. Electronegative impurities in the LXe can trap drifting electrons, causing an exponential loss with drift time ("electron lifetime", see Section 3.3.3: ∼10–30 ms in SR0 and SR1, much larger than the maximum drift time of 2.25 ms). In the horizontal plane, the S2 response varies due to non-uniform extrac-

tion fields and light collection. Further time-dependent effects stem from changes in electron extraction efficiency and single-electron gain. Correction factors and position/time-dependent maps are derived from calibration data or radioactive contaminants. After all corrections, the signals are denoted as corrected S1 (cS1) and corrected S2 (cS2).

The energy is reconstructed via Equation (3.7) though using the corrected S1 and S2 signals. The required detector parameters g_1 and g_2 are determined using several monoenergetic ER peaks: $g_1 = (0.1515 \pm 0.0014)\,\mathrm{PE/ph}$, $g_2 = (16.5 \pm 0.6)\,\mathrm{PE/e}$ in SR0; $g_1 = (0.1367 \pm 0.0010)\,\mathrm{PE/ph}$, $g_2 = (16.9 \pm 0.5)\,\mathrm{PE/e}$ in SR1.

4.3 Data Selection

Selection criteria are applied to identify well-reconstructed, physically valid events and to suppress backgrounds. An overview of the criteria used in the WIMP and CEνNS searches is provided in Table 4.1. The expected distributions of the discriminating variables are derived from validated simulations or high-quality calibration data.

The TPC is surrounded by the NV and muon veto (MV) detectors (see Section 3.3). While muons interacting in the TPC are easily identified, muon-induced neutrons entering the TPC pose a potential background. To suppress these, events in the TPC coincident with a signal in the MV are rejected. Neutrons that scatter in the TPC and then exit can be detected in the NV, allowing coincident signals in the TPC to be rejected.

At the peak level, we remove signals likely to be misreconstructed, misclassified, or affected by PMT artifacts. PMTs can malfunction, producing afterpulses or light emission [144], which may cause a single PMT to dominate the S1 signal; such cases are rejected. For the ^{8}B CEνNS search, where S1 signals with two or three hits are selected, the probability of two photons hitting the same PMT is negligible, so such signals are excluded. Single-electron signals misidentified as S1s are suppressed by a selection criterion on the S1 temporal width. S2 signals with unexpected PMT hit patterns are rejected. Events originating in the gas phase above the anode produce signals with an abnormally large fraction of light in the top PMT array, which is used to reject them.

At the event level, we check whether the S1 and S2 signals are consistent with expectations based on the reconstructed event position. Inconsistencies may indicate misreconstructed or unresolved multiple-scatter events. For S1s, the PMT hit pattern and the fraction of light in the top array are used. For S2s, the temporal width is compared to the expected value from the reconstructed drift time, as electron diffusion causes the S2 width to increase with the square root of drift time. A dedicated boosted decision tree (BDT) model, described in Section 6.1 based on multiple S2 shape parameters, is implemented alongside a simple two-dimensional selection criterion.

WIMPs and neutrinos have a negligible probability to scatter more than once in the TPC, whereas for radiogenic neutrons the probability exceeds 80 % [168]. Selection criteria are therefore applied to identify and reject potential multi-scatter events. If an alternative potential event is found in the same time window, the event is rejected.

A common background in LXe detectors is the presence of strongly delayed signals up to a second after high-energy events [183–187], which can resemble low-energy signals. Specifically, delayed single photon PMT hits and single and few-electron S2 signals are observed up

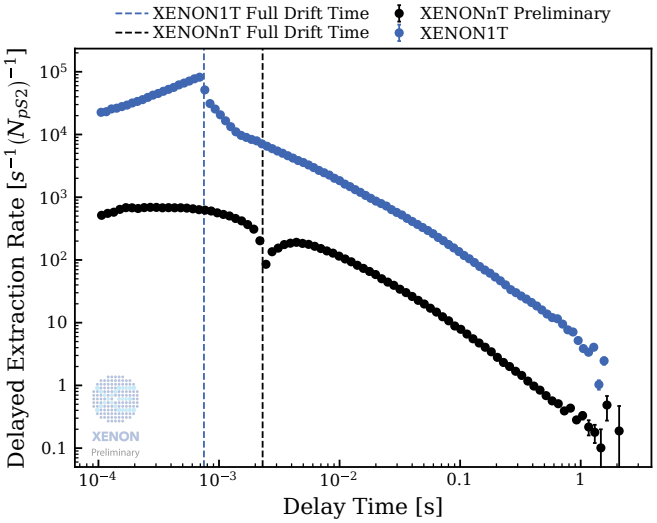

Figure 4.3.: Delayed single-electron rate as a function of delay time relative to the preceding S2 signal. Data from XENONnT are from the beginning of the tritium-enhanced dataset (TED) at the end of SR0. The data from XENON1T are from [185]. Courtesy of the XENON collaboration.

to seconds after high-energy events, as shown in Figure 4.3. These delayed signals are important because they can produce high rates of accidental coincidence (AC) events with low reconstructed energy (see Section 4.4). Many delayed signals are correlated in both time and position with the preceding high-energy event, which is exploited in the "shadow of large peaks" criterion. Additionally, a requirement on the local rate of small peaks ("ambience") is imposed for a peak to be accepted. Furthermore, single-electron hot spots are identified and rejected based on their known positions.

An inner fiducial volume (FV) of the TPC is defined to exclude regions with less well-understood detector response, especially near the edges. It is shown for the WIMP and ^{8}B CEνNS search in R–Z space in Figure 4.4. The strong self-shielding of LXe means most background events occur in the outer volume, so the sensitivity loss from fiducialization is usually small. Near the transverse support wires (see Section 3.3), field distortions affect drift times and thus S2 widths, requiring separate modeling. Since no complete model exists, the S2 BDT cannot be trained on simulation data in these regions; the selection criterion is dropped near the wires for the WIMP search, and the regions are treated separately (see Section 5.2). For the ^{8}B CEνNS search, the S2 BDT is essential. Thus, the region near the wires is excluded, with the exclusion volume dependent on S2 size to account for the increased position reconstruction uncertainty at low S2 signals.

The region of interest (ROI) is defined in quantities related to the prompt scintillation and the charge signal. For the ^{8}B CEνNS search, S1 signals with 2 or 3 hits and S2 signals between 120 and 500 PE are selected. For the WIMP search, we select cS1 $\in [0, 100]$ PE and cS2 $\in [10^{2.1}, 10^{4.1}]$ PE. In addition, a threshold of S2 > 200 PE (SR0) and S2 > 320 PE (SR1) is applied (the increase for SR1 is discussed in Section 5.3.2).

The signal acceptances of the selection criteria are determined using data-driven methods and simulated Monte Carlo (MC) data. Correlations between criteria are accounted for, and the resulting total signal acceptance – shown as a function of recoil energy in Figure 4.5 – is propagated to the signal and background modeling. The total acceptance plateaus at a value

Table 4.1.: Selection criteria and their application to the ^{8}B CEνNS (C) and WIMP (W) searches.

Selection name	Concept	C	W
	External vetoes		
Muon veto	All events in time coincidence with the muon veto are rejected.	✓	✓
Neutron veto	S1 signals in coincidence with an event in the neutron veto are rejected.	✓	✓
	Peak quality criteria		
Max. S1 PMT area	Reject S1 signals with unexpectedly large contribution from one PMT.	✓	✓
S1 per-PMT hits	Reject signals with more than one S1 hit in the same PMT.	✓	
Width of S1	Reject S1 signals with unexpectedly large temporal width.		✓
S2 PMT hit pattern	Reject events with unexpected hit pattern in the top PMT array.	✓	✓
Fraction of S2 signal in top PMTs	Reject signals with an abnormal fraction of the cS2 signal detected by the top PMT array.	✓	✓
	S1–S2 pairing criteria		
S1 PMT hit pattern	Reject events with unexpected PMT hit patterns given the reconstructed position in the TPC.		✓
Fraction of S1 area in top PMTs	Reject events with an unexpected fraction given the reconstructed position in the TPC.		✓
Width of S2	Reject events where the temporal S2 width does not match the expectation from the reconstructed drift time.	✓	✓
S2 BDT	Similar to the above, but using more S2 shape information. See Section 6.1.2.	✓	✓
	Single scatter criteria		
S1 single scatter	Reject events for which the alternative S1 paired with the main S2 signal is a viable event.		✓
S2 single scatter	Reject events with a sizeable second S2 signal.	✓	✓
	Environmental criteria		
Shadow of large peaks	Reject signals close in time and space to large signals.	✓	✓
Peak ambience	Reject peaks surrounded in time or space by a large number of small peaks.	✓	✓
Hot spot veto	Reject events close in time and space to known hot spot locations.	✓	✓
	Other criteria		
Fiducial volume	Select well-understood, clean inner volume, see Figure 4.4.	✓	✓
Region of interest	Analysis-specific selection in light and charge signal.	✓	✓

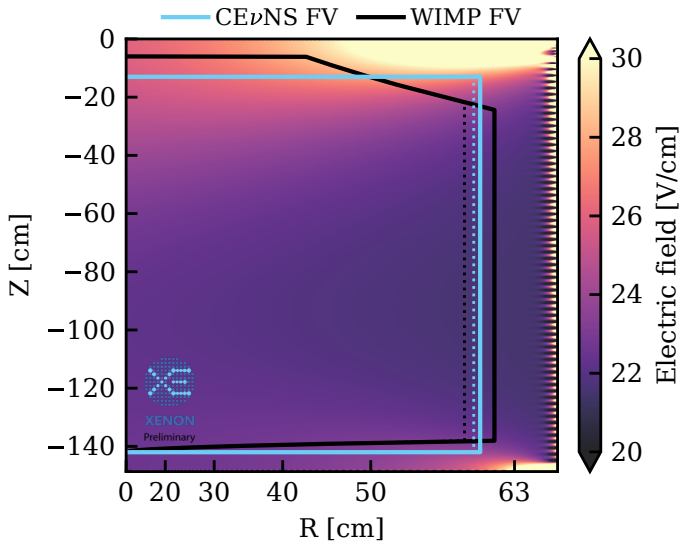

Figure 4.4.: Definition of the fiducial volume (FV) boundaries in R–Z space for the ^{8}B CEνNS search (light blue) and the WIMP search (black), shown for SR0 (solid lines) and SR1 (dotted lines). The shading indicates the absolute electric field in the active volume. Courtesy of the XENON collaboration.

above 70 % for WIMP and approximately 12 % for the ^{8}B CEνNS search with 10 % acceptance reached at an NR energy of 3.3–3.8keV$_{\mathrm{NR}}$ (WIMP) and 2.3 keV$_{\mathrm{NR}}$ (^{8}B CEνNS).

4.4 Signal and Background Modeling

This section provides an overview of the strategies for signal and background modeling in XENONnT. Further details are given in [Paper I], while the specific models for the WIMP and ^{8}B CEνNS searches are described in Sections 5.1 and 6.1.

4.4.1 Modeling the detector response

The foundation of most signal and background models are the LXe emission and detector reconstruction models, which are obtained by fits to calibration data. The LXe emission model describes the production of scintillation photons and ionization electrons following an energy deposition, using the "Noble Element Simulation Technique" (NEST) [129, 130]. The detector reconstruction model translates these quanta into observed signals. A Markov chain MC approach is used to sample the Bayesian posterior as implemented in the `appletree` framework [188, 189]. After convergence of the chain, the maximum-posterior parameters provide the best-fit model, while the posterior samples are used to quantify uncertainties. Figure 4.6 shows the calibration NR and ER datasets and their best-fit model distributions in cS1–cS2 for SR1, highlighting the separation between NR and ER events.

For the ER response, internal ^{220}Rn calibration data were used. The calibration campaigns yielded approximately 2000 events in SR0 and 4700 in SR1. In SR0, additional ^{37}Ar calibration improved constraining the low-energy ER response. Separate fits were performed for SR0 and SR1 to account for subtle differences between SRs, since studies showed that even a 1 % shift in cS2 can alter WIMP sensitivity by 10 % [Paper II].

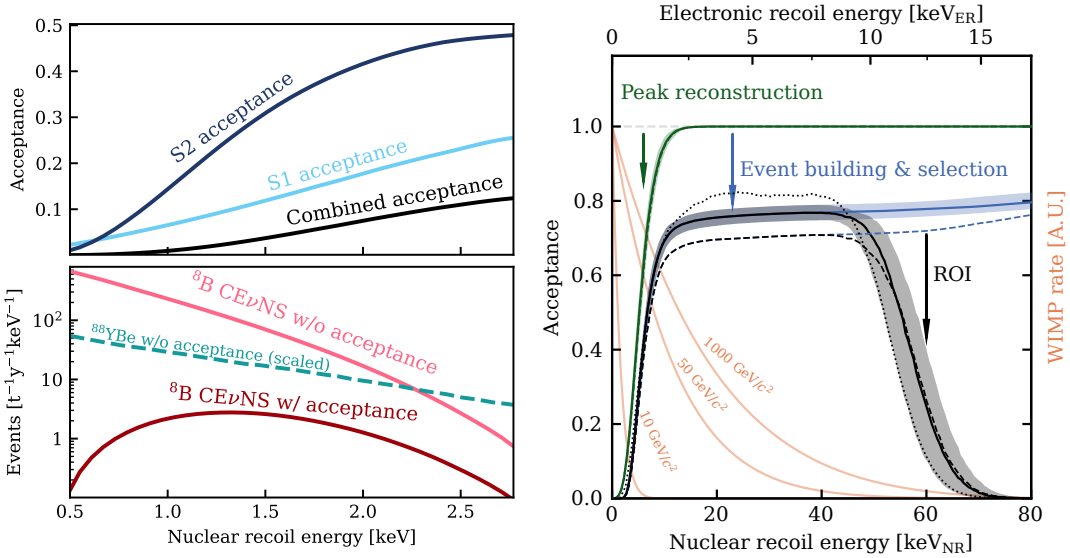

Figure 4.5.: Signal acceptance for NR events. *Left:* Acceptance for the ^{8}B CEνNS search (reproduced from [Paper III]). Shown are the individual S1 and S2 acceptances and their combination. The bottom panel compares the signal recoil spectrum before and after acceptance, and includes the YBe neutron calibration spectrum for reference. *Right:* Acceptance for the WIMP search (adapted from [Paper II]). Acceptances for SR0 (dotted), SR1$_a$ (dashed), and SR1$_b$ (solid) are shown. Orange lines indicate recoil spectra for three WIMP masses before acceptance.

The NR response for the WIMP search was calibrated using an external AmBe source in both SRs. Clean event selection was achieved by requiring a coincident 4.44 MeV γ-ray in the NV, emitted with the neutron in ∼50 % of cases [175]. After selection criteria, approximately 5700 events in the WIMP ROI were obtained for SR0 and SR1 combined. Fits to SR0 and SR1 data separately showed a $>1\sigma$ difference in charge yield, which could indicate potential mismodeling. The impact of this on the WIMP sensitivity was found to be small (see Section 5.3.4), so a combined fit was performed with shared emission model parameters across runs. The combined fit provided a more precise constraint on the single-scatter NR response from calibration data, which contains remaining multi-site neutron events.

The ^{8}B CEνNS signal produces very low-energy NRs, mostly between 1 and 2 keV$_{NR}$, where AmBe calibration has little constraining power. To address this, a dedicated low-energy NR calibration was performed with a YBe neutron source, which resembles the ^{8}B CEνNS recoil spectrum (see Figure 4.5, left). This enabled calibration of the NR response down to 0.5 keV$_{NR}$ [177]. The dataset taken during SR1 contains approximately 500 events after selection criteria. Special attention was paid to mitigating and modeling AC backgrounds and multiple-scatter events.

The agreement of best-fit models with calibration datasets was evaluated using 2D binned Poisson likelihood χ^2 goodness of fit (GOF) tests with equiprobable binning [190, 191]. No significant mismodeling was observed, although the SR1 NR model p-value was slightly below the predefined threshold.

The best-fit NR charge and light yields as a function of deposited NR energy are shown in Figure 4.7. The yields generally agree with the nominal NEST v2 model within $1\,\sigma$, except for the AmBe NR light yield, which is noticeably lower. A similar, though less significant, trend is

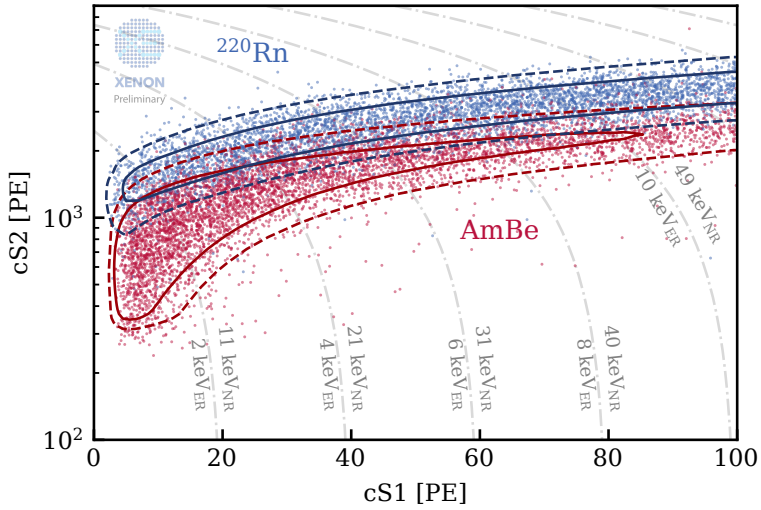

Figure 4.6.: Distribution of electronic recoil (ER) calibration data from ^{220}Rn progeny and nuclear recoil (NR) calibration data from an AmBe source in cS1–cS2 for SR1. Solid and dashed lines show the 68 % and 95 % contours of the respective best-fit models; dash-dotted lines indicate iso-energy contours. Adapted from the XENON collaboration.

seen in the YBe NR light yield above $\sim$1.5 keV$_{\mathrm{NR}}$. However, as the plots also show, the data points underlying the NEST model exhibit substantial spread.

4.4.2 NR and ER signal and background models

For signals and backgrounds producing NR and ER events, the models derived from calibration data are used to predict their distributions in the analysis space. Any physically motivated energy spectrum and spatial distribution in the TPC can be injected into these models, provided the model is valid for the relevant energy range. Toy Monte-Carlo (toyMC) data are then generated and used to populate high-statistics histograms, forming "template" probability density functions (PDFs) for each component. The top panels of Figure 4.8 show representative NR and ER PDFs for the SR0 WIMP search in cS1–cS2.

WIMP and CEνNS signal or background

The WIMP signal PDFs for spin-independent (SI) and spin-dependent (SD) couplings are constructed based on the differential cross sections in Equations (1.4) and (1.5). To ensure comparability, the dark matter velocity distribution follows the standard halo model (SHM) with astrophysical parameters from [42, 201–204] as recommended in [43] and a local dark matter density of 0.3 GeV/(c^2 cm^3) [41]. The nuclear form factor for SI scattering is taken from [205] and the structure factors relevant for SD scattering are taken as the medians from [51].

The SI WIMP signal distribution in cS1–cS2 for different masses is shown in Figure 4.9. For masses of a few GeV/c^2, most recoils fall below threshold (see Figure 1.7, right), and only events with statistical upward fluctuations in the number of emitted photons are detected. For higher masses, the distribution extends to larger cS1. The contour begins to saturate above approximately 200 GeV/c^2 as the reduced mass of the WIMP-nucleus system in Equation (1.1)

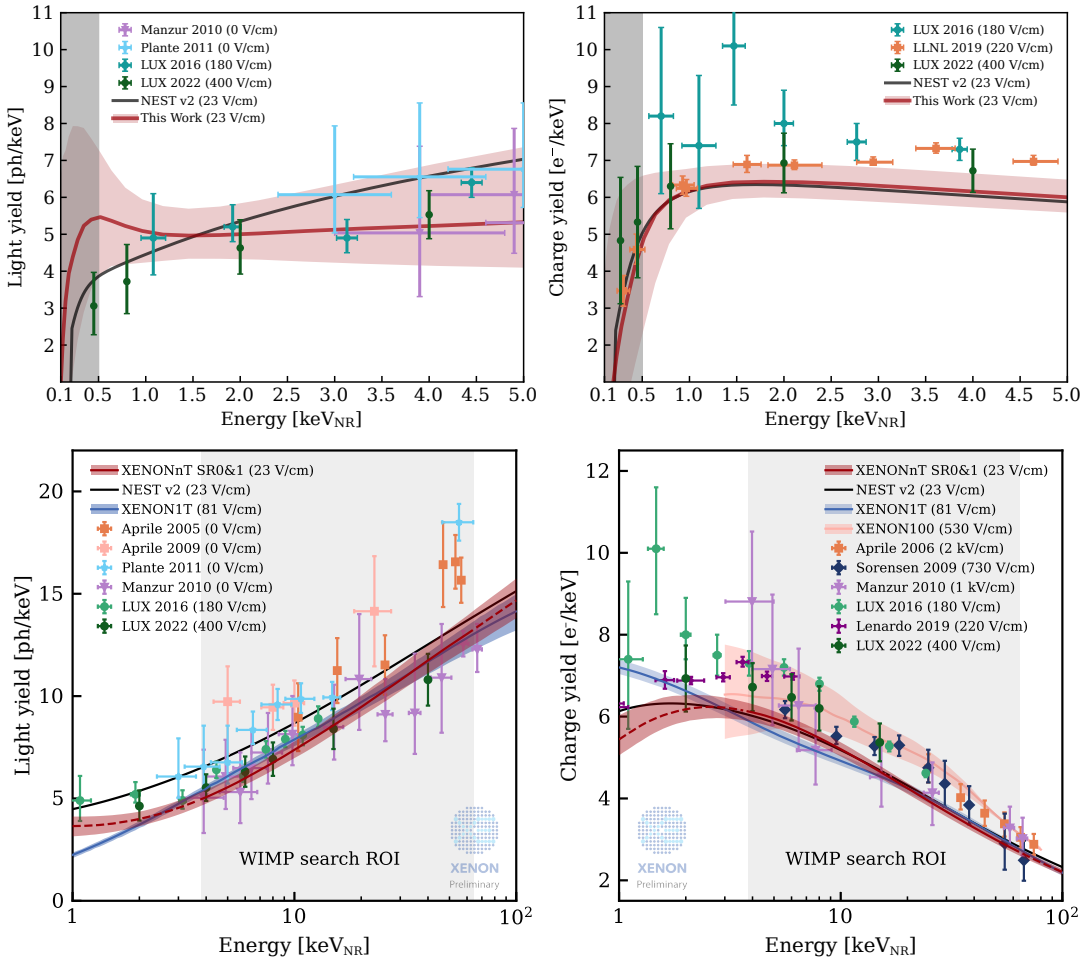

Figure 4.7.: Nuclear recoil (NR) light (left) and charge yields (right) as a function of NR energy, obtained from YBe (top, from [177]) and AmBe (bottom, courtesy of the XENON collaboration) calibrations. Results from other experiments [118, 135, 192–200] at different drift fields are also shown for comparison.

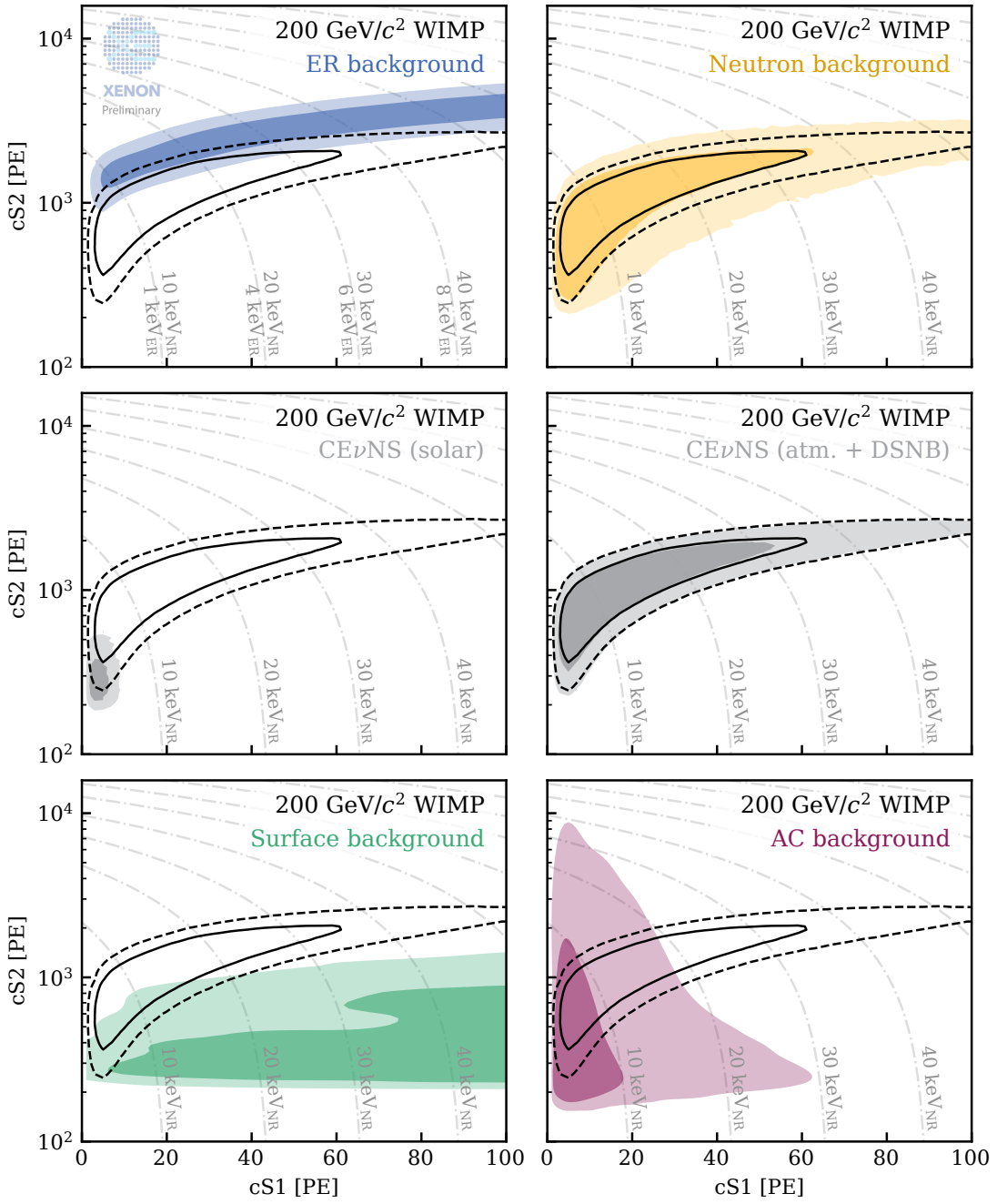

Figure 4.8.: Representative templates of signal and background probability density function (PDF) in cS1–cS2 for the SR0 WIMP search. Shown are the electronic recoil (ER), neutron, CEvNS, surface, and accidental coincidence (AC) components, all overlaid with the probability density function (PDF) of a 200 GeV/c^2 WIMP. Dark (light) and solid (dashed) contours indicate regions that contain 68 % (95 %) of expected events in the ROI. Dash-dotted lines indicate iso-energy contours. Extended from [Paper I].

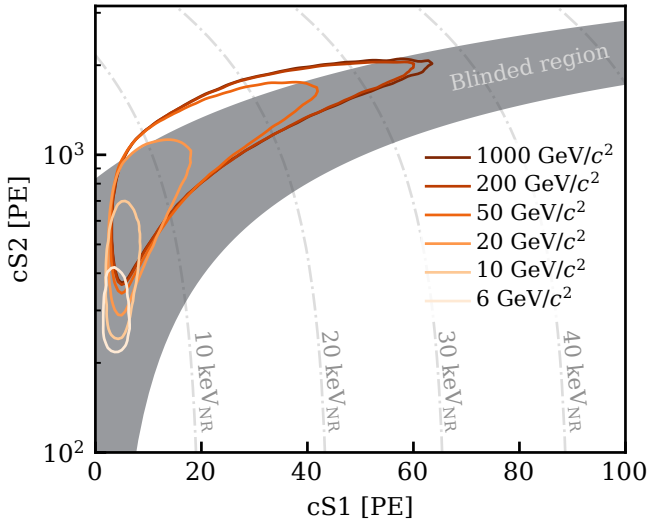

Figure 4.9.: WIMP templates for different masses in cS1–cS2. The contours indicate regions contain 68 % of events in the region of interest (ROI). Dash-dotted lines indicate iso-energy contours. The gray region indicates the region blinded before the analysis is finalized. Reproduced from [Paper I].

approaches the nuclear mass m_A. Spectra for SD scattering are similar in shape [206], with event rates at equal cross section roughly scaling as $R^{\mathrm{SI}} : R^{\mathrm{SD}}_{\chi\mathrm{n}} : R^{\mathrm{SD}}_{\chi\mathrm{p}} = 5 \times 10^6 : 30 : 1$.

The ^{8}B CEνNS signal, which is a background for the WIMP search, uses a flux of $(5.25 \pm 0.20) \times 10^6\,\mathrm{cm}^{-2}\mathrm{s}^{-1}$ [207], the spectrum from [208], and the CEνNS cross section predicted by the Standard Model (SM) [209]. Additional CEνNS backgrounds from atmospheric neutrinos [210] and the diffuse supernova neutrino background (DSNB) [75] are also considered. As discussed in Section 2.2, the ^{8}B CEνNS recoil spectrum closely matches that of a $6\,\mathrm{GeV}/c^2$ WIMP, which reflects in the distribution in cS1–cS2. Atmospheric and DSNB neutrinos, with higher average energies, resemble higher-mass WIMP recoils.

Neutron background

Neutrons scattering off xenon nuclei produce NRs and are thus a key background for NR signal searches. Radiogenic neutrons arise mainly from spontaneous fission and (α, n) reactions from trace amounts of radioactive impurities in materials near the LXe target. Cosmogenic neutrons are subdominant and are not modeled [90].

Material radioactivity levels are determined in situ from measured high-energy γ-spectra in combination with radioassay campaigns performed prior to detector construction [140, 141]. Neutron yields and spectra for each material are then computed using the `SOURCES 4A` framework [211]. These inputs feed MC simulations to obtain the expected event distribution in analysis space and (R, Z), as well as a neutron rate estimate for reference. However, the actual neutron background in data is estimated using a more robust, data-driven approach based on the neutron sideband: single- and multiple-scatter events with a coincident NV signal. In contrast to previous work [89], which relied solely on radioactivity levels from radioassay campaigns, the new model yields simulation-driven rate estimates that agree with the data-driven sideband measurement. This improvement is primarily due to the identification of higher radioactivity in the inner cryostat flanges.

Because neutrons have a high probability of scattering multiple times in the TPC, special attention is given to the modeling of double-scatter events where one interaction occurs in a charge-insensitive region. Such events can be misreconstructed as single-scatter events with an anomalously high S1-to-S2 ratio. In addition to the previously mentioned charge-insensitive region near the TPC wall, there is an intrinsic charge-insensitive volume of approximately 250 kg located between the bottom PMT array and the cathode. This arises from the electric field in this region pointing opposite to the drift field.

Electronic recoil background

In terms of event counts, the largest background in the WIMP-search ROI is from ER events. At low energies, these arise mainly from β-decays of intrinsic radioactive contaminants such as ^{214}Pb (from the ^{222}Rn chain) and ^{85}Kr. While distillation can suppress those backgrounds, an irreducible ER background comes from low-energy solar neutrinos (especially *pp* neutrinos) scattering off atomic electrons. Additional contributions include double-β decay of ^{136}Xe and, to a lesser extent, γ-rays from detector materials, which are effectively mitigated by fiducialization. Overall, the combined spectrum of these components is approximately flat in the ROI of both NR searches. Rate estimates are based on ancillary measurements and extrapolation from outside the ROI.

In SR1, backgrounds from EC of ^{37}Ar and potentially ^{3}H β-decay were also observed and modeled with non-flat energy spectra for the WIMP search. A subdominant ER background, scrutinized in the SR0 + SR1 WIMP search due to its potentially lower charge yield, is the double electron capture (DEC) of ^{124}Xe (see Section 5.4).

4.4.3 Data-driven background models

In the absence of complete physics-driven models, two backgrounds are modeled using data-driven approaches. Their PDFs in cS1–cS2 are shown in the bottom panels of Figure 4.8.

Accidental coincidence background

AC background arises when S1 and S2 signals from unrelated events are incorrectly paired during event reconstruction. This is the dominant background in the ^{8}B CEνNS search ROI, and also plays an important role in the WIMP search. The signals responsible are called "isolated" S1 and S2, meaning they lack a physical partner signal. If such isolated S1 and S2 signals occur within the event-building time window (see Section 4.2), they can be falsely combined into an event.

A complete physics-driven model for isolated S1 and S2 signals is still missing, though progress has been made [212]. Before selection criteria, the rates of isolated S1 and S2 in the WIMP search (3-fold coincidence) are $R_{\mathrm{isoS1}} = 1.5\,\mathrm{Hz}$ and $R_{\mathrm{isoS2}} = 80\,\mathrm{mHz}$ [Paper I] and for the ^{8}B CEνNS search (2-fold) $R_{\mathrm{isoS1}} = 15\,\mathrm{Hz}$ and $R_{\mathrm{isoS2}} = 150\,\mathrm{mHz}$ [182]. Below is a summary of possible origins. While some of these processes can produce sizeable signals, others generate only single photons or electrons, which can nonetheless pile up and be reconstructed as S1 or S2 signals.

- **Isolated S1 signals:** Randomly distributed isolated S1s can originate from physical events in LXe where the charge signal is lost (e.g., near the TPC wall), Cherenkov radiation in the PMT windows [213], or PMT dark counts. Misclassified single-electron S2s can appear as S1s. Additionally, delayed S1s correlated with high-energy events have been observed, following a power-law time distribution [187]. Delayed photons may arise from fluorescence of detector materials such as PTFE [187, 214, 215], attached residues [216], or PMT quartz windows [217].
- **Isolated S2 signals:** Randomly distributed isolated S2s may result from events where the S1 falls below threshold, or from radioactive decays on the cathode electrode [218]. Delayed electrons correlated with high-energy events are well documented in LXe [184], see Figure 4.3. For the applied field, the electron extraction efficiency is approximately 53 % [146]; remaining electrons may be trapped near the liquid-gas interface and later released [219, 220]. Another possibility is that electrons are trapped on impurities in LXe and detach with a delay, either via collisions or via photoionization [221]. In argon, delayed electrons are additionally attributed to metastable molecular ions in the gas phase [222, 223].

To suppress AC background, powerful data selections are used, notably the S2 BDT, "shadow of large signals", and "peak ambience" selection criteria described in Section 4.3. The S2 BDT targets correct S1–S2 pairing via S2 width, while the other selection criteria select periods and locations with low AC probability.

Data-driven AC modeling is implemented in `axidence` [224]. Isolated S1 and S2 waveforms are sampled from data, assigned random drift times, and paired into artificial AC events, which are then processed like regular events (Sections 4.2 and 4.3). Artificial AC events passing selections are used to construct AC templates and estimate background rates. Validation is particularly important for data-driven models. The AC background model is validated using multiple AC-rich sidebands, for example, events passing all but the AC-targeting selection criteria. The observed distributions are compared to artificial AC events using GOF tests. Further details on the validation of the AC model for the ^{8}B CEνNS search can be found in Section 6.1.3.

Surface background

Surface background arises from β-decays in the ^{210}Pb chain on the TPC's PTFE wall. These events can lose much of their ionization charge, resulting in strongly reduced S2 signals compared to regular ER events. Because of their strong radial dependence, surface background can be suppressed by modeling the radial distribution in the likelihood function or by fiducialization.

Precise modeling of the electric field near the PTFE surface and electron loss to the wall is challenging [225], so a data-driven approach is used. The surface background is modeled in (cS1, cS2, R, Z). The (R, Z) distribution is obtained from ^{210}Pb events outside the WIMP ROI (cS1 $\in$ [100, 300] PE). The radial profile is fitted with a skewed generalized t-distribution in S2 slices (see Figure 4.10 for an illustration using ^{210}Po data). The Z-distribution is modeled using a linear function. The distribution in cS1–cS2 is taken from data with positions reconstructed outside the TPC wall and smoothed with adaptive kernel density estimation. Events reconstructed outside the FV are used to validate the radial model, showing good agreement.

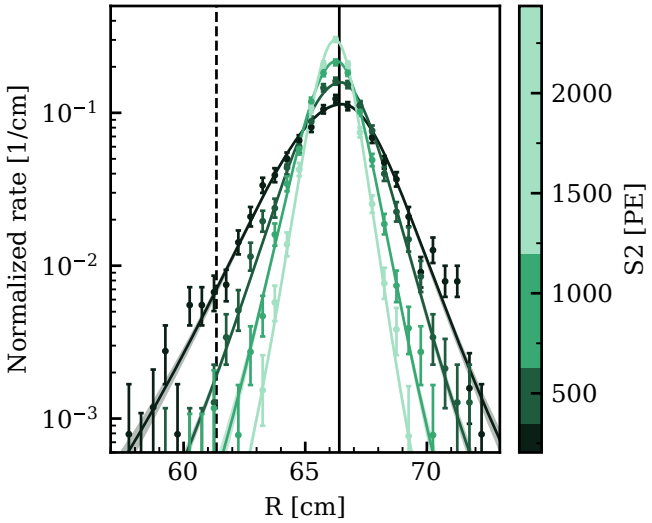

Figure 4.10.: Radial surface background model from [89], shown for four S2 slices. Here, ^{210}Po α-decays were selected. The wall of the active volume is indicated as a solid vertical line and the outer radius of the SR0 WIMP fiducial volume (FV) as a dotted line. In the updated radial model, ^{210}Pb events outside the region of interest (ROI) were used, which results in a similar but more robust model. Figure from [Paper I].

4.5 Statistical Inference

The primary goal of the searches discussed in this thesis is to determine whether the data contain evidence for a potential signal or only known backgrounds. Regardless of the outcome, we seek to place constraints on the physical parameters associated with the potential signal. We use frequentist statistical methods based on the profile likelihood ratio to construct confidence intervals and assess the significance of any observed excess. Both are related to hypothesis tests that quantify the agreement between data and specific hypotheses using a test statistic.

Most XENONnT analyses are performed in a blinded way, which means the region where signal events are expected to appear remains inaccessible until all analysis decisions are finalized (data selection, signal and background models, and statistical procedures). Only after this step is the data unblinded and the predefined inference procedure executed. Any subsequent changes are clearly documented as post-unblinding changes. This approach, or similar methods, prevents unintentional experimenter bias from affecting the results [226].

4.5.1 Test statistic and likelihood function

In a hypothesis test, the goal is to assess how well the observed data $\mathbf{x}$ align with a specific hypothesis. To quantify this agreement, the information in x is condensed into a summary measure called the test statistic $t(\mathbf{x})$, which is a function of the data. The test statistic used in this work, and commonly employed in particle physics, is based on the profile likelihood ratio:

$$t_\mu(\mathbf{x}) = -2 \ln \frac{\mathcal{L}(\boldsymbol{x}|\mu, \hat{\hat{\boldsymbol{\theta}}}(\mu))}{\mathcal{L}(\boldsymbol{x}|\hat{\mu}, \hat{\boldsymbol{\theta}})}, \tag{4.1}$$

where the likelihood function $\mathcal{L}(\boldsymbol{x}|\mu, \boldsymbol{\theta})$ is defined as the joint PDF of the observed data $\boldsymbol{x}$ for given parameter values. Here, μ is the parameter of interest (e.g., the signal strength in the

form of a cross section or flux) and $\boldsymbol{\theta}$ represents nuisance parameters, such as background rates and shapes, that are not of primary interest. The values $\hat{\hat{\boldsymbol{\theta}}}(\mu)$ maximize the likelihood function for a fixed μ, whereas $\hat{\mu}$ and$\hat{\boldsymbol{\theta}}$ are the global best-fit values. By construction, perfect agreement between data and the hypothesized value ($\hat{\mu} = \mu$) results in $t_\mu = 0$, and larger values indicate increasing tension between data and the hypothesis μ. In this work, all signal and background rates are constrained to be non-negative. For clarity, the explicit data dependence is omitted in the following.

For observed data yielding t_μ^{obs}, we quantify the agreement with a hypothesis μ via the p-value:

$$p(t_\mu^{\text{obs}}|\mu) = P(t_\mu \geq t_\mu^{\text{obs}}|\mu) = \int_{t_\mu^{\text{obs}}}^{\infty} f(t_\mu|\mu)\,\mathrm{d}t_\mu, \tag{4.2}$$

where $f(t_\mu|\mu)$ is the test statistic distribution, assuming μ is true. This represents the probability of observing a test statistic at least as extreme as t_μ^{obs} if μ were true. We exclude the hypothesis μ when $p < \alpha$, where α is the test size or significance level.[2] Discovery p-values are often expressed as equivalent significance levels:

$$Z = \Phi^{-1}(1 - p), \tag{4.3}$$

where Φ^{-1} is the inverse cumulative standard normal distribution. Common discovery thresholds are $Z = 3\,\sigma$ ($p = 1.35 \times 10^{-3}$) and $Z = 5\,\sigma$ ($p = 2.87 \times 10^{-7}$).

4.5.2 Discovery significance

Signal discovery requires rejecting the background-only hypothesis ($\mu = 0$) in favor of signal-plus-background. The discovery significance is given by $p(t_0^{\text{obs}}|\mu = 0)$. For WIMP searches testing multiple masses, observing an excess becomes more likely as more hypotheses are tested. Any significant excess requires correcting the "local" significance for this "look-elsewhere effect" (trial correction). The global discovery significance accounts for multiple testing using toyMC methods [227].

4.5.3 Confidence intervals

Confidence intervals identify parameter regions compatible with the data. Unlike Bayesian credible intervals, frequentist confidence intervals do not assign probabilities to parameter values. Instead, they are constructed so the true value is "covered" by a specified fraction of intervals in repeated experiments (the coverage probability). Intervals are constructed to have a coverage probability at least equal to a specified confidence level (CL), regardless of the true value of μ. In our case, CL= 90 %, which means that the true signal strength is not contained in 10 % of intervals constructed using this procedure. If the coverage probability for a given signal strength exceeds the specified CL, it is referred to as over-coverage; in the inverse case, under-coverage.

[2] Since by construction, the p-value distribution is uniform between 0 and 1 in case the tested hypothesis is true, α also corresponds to the probability of rejecting a tested hypothesis even though it is true (statistical error of the first kind).

The construction of confidence intervals can be understood as a set of hypothesis tests of different signal strengths μ with size $\alpha = 1-\text{CL}$. Values satisfying

$$p(t_\mu^{\text{obs}}|\mu) \geq 1 - \text{CL}. \tag{4.4}$$

form the confidence interval, with the smallest and largest such values defining the lower limit and upper limit (UL), respectively. Signal strengths outside this interval are considered incompatible with the data.

Our likelihood-ratio-based test statistic is "two-sided," producing large values for both $\hat{\mu} > \mu$ and $\hat{\mu} < \mu$. This follows the unified interval construction of Feldman and Cousins [228], avoiding under-coverage issues when switching between one- and two-sided constructions based on the experiment's outcome. Unified intervals solve this by smoothly transitioning from one-sided to two-sided intervals.

For WIMP searches, two-sided intervals are reported only when the discovery significance exceeds $3\,\sigma$. Otherwise, only ULs are given, leading to conservative over-coverage at low signal strengths [227].

4.5.4 Asymptotic distributions

Evaluating the p-values in Equation (4.2) requires knowledge of $f(t_\mu|\mu)$ under different μ. In the limit of large datasets, Wilks' theorem [229] shows that t_μ asymptotically follows a chi-squared distribution with one degree of freedom[3] χ^2_1 when μ is true. In addition, certain regularity conditions must hold, nicely discussed in [230]. Notably, μ must be far from boundaries (here $\mu \geq 0$).

The boundary case $\mu = 0$, which is needed to compute the discovery significance, requires special treatment. Chernoff [231] showed that asymptotically $f(t_0|\mu = 0) = \frac{1}{2}\chi^2_1(t_0) + \frac{1}{2}\delta(t_0)$, where δ is the Dirac-delta function. This yields the simple asymptotic discovery significance formula [232]:

$$Z = \sqrt{t_0^{\text{obs}}}. \tag{4.5}$$

4.5.5 Toy Monte Carlo-based inference

In low-background searches, sufficient data is often lacking, making asymptotic distributions invalid. Using these distributions regardless to construct confidence intervals can result in under-coverage, as shown for the WIMP search in [227]. When asymptotic distributions are invalid, we instead obtain $f(t_\mu|\mu)$ from MC simulations. Rather than computationally expensive full simulations, we use toyMC where data are sampled directly from parameter-space PDFs.

We typically generate 10^4–10^5 toyMC datasets for various signal strengths and compute t_μ for each to build the distributions $f(t_\mu|\mu)$. Discovery significance follows directly from Equation (4.2) using $f(t_0|\mu = 0)$ from toyMC. For confidence intervals, we pre-compute critical values t_μ^{crit} satisfying $p(t_\mu^{\text{crit}}|\mu) = 1-\text{CL}$ at 10–20 signal strengths, then interpolate linearly. Confidence intervals are found where the observed test statistic curve intersects the critical region. Figure 4.11 illustrates this procedure for three example datasets.

[3]The number of degrees of freedom corresponds to the number of parameters of interest, in our case one.

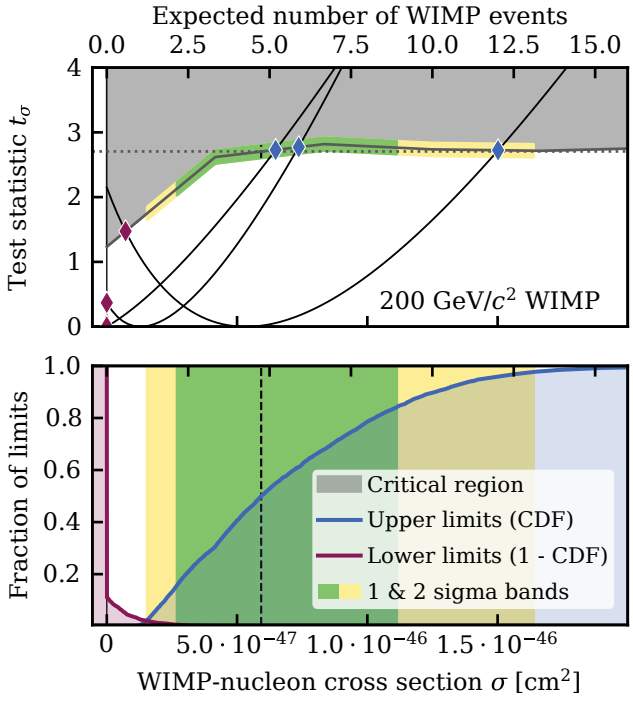

Figure 4.11.: Confidence interval construction and sensitivity for a 200 GeV/c^2 WIMP. *Top:* Test statistic curves for three background-only experiments. The 90 % CL critical region (gray) defines lower (purple diamonds) and upper (blue diamonds) limits at intersections. The asymptotic threshold (dotted) is shown for reference. *Bottom:* The upper limit distribution from many background-only experiments yields the sensitivity band (median dashed, 68 % and 95 % intervals as green/yellow bands). The lower limit distribution is shown in purple (10 % have non-zero values). Both panels share the same x-axis with cross section shown at the bottom and number of WIMP events at the top. Adapted from [Paper I].

In general, in the presence of nuisance parameters, the correct coverage probability is not guaranteed, as the distribution of t_μ may depend on the values of nuisance parameters $\boldsymbol{\theta}$. We compute critical regions using nominal nuisance parameter values. The coverage probability of this approach for a WIMP model similar to the one used here was verified in [227].

4.5.6 The `alea` computing framework

For the toyMC-based inference performed in XENONnT, the open-source framework `alea` [233] was developed together with Knut Morå and Dacheng Xu. The **statistical model** is defined in a human-readable configuration file, specifying parameters, uncertainties, and the likelihood function. A **runner** class manages large computing jobs (e.g., "generate 10^4 toyMC datasets for 15 signal strengths") with parallel execution on computing clusters. In particular, it is compatible with the Open Science Grid, enabling efficient large-scale parallel computation.

As sketched in Figure 4.12, the toyMC generation distinguishes between:

- **Science/calibration data:** Modeled via PDFs in analysis space. Event counts drawn from Poisson distributions, then sampled from component PDFs.
- **Ancillary measurements:** External constraints (e.g., of background rates) characterized by nominal values and uncertainties, sampled from constraint distributions.

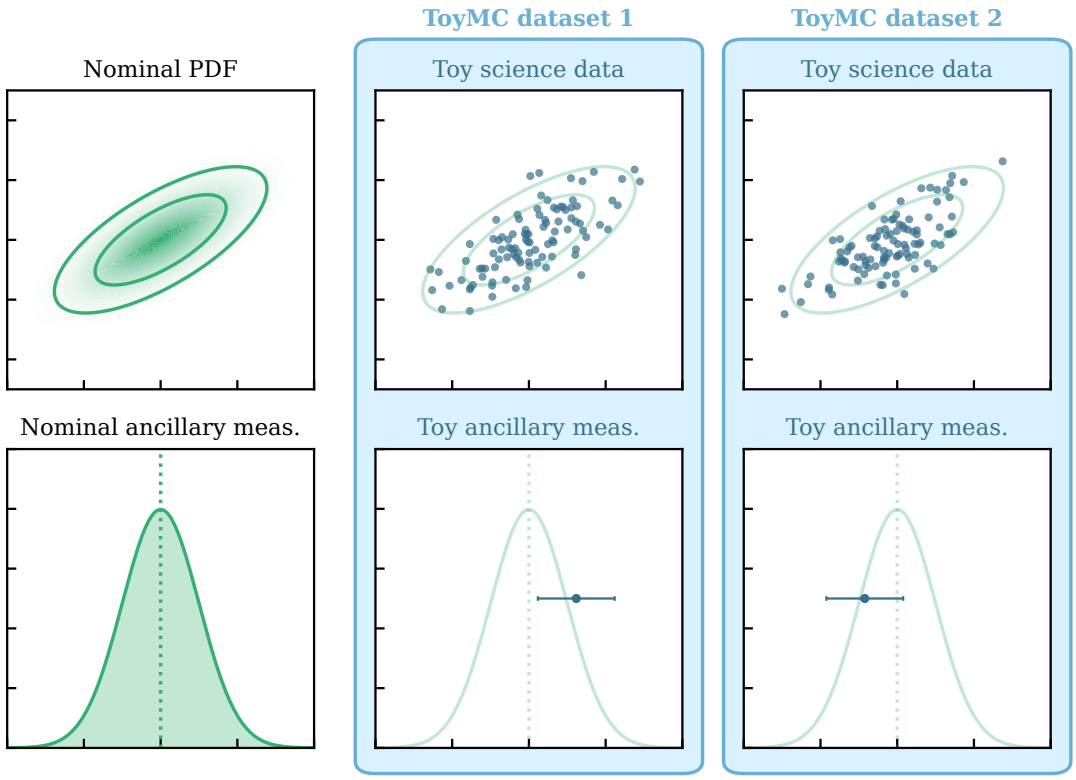

Figure 4.12.: Illustration of the Toy Monte-Carlo (toyMC) generation procedure. The left column shows the nominal probability density function (PDF) for science data (top) and an ancillary measurement (bottom). The two columns on the right illustrate two independent toyMC datasets, each composed of a toy science dataset (blue points, top) and a toy ancillary measurement (blue datapoint with errorbar, bottom). The nominal PDF and ancillary measurement (green) are overlaid for reference.

The likelihood functions used for the analyses described here are implemented via `blueice` [234], which enables the definition of shape nuisance parameters via linear interpolation between PDFs evaluated at discrete "anchor points" of the parameters ("vertical morphing").[4]

Sensitivity and mismodeling studies

The toyMC framework also allows for computing sensitivity projections and robustness studies. Experimental sensitivity quantifies the expected performance under nominal conditions. For WIMP searches, sensitivity is commonly defined as the median UL on the WIMP-nucleon cross section assuming no signal (background-only hypothesis). To compute this, we generate many background-only toyMC datasets and calculate the UL for each using the pre-computed critical region. In addition to the median of the UL distribution, sensitivity bands are typically reported and shown as green ($1\,\sigma$) and yellow ($2\,\sigma$) regions, which contain 68 % and 95 % of ULs, respectively, as illustrated in Figure 4.11 (bottom panel).

Other sensitivity metrics include median discovery significance or discovery probability for a given significance threshold. These require generating toyMC data with specified signal strength and computing the discovery significance for each realization. `alea` facilitates systematic studies

[4] Extended here to enable component-wise interpolation for ^{124}Xe yield parameters (Section 5.4).

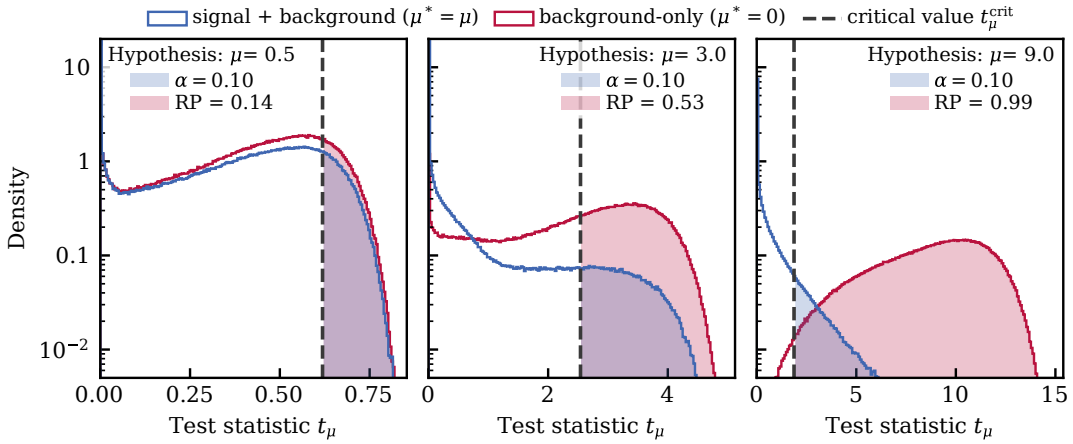

Figure 4.13.: Example test statistic distributions under signal-plus-background (blue) and background-only (red) hypotheses. Large tested signals (right) show clear separation and high rejection power, while small signals (left) exhibit overlapping distributions and poor discrimination.

of how background rate variations affect sensitivity. Robustness studies assess analysis performance under imperfect modeling conditions. This is achieved by generating toyMC data using one model and analyzing it with a different model. Examples include testing the impact of unmodeled background components, biased rate constraints, or altered signal and background PDF shapes.

4.5.7 Power-constrained limits

When no WIMP signal is observed, we report ULs on the cross section. However, statistical downward fluctuations or modeling issues (e.g., overestimated backgrounds) can lead to exclusions beyond the experiment's sensitivity. While statistically valid for fluctuations, such results are not very informative for other scientists.[5]

Figure 4.13 illustrates the issue with excluding low signal strengths. For large signals, signal-plus-background and background-only distributions are well-separated, yielding high rejection power, defined as the probability to reject the signal strength μ if the true signal strength is $\mu^* = 0$

$$\text{RP}(\mu) = P(\text{reject}\,\mu|\mu^* = 0) = \int_{t_\mu^{\text{crit}}}^{\infty} f(t_\mu|\mu^* = 0). \tag{4.6}$$

For small signals, overlapping distributions make the rejection power comparable to the test size α as we lack meaningful discrimination between the hypotheses. This means the probability of rejecting a small signal hypothesis is nearly identical whether the signal exists or not. To address this, methods have been developed to prevent such spurious exclusions [235–238].

Following community recommendations [43], direct dark matter searches use power-constrained limits (PCL) [238]. This method requires minimum rejection power $\text{RP}(\mu) \geq \text{RP}_{\text{min}}$ to exclude a signal hypothesis μ (equivalent to a WIMP-nucleon cross section). When power is insufficient, we instead report the weakest signal strength still achieving adequate rejection power.

[5] For example, they might wonder, "Should I continue searching for signals if another experiment has already excluded the parameter space I am sensitive to?"

We choose $\mathrm{RP}_{\mathrm{min}} = \Phi(-1) \simeq 0.16$, equivalent to reporting no UL below the $-1\,\sigma$ sensitivity quantile.[6]

4.5.8 Goodness-of-fit tests

GOF tests evaluate how well a best-fit model describes observed data. Unlike classical hypothesis tests comparing two specific alternatives, GOF tests assess the best-fit hypothesis without an explicit alternative hypothesis.[7] Failing to reject the best-fit model with a suitable test suggests adequate data description.

We apply GOF tests to science data with best-fit models, calibration data fits, and data-driven model validation. Tests are streamlined using the `GOFevaluation` package [190]. For distributions in cS1–cS2 often spanning wide ranges of expectation values, an equiprobable binning scheme is implemented [191]. For science results, test statistic distributions under the best-fit hypothesis come from toyMC data. Each toy realization is fitted independently, and the GOF test statistic is computed for the fitted model.

No uniformly most powerful GOF test exists, so tests are aimed to be sensitive to broad classes of unspecified alternative models. Performance studies using toyMC help identify suitable tests for specific mismodelings. Such a study for the ^{8}B CEνNS search is discussed in Section 6.4.

[6] Originally, [43] suggested 0.16 but defined PCL using discovery power rather than rejection power. After a strong downward fluctuation observed by the LUX-ZEPLIN (LZ) experiment [239] highlighted this distinction, XENONnT initially adopted a conservative threshold of 0.5 [89]. Studies with toyMC data showed no issues that would prohibit using a power threshold of 0.16, so XENONnT returned to this definition for experimental comparability.

[7] It can be understood as a test against the set of all possible alternative hypotheses.

5

Statistical Model and Sensitivity Studies for the XENONnT WIMP Search

This chapter presents the statistical analysis framework and sensitivity studies for the weakly interacting massive particle (WIMP) search with XENONnT. For the search with the first two science runs (SRs) (SR0 and SR1) [Paper II], the statistical model is detailed, in particular the signal and background components (Section 5.1) and the likelihood function (Section 5.2). Sensitivity studies that informed key analysis decisions are presented in Section 5.3, followed by a dedicated section on the statistical treatment of double electron capture (DEC) background in Section 5.4. The chapter concludes with long-term sensitivity projections that guided the collaboration's decision regarding the replacement of the detector's electrodes in Section 5.5.

5.1 Signal and Background Modeling

Building on the general modeling framework discussed in Section 4.4, this section presents specific features of the WIMP search analysis. Signal and background templates and rate estimates were provided by collaborators.

The statistical model includes background contributions from electronic recoils (ERs), neutron interactions, accidental coincidence (AC) events, surface events, and coherent elastic neutrino-nucleus scattering (CEνNS) from solar and atmospheric neutrinos as well as the diffuse supernova neutrino background (DSNB). Due to approximately five-fold higher AC rates near transverse support wires (see Section 3.3), separate modeling was performed for near- and far-wire regions. Signals and backgrounds were modeled in cS1–cS2–R for the far-wire region; the radial coordinate was omitted for the near-wire region. Figure 5.1 illustrates the signal and background distributions in cS1–cS2 space, demonstrating the strong signal-background discrimination power, while Figure 5.2 shows the evolution of background rates across the dif-

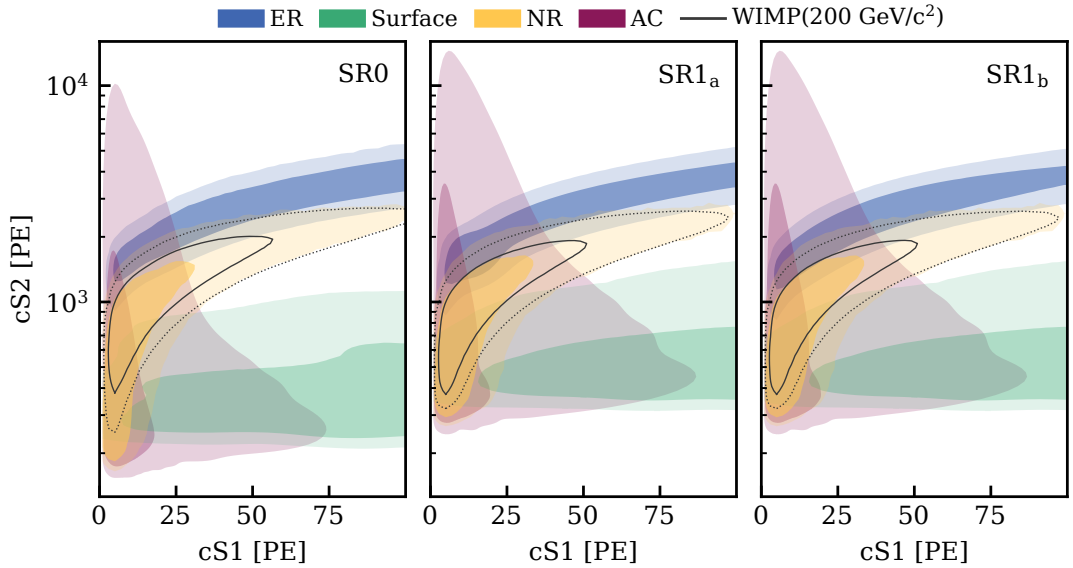

Figure 5.1.: Signal and background probability density functions (PDFs) in cS1–cS2 space for SR0, $SR1_a$, and $SR1_b$. Dark/solid and light/dashed regions indicate $1\,\sigma$ and $2\,\sigma$ containment regions, respectively. Nuclear recoil (NR) backgrounds includes contributions from neutrons and CEνNS and electronic recoil (ER) shows the combination of all sub-components.

ferent SRs. Templates describing the probability density functions (PDFs) are finely binned histograms.[1] The total number of expected background events is reported in Table 7.1.

5.1.1 Electronic recoil background

The largest number of background events in the WIMP-search region of interest (ROI) came from ERs. Various contributions with approximately flat energy spectra in the ROI were combined into a single "flat" component, primarily from (double) beta decays of ^{214}Pb, ^{85}Kr, and ^{136}Xe, as well as neutral and charged current interactions of solar neutrinos with electrons. In addition, in SR1, a ^{3}H-like background and background from ^{37}Ar were modeled separately. The background rate varied across SRs as discussed in Section 4.1: the lowest rate occurred in SR0, while elevated levels of ^{85}Kr in $SR1_a$ resulted in a higher flat ER background, alongside additional ^{37}Ar and ^{3}H-like backgrounds. In $SR1_b$, although the ^{3}H-like background persisted, cryogenic distillation reduced the flat component to below SR0 level.

Accurate modeling of the ER background distribution in cS1–cS2 is crucial, as mismodeling can significantly affect the inference results. This was achieved by fitting the liquid xenon (LXe) emission and detector reconstruction models to calibration data, as described in Section 4.4. To account for uncertainties of the ER response model, two shape parameters per SR were introduced, parameterizing deviations from the nominal best-fit model. While the full ER response model has ∼20 parameters, dimensionality was reduced by identifying the directions of maximal variance via a principal component analysis (PCA) of the sampled posterior. For SR0, both shape parameters were derived from PCA [Paper I]. For SR1, one parameter was from PCA (see Figure 5.3, left), and the second was obtained as a linear combination of the detector parameters g_1 and g_2, shifting the ER band position (see Figure 5.3, right).

[1] 50 bins in cS1, 100 log-spaced bins in cS2, and 18 (14) bins in R for SR0 (SR1).

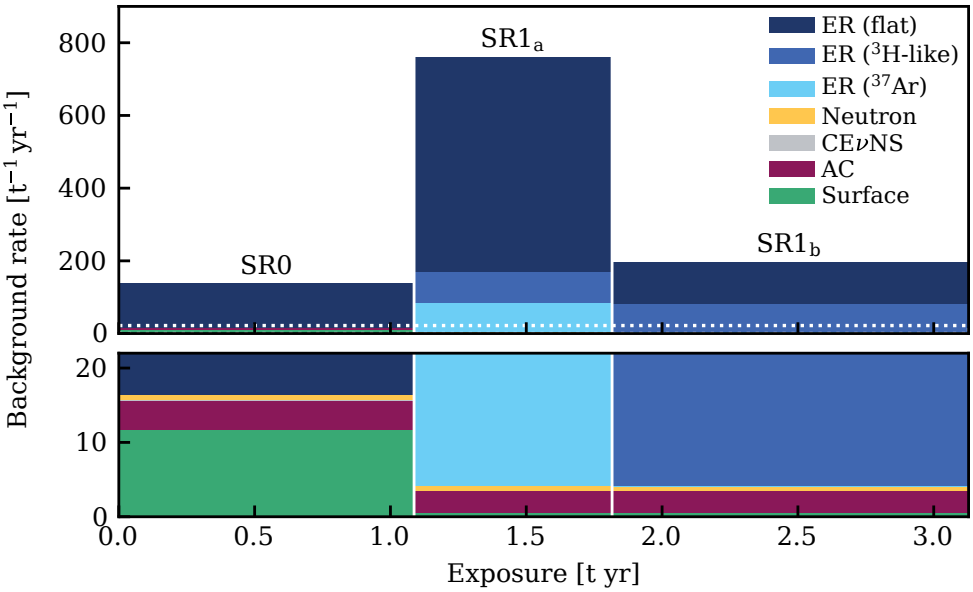

Figure 5.2.: Background rates for the three SRs, shown as stacked histograms to highlight individual contributions from electronic recoil (ER), neutron, CEνNS, accidental coincidence (AC), and surface backgrounds. The bottom panel magnifies rates up to $20\,\mathrm{t}^{-1}\,\mathrm{yr}^{-1}$ (white dashed line in the top panel). Bin widths reflect the exposure for each SR. It is important that the three-dimensional analysis space provides substantial discrimination power, particularly against ER and surface backgrounds.

5.1.2 Changes to the SR0 model

Data selections remained unchanged from the original SR0-only WIMP search [89], but small improvements were made to the signal and background models. The neutron background model was updated based on in-situ radioactivity measurements of detector materials via their γ-rays, as described in Section 4.4. Since the neutron background rate was estimated from neutron sideband events, this change mainly affected the radial distribution and not the rate. Combining neutron sideband data from both SRs led to a slightly different central value for SR0 compared to [89]. The response model for all nuclear recoil (NR) signals and backgrounds in SR0 was updated to the best-fit model from the combined SR0 + SR1 calibration fit. The radial surface background model was revised and now derived from a fit to ^{210}Pb β-decays outside the ROI, rather than ^{210}Po α-particle events. This approach provided a more accurate representation of the actual background. Also, a minor correction to the rate estimate reduced the central value by 6 %.

5.2 Definition of the Likelihood Function

The likelihood function $\mathcal{L}(\boldsymbol{x}|\sigma,\boldsymbol{\theta})$ depends on data $\boldsymbol{x}$, the WIMP-nucleon cross section $\sigma \geq 0$ for a given WIMP mass, and nuisance parameters $\boldsymbol{\theta}$ describing background rates and shapes. It factorizes as:

$$\mathcal{L}(\boldsymbol{x}|\sigma,\boldsymbol{\theta}) = \mathcal{L}_{\mathrm{sci}}(\boldsymbol{x}|\sigma,\boldsymbol{\theta}) \times \mathcal{L}_{\mathrm{cal}}(\boldsymbol{x}|\boldsymbol{\theta}) \times \mathcal{L}_{\mathrm{anc}}(\boldsymbol{\theta}). \tag{5.1}$$

The first likelihood function, $\mathcal{L}_{\mathrm{sci}}$, models the actual search data using extended unbinned

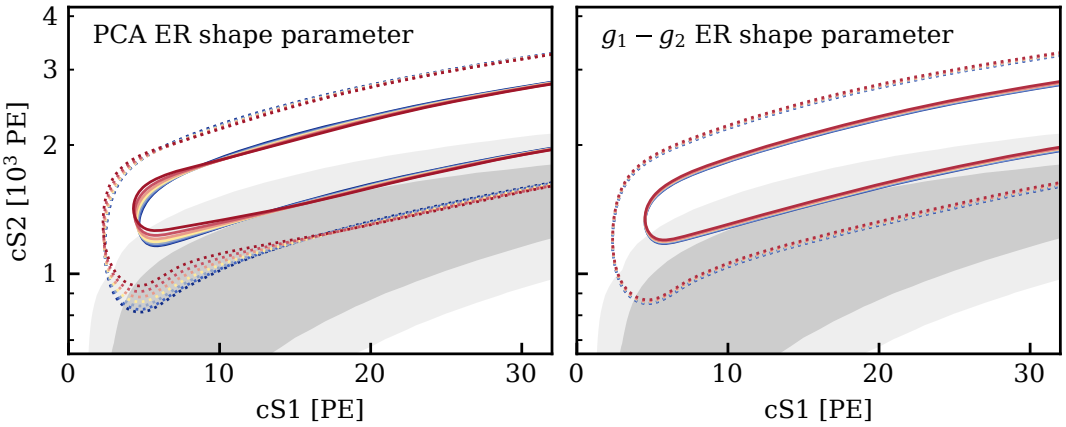

Figure 5.3.: Shape parameter variations of electronic recoil (ER) background for SR1, obtained from principal component analysis (PCA) and from combining photon and electron gain parameters (g_1, g_2). Solid and dotted contours show the $1\,\sigma$ and $2\,\sigma$ containment regions. The nominal model is shown in yellow; red and blue indicate positive and negative parameter variations. Gray contours show $1\,\sigma$ and $2\,\sigma$ containment regions of a $200\,\mathrm{GeV}/c^2$ WIMP signal for reference.

likelihood functions. The data are divided into six categories: three runs (SR0, $\mathrm{SR1_a}$, $\mathrm{SR1_b}$), each split into near-wire and far-wire regions. Each of the six likelihood functions has the form:

$$\mathcal{L}^{\mathrm{sr}}_{\mathrm{region}}(\boldsymbol{x}|\sigma,\boldsymbol{\theta}) = \mathrm{Pois}(N|\mu_{\mathrm{tot}}(\sigma,\boldsymbol{\theta})) \times \prod_{i=1}^{N}\left[\sum_c \frac{\mu_c(\sigma,\boldsymbol{\theta})}{\mu_{\mathrm{tot}}(\sigma,\boldsymbol{\theta})} \times f_c(\vec{x}_i|\boldsymbol{\theta})\right], \tag{5.2}$$

where:

- sr: science run index
- region: near/far-wire
- N: number of events in each SR and wire region
- c: index over all signal and background components
- $\mu_c(\sigma,\boldsymbol{\theta})$: expected number of events for component c
- $\mu_{\mathrm{tot}}(\sigma,\boldsymbol{\theta}) = \sum_c \mu_c(\sigma,\boldsymbol{\theta})$, i.e. total number of expected events
- $\vec{x}_i$: measured observables (cS1,cS2,R) for event i
- $f_c(\vec{x}_i|\boldsymbol{\theta})$: PDF[2] of component c evaluated at event i

The second likelihood function $\mathcal{L}_{\mathrm{cal}}$ uses ^{220}Rn calibration datasets in cS1–cS2 to constrain the ER shape nuisance parameters, with separate terms for SR0 and SR1, each similar to Equation (5.2). The ancillary likelihood function $\mathcal{L}_{\mathrm{anc}}$ incorporates external measurements that constrain background rates. For measurements with expectation μ_c^{anc} and uncertainty σ_c, the ancillary likelihood function is

$$\mathcal{L}_{\mathrm{anc},c}(\boldsymbol{\theta}) = \mathrm{Gaus}(\mu_c^{\mathrm{anc}}|\mu_c,\sigma_c). \tag{5.3}$$

Rate parameters are treated as fully correlated when backgrounds have common physical origins or when systematic variations between regions/runs are negligible compared to the overall rate

[2]Described by granularly binned templates.

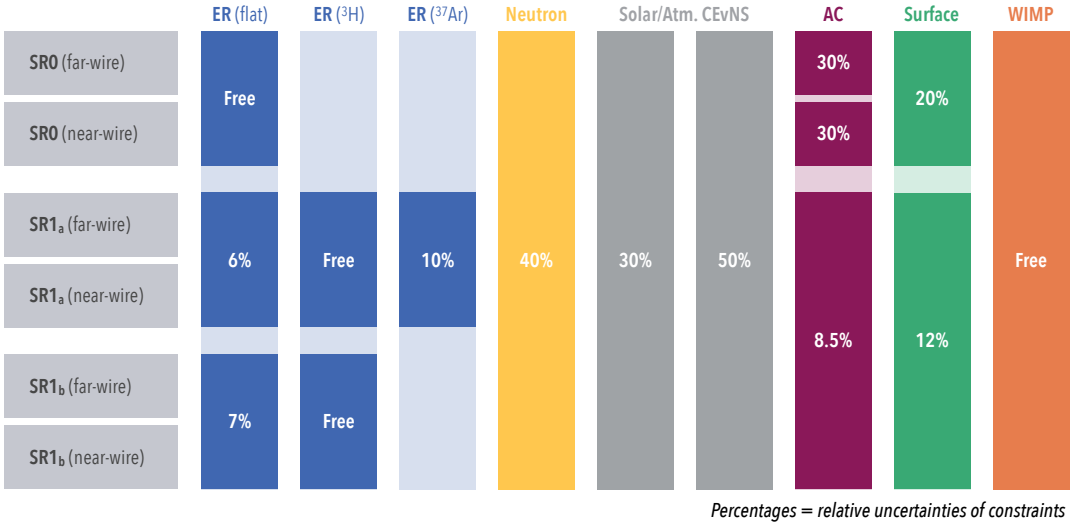

Figure 5.4.: Overview of rate parameters in the WIMP-search likelihood function. Each tile represents one rate parameter; links between rows indicate shared rate parameters across science runs. Percentages denote relative uncertainties, while "Free" indicates the absence of ancillary constraints.

uncertainty. Near- and far-wire background rates were treated as fully correlated except for SR0 AC background, which was treated independently. Neutron, CEνNS, and WIMP rates were fully correlated across SRs. This was implemented using shared rate parameters $r_c = \mu_c/\mu_c^{\text{anc}}$ with nominal values of 1. The corresponding ancillary likelihood function is given by

$$\mathcal{L}_{\text{anc},c}(\boldsymbol{\theta}) = \text{Gaus}(1|r_c, \sigma_c/\mu_c^{\text{anc}}). \tag{5.4}$$

An overview of the individual signal and background components, along with the relative uncertainties of rate constraints, is provided in Figure 5.4. The flat ER component was estimated by fitting the ER background outside the WIMP ROI. For SR0, no ancillary constraint was applied to the ER rate, as it was already strongly constrained by the science dataset. In SR1_a and SR1_b, the uncertainty from the outside-ROI fit was propagated as a constraint, since an additional ^{3}H-like component, which is fully contained within the WIMP ROI, was strongly anticorrelated with the flat ER background. The ^{37}Ar contribution in SR1_a was constrained using the preceding phase 0 data, which was not included in this analysis ($\text{SR1}_\text{a}{}^0$, see Figure 4.1). The dominant uncertainties in the neutron, AC, and surface background rates arose from the limited statistics of the sidebands used for their estimation and validation (see Section 4.4). In SR0, the AC rate uncertainty was conservatively increased to 30 % due to an over-fitting issue in the boosted decision tree (BDT) training process discovered after unblinding [Paper I]. Uncertainties of CEνNS background rates are a combination of the NR yield and flux uncertainties.

As introduced above, the uncertainty in the ER models for SR0 and SR1 was accounted for using two shape parameters per SR. Given the low expected number of NR events from both signal and background, explicit shape parameterization for these components is not required. Instead, only the uncertainty on the WIMP event rate was propagated, arising from the NR response model and reconstruction efficiency. The yields and efficiency determine the number of events above threshold, so their uncertainties directly translate into an uncertainty in the event rate. This was implemented as a WIMP-mass-dependent relative signal efficiency uncertainty,

ranging from $\sim 35\,\%$ ($\sim 15\,\%$) at $10\,\mathrm{GeV}/c^2$ to $\sim 15\,\%$ ($\sim 5\,\%$) at $1000\,\mathrm{GeV}/c^2$ in SR0 (SR1). The smaller uncertainty in SR1 was due to smaller selection efficiency uncertainty.

5.3 Sensitivity Studies for the SR0 + SR1 Analysis

The nominal sensitivity for the combined SR0 + SR1 analysis was evaluated through Toy Monte-Carlo (toyMC) methods using the `alea` framework [233], as described in Section 4.5. Figure 5.5 presents the sensitivity as a function of WIMP mass, showing both exclusion capability (median of expected upper limits (ULs) under the background-only hypothesis) and discovery potential (discovery probability for $3\,\sigma$ significance threshold). Including SR1 data improved the exclusion sensitivity by up to a factor of 1.8 compared to the SR0-only search. The figure also shows the $-1\,\sigma$ quantile of the UL distribution, representing the most stringent possible UL after applying power-constrained limits (PCL) (see Section 4.5). The median ($-1\,\sigma$ quantile) corresponds to approximately 5 (2) WIMP events at $10\,\mathrm{GeV}/c^2$, increasing to 8 (4) events above $100\,\mathrm{GeV}/c^2$. The combined SR0 + SR1 search offered substantial discovery potential for high-mass WIMPs at cross sections not excluded by the SR0-only search.

Several studies were performed to investigate the impact of different analysis choices on the sensitivity, which are summarized in the following. For these, typically 5 000–50 000 toyMC experiments were used per condition. While some were conducted using earlier versions of the statistical model to guide decisions, conclusions remain valid for the final analysis.

5.3.1 Impact of excluding $\mathrm{SR1_a}$ phase 0

$\mathrm{SR1_a}$, which featured strongly elevated ^{85}Kr background rates, was subdivided into two phases as discussed in Section 4.1 and illustrated in Figure 4.1. Phase 0 ($\mathrm{SR1_a}^0$) used SR0 detector conditions (liquid level, anode voltage) but applied the updated processing and reconstruction algorithms developed for SR1. The detector conditions were subsequently adjusted to mitigate single-electron hot spots, marking the beginning of phase 1 ($\mathrm{SR1_a}^1$). Critically, $\mathrm{SR1_a}$ phase 0 did not have dedicated calibration campaigns. Although the differences between phases were subtle, modeling this period with calibration data from SR0 or the remainder of SR1 could have introduced systematic biases in the ER and NR response models.

Excluding $\mathrm{SR1_a}$ phase 0 reduced exposure by approximately 20 livetime days with high ^{85}Kr background. Sensitivity studies demonstrated that the impact scaled approximately with the square root of exposure loss, as expected for a statistics-limited search, resulting in only a 3 % degradation of median UL across tested masses. Given the modest sensitivity loss, $\mathrm{SR1_a}$ phase 0 was excluded from the WIMP search.

5.3.2 Raising the S2 threshold for SR1

A discrepancy was observed between the SR1 AC background model derived using simulated AC events and sideband data at low S2 values, likely resulting from an increased rate of delayed electrons due to photoionization of impurities. Addressing this issue would have been challenging, so the impact on the sensitivity of raising the S2 threshold from 200 photoelectron (PE) for SR1 was studied as a practical alternative to avoid unnecessary analysis delays. This was a conceivable option, especially in view of the preceding dedicated XENONnT search for low-mass

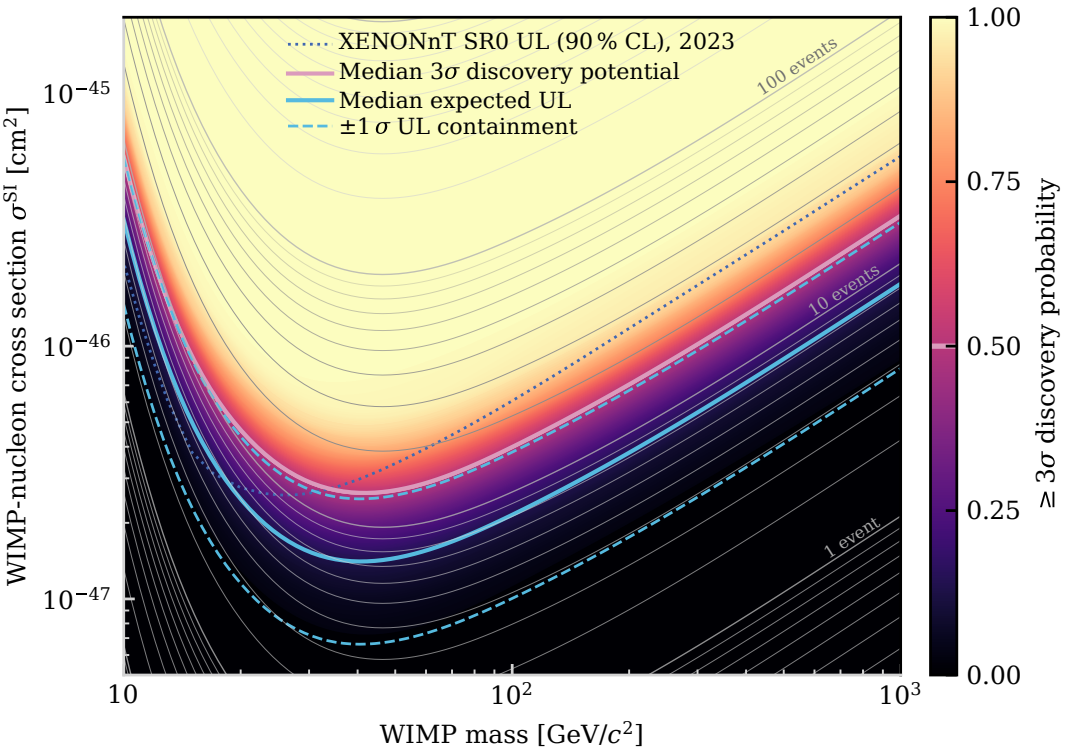

Figure 5.5.: Sensitivity versus WIMP mass for the SR0 + SR1 search. The colormap indicates the probability of achieving a $\geq 3\,\sigma$ discovery, the median (50 % discovery probability) is highlighted in a lighter color. The median and $\pm 1\,\sigma$ containment region of upper limits (ULs) under the background-only hypothesis are shown in blue. The overlaid grid shows the expected number of WIMP events, and the dotted line marks the UL from XENONnT's SR0-only result (recast with a power threshold of 0.16) [89].

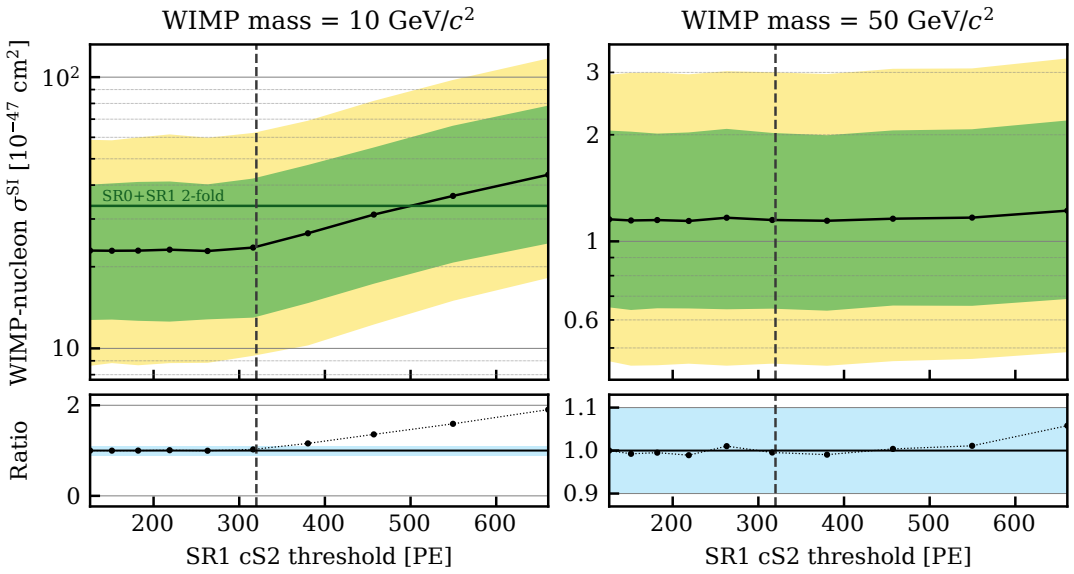

Figure 5.6.: Impact of varying the cS2 threshold for SR1 on the sensitivity for two WIMP masses. The top panels show the sensitivity as a function of the cS2 threshold. The bottom panels display the ratio to the sensitivity without applying an additional cS2 threshold. The green line for 10 GeV/c^2 corresponds to the sensitivity of the low-mass WIMP search reported in [59]. The chosen S2 threshold of 320 PE is indicated as a dashed vertical line.

WIMPs (see [59] and Section 7.2), allowing the present search to focus on higher masses. Since all PDF templates were available in cS1–cS2–R space, the cS2 threshold was used as a proxy for the S2 threshold and simply raised in `alea`, without the need to re-generate templates. The sensitivity was computed for three WIMP masses and ten cS2 thresholds between ∼125 and ∼670 PE using asymptotic critical regions.

Figure 5.6 shows the sensitivity as a function of cS2 threshold, with ratios to nominal (no additional cS2 threshold) sensitivity in the bottom panels. For 50 and 1000 GeV/c^2, sensitivity degradation begins around 600 PE with an increase of the median UL of less than 10 %. For 10 GeV/c^2, degradation starts already for lower thresholds, with 10 % increase at ∼300 PE. The reason for this is that low-WIMP-mass signals are concentrated at low cS1 and cS2 (see Figure 4.9). Based on these results, an S2 threshold of 320 PE was chosen for SR1.

5.3.3 Choice of the fiducial volume for SR1

The WIMP fiducial volume (FV) in SR0 was optimized based on the spatial distribution of signal and background events, while additionally excluding parts of the detector with limited understanding of the detector conditions (field inhomogeneities, charge-insensitive volume, gas effects) [168]. This yielded a maximum radius of 63 cm, which was used for the low-energy ER search [146]. For the SR0 WIMP search, it was reduced to 61.35 cm to minimize the risk of surface background mismodeling [Paper I]. However, the impact of the maximum radius on WIMP sensitivity had not been directly assessed.

Due to the different field distortion correction (FDC) algorithm used in SR1 (see Section 4.2), surface backgrounds were reconstructed approximately 0.55 cm further inward. To maintain equivalent shielding from surface backgrounds, a tighter maximum radius was needed compared

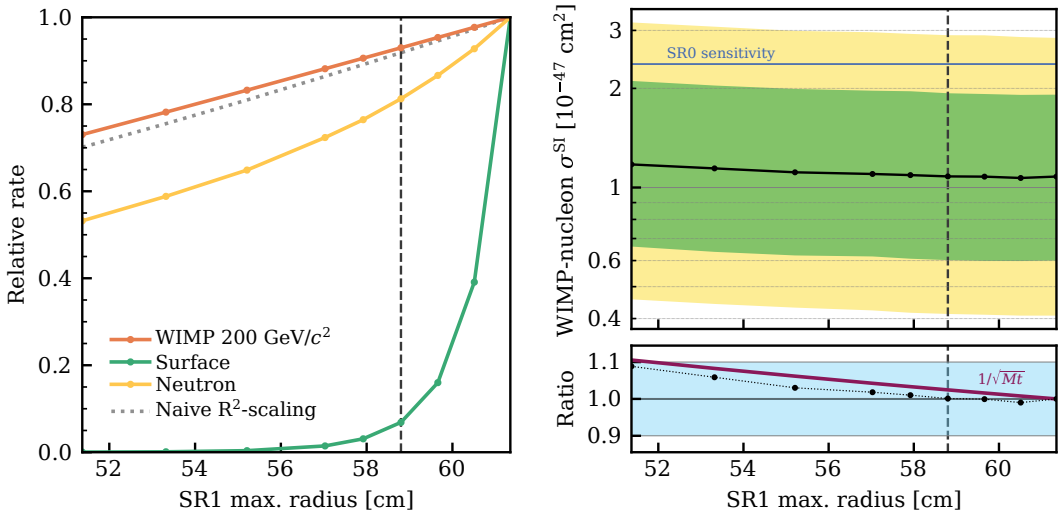

Figure 5.7.: *Left:* Relative signal and background rates versus maximum radius of the fiducial volume (FV) for SR1. For reference, the naive rate scaling with $1/R^2$ is shown as a dotted line. The observed WIMP signal rate declines more slowly due to the FV's reduced Z-range at large radii (see Figure 4.4). *Right:* Sensitivity impact for a 50 GeV/c^2 WIMP. The top panel shows absolute sensitivity, while the bottom panel shows the ratio to the scenario with the largest radius. The purple line indicates the expectation from square-root exposure scaling. The vertical dashed line indicates the chosen maximum radius of 58.80 cm.

to SR0. If the sensitivity was not significantly impacted, an even stricter radial selection criterion could further reduce the risk of background mismodeling.[3]

The sensitivity was evaluated across three WIMP masses and nine maximum radii using asymptotic critical regions. Figure 5.7 shows relative rates (left) and sensitivity (right) for 50 GeV/c^2 (representative of all masses) versus maximum radius. At 58.80 cm, the surface background was reduced by 93 % (factor 15 suppression) and the neutron background by approximately 19 % while retaining approximately 93 % of the WIMP signal. The sensitivity remained nearly constant down to approximately 58 cm, with only 10 % loss at 51.4 cm. Based on these results, a maximum radius of 58.80 cm (geometric fiducial mass of 4.03 t) was chosen for SR1, reducing the surface background to a negligible level while preserving most of the WIMP signal with <1 % sensitivity loss. The final LXe masses contained in the FVs after accounting for FDC effects are (4.17 ± 0.13) t in SR0 and (4.00 ± 0.15) t in SR1.

5.3.4 Impact of NR yield mismodeling

The NR band was modeled based on AmBe neutron calibration data (see Sections 4.1 and 4.4). Individual AmBe calibration fits for SR0 and SR1 provided NR yield models differing by $>1\,\sigma$. The chosen solution was to perform a combined fit sharing NR yield parameters across SRs but maintaining separate detector reconstruction models. To evaluate the potential impact of mismodeling the NR band, alternative SR1 templates were created using artificially enlarged SR0 NR yields with the SR1 detector reconstruction model. While this hybrid model inadequately

[3] Since radial distributions are already modeled in the likelihood (far-wire regions), radial selection criteria inherently reduce sensitivity. However, modest losses may be acceptable for enhanced robustness against background mismodeling.

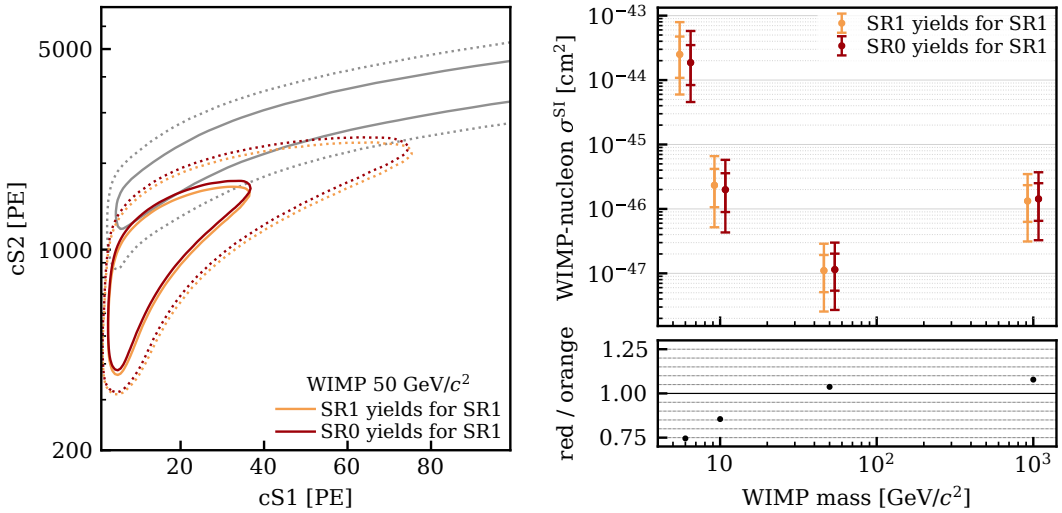

Figure 5.8.: *Left:* Comparison of nominal (yellow) and modified (red) SR1 WIMP templates using SR0 NR yields. The flat ER band is shown in gray for reference. Solid and dashed lines indicate $1\,\sigma$ and $2\,\sigma$ containment contours. *Right:* Impact of mismodeling the NR band on the sensitivity for four WIMP masses. The top panel shows the sensitivity versus WIMP mass, while the bottom panel presents the ratio of median sensitivities for the two scenarios.

described SR1 calibration data, it provided a useful estimate of the worst-case scenario for how NR band mismodeling could affect the WIMP sensitivity.

The resulting templates exhibit a shift in cS1–cS2, reducing the separation between the ER and NR bands, as illustrated in Figure 5.8 (left). Another effect, primarily relevant for low WIMP masses, is that the higher yields increase the signal rate for a given cross section, as more events surpass the detector threshold. The sensitivity was computed for four WIMP masses, which is compared to the nominal model (SR1 yields for SR1) in Figure 5.8 (right). For 50 and 1000 GeV/c^2, the increased overlap of NR and ER band from SR0 yields worsens the median UL by 4 % and 8 %, respectively. For 10 and 6 GeV/c^2, the dominant difference is the larger expected WIMP rate using SR0 yields, shifting the median by 15 % and 25 % in the other direction. Since this analysis focused on WIMP masses above 10 GeV/c^2, and the scenario considered here is a worst-case scenario, the impact of mismodeling the NR band was considered to be acceptably small.

5.4 Treatment of ^{124}Xe Double Electron Capture

With successful efforts to reduce backgrounds from radioactive impurities to ever-lower levels, the rare double-weak decays of xenon have started to contribute sizeable backgrounds. ^{124}Xe DEC contributed 13.6±1.5 expected events to the ER background in the SR0 + SR1 WIMP ROI, split between LM+LN-shell (∼6 keV) and LL-shell (∼10 keV) transitions with an approximate 1:2 ratio. Given this low rate relative to the total ER background (>900 events), the nominal model incorporates DEC into the flat ER component.

However, DEC and β-decay exhibit different event topologies that may produce distinct charge and light responses. Electron capture (EC) generates cascades of low-energy Auger-Meitner electrons with shorter track lengths than single β-particles of equivalent total energy. The

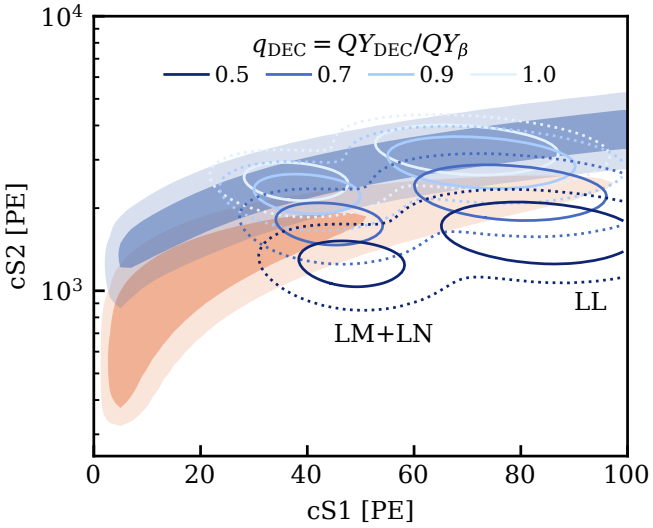

Figure 5.9.: Impact of varying double electron capture (DEC) charge yields on peak positions in cS1–cS2 space. Though LM+LN and LL yields are independent fit parameters, they are varied together here ($q_{DEC} = q_{LM} = q_{LL}$) for illustration. The flat ER band (blue) and 200 GeV/c^2 WIMP signal (orange) contours are shown for reference. $1\,\sigma$ (dark/solid) and $2\,\sigma$ (light/dashed) containment contours are shown.

resulting higher track density and therefore higher ionization density could enhance the electron-ion recombination fraction, potentially reducing the charge yield (QY) and increasing the light yield compared to β-events.

The XELDA experiment reported that L-shell EC of ^{127}Xe produces charge yields approximately 10 % lower than those from β-decays of the same energy at drift fields of ∼260 and ∼360 V/cm [240]. In addition, the LUX-ZEPLIN (LZ) experiment recently[4] reported a relative charge yield for LL-shell capture of $q_{LL} \equiv QY_{LL}/QY_\beta = 0.70 \pm 0.04$ [58]. For LM+LN-shell capture, they adopted a fixed value of $q_{LM} \equiv QY_{LM}/QY_\beta = 0.87$ based on single EC measurements in ^{127}Xe and ^{125}Xe. This approach was justified by their argument that M- and N-shell contributions to ionization density, and thus charge suppression, are subdominant compared to the L-shell contribution [241]. These measurements used higher drift fields than XENONnT's 23 V/cm, which could influence the yields.

The only dataset available to XENONnT for testing the hypothesis of reduced DEC charge yields was the WIMP search dataset itself. For this purpose, an alternative statistical model was devised with a likelihood function $\mathcal{L}^{mod}$, where the LM+LN and LL peaks were modeled explicitly. The charge yields of both peaks relative to single-β yields, q_{LL} and q_{LM}, are independent fit parameters, with light yields varying according to their anti-correlation with charge. Figure 5.9 shows possible DEC peak variations in cS1–cS2 space. Using the already-unblinded SR0 dataset, best-fit values of $q_{LL} \simeq 0.8$ and $q_{LM} =\simeq 0.7$ were obtained, though with large uncertainties.

For the LM+LN yield, a broad constraint $q_{LM} = 0.9 \pm 0.1$ based on XELDA measurements was included in $\mathcal{L}^{mod}$, with enlarged uncertainty for unknown field dependence and LM+LN versus L-shell differences. No ancillary constraint was used for q_{LL}; its value was determined solely by WIMP search data. Both parameters are bounded to [0.5, 1.0], where unity represents no

[4] Only preprint available before XENONnT unblinding.

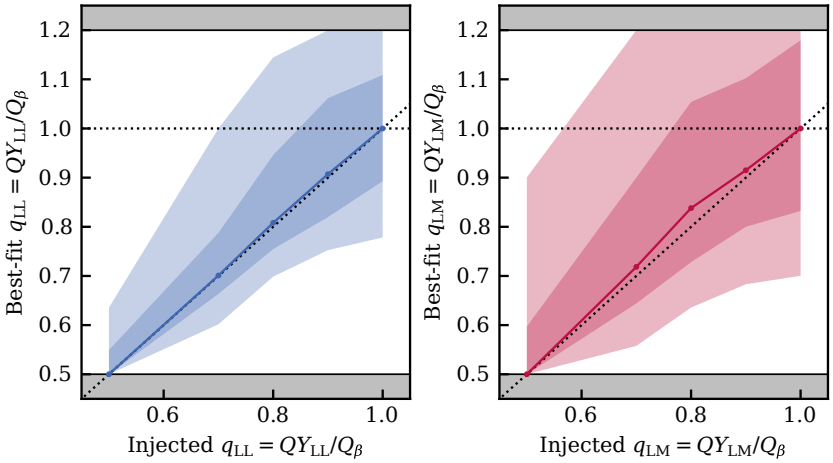

Figure 5.10.: Distribution of best-fit relative charge yields versus injected values from background-only toyMC experiments. Solid lines show medians; dark and light shading indicates $1\,\sigma$ and $2\,\sigma$ containment regions.

charge suppression relative to β-decays. Both DEC peak rates were treated as fully correlated via a common rate parameter. The combined rate was constrained via the KK and KL-shell DEC peaks outside the WIMP ROI, with branching fractions 72.4 % (KK: ∼64 keV), 20.0 % (KL: ∼37 keV), 1.4 % (LL: ∼10 keV), and 0.7 % (LM + LN: ∼6 keV) [110]. The resulting relative rate uncertainty is 15 %.

To assess the accuracy of a charge yield measurement with the WIMP search dataset, a study with background-only toyMC experiments was performed with a range of injected DEC charge yield values. The resulting spread of best-fit yield values is shown in Figure 5.10, without any ancillary yield constraints and with parameter bounds extended to 1.2. The analysis revealed limited constraining power except for significantly reduced true values. For the LM+LN peak, the $1\,\sigma$ containment interval of best-fit values included unity for injected relative yields above $\sim$ 0.75, while for the LL peak this occurred above $\sim$ 0.85. At the same time, this clearly shows that the observation of best-fit values below 1.0 is by no means a sufficient criterion to conclude the presence of reduced DEC charge yields. Several studies based on toyMC data were performed pre-unblinding to assess the potential impact on the sensitivity and assess the implications of mismodeling.

5.4.1 Impact of reduced DEC charge yields on the sensitivity

The impact of reduced DEC charge yields on the WIMP search sensitivity was studied using background-only toyMC experiments across three WIMP masses and five injected yield sets ($q_{DEC} = q_{LL} = q_{LM}$ for injection, though fit parameters could vary independently). Figure 5.11 shows the sensitivity versus injected yields for 10 and 1000 GeV/c^2 WIMPs. For 10 GeV/c^2, DEC yield effects are minimal since these WIMP signals barely extended above ∼20 PE in cS1, remaining largely unaffected by increased background leakage at higher cS1 values. Conversely, the 1000 GeV/c^2 case shows a strong sensitivity degradation due to substantial overlap between the signal region and the DEC peaks. Reduced yields of $q_{DEC} = 0.7$ worsen the median ULs by 25 % compared to β-like yields ($q_{DEC} = 1.0$). Interestingly, for even lower charge yields, the sensitivity impact diminishes as the DEC peaks shift below the NR band (see Figure 5.9).

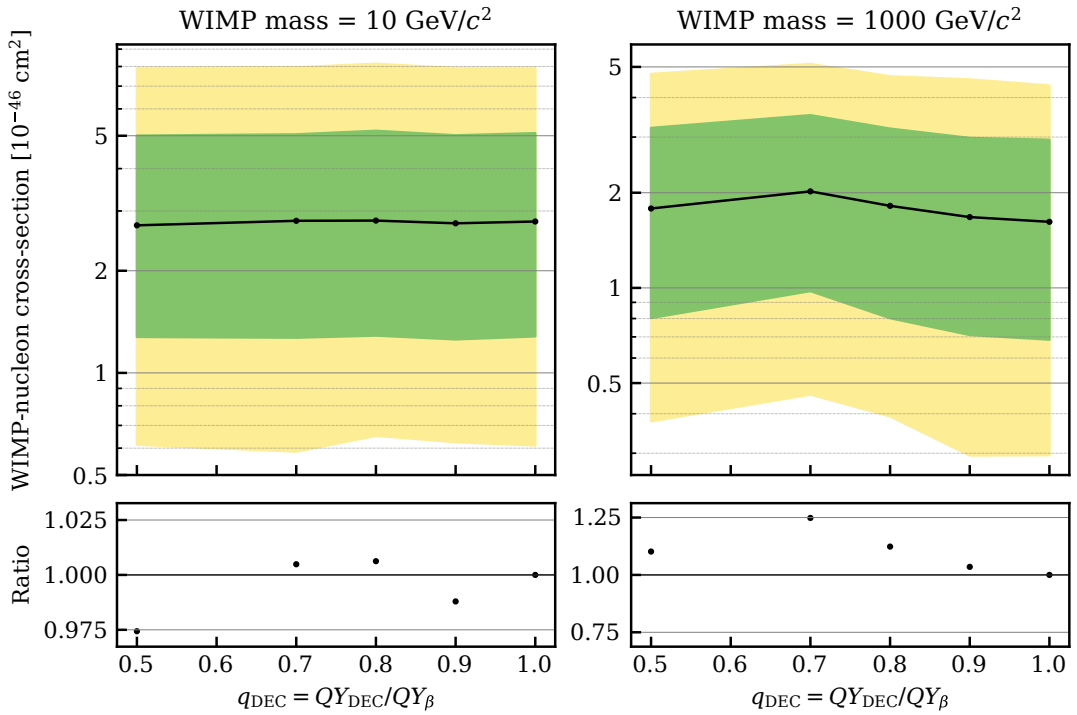

Figure 5.11.: WIMP sensitivity versus injected DEC charge yields ($q_{DEC} = q_{LL} = q_{LM}$) for 10 GeV/$c^2$ (left) and 1000 GeV/c^2 (right). Top panels show sensitivity bands containing 68 % and 95 % of ULs (green/yellow) and the median (black line). Bottom panels show ratios to the nominal β-yield case ($q_{dec} = 1.0$).

5.4.2 Implications of DEC charge yield mismodeling

While we generally aim for conservative modeling choices, what constitutes "conservative" for UL setting may differ from what is conservative for claiming WIMP discovery. Two mismodeling scenarios were used to assess implications for the WIMP search: (1) allowing reduced yields when the truth is β-yields and (2) fixing yields at β-values when the true values are reduced.

The first scenario (true $q_{LL} = q_{LM} = 1.0$, model allowed $q \leq 1.0$) used toyMC data with β-like DEC yields. For the same datasets, ULs were computed using two statistical models: one with DEC yields fixed at their true values $q_{LL} = q_{LM} = 1.0$, and another allowing fits with $q \leq 1.0$. The median of ULs with floating yields was ∼9 % lower than for the fixed-parameter case. Figure 5.12 shows UL distributions versus best-fit q_{LM} from background-only fits with floating yields. Systematic UL reductions are most pronounced when the fits favor reduced q_{LM}, indicating that the additional nuisance parameters absorb statistical fluctuations of ER background events, artificially tightening the limits. It should be noted that this particular analysis used a simplified statistical model without other ER shape parameters and asymptotic critical regions.

To test the second scenario (true $q_{LL}, q_{LM} < 1.0$, model fixed $q_{LL} = q_{LM} = 1.0$), toyMC datasets with three reduced yield sets were used (see Figure 5.13): moderate reduction ($q_{LL} = q_{LM} = 0.9$), SR0 best-fit ($q_{LL} = 0.8$, $q_{LM} = 0.7$), and LZ best-fit ($q_{LL} = 0.70$, $q_{LM} = 0.87$). When DEC peaks significantly overlap with the WIMP signal region, a fraction of DEC events can be misattributed to WIMP interactions if the analysis assumes fixed β-yields. The false WIMP discovery rate quantifies the probability of incorrectly rejecting the background-only

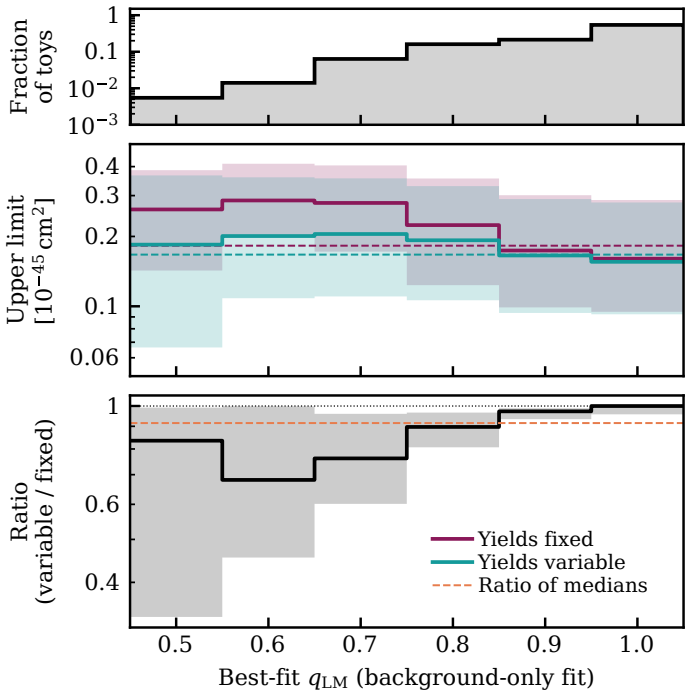

Figure 5.12.: Upper limit distributions for 1000 GeV/c^2 WIMP cross sections using identical toyMC data with fixed double electron capture (DEC) yields (purple) versus variable yields as nuisance parameters (teal). The bottom panel shows UL ratios between models. Solid lines indicate medians, shaded regions show central 68 % regions, and dashed lines mark the global median values. The top panel shows the distribution of best-fit q_{LM} values.

hypothesis ($\mu = 0$) when it is, in fact, true ($\mu^* = 0$). Formally, this is expressed as

$$P(\text{reject } \mu = 0 | \mu^* = 0). \tag{5.5}$$

By design, this rate (statistical error of the first kind) should correspond to $\Phi(3) \simeq 0.13\,\%$, where Φ is the cumulative standard normal distribution. In other words, in 0.13 % of cases, the background-only hypothesis should be rejected with at least $3\,\sigma$ significance in the absence of any true signal. However, in the SR0 best-fit scenario, where the LM+LN peak substantially overlaps with the NR band, the false discovery rate at $3\,\sigma$ significance threshold rises to 3.5 %, which is more than 25 times higher than the nominal expectation.

5.4.3 Definition of the DEC hypothesis Test

To robustly assess whether ^{124}Xe DEC peaks exhibit significantly reduced charge yields in the XENONnT dataset, a dedicated hypothesis test was defined prior to unblinding. The test statistic is based on the profile-likelihood ratio, similar to Equation (4.1), but incorporates two parameters of interest: q_{LL} and q_{LM}. Specifically, it is defined as

$$t_{\mathrm{DEC}} = -2 \ln \left[\frac{\mathcal{L}^{\mathrm{mod'}}(q_{\mathrm{LL}} = 1.0, q_{\mathrm{LM}} = 1.0, \hat{\hat{\boldsymbol{\theta}}})}{\mathcal{L}^{\mathrm{mod'}}(\hat{q}_{\mathrm{LL}}, \hat{q}_{\mathrm{LM}}, \hat{\boldsymbol{\theta}})} \right], \tag{5.6}$$

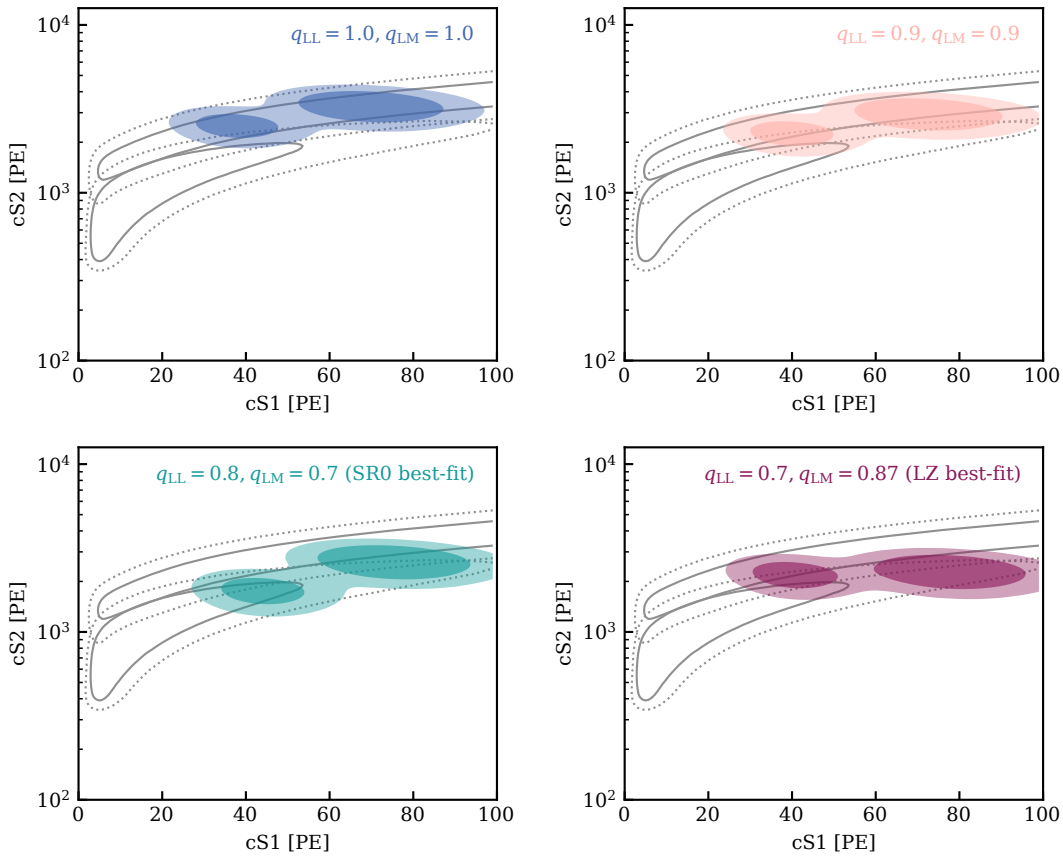

Figure 5.13.: Four double electron capture (DEC) charge yield combinations used to evaluate the impact of their mismodeling and the performance of the DEC hypothesis test. Each panel shows $1\,\sigma$ (dark/solid lines) and $2\,\sigma$ (light/dotted lines) containment contours for LM+LN and LL DEC peaks (colored) overlaid with the flat ER background and $1000\,\mathrm{GeV}/c^2$ WIMP signal contours (gray) for reference.

where the prime on $\mathcal{L}^{\text{mod'}}$ indicates that the ancillary constraint on q_{LM} is omitted, allowing both DEC charge yield parameters to be independently determined solely from the science data.[5] Figure 5.14 (left) shows correlations between the WIMP discovery (t_0) and DEC hypothesis (t_{DEC}) test statistics for the same three reduced-yield models from above and the nominal $q_{\text{LL}} = q_{\text{LM}} = 1.0$. Correlations become pronounced for low DEC charge yields, with a correlation coefficient (Pearson's r) of 0.55 for the SR0 best-fit case.

It was decided that the model with explicit DEC peaks would be used only if the hypothesis test rejected the β-yield hypothesis $q_{\text{LM}} = q_{\text{LL}} = 1.0$. To evaluate this conditional modeling approach, the false WIMP discovery rate (Equation (5.5)) was computed as a function of the DEC test size α_{DEC} (corresponding to a confidence level (CL) of $1 - \alpha_{\text{DEC}}$), accounting for model switching triggered by β-hypothesis rejection. One difficulty for this analysis was that the distribution of the test statistic for the WIMP discovery test t_0 depends to some extent on the true injected DEC yield values. Since computing critical regions for every set of best-fit yield parameters is computationally intractable, these regions were approximated using their values for the respective injected DEC yield values.

The β-yield rejection power for true values $q^*_{\text{LL}}, q^*_{\text{LM}}$ is:

$$P(\text{reject } \; q_{\text{LL}} = q_{\text{LM}} = 1.0 | q^*_{\text{LL}}, q^*_{\text{LM}}). \tag{5.7}$$

Figure 5.14 (right) shows β-yield rejection power (top) and false WIMP discovery rates (bottom) versus test size α_{DEC}. The highest β-yield rejection power is observed for LZ best-fit yields, which is plausible given that in this scenario the dominant LL peak is strongly shifted into a low-background region. Conversely, the highest false WIMP discovery rate arises from the SR0 best-fit yields, where strong suppression of the LM+LN yield results in significant overlap with the WIMP signal PDF. Crucially, the substantially elevated false discovery rates in case of strongly reduced yields can be restored to nominal levels by selecting sufficiently large α_{DEC}.

For the SR0 + SR1 WIMP search, a test size of $\alpha_{\text{DEC}} = 5\,\%$ was chosen. Under the tested worst-case scenario, this corresponds to a false WIMP discovery rate of 0.16 %, only slightly above the nominal 0.13 %. At the same time, the test achieves 66 % rejection power of the β-yield model if the true scenario matches the SR0 best-fit, and 80 % rejection power for the LZ best-fit case. To avoid bias from the already unblinded SR0 dataset, it was ultimately decided to perform the test on the SR1 dataset alone, slightly reducing the test power (49 % for SR0 best-fit, 66 % for LZ best-fit).

5.5 Long-term WIMP Sensitivity Projections

Long-term sensitivity projections serve as vital tools for both designing new experiments and guiding operational decisions for existing ones. These studies enable evaluation of different scenarios, helping balance risk and potential gain for informed strategic decisions.

XENONnT faces a critical operational challenge: a short-circuit between bottom screening and cathode electrodes reduced the drift field to 23 V/cm [146], significantly below the 200 V/cm

[5] In practice, if the DEC hypothesis test would fail to reject the β-yield hypothesis, the likelihood function from Equation (5.1) would be used rather than $\mathcal{L}^{\text{mod'}}$. However, the dominant flat ER background makes both approaches nearly equivalent.

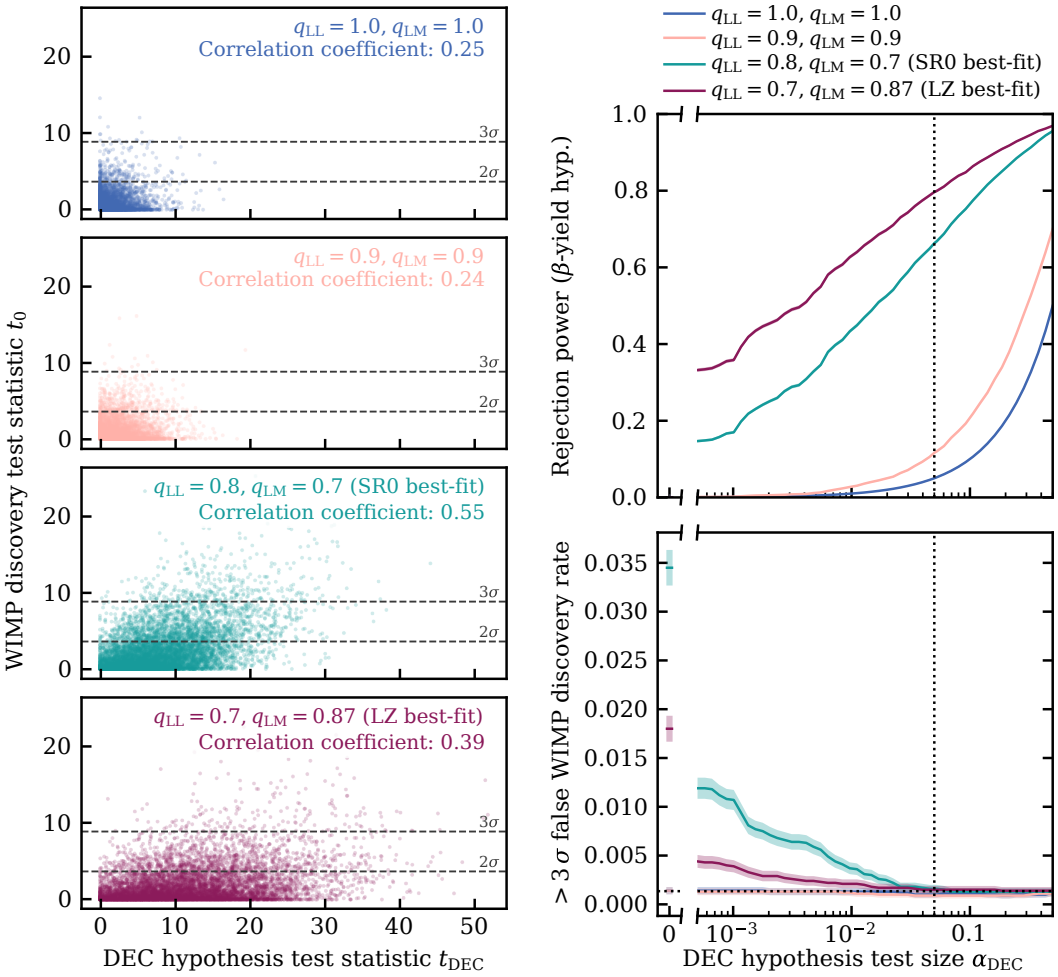

Figure 5.14.: *Left:* Correlation between double electron capture (DEC) and WIMP discovery test statistics for various injected DEC yields. *Right:* β-yield rejection power (top) and false WIMP discovery rates (bottom) versus DEC test size α_{DEC}. The shading indicates binomial uncertainties from finite toyMC samples. A dotted horizontal line indicates the nominal false discovery rate of 0.13 % and a vertical dotted line marks the chosen test size $\alpha_{DEC} = 5\,\%$.

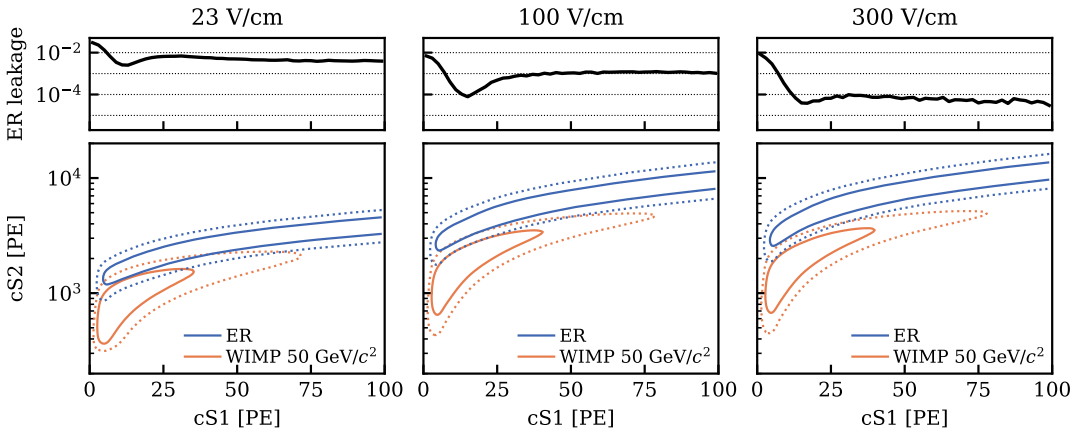

Figure 5.15.: Impact of the electric drift field on ER/NR band separation in cS1–cS2 space. Bottom panels show PDFs of a 50 GeV/c^2 WIMP signal and flat-spectrum ER background ($1\,\sigma$ and $2\,\sigma$ containment contours) at 23, 100, and 300 V/cm. Top panels display the ER leakage fractions below the NR median in cS2 versus cS1, illustrating strong background suppression with increasing drift field.

design goal [90]. This reduced field diminishes ER/NR band separation, increasing background leakage into the WIMP signal region. Additionally, the extraction field had to be set to 2.9 kV/cm to suppress single-electron hot spots, resulting in only ∼50 % electron extraction efficiency. In addition, elevated single- and few-electron S2 rates near the transverse support wires [186] further increase AC background rates (see Section 4.4).

Initially, XENONnT achieved a sensitivity comparable to LZ [89, 239]. However, LZ's latest result with 4.2 t yr exposure [58] demonstrates a sensitivity 2.5 to 3 times better than XENONnT's 3.1 t yr result [Paper II], primarily due to significant ER leakage in XENONnT's signal region. Figure 5.15 illustrates the importance of drift field for background suppression by comparing the PDFs of a 50 GeV/c^2 WIMP signal and flat-spectrum ER background in cS1–cS2 space for 23, 100, and 300 V/cm drift fields. Top panels show ER leakage fractions below the NR band median versus cS1. Each drift field increase reduces leakage by approximately one order of magnitude on average.

New cathode, gate, and anode electrodes, designed without transverse support wires, have been manufactured and successfully tested. Their installation is expected to enable drift fields ≥100 V/cm and ∼95 % electron extraction efficiency, matching the performance demonstrated in XENON100 [184] and XENON1T [82], and fulfilling XENONnT's original design goal [90]. However, the interruption in data taking for this operation, entailing at least a full year of downtime, had to be weighed against the option of continuing under current conditions. This section presents sensitivity projection studies performed to inform this decision, exploring XENONnT operation scenarios through 2035. The new PDF templates were computed using the xenon emission model of XENON1T [200].

5.5.1 Operational scenarios

This study was conducted in November 2024, while SR2 data-taking was still ongoing. It was assumed that the earliest feasible date to halt data-taking and begin operations for the electrode replacement would be July 1, 2025. Any data-taking period after this date is termed SR3 here, either as direct continuation without repair or post-repair operation at increased

drift field. All projections assume combined analyses including SR0 and SR1 using signal and background models from [Paper II]. Key assumptions for other SRs, established through expert consultation on background sources and detector subsystems, are summarized below. Optimistic SR3 scenarios are stated in italicized parentheses.

SR2

Identical to $SR1_b$ conditions but with 75 % neutron veto (NV) tagging efficiency (up from 53 %) due to 0.05 % Gd salt loading, which is expected to reduce neutron backgrounds by a factor of 1.9 [148]. A 61 % duty cycle (time fraction the detector is collecting science search data) compared to ∼50 % for SR0/SR1 was assumed throughout the run, which corresponds to the achieved value at the time this study was prepared.

SR3 without electrode repair

Based on the $SR1_b$ model with adjusted background rates:

- **ER background:** 50 % increase in ^{222}Rn background due to a newly-installed charcoal filter targeting photoionizable backgrounds (see Section 4.1). This is expected to result in a total increase in the flat ER component of 20 %.
- **AC background:** Reversion to SR0 levels due to installation of the charcoal filter.
- **Neutron background:** 75 % NV tagging efficiency as in SR2, expected to reduce neutron backgrounds by factor 1.9 *(optimistic: 0.5 % Gd loading achieving 90 % tagging efficiency, reducing neutron backgrounds by factor 4.7 relative to $SR1_b$.*[6]*)*
- **Duty cycle:** 60 %, similar to SR2 *(optimistic: 65 %).*

SR3 with electrode repair

Based on $SR1_b$ background rates with new PDF templates for higher drift and extraction fields. Since AC and surface models are data-driven, SR0 templates were scaled in cS2 to account for higher extraction efficiency and slightly increased single-electron amplification with new electrodes. A fiducial mass of 4.2 t (as in SR0) was assumed.

- **Electric fields:** 100 V/cm drift field (up from 23 V/cm) and 95 % extraction efficiency (up from ∼50 %) *(optimistic: 300 V/cm drift field).*
- **Neutron background:** Full 0.5 % Gd loading achieving 90 % tagging efficiency, which suppresses neutron backgrounds by a factor of 4.7 compared to $SR1_b$ *(optimistic: additional 30 % reduction from improved multi-scatter discrimination).*
- **AC background:** Factor 5 reduction versus SR0 from doubled drift velocity with higher drift field,[7] elimination of the transverse support wires associated to high AC background rates, and possibly reduced delayed electron rate via higher extraction efficiency[8] *(optimistic: factor 10 reduction).*
- **ER background:** Nominal $SR1_b$ levels *(optimistic: no ^{3}H-like component).*
- **Duty cycle:** 65 %, improved by reduced downtime related to single-electron hot spots and anode trips with new electrodes *(optimistic: 70 %).*

[6] This further loading would likely require additional maintenance inside the water tank to ensure high transparency under the lower pH conditions [148]. It is therefore considered only as an optimistic scenario.

[7] From 0.675 mm µs^{-1} at 23 V/cm [168] to ∼ 1.3 mm µs^{-1} at 100 V/cm [242, 243].

[8] SR0 total AC rate: 3.9 t^{-1} yr^{-1} with 11.4 t^{-1} yr^{-1} near wires and 2.3 t^{-1} yr^{-1} far from them [Paper I]. The factor 5 reduction yields a rate of 0.8 t^{-1} yr^{-1}, matching LZ's rate [58].

- **Downtime:** Nominal 1.5 calendar years for replacement and recommissioning, varied between 0.5–2.5 years in Section 5.5.4.

5.5.2 Simplified statistical model

The likelihood function used for this study is defined as the product of extended unbinned likelihoods in (cS1, cS2, R) space with separate functions per SR (Equation (5.2)). SR3 with electrode upgrades eliminates the need for near/far-wire separation since the new electrodes require no support wires. Confidence intervals were computed based on toyMC methods described in Section 4.5.5 for 10, 50, and 1000 GeV/c^2 WIMP masses; the latter yielded identical conclusions to 50 GeV/c^2 and is thus not explicitly discussed here. For computational tractability, the statistical model was simplified compared to the complete WIMP-search model described in Sections 5.1 and 5.2. Specifically, ER shape nuisance parameters were omitted, which also allowed dropping the calibration likelihood function $\mathcal{L}_{\mathrm{cal}}$ from Equation (5.1). Additionally, the signal efficiency uncertainty was not considered.

5.5.3 Background importance assessment

Understanding relative background importance is crucial for any physics search. Except for neutrino-induced backgrounds, all predicted rates depend on detector conditions and radioactivity levels with considerable prediction uncertainties. However, not all backgrounds affect the WIMP sensitivity equally. To prioritize mitigation strategies and evaluate the robustness of the sensitivity projections, it is useful to first identify the most important background sources.

To illustrate this, a cumulative signal PDF is constructed by iteratively adding template bins in (cS1, cS2, R) space starting from those with the highest signal-to-background ratio. For any given fraction of the WIMP signal, this method identifies the region of parameter space with the lowest possible background contamination. Figure 5.16 shows this, broken down into the individual background components for 10 GeV/c^2 (left) and a 50 GeV/c^2 (right) WIMPs for SR3 without (top) and with (bottom) electrode repair. The lowest background rates at 50 % signal acceptance are marked and visualized as a pie chart. Backgrounds with distributions distinct from the signal, such as ER and surface backgrounds, show a slow increase with the included signal fraction until a sharp rise near full signal acceptance. In contrast, backgrounds more similar to the signal, like CEνNS for 10 GeV/c^2 or atmospheric CEνNS and neutrons for 50 GeV/c^2, increase more steadily.

Evaluating background rates at 50 % signal acceptance was found to be a useful benchmark for relative importance. For 10 GeV/c^2 WIMPs, AC background dominates. For 50 GeV/c^2 WIMPs, the ER background is the primary contributor without electrode repair; with new electrodes, both ER and AC backgrounds contribute similarly. Notably, electrode replacement is expected to significantly lower total background rates at 50 % signal acceptance, by roughly a factor of two for 10 GeV/c^2 and five for 50 GeV/c^2 WIMPs. Beyond background reduction, the improved electron extraction efficiency of new electrodes would also lower the energy threshold,

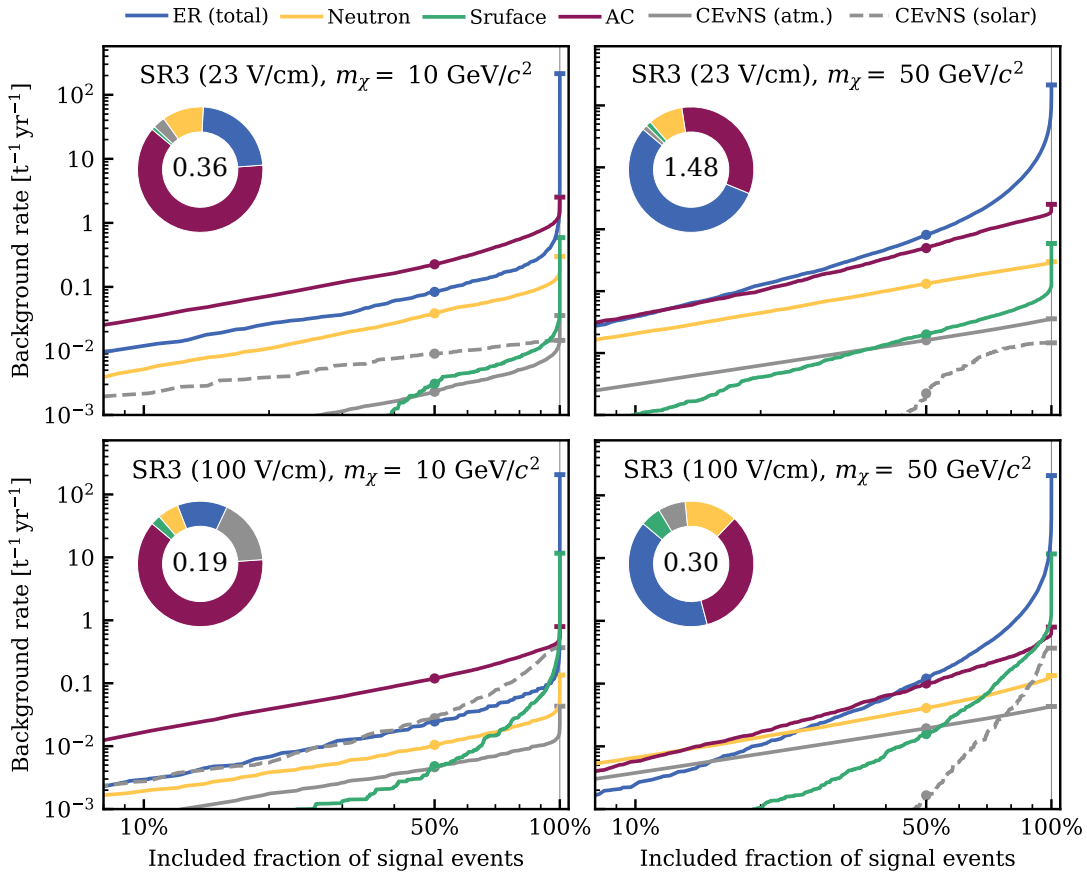

Figure 5.16.: Background composition as a function of the accumulated signal fraction, starting from regions of highest signal-to-background ratio in (cS1, cS2, R) space. Results are shown for 10 GeV/c^2 (left) and 50 GeV/c^2 (right) WIMP signals, comparing the SR3 scenario without electrode replacement (top) and with new electrodes achieving a drift field of 100 V/cm (bottom). Pie charts show background rates at 50 % signal acceptance (values in [t^{-1} yr^{-1}]), highlighting dominant components in signal-like regions.

especially benefiting low-mass WIMP searches.[9] For a 10 GeV/c^2 WIMP, this would result in signal rates approximately 1.7 times higher than SR0 and 2.4 times higher than SR1. For a 50 GeV/c^2 WIMP, the improvement would be approximately 20 % over previous SRs.

5.5.4 Sensitivity projections and break-even analysis

Figure 5.17 shows the resulting sensitivity as a function of calendar time. Projections cover the period from the beginning of SR2 data-taking (end of 2023) until mid-2035. The initial point corresponds to the SR0 + SR1 sensitivity, which agrees well with the complete statistical model (see Figure 5.5), indicating minimal impact from the simplifications discussed in Section 5.5.2. Until mid-2025, data-taking under SR2 conditions was assumed (gray), reaching a sensitivity to 0.6 times lower cross sections compared to the SR0 + SR1 search. From that point, two

[9] In SR0 and SR1, thresholds of S2 > 200 PE and 320 PE were applied, respectively, corresponding to approximately 6 and 10 extracted electrons. With higher electron extraction efficiency after electrode replacement, the same S2 thresholds would correspond to smaller initial charge signals, effectively lowering the energy threshold. Charge and light yields also vary with the drift field, but the signal rate is mostly influenced by the higher extraction efficiency.

SR3 scenarios are compared: operation without replacing the electrodes (red) and with new electrodes, reaching a drift field of 100 V/cm (blue). While the sensitivity in the latter scenario would not improve during the nominal downtime of 1.5 calendar years, it would quickly catch up to the alternative scenario once data-taking resumes.

Reference lines show currently leading experimental limits and sensitivity [58] and XENONnT's design projections for 20 t yr exposure [90].[10] Figure 5.17 shows that with new electrodes, XENONnT could reach LZ's 2025 sensitivity in 2027, whereas without them, this level would only be achieved by 2029. With new electrodes, XENONnT would reach the design sensitivity for 10 GeV/c^2 by the end of 2031 (with a total exposure of ∼21 t yr, ∼14 t yr of which acquired in SR3) but would fall short of the design sensitivity for 50 GeV/c^2 by a factor of ∼1.6. The shortcoming with respect to the design sensitivity can be attributed to that study neglecting AC backgrounds and assuming a 200 V/cm drift field (versus 100 V/cm here). The 10 GeV/c^2 scenario seems less affected by this, likely due to a cS1 > 3 PE cutoff applied in the design projection, primarily reducing low-mass WIMP rates. The impact of individual background rates on the SR3 sensitivity projection with new electrodes is discussed in Appendix A.

While catching up with other experiments remains challenging as they continue taking data, a critical metric for assessing the benefit of electrode replacement is the *time to break even*: the time after resuming data-taking with new electrodes to surpass the sensitivity achievable by an uninterrupted operation in low-field conditions. This metric is critical because it quantifies the recovery time required to offset the initial downtime caused by upgrading the detector. Figure 5.18 shows break-even times in months for 10 and 50 GeV/c^2 as a function of the total downtime, which includes electrode replacement and recommissioning of the upgraded detector. Solid lines represent break-even times for nominal scenarios, and shaded bands span combinations of nominal and optimistic assumptions. Break-even would be achieved within 2 to 10 months after resuming data-taking with new electrodes across all scenarios. Even for a pessimistic 2.5-year downtime, break-even would be reached before the end of 2028. This remarkable recovery time was a key factor influencing the collaboration's decision to proceed with the electrode replacement.

5.6 Conclusions

This chapter detailed the statistical framework and sensitivity studies for the XENONnT WIMP search using the first two SRs. The combined SR0 + SR1 analysis achieved up to 1.8× improved sensitivity compared to the analysis with SR0 alone. Key analysis decisions were informed by comprehensive sensitivity studies: $SR1_a$ phase 0 was excluded with minimal 3 % sensitivity impact, the S2 threshold was raised from 200 to 320 PE to alleviate issues with AC background modeling with minimal loss in sensitivity, and the fiducial volume was selected to increase robustness against background mismodeling with < 1 % sensitivity loss. Possible NR yield mismodeling was found to have acceptable impacts on sensitivity, validating the combined calibration approach across SRs. A dedicated hypothesis test was introduced to determine the treatment of ^{124}Xe DEC charge yields, switching to a reduced-yield model only if the data provided evidence for it. This balances the biases that could otherwise arise in the false WIMP discovery rate or limit setting.

[10] LZ's designed final sensitivity matches XENONnT above 50 GeV/c^2 but is 1.6× better at 10 GeV/c^2 [244].

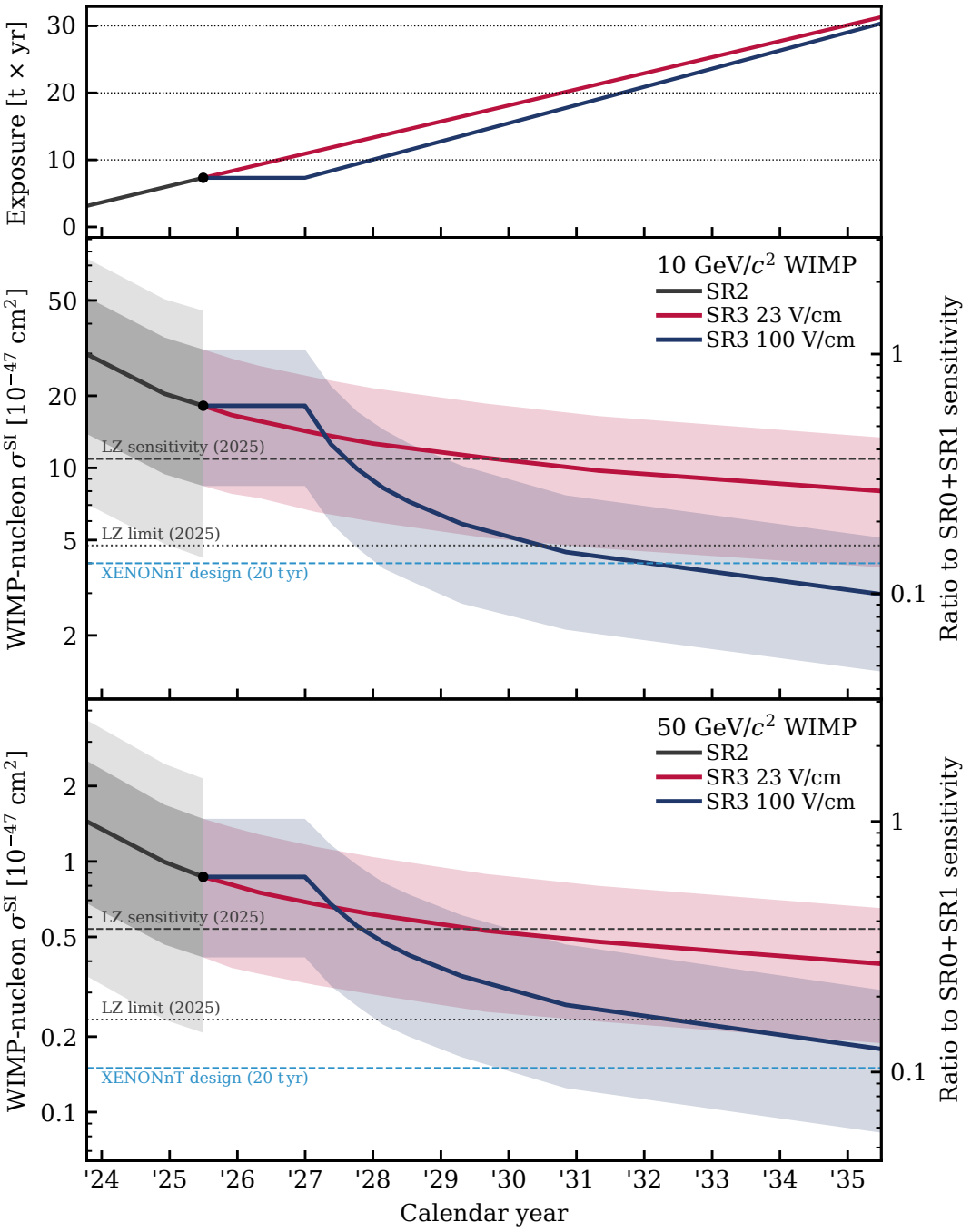

Figure 5.17.: Long-term WIMP sensitivity projections for XENONnT for 10 GeV/c^2 (middle) and 50 GeV/c^2 (bottom); the top panel shows corresponding exposures. Solid lines show the median projected upper limit (UL) as a function of time, with dark and light shaded bands indicating the 1 σ and 2 σ UL containment regions, respectively. Following SR2 (gray), two scenarios for SR3 are shown: continued operation under low-field conditions (red) and operation with new electrodes (blue), the latter assuming a 1.5-year downtime for electrode replacement and detector recommissioning. For comparison, the 2025 sensitivity and ULs from LZ [58] and the XENONnT design goal [90] are indicated as horizontal lines.

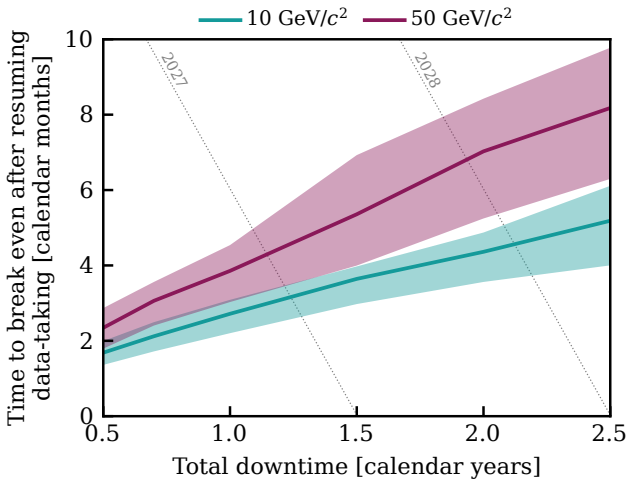

Figure 5.18.: Break-even time versus total downtime for electrode replacement and detector recommissioning. The plot shows the duration to surpass the sensitivity achievable with low-field conditions after resuming data-taking with new electrodes. Diagonal lines indicate the beginning of a corresponding year. Solid lines represent nominal scenarios; shaded bands show variation across combinations of nominal and optimistic assumptions.

Long-term projections through 2035 provided crucial guidance for XENONnT's electrode replacement decision. Operations with 23 V/cm drift fields suffer from significant leakage from ER background, limiting sensitivity compared to other experiments. New electrodes enabling $\geq$100 V/cm drift fields and 95 % electron extraction efficiency promise clear improvements. Despite a downtime above one year, break-even analysis demonstrated recovery within 2–10 months of resumed operations, with XENONnT reaching LZ's 2025 sensitivity by 2027 versus 2029 without upgrades. In December 2024, the XENONnT collaboration decided to proceed with electrode replacement. Data-taking was stopped in early 2025; the water tank was drained, the NV disassembled, and a cleanroom constructed around the cryostat. The cryostat was successfully opened in summer 2025 to begin electrode replacement. With upgrades underway, the collaboration anticipates resuming operations in 2026 – better equipped for advancing dark matter searches through the end of the decade.

6

Statistical Model and Sensitivity Studies for the XENONnT ^{8}B CEνNS Search

This chapter presents the statistical model and Toy Monte-Carlo (toyMC)-based sensitivity studies for the search for coherent elastic neutrino-nucleus scattering (CEνNS) from ^{8}B solar neutrinos using an exposure of 3.51 t yr from XENONnT's first two science runs (SRs) (SR0 and SR1), published in [Paper III]. The statistical model is detailed in this chapter, including signal and background modeling (Section 6.1) and the definition of the likelihood function (Section 6.2). Sensitivity studies that guided analysis decisions and tested the robustness of the search are summarized in Section 6.3, followed by a study on the power of goodness of fit (GOF) tests in Section 6.4.

6.1 Signal and Background Modeling

General signal and background modeling concepts of XENONnT are described in Section 4.4. This section focuses on analysis-specific modeling for the ^{8}B CEνNS search with SR0 + SR1 data. The dominant background arose from accidental coincidence (AC) events, which were modeled using data-driven methods. Additional backgrounds from neutrons and electronic recoil (ER) events were also included. A crucial difference from the weakly interacting massive particle (WIMP) search analysis presented in Sections 5.1 and 5.2 was the significantly lower analysis threshold, necessary to achieve sensitivity for solar CEνNS.

6.1.1 Lowering the analysis threshold

The ^{8}B CEνNS rate in the SR0 WIMP search region of interest (ROI) is only $\sim 0.17\,\mathrm{t}^{-1}\,\mathrm{yr}^{-1}$ [Paper I], yielding fewer than one expected event for the combined SR0 + SR1 exposure. Most nuclear recoils (NRs) from CEνNS simply fall below the analysis threshold of $\sim$3.5 keV$_{\mathrm{NR}}$. Therefore, detecting solar neutrinos required lowering the analysis threshold. This was achieved by reducing the tight coincidence requirement from 3 to 2 photomultiplier tube (PMT) hits

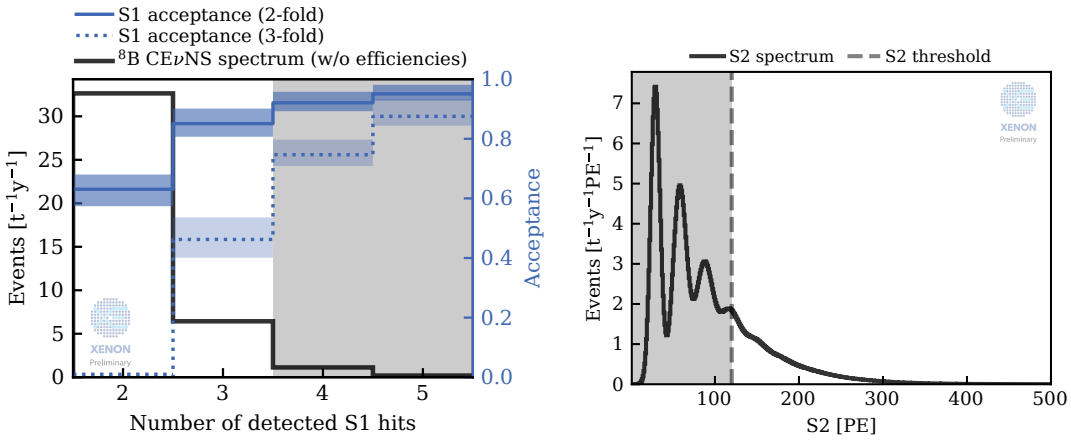

Figure 6.1.: Expected ^{8}B CEνNS event rate versus S1 and S2 signal size. *Left:* Signal rate versus S1 hit multiplicity. The right axis shows the S1 reconstruction efficiency (acceptance) for 2-fold (solid) and 3-fold (dotted) tight coincidence requirements. The gray region ($\geq$ 4 hits) is excluded from the search. *Right:* Signal rate versus S2 area. Bumps in the gray region below threshold correspond to 1, 2, and 3 extracted electrons. Courtesy of the XENON collaboration.

and lowering the S2 threshold from 200 to 120 photoelectrons (PE). Combined, these changes increased the event rate by approximately a factor of 17 (after selection criteria). The ROI was defined as S1 signals with 2 or 3 PMT hits and S2 areas of 120–500 PE, corresponding to roughly 4–16 extracted electrons. The expected distributions of ^{8}B CEνNS signals in these parameters are shown in Figure 6.1.

Lowering the thresholds led to a substantial increase in AC background rates. For the analysis with 2-fold coincidence, isolated S1 and S2 rates in the ROI before selection criteria were $R_{\mathrm{isoS1}} = 15$ Hz and $R_{\mathrm{isoS2}} = 150$ mHz [182]. Random pairing within the maximum drift time of 2.25 ms would yield ∼400 AC events per day (∼150 000 per year). Despite a higher expected CEνNS signal compared to a 3-fold analysis, rates remained below 15 events per year. Thus, reducing the AC background by several orders of magnitude was essential for the detection of ^{8}B CEνNS.

Selection criteria targeting AC background are described in Section 4.3, with background origins discussed in Section 4.4. After peak-level quality criteria, isolated signal rates dropped to $R_{\mathrm{isoS1}} \simeq 2.25$ Hz and $R_{\mathrm{isoS2}} \simeq 20$ mHz [Paper III]. Additional event-level criteria further suppressed AC background, including the fiducial volume (FV) selection, which also excluded regions near the transverse support wires (see Section 3.3), and the S2 boosted decision tree (BDT) selection criterion.

The ^{8}B CEνNS signal in S1–S2 lies well below the ER and even the NR band (see Figure 4.8). Only events with upward fluctuations in the number of emitted photons can be observed. Consequently, ER and neutron backgrounds contributed only 0.7 ± 0.7 and $0.5^{+0.2}_{-0.3}$ expected events, respectively. The final expected number of AC background events in SR0 + SR1 is 25.3 ± 1.2, yielding a total background estimate of $26.4^{+1.4}_{-1.3}$. The expected number of ^{8}B CEνNS events is $11.9^{+4.5}_{-4.2}$. Details on background rate uncertainties are given in Section 6.2.

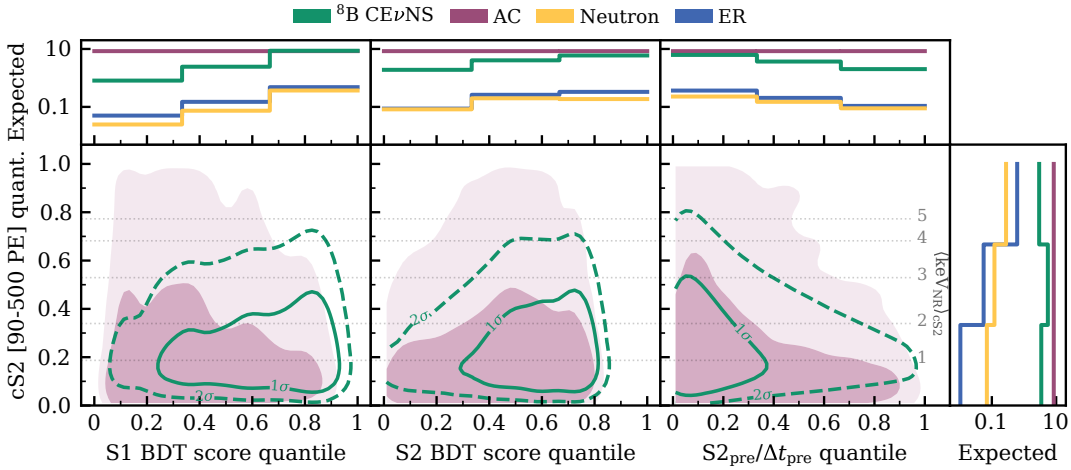

Figure 6.2.: ^{8}B CEνNS signal and background distributions in the four-dimensional analysis space. The $1\,\sigma$ ($2\,\sigma$) containment regions for ^{8}B CEνNS signal AC background are shown as solid (dashed) contours and dark (light) shaded regions, respectively. One-dimensional projections show the number of expected events per bin. Based on a plot from [59].

6.1.2 Four-dimensional analysis space

A four-dimensional binned analysis space was chosen to maximize discrimination between ^{8}B CEνNS signals and AC background. Signal and background distributions in this space are shown in Figure 6.2. The four analysis dimensions are:

Corrected S2 area

The corrected S2 area measures the number of detected electrons, which is related to the deposited energy. For physical signals, the cS2 distribution reflects recoil energy spectra.

S2 time shadow

The "S2 time shadow" ($S2_{pre}/\Delta t_{pre}$) quantifies the proximity of a signal to a preceding high-energy event, defined using the S2 area of the previous event and the time difference Δt_{pre}. Large $S2_{pre}/\Delta t_{pre}$ values indicate the signal is close in time to a large S2, increasing the chance of forming AC background. A selection criterion on $S2_{pre}/\Delta t_{pre}$ removed >80 % of 2-hit isolated S1 signals while retaining 87 % of the signal. After applying the selection, $S2_{pre}/\Delta t_{pre}$ serves as an analysis variable for the remaining data.

S1 BDT score

Multiple parameters distinguish physical S1 signals from random PMT hit pileup that can form AC S1 signals:

- **Double-PE effect:** Vacuum ultraviolet (VUV) scintillation photons occasionally produce two PE per photon, while longer-wavelength fluorescence light and dark counts do not exhibit this behavior. Consequently, on average, AC S1 signals show smaller maximum single-PMT fractions.
- **Photon arrival timing:** Physical signals follow the scintillation pulse shape, while pileup appears random. The minimum hit time difference characterizes this.
- **Top array contribution:** Physical S1 signals show characteristic top/bottom PMT array distributions based on optical propagation in the active volume.

- **Total PMT hits:** On average, CEνNS S1 signals have more contributing hits than AC S1 signals.

A BDT model was trained to distinguish AC S1 signals (isolated S1s sampled from data) from ^{8}B CEνNS S1 signals (simulated waveforms), returning scores from 0 (most AC-like) to 1 (most signal-like). This score was fully used as an analysis dimension without applying a prior selection.

S2 BDT score
A second BDT model selected well-reconstructed events based on drift-time-dependent S2 signal width due to electron diffusion. Instead of a simple selection in drift time versus S2 width, a BDT using three S2 pulse shape parameters (rise time, temporal widths of central 50 % and 90 %) and reconstructed depth (Z) was trained. The resulting score was used for both selection ($\sim$ 90 % AC rejection at $\sim$ 80 % signal acceptance) and as an analysis variable.

Binning
For each SR, signal and backgrounds were modeled in 3 bins per analysis dimension, yielding $3^4 = 81$ bins per SR. Bin boundaries were chosen to ensure equal numbers of expected AC events in each bin when projected onto a single dimension. For the BDT scores and $S2_{pre}/\Delta t_{pre}$, these boundaries are thus represented as quantiles of the AC background. While binned likelihoods are typically employed for high-statistics analyses to reduce computational complexity [245, 246], a binned approach was adopted here despite the low expected event count. This choice was motivated by the data-driven AC modeling, which constrains the granularity and validation of probability density function (PDF) templates, especially when incorporating the hyper-parameter BDT scores as discriminating variables.

6.1.3 AC background validation

Validating the data-driven AC background model in the analysis dimensions was essential for a robust ^{8}B CEνNS search (see Section 6.3.1). This was achieved using various AC-rich datasets, including sidebands and calibration data; two key validation datasets are discussed here. Both were assessed using a four-dimensional binned Poisson likelihood χ^2 GOF test.

A crucial AC sideband consisted of events passing all selection criteria except those targeting AC events, mainly the S2 BDT criterion. This sideband was unblinded after finalizing the AC prediction and event selections. With an initial S2 threshold of 100 PE, a GOF p-value of 0.03 indicated a mismatch in SR1. Detailed inspection showed this mismatch was limited to S2 $<$ 120 PE, possibly due to higher photoionization in SR1. Consequently, the S2 thresholds for both SRs were raised to 120 PE. The post-adjustment sideband data are shown in Figure 6.3 (left), with prediction and observation in good agreement and GOF p-values above threshold. The observed number of AC sideband events in SR0 (SR1) was 121 (326), consistent with the expected 122.7 (302.5).

Another high-statistics validation used ^{37}Ar calibration data. The ERs from L-shell electron capture (EC) at 0.27 keV fall within the ^{8}B CEνNS ROI. A blind analysis was performed to estimate the low-energy ER light yield. A total of 1676 events were observed in the ROI (Figure 6.3, right), with 1063 ± 53 predicted from the AC model. The four-dimensional GOF test, including the ^{37}Ar signal, showed no indication of mismodeling.

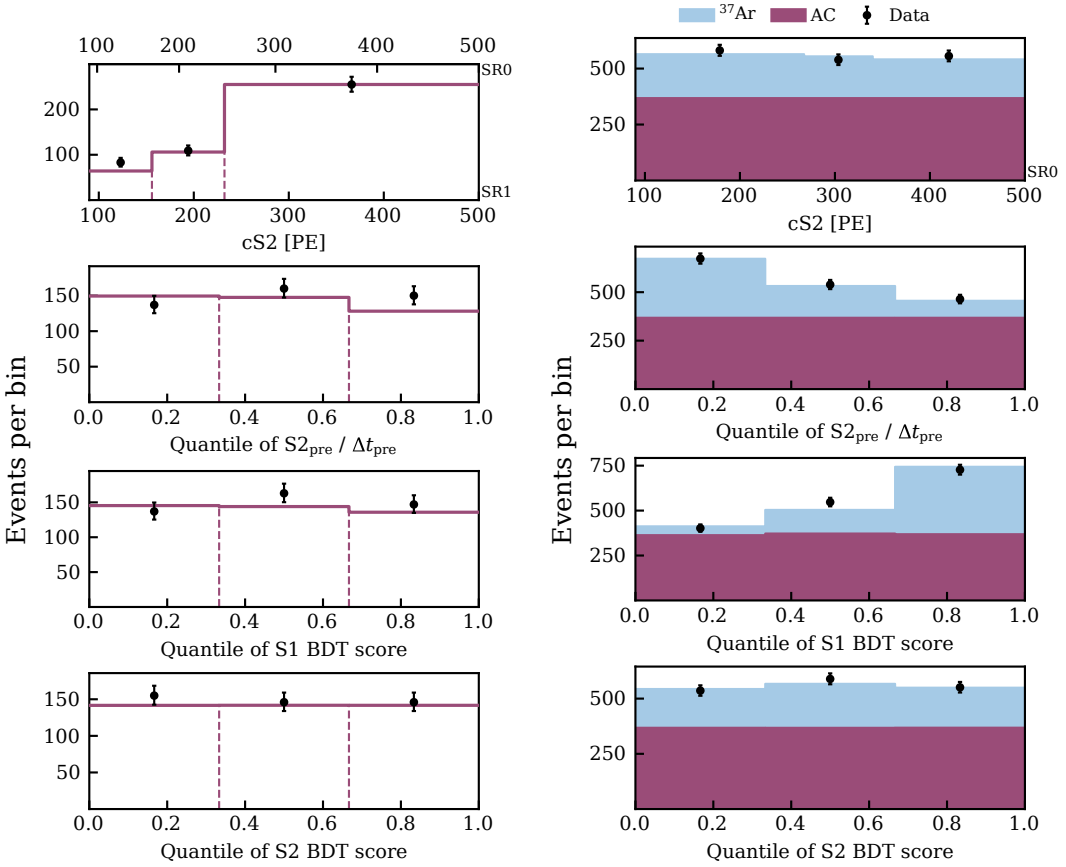

Figure 6.3.: Validation of the accidental coincidence (AC) background model in the four-dimensional analysis space. *Left:* Comparison of predicted (purple histogram) and observed (black points) events in the AC sideband. *Right:* Best-fit model including AC background and ^{37}Ar signal (black points: data) demonstrating successful validation.

6.2 The ^{8}B CEνNS Likelihood Function

The likelihood function for the ^{8}B CEνNS search is defined as

$$\mathcal{L}(\boldsymbol{x}|\sigma,\boldsymbol{\theta}) = \mathcal{L}_{\mathrm{sr0}}(\boldsymbol{x}|\sigma,\boldsymbol{\theta}) \times \mathcal{L}_{\mathrm{sr1}}(\boldsymbol{x}|\sigma,\boldsymbol{\theta}) \times \mathcal{L}_{\mathrm{anc}}(\boldsymbol{\theta}), \tag{6.1}$$

where $\boldsymbol{x}$ represents the data, $\sigma \geq 0$ is the parameter of interest (CEνNS cross section or ^{8}B neutrino flux), and $\boldsymbol{\theta}$ are nuisance parameters. In contrast to the WIMP search (see Section 5.2), this definition omits $\mathrm{SR1_a}/\mathrm{SR1_b}$ separation since ER backgrounds are subdominant. Thus, differentiating between periods with different ER rates offers no significant benefit. Regions near transverse support wires are excluded, eliminating the need for near/far-wire separation. The science likelihood function thus comprises only two extended binned functions for SR0 and SR1:

$$\mathcal{L}_{\mathrm{sr}}(\boldsymbol{x}|\sigma,\boldsymbol{\theta}) = \prod_{i=1}^{k} \mathrm{Pois}(x_i|\mu_i(\sigma,\boldsymbol{\theta})), \tag{6.2}$$

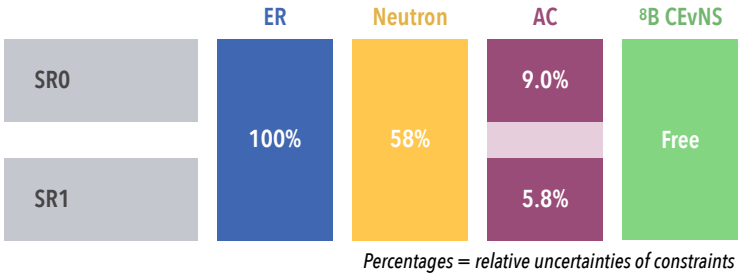

Figure 6.4.: Overview of rate parameters in the ^{8}B CEνNS search likelihood function. Each tile represents one rate parameter; links between rows indicate shared parameters across science runs (SRs). Percentages denote relative uncertainties, while "Free" indicates the absence of ancillary constraints.

where x_i is the observed event count in bin i and $k = 81$ is the total number of bins per SR. The expected number of events in bin i is given by

$$\mu_i(\sigma, \boldsymbol{\theta}) = \sum_c \mu_c(\sigma, \boldsymbol{\theta})\, \epsilon_{i,c}(\boldsymbol{\theta}), \tag{6.3}$$

where:

- c: index over all signal and background components
- $\mu_c(\sigma, \boldsymbol{\theta})$: expected number of events for component c
- $\epsilon_{i,c}(\boldsymbol{\theta}) = \int_{\text{bin}\,i} f_c(\boldsymbol{\theta})$: PDF of component c integrated over bin i

In practice, these integrals are evaluated by filling histograms with high-statistics Monte Carlo (MC) data, directly yielding $\epsilon_{i,c}(\boldsymbol{\theta})$.

The ancillary likelihood function $\mathcal{L}_{\text{anc}}$ is a product of Gaussian constraints from ancillary measurements of nuisance parameters. For background rates, these constraints follow Equation (5.4). Backgrounds from ER, neutrons, and the signal are each scaled with a common rate parameter across both SRs. The AC background rates in SR0 and SR1 are allowed to vary independently to account for possible systematic differences. An overview of rate parameters and their relative uncertainties from ancillary measurements is provided in Figure 6.4. The ER background rate was estimated from a non-blinded region outside the ROI. A conservative 100 % relative rate uncertainty was chosen to account for low-energy emission model uncertainties. The neutron background rate uncertainty of 58 % is dominated by the statistical uncertainty of the neutron sideband dataset used to estimate it (see Section 4.4). For the AC background, combining data from various sidebands and calibrations allowed the relative systematic rate uncertainty to be estimated to below 5 %. Nevertheless, to be conservative, the uncertainty in the AC rate prediction was instead solely determined by the statistical uncertainty in the most relevant sideband: events passing all selection criteria except those specifically targeting AC events (see Section 6.1.3). This approach yields a relative rate uncertainty of 9.0 % in SR0 and 5.8 % in SR1.

Charge and light yields carry significant uncertainties at low NR energies, affecting both rates and shapes of the CEνNS signal and neutron backgrounds. Two shape nuisance parameters, t_{ly} and t_{qy}, were introduced to parameterize these variations (see Figure 6.5). Here $t = 0$ corresponds to nominal yield curves, while $t = \pm 1$ represents shifts to the $\pm 1\,\sigma$ uncertainty bands [177]. For other values, yields are linearly interpolated or extrapolated. Both parameters are independently constrained by standard normal distributions in the ancillary likelihood

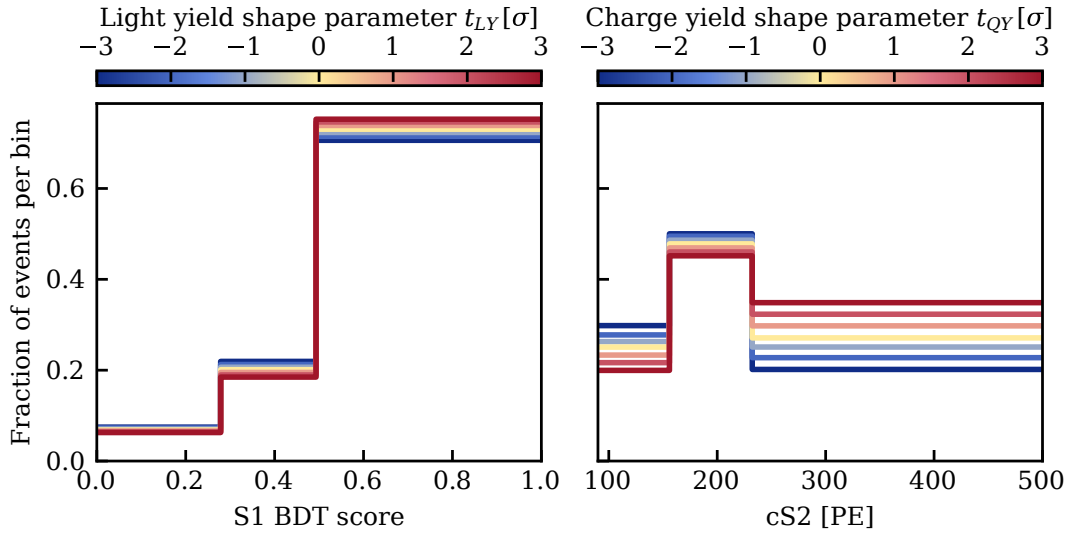

Figure 6.5.: Effects of the shape nuisance parameters t_{ly} and t_{qy} on normalized signal templates. The shape parameters change the shape in the full four-dimensional parameter space. Here, only the variations projected onto the S1 BDT score (t_{ly}) and cS2 (t_{qy}) are shown for SR1.

function. Signal detection efficiency uncertainties are implemented via a scaling parameter with a Gaussian constraint (mean 1, 25% relative uncertainty).

6.3 Sensitivity Studies for the Search with SR0 + SR1

ToyMC methods implemented in the `alea` framework [233] were used to evaluate the sensitivity for the combined SR0 + SR1 analysis, following the procedures described in Section 4.5.5. The sensitivity of this search was primarily quantified by the expected discovery significance. The test statistic for discovery, t_0, is defined in Equation (4.1). The distributions of t_0 under the background-only and the nominal signal-plus-background hypotheses, obtained from toyMC data, are shown in Figure 6.6. As illustrated in the figure, the asymptotic approximation leading to Equation (4.5) holds reasonably well for this analysis, and was therefore used in some of the studies discussed here. However, for the final result, the significance was computed based on toyMC data. The four-dimensional analysis achieves a median expected discovery significance of approximately $2.9\,\sigma$, meaning half of all equivalent experiments would detect the signal above this value under nominal assumptions. The width of the band containing 68 % of toyMC realizations spans approximately $\pm 1\,\sigma$ in significance around this median, reflecting the large statistical fluctuations inherent to this search. In contrast, a pure counting experiment would achieve only $2.1\,\sigma$ median significance,[1] illustrating the importance of signal-background discrimination in the four-dimensional likelihood analysis.

Several studies were conducted to assess the robustness of the analysis, which are summarized below. Some of these studies were performed using earlier versions of the statistical model to inform analysis decisions. Thus, numerical values might differ from the final sensitivity, but the conclusions remain valid.

[1] In this case, the discovery p-value for n observed events is computed as $p = \sum_n^\infty \mathrm{Pois}(n|\mu_\mathrm{b}) = 1 - \sum_1^{n-1} \mathrm{Pois}(n|\mu_\mathrm{b})$, where μ_b is the expected number of background events.

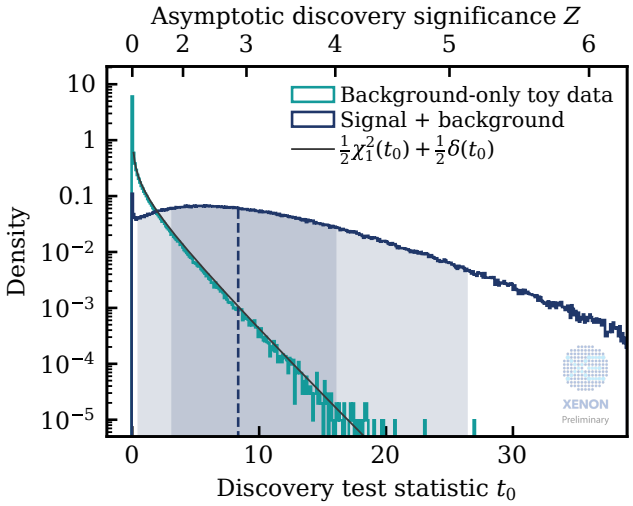

Figure 6.6.: Distribution of the discovery test statistic t_0 under the background-only (teal) and signal-plus-background (blue) hypotheses, obtained from toyMC data. The asymptotic distribution under the background-only distribution is shown in gray. The dashed blue line marks the median t_0 for the signal-plus-background hypothesis. Dark and light shaded regions indicate central 68 % and 95 % containment regions of the distribution, respectively.

6.3.1 Impact of AC background rate mismodeling

Systematic uncertainties in background rate estimates can significantly bias discovery significance calculations, particularly in searches with weak signal-to-background discrimination like this one. This study quantified how much mismodeling of the dominant AC background could be tolerated. The study employed an earlier version of the statistical model that achieved similar sensitivity to the final analysis, with comparable signal and background expectations. In this model, a common scaling parameter linked AC background rates across SRs, constrained by a 5 % relative uncertainty.

In the following, we distinguish between:

- $\mu_{\mathrm{AC}}^{\mathrm{nom}}$: the fixed nominal expectation value of this analysis ($\mu_{\mathrm{AC}}^{\mathrm{nom}} = 21.1$ in this study).
- μ_{AC}: the mean number of AC events in the science datasets.
- $\mu_{\mathrm{AC}}^{\mathrm{anc}}$: the mean number of AC events predicted by ancillary measurements, used to constrain the AC rate in the analysis.

In an ideal scenario, $\mu_{\mathrm{AC}}^{\mathrm{nom}} = \mu_{\mathrm{AC}} = \mu_{\mathrm{AC}}^{\mathrm{anc}}$, but a biased ancillary measurement would result in $\mu_{\mathrm{AC}} \neq \mu_{\mathrm{AC}}^{\mathrm{anc}}$, the impact of which was studied with toyMC data. The true injected AC rate in the science dataset was varied from $\mu_{\mathrm{AC}} = 0.7\mu_{\mathrm{AC}}^{\mathrm{nom}}$ to $\mu_{\mathrm{AC}} = 1.3\mu_{\mathrm{AC}}^{\mathrm{nom}}$. For each dataset, discovery significances were computed for two scenarios: (1) using unbiased ancillary measurements ($\mu_{\mathrm{AC}}^{\mathrm{anc}} = \mu_{\mathrm{AC}}$) and (2) using biased ancillary measurements ($\mu_{\mathrm{AC}}^{\mathrm{anc}} = \mu_{\mathrm{AC}}^{\mathrm{nom}}$ regardless of the value μ_{AC}). Figure 6.7 shows the fraction of $3\,\sigma$ and $5\,\sigma$ discoveries as a function of injected AC rate normalized by $\mu_{\mathrm{AC}}^{\mathrm{nom}}$, with the bottom panels showing the ratio and difference of discovery probabilities when using biased or correct ancillary models.

With correct modeling, the discovery probability decreases with increasing background rate, as expected. However, when the ancillary model is biased, higher true background rates paradoxically appear to increase discovery rates due to the statistical analysis incorrectly interpreting

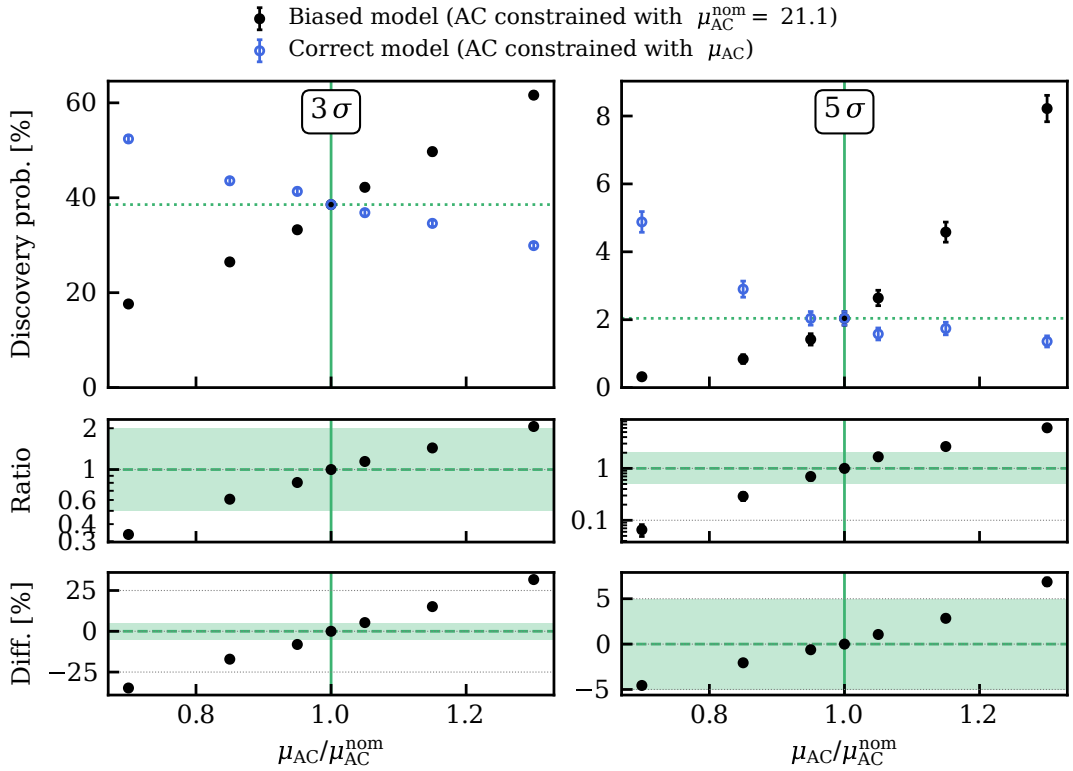

Figure 6.7.: Fraction of ^{8}B CEνNS discoveries at $3\,\sigma$ (left) and $5\,\sigma$ (right) significance threshold as a function of the mean number of accidental coincidence (AC) background events injected in the science dataset μ_{AC} normalized by the nominal value μ_{AC}^{nom}. Results are shown for both biased (black) and unbiased ancillary measurements (blue). The dotted green line indicates the discovery probability for the nominal case. Bottom panels show the ratio and absolute difference between biased and correct model discovery probabilities. Green bands indicate factor 2 ratio and ±5 % difference deviations for visual reference.

excess events as signal. Overestimating the AC rate by approximately 15 % (i.e. injecting a rate 15 % smaller than nominal $\mu_{AC}/\mu_{AC}^{nom} = 0.85$) results in missing approximately 40 % of $3\,\sigma$ discoveries (dropping from $\sim$ 44 % to $\sim$ 26 %). Conversely, underestimating it by 15% ($\mu_{AC}/\mu_{AC}^{nom} = 1.15$) leads to 44 % too many $3\,\sigma$ discovery claims (from $\sim$ 35 % up to $\sim$ 50 %). The impact is even larger for $5\,\sigma$ significance level, where a $\sim$ 10% rate mismodeling could double or halve the discovery probability.

These results reveal two critical effects when the true background rate exceeds nominal expectations: First, pre-experiment sensitivity calculations become overly optimistic. Second, due to limited signal-background discrimination, the excess background events are misidentified as signal, leading to inflated discovery significance and false positive claims. If the nominal background is overestimated, the reverse happens. The observed high susceptibility to background rate mismodeling triggered further validation of the AC background modeling using the high-statistics ^{37}Ar calibration dataset described in Section 6.1.3. This validation confirmed the reliability of the AC background estimate, with systematic rate uncertainties below 5 %.

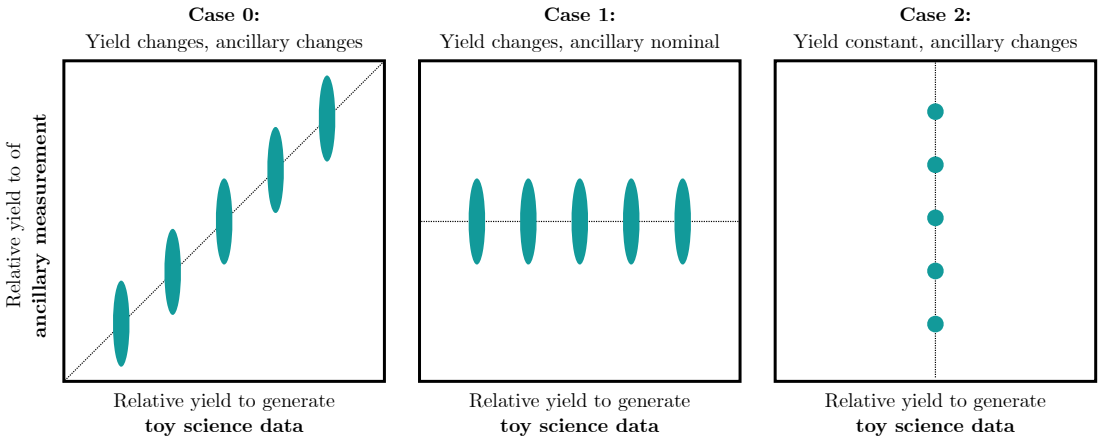

Figure 6.8.: Illustration of the three cases used to study the impact of yield mismodeling. Case 0 used toyMC data that was not manipulated and thus serves as a baseline model. In case 1, the yields used to generate the toyMC science data were varied, but the ancillary measurements were overwritten by the nominal ones. For case 2, the nominal yields were used to generate the toyMC science data, but the ancillary measurements were overwritten by discrete constant values.

6.3.2 Impact of yield mismodeling

The expected rate of ^{8}B CEνNS events, and consequently the expected discovery significance of this search, depends on the true values of the light and charge yields at low energies. These yields were determined from YBe calibration data [177]. Potential biases could arise, for example, if effects dependent on the event rate occurred, which was much higher during calibration. This study investigated how mismodeling of the yields would impact inference results.

Yields near the detection threshold are particularly uncertain, leading to sizeable variation in the expected number of ^{8}B events in the SR0 + SR1 dataset. This uncertainty was incorporated into the fit via the shape parameters t_{ly} and t_{qy} (see Figure 6.5), which linearly shift the yields as a function of energy. In the following, the effect of t_{ly} and t_{qy} is expressed in terms of the yield relative to its nominal value at a fixed NR energy of 1.3 $\mathrm{keV_{NR}}$, which is close to the mode of the expected ^{8}B recoil spectrum after acceptance (see Figure 4.5 left). Varying the yields by $\pm 3\,\sigma$ of the constraint changes the charge yield by approximately $\pm 15\,\%$ and the light yield by approximately $\pm 30\,\%$, which in turn scales the signal rate approximately linearly by $\pm 20\,\%$ and $\pm 50\,\%$, respectively. In the following, results for light yield mismodeling are shown; results for varying charge yields are equivalent and thus not shown explicitly.

To assess the effect of yield mismodeling, toyMC data were generated with different injected true values of the yields. The science data, the ancillary data (yield constraints from the fit to YBe calibration data), or both were then manipulated, and the discovery significance was computed. Three scenarios were considered, illustrated in Figure 6.8:

- **Case 0: Yields are higher/lower and so are their constraints.** This baseline case assumes no systematic bias between the yields in the science data and the constraints. It shows how discovery probability naturally depends on the true yield values when correctly modeled.
- **Case 1: True yields are higher/lower with respect to their central nominal constraints.** Science data were generated with yields differing from nominal values. An-

cillary measurements, however, follow the nominal distribution. This simulates scenarios in which the true yields are higher or lower than estimated from calibration data.

- **Case 2: True nominal yields, but the constraints are higher/lower.** Here, all ancillary measurements were set to the respective higher/lower central values, thereby neglecting statistical fluctuations of the ancillary measurement. While this is not a realistic scenario, it illustrates the impact of biased yield constraints.

The impact of different light yields, with and without mismodeling, on the discovery probability with $3\,\sigma$ significance threshold is shown in Figure 6.9 (top). Both case 0 (variation of yields without mismodeling) and case 1 (science data yields systematically differ from calibration constraints) show a strong dependence of the discovery probability on the true light yield. Importantly, both vary equally, which indicates that the computation of discovery significance is robust against yield mismodeling. Even if a systematic bias were present in YBe calibration, the significance would depend only on the true yields. Case 2 further confirms this: the same toyMC science datasets obtained with nominal yields result in a constant discovery probability, regardless of how incorrect the yield constraints are. Because yield variations produce only small changes in signal shape, the fit tends to maintain yields near their constrained values. Instead, it compensates for rate mismatches by varying the unconstrained neutrino flux parameter. This is illustrated in Figure 6.9 (bottom) for case 1. The higher signal rate resulting from an increased light yield is, on average, almost entirely absorbed as a higher ^{8}B neutrino flux. However, due to the relatively low statistics in this search, the nominal signal rate remains within the $1\,\sigma$ variation of best-fit results for nearly all mismodelings considered. Since the primary goal of this analysis with the SR0 + SR1 dataset was the first measurement of ^{8}B CEνNS and not a precise flux measurement, yield biases of up to 20 % were not a major concern. Uncertainties from yield estimation were propagated to the flux estimate, appropriately broadening the confidence interval.

6.3.3 Acceptable unmodeled surface background and definition of the fiducial volume

The radial dependence of the surface background rate was modeled using a data-driven approach similar to the one described in [Paper I]. However, limited statistics in sideband regions made it impossible to reliably construct and validate a surface background model for the 2-fold coincidence analysis in our four-dimensional parameter space. To address this limitation, the FV was defined such that surface background contributions could be safely neglected in the statistical inference.

Since no explicit background model was available for the surface background, the worst-case scenario of a signal-like background was assumed. The impact of background mismodeling was quantified through the false n-sigma discovery rate – the rate of observing an n-sigma discovery in the absence of a signal (Equation (5.5)). While we expect genuine ^{8}B CEνNS signals in our data, understanding the background-only scenario is crucial because this is the hypothesis we must confidently reject to claim a discovery.

ToyMC datasets were generated with varying rates of injected signal-like background. For each dataset, the local discovery p-value was calculated using Equation (4.2), where the test statistic distribution under the background-only hypothesis, $f(t_0|\mu = 0)$, was obtained from background-only toyMC data without any unmodeled backgrounds. The resulting false discovery rate as

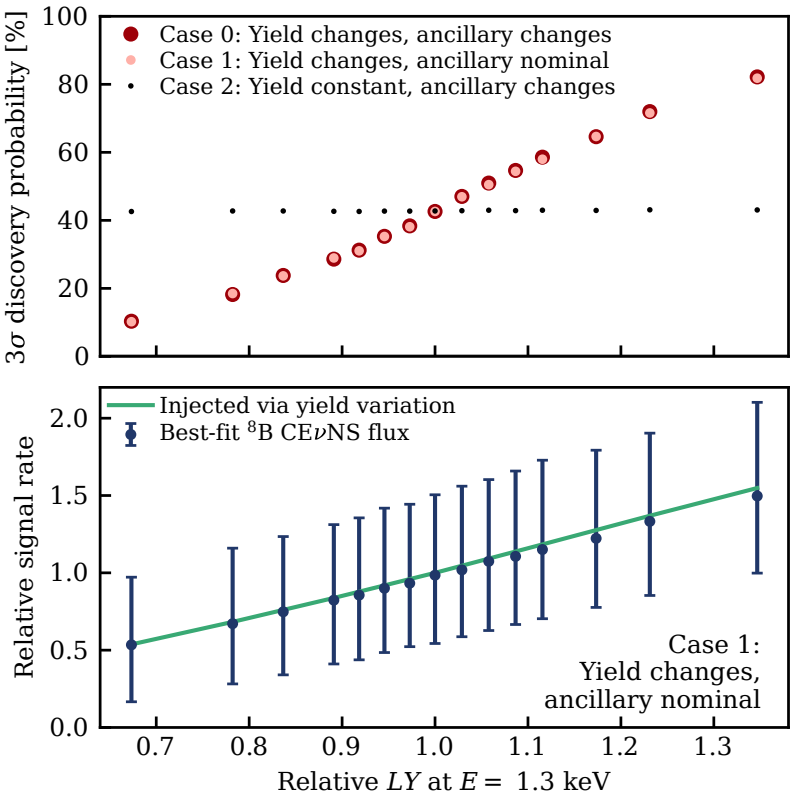

Figure 6.9.: Impact of light yield mismodeling on the discovery probability and rate estimation as a function of the injected light yield at 1.3 $\mathrm{keV_{NR}}$, normalized to nominal yield. *Top:* Fraction of toyMC experiments with an excess exceeding $3\,\sigma$ significance. The results for three cases are shown, and the value at nominal yield is shown as a horizontal black line. *Bottom:* Best-fit signal rates for case 1, where true yields vary but constraints remain nominal. The points show the median best-fit ^{8}B CEνNS flux and the interval containing 68 % of best-fit results (errorbars). The green line indicates the injected rate due to a higher or lower than nominal light yield.

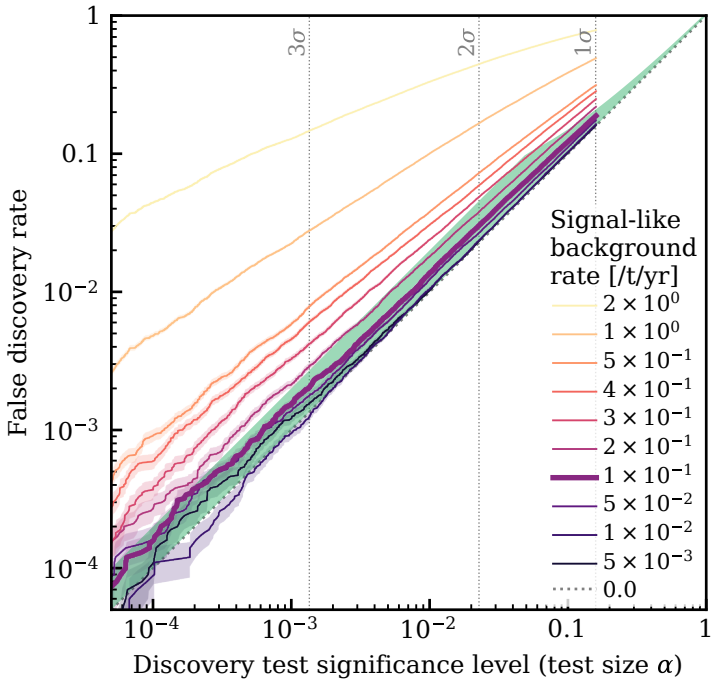

Figure 6.10.: False discovery rate for the ^{8}B CEνNS search as a function of the discovery test size α, shown for various rates of unmodeled signal-like background. In the ideal case without background mismodeling, the false discovery rate matches the test size α (diagonal dotted line). The presence of unmodeled signal-like backgrounds systematically biases p-values toward smaller values, leading to inflated discovery rates. The green shaded region indicates the threshold for acceptable deviation.

a function of the injected background rate is shown in Figure 6.10. In an ideal background-only scenario, false discovery rates should equal the chosen significance level α, indicated by the diagonal line in Figure 6.10. However, unmodeled background components bias p-values toward artificially small values, inflating false discovery rates above their nominal levels. No universal criterion for what constitutes an acceptable deviation from the nominal false discovery rate exists. In this work, deviations were considered acceptable if they remained below both a factor-of-two increase and a 5 percentage point absolute increase from nominal levels, indicated by the green shaded region. Applying this criterion to the simulation results revealed that unmodeled background rates below $0.1\,\mathrm{t}^{-1}\,\mathrm{yr}^{-1}$ could be safely neglected without compromising discovery reliability. Since signal-like spectral shapes represent the worst-case scenario, this threshold serves as a conservative bound for any specific background source. To complete the assessment, another study investigated how unmodeled backgrounds would bias the discovery significance when a genuine signal is present. At the established threshold of $0.1\,\mathrm{t}^{-1}\,\mathrm{yr}^{-1}$, the median discovery significance is only slightly biased, shifting from $2.95\,\sigma$ to $3.04\,\sigma$, a shift well below the variations expected from statistical fluctuations in the dataset.

The FV for the ^{8}B CEνNS search was defined as a cylinder with $-142\,\mathrm{cm} < \mathrm{Z} < -13\,\mathrm{cm}$, excluding regions of limited understanding of backgrounds and detector conditions, such as electric field non-uniformity (Figure 4.4). The maximum radii fulfilling the background rate threshold criterion established in this study are $\mathrm{R}_{\mathrm{max}} = 60.15\,\mathrm{cm}$ for SR0 and $\mathrm{R}_{\mathrm{max}} = 59.60\,\mathrm{cm}$ for SR1. The improved field distortion correction (FDC) algorithm implemented in SR1 (see Section 4.2) caused surface background events to be reconstructed 0.55 cm further inward on average. Accounting for reconstruction mismatches for both FDC methods, the final fiducial

masses are (3.97 ± 0.20) t for SR0 and (4.10 ± 0.19) t for SR1, with systematic uncertainties from FDC and position reconstruction.[2]

6.4 Goodness of Fit

To assess whether the best-fit model is consistent with the data, GOF tests are employed. As discussed in Section 4.5.8, no uniformly most powerful GOF test exists. Therefore, the performance of various tests was evaluated using toyMC experiments. A mismodeling study was conducted with a simplified statistical model that included only the dominant AC background. ToyMC data were generated from a biased model and fit with the nominal model, which in this case had only two free parameters: the AC rates of SR0 and SR1. Multiple GOF tests were performed to identify those most effective at detecting mismodeling.

This study investigated sensitivity to the worst-case scenario of signal-like mismodeling in the background. To explore this, biased models were constructed by adding a signal-like component to the AC background, parameterized by a mismodeling fraction (MMF) a_{mm}, following the approach in [200]. Specifically, a fraction a_{mm} of the signal PDF f_{s} was added to the AC background PDF f_{AC}, resulting in $f'_{\mathrm{AC}} = b\,[(1 - a_{\mathrm{mm}})\, f_{\mathrm{AC}} + a_{\mathrm{mm}}\, f_{\mathrm{s}}]$, where b ensures normalization after setting negative bins to zero. In this parametrization, $a_{\mathrm{mm}} = 0$ corresponds to the nominal AC background, while $a_{\mathrm{mm}} = 1$ yields the nominal signal model. Projections of these AC models for various MMFs are shown in Figure 6.11.

All GOF tests used in this study are binned Poisson likelihood χ^2 tests [247]. Rather than relying on the asymptotic chi-squared distributions, the distribution of the test statistic for each best-fit model was determined using toyMC data. Combining bins from SR0 and SR1 was found to generally enhance test performance, so only results from the combined test are presented here.

The dimensionality and choice of parameters for the tests were varied. With expected counts below one in most of our 81, the test power can suffer even without relying on asymptotic distributions [191, 248]. To mitigate this, lower-dimensional and combined one-dimensional tests were explored. In the latter approach, n separate one-dimensional tests are performed in projected analysis dimensions, and the best-fit hypothesis is rejected if any individual test rejects it. To maintain the desired global confidence level (CL), the critical p-value for each test is adjusted to $p_{\mathrm{crit}} = 1 - \mathrm{CL}^{1/n}$. For four one-dimensional tests, this means the best-fit model is rejected if any p-value is below 0.013.

Test performance is quantified by the rejection power, defined as the fraction of best-fit hypotheses rejected at 95 % CL. A higher rejection power indicates a more sensitive test. The rejection power as a function of the MMF a_{mm} is shown in Figure 6.12. For $a_{\mathrm{mm}} = 0$ (no mismodeling), the rejection power for all tests is close to the expected baseline value of $1 - \mathrm{CL} = 0.05$. As discussed above, the low expected event counts in most bins render the four-dimensional test largely insensitive, particularly for $a_{\mathrm{mm}} < 0$, where its rejection power barely exceeds the baseline. Among all tests, the one-dimensional test in the S1BDT score demonstrates the highest sensitivity across the range of MMFs considered. The rejection power for combinations of three or four one-dimensional tests is comparable, differing only slightly from that of the test using

[2] The rejection of the near-wire region is S2-dependent and thus not subtracted from the fiducial mass but instead included in the S2-dependent acceptance of selection criteria.

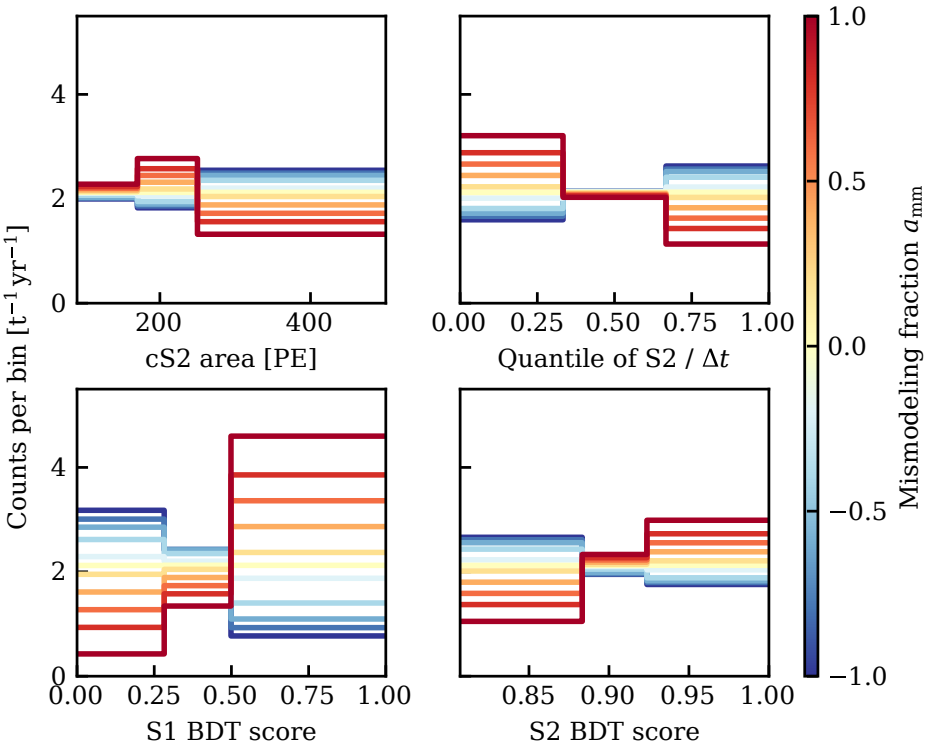

Figure 6.11.: Projections of the biased accidental coincidence (AC) templates onto the four analysis dimensions, with colors representing different mismodeling fractions (MMFs) a_{mm}. All templates are normalized to the nominal AC rate. The case $a_{\mathrm{mm}} = 0$ corresponds to the nominal AC template.

the S1BDT score alone. To ensure robust sensitivity to mismodeling in any analysis dimension while maintaining high rejection power, the combined test using all four one-dimensional analysis dimensions was selected for this analysis.

6.5 Conclusions

This chapter presented the statistical model and sensitivity studies for the XENONnT ^{8}B CEνNS search with SR0 + SR1. Significant modifications to the standard WIMP analysis were required to lower the analysis threshold while maintaining controllable background levels. The challenging signal-to-background environment is evident from the final expectations: $26.4^{+1.4}_{-1.3}$ background events (dominated by AC background) versus $11.9^{+4.5}_{-4.2}$ expected ^{8}B CEνNS events. To maximize discrimination in this regime, we adopted a four-dimensional binned analysis space optimized for separating ^{8}B CEνNS signals and AC background events. The final nominal sensitivity shows a median discovery significance of $\sim 2.9\,\sigma$, demonstrating that the first detection of ^{8}B solar neutrinos via CEνNS is in reach for XENONnT.

The studies in this chapter demonstrated that a 15 % mismodeling of the AC rate could lead to a 40 % reduction or excess of $3\,\sigma$ discoveries. Validation using AC sidebands and high-statistics ^{37}Ar calibration data confirmed the model's reliability with systematic rate uncertainties below 5 %. Yield mismodeling studies revealed that neutrino flux and yield parameters are highly degenerate in the fit, making the discovery significance robust against yield biases. While this

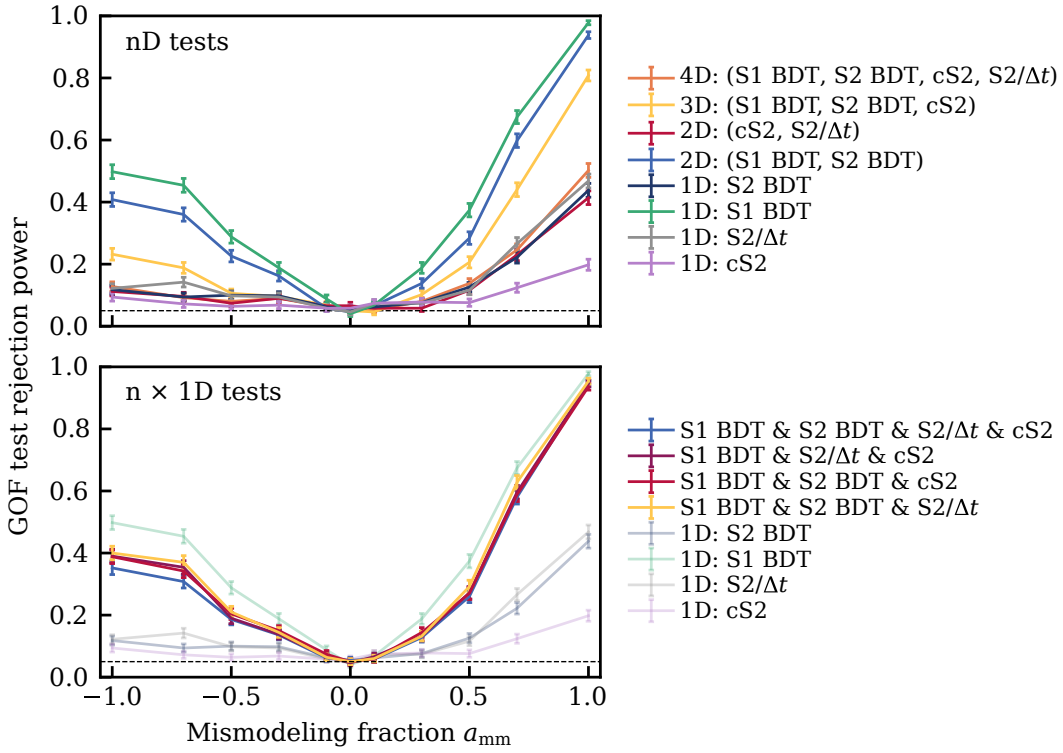

Figure 6.12.: Fraction of goodness of fit (GOF) tests rejecting the best-fit models as a function of the mismodeling fraction (MMF) a_{mm} for GOF tests in different parameter spaces. *Top:* Results for individual tests in four, three, two, and one dimensions. *Bottom:* Results for combinations of three or four one-dimensional tests; the individual one-dimensional tests are shown with reduced opacity for direct comparison.

degeneracy protects discovery claims, it limits precision: future measurements aiming for accurate flux and cross section determination will need to scrutinize low-energy yield calibrations. A study of signal-like background tolerance demonstrated that unmodeled backgrounds with rates below $0.1\,\mathrm{t}^{-1}\,\mathrm{yr}^{-1}$ do not significantly affect the results, making their omission acceptable when modeling is not viable. This threshold informed the definition of the FV, limiting radii to below 60.15 cm for SR0 and 59.60 cm for SR1. GOF test performance was evaluated via toyMC experiments using biased AC models. This led to the adoption of a combined approach of four one-dimensional tests, which maintains sensitivity across all analysis dimensions with high rejection power against mismodeling. With these systematic studies validating the analysis framework and demonstrating the robustness of results, the statistical model was ready for application to the unblinded XENONnT data, as presented in Section 7.2.

7

Results of the XENONnT Experiment

This chapter presents two major scientific results of the XENONnT experiment: its currently most sensitive search for weakly interacting massive particle (WIMP) dark matter and the first measurement of ^{8}B solar neutrinos via coherent elastic neutrino-nucleus scattering (CEνNS). The general analysis strategy employed for both searches using the first two science runs (SRs) of XENONnT (SR0 and SR1) is outlined in Chapter 4, while specific details on these dedicated analyses and the contributions made to these searches in the context of this thesis are presented in Chapters 5 and 6. Additionally, other notable results obtained with XENONnT data are briefly summarized.

7.1 Search for WIMP Dark Matter

A search for WIMP dark matter was conducted using the first two SRs of XENONnT [Paper II]. The analyzed dataset encompassed a total livetime of 281.7 d after accounting for dead time from the data acquisition (DAQ) and vetoes, comprising 95.1 d from SR0 (already published in [89]), 66.6 d from $\mathrm{SR1_a}$, and 119.9 d from $\mathrm{SR1_b}$. With the fiducial masses of (4.17 ± 0.13) t for SR0 and (4.00 ± 0.15) t for SR1 (see Section 5.3.3), corresponding to a total exposure of 3.1 t yr.

A blind analysis was performed on nuclear recoil (NR) events with energies above $\sim$3.5 $\mathrm{keV_{NR}}$. For this, candidate signal events were blinded if they fell within a specific region of the cS1–cS2 parameter space (indicated in gray in Figure 7.1). This region was defined by events with reconstructed electronic recoil (ER) energies below 10 $\mathrm{keV_{ER}}$ lying between the $-2\,\sigma$ quantiles of the SR0 ER and NR bands. The unblinding of SR1 data proceeded in two steps: Initially, a small region above the median of the NR band with energies above 5 $\mathrm{keV_{ER}}$ was unblinded (region indicated in solid gray in Figure 7.1). This step enabled investigating a potential systematic excess of ER leakage events, similar to what was observed in [89]. No discrepancy relative to the nominal model was observed. Subsequently, all remaining data in the region of interest (ROI) (gray hatched region in Figure 7.1) were unblinded. The total number of events observed in the ROI was as follows:

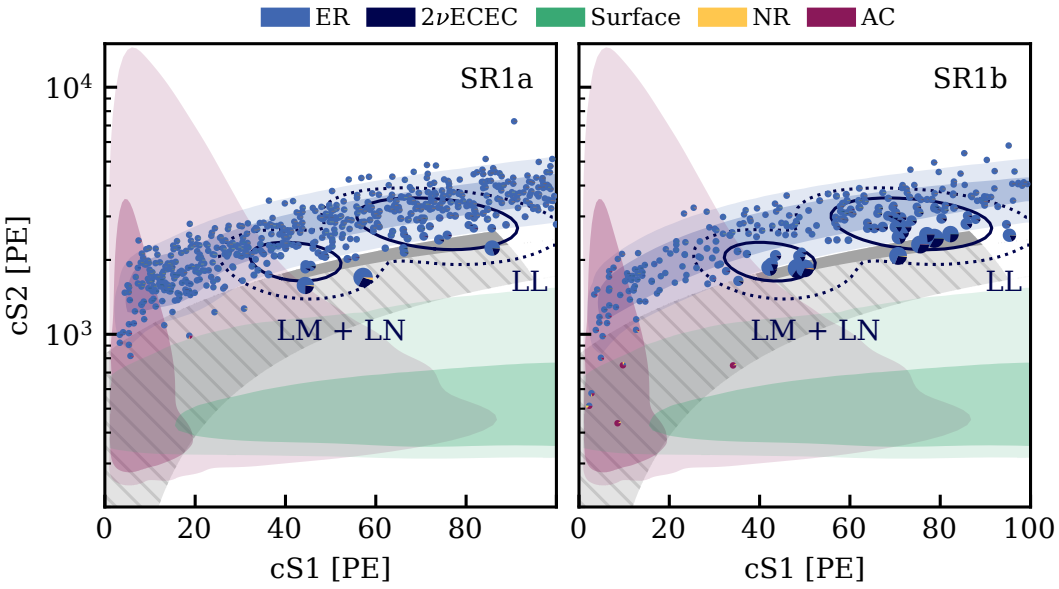

Figure 7.1.: Distribution of SR1 data in the cS1–cS2 parameter space overlaid with the best-fit background-only model, including LM+LN and LL ^{124}Xe DEC (double electron capture, here 2νECEC) peaks with unconstrained yields. Data points are displayed as pie charts indicating the fractional contribution of individual components from the best-fit likelihood evaluated at each data point. The pie chart sizes are scaled according to the relative contribution from ^{124}Xe DEC. Dark (light) shaded regions and solid (dashed) lines indicate 68 % (95 %) contours of individual components. The first unblinding step (solid gray) and second unblinding step (hatched gray) regions are indicated. Adapted from [Paper II].

- SR0: 152 events (16 in the blinded region)
- $\mathrm{SR1_a}$: 560 events (14 in the blinded region)
- $\mathrm{SR1_b}$: 245 events (13 in the blinded region, +2 events already unblinded in [Paper III]).

7.1.1 Results of the DEC hypothesis test

After unblinding, the double electron capture (DEC) hypothesis test was performed, as defined in Section 5.4, to assess whether the ^{124}Xe DEC background in the SR1 dataset was compatible with nominal β-like charge yields. A p-value of 0.09 was observed, which exceeds the pre-defined significance threshold of $\alpha_{\mathrm{DEC}} = 5\,\%$. Consequently, the hypothesis of β-like DEC yields was not rejected, and the nominal model, incorporating DEC peaks within the flat ER component, was adopted for reporting the main WIMP search results. The best-fit values with unconstrained DEC yields, obtained from the SR1 dataset, are $q_{\mathrm{LL}} \simeq 0.9$ and $q_{\mathrm{LM}} \simeq 0.8$, as shown in Figure 7.1. Combining data from both SR0 and SR1 provides the best data-driven estimates: $q_{\mathrm{LL}} = 0.80^{+0.08}_{-0.04}$ and $q_{\mathrm{LM}} = 0.72^{+0.11}_{-0.04}$.

7.1.2 Best-fit results

Figure 7.2 presents the best-fit result including an unconstrained 200 GeV/c^2 spin-independent (SI) WIMP component in the cS1–cS2 parameter space. The corresponding best-fit expectation values are reported in Table 7.1, showing good agreement with nominal values.

Table 7.1.: Nominal (pre-fit) and best-fit expectation values from a fit that includes an unconstrained 200 GeV/c^2 SI WIMP signal. The results are presented separately for SR0 (1.09 t yr), $SR1_a$ (0.73 t yr), and $SR1_b$ (1.31 t yr). Background components with the same rate parameter are represented by connected colors (see Figure 5.4). The uncertainties shown in the 'nominal' columns reflect the widths of the Gaussian constraint terms used in the fit.

	SR0		$SR1_a$		$SR1_b$	
	Nominal	Best fit	Nominal	Best fit	Nominal	Best fit
ER (flat)	134	136 ± 12	430 ± 30	450 ± 20	151 ± 11	154 ± 10
ER (^{3}H-like)	–	–	62	40 ± 30	101	80^{+18}_{-17}
ER (^{37}Ar)	–	–	58 ± 6	55 ± 5	–	–
Neutron	0.7 ± 0.3	0.6 ± 0.3	0.47 ± 0.19	0.45 ± 0.19	0.7 ± 0.3	0.7 ± 0.3
CEνNS (solar)	0.16 ± 0.05	0.16 ± 0.05	0.010 ± 0.003	0.010 ± 0.003	0.019 ± 0.006	0.019 ± 0.006
CEνNS (atm.+DSNB)	0.04 ± 0.02	0.04 ± 0.02	0.024 ± 0.012	0.024 ± 0.012	0.05 ± 0.02	0.05 ± 0.02
AC	4.3 ± 0.9	$4.4^{+0.9}_{-0.8}$	2.12 ± 0.18	2.10 ± 0.18	3.8 ± 0.3	3.8 ± 0.3
Surface	13 ± 3	11 ± 2	0.43 ± 0.05	0.42 ± 0.05	0.77 ± 0.09	0.76 ± 0.09
Total background	152	152 ± 12	553	550 ± 20	257	239 ± 15
WIMP (200 GeV/c^2)	–	1.8	–	1.1	–	2.1
Observed	152		560		245	

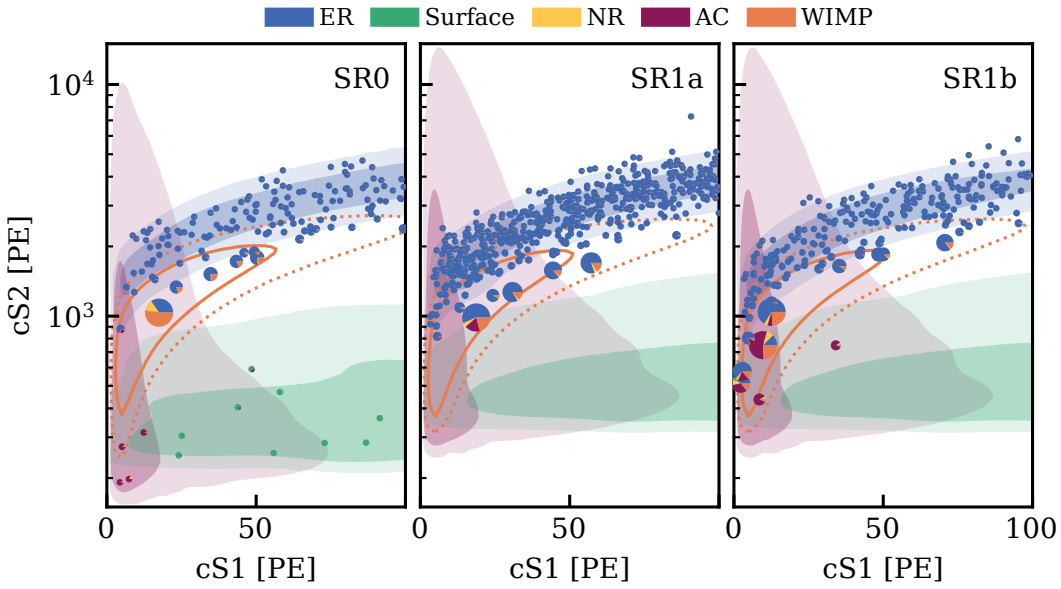

Figure 7.2.: Data distribution and best-fit results for an unconstrained 200 GeV/c^2 spin-independent (SI) WIMP component in cS1–cS2 space for SR0 (left), $SR1_a$ (middle), and $SR1_b$ (right). $SR1_a$ (middle), and $SR1_b$ (right). Data points are shown as pie charts indicating the fraction of individual components of the best-fit likelihood evaluated at each data point. The sizes are scaled according to the WIMP share. Dark (light) shaded regions and solid (dashed) lines indicate 68 % (95 %) containment regions of signal and background components. Extended from [Paper II].

For some of the background rates, the science dataset has much weaker constraining power compared to the ancillary constraint. In this case, the parameter is not expected to pull away strongly from its constrained value if the nominal model resembles the truth. It is therefore more informative to compare the best-fit values to the expected variation arising solely from statistical fluctuations in the science dataset. The expected distribution was obtained from Toy Monte-Carlo (toyMC) data where ancillary data was not randomized. The parameter pulls with respect to this distribution are shown in Figure 7.3. The x-axis represents the normalized difference $(\hat{\theta} - \theta_{\text{toy}})/\sigma_{\text{toy}}$, where $\hat{\theta}$ is the best-fit value of this analysis, and θ_{toy} and σ_{toy} are the median and width of the toyMC best-fit distribution. Except for the flat ER rate parameter of SR1, which is pulled slightly above the $+2\,\sigma$ quantile, close to the $+1\,\sigma$ value of the ancillary constraint, all parameters are contained within the $\pm 2\,\sigma$ band of expected pulls.

Independent goodness of fit (GOF) tests were performed on the $SR1_a$ and $SR1_b$ datasets, with test criteria defined prior to unblinding. Each test employed a p-value threshold of 2.5 % to achieve a combined 95 % confidence level (CL). An unbinned Anderson-Darling test [249] was performed on cS2 after subtracting the cS1-dependent median of the best-fit model. Additionally, a binned Poisson likelihood χ^2 test with an equiprobable binning scheme in cS1–cS2 space was performed. None of the tests showed indication of mismodeling, with p-values of 0.34 ($SR1_a$) and 0.85 ($SR1_b$) from the Anderson-Darling tests and 0.33 (same for both $SR1_a$ and $SR1_b$) from the χ^2 tests. Another test examined the uniformity of the distribution in XY coordinates, motivated by an asymmetry observed in [89]. This test was defined via the fraction of unblinded events in the densest quarter and half in XY compared to the distribution expected from backgrounds. No indication of an anomalous distribution was observed, with p-values of 0.18 (densest quarter) and 0.35 (densest half).

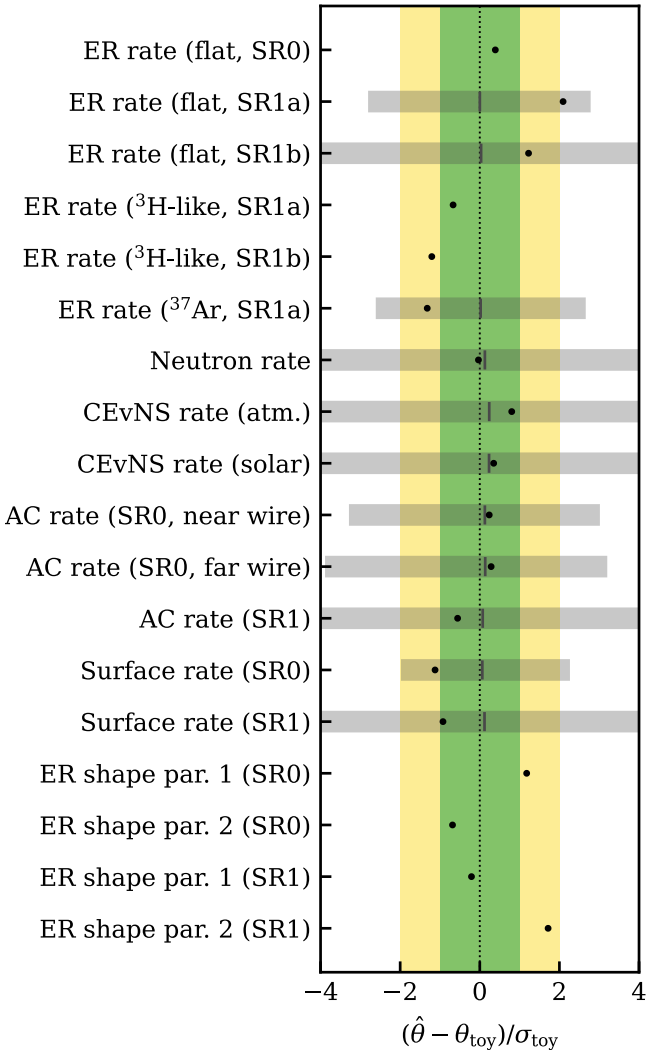

Figure 7.3.: Pull plot showing the deviation of best-fit values from the expected distribution of best-fit values, arising from statistical fluctuations in the science dataset. The green and yellow bands represent the $1\,\sigma$ and $2\,\sigma$ containment regions of pulls derived from toyMC simulations. For comparison, the $1\,\sigma$ widths of the ancillary constraints, typically much broader for most rate parameters, are shown as gray bands.

7.1.3 Discovery significance and confidence intervals

The discovery significance was computed for various WIMP masses, as shown in Figure 7.4. The lowest local discovery p-value of 13 % is observed for a SI WIMP with mass of $1000\,\text{GeV}/c^2$. No local significance above $2\,\sigma$ was found, indicating no significant excess above background expectations.

Thus, new upper limits (ULs) at 90 % CL were derived on the WIMP-nucleon cross section for masses above $10\,\text{GeV}/c^2$, shown in Figure 7.5 (left). The lowest cross section of $1.7 \times 10^{-47}\,\text{cm}^2$ is excluded for a mass of $30\,\text{GeV}/c^2$. Since no limits fall below the $-1\,\sigma$ quantile of the sensitivity band, the limits already satisfy the power-constrained limits (PCL) requirement. Above $\sim 200\,\text{GeV}/c^2$, the limit scales linearly with mass according to $M_{\text{WIMP}}/(1\,\text{TeV}/c^2) \times 3.7 \times 10^{-46}\,\text{cm}^2$. The equivalent sensitivity and limit expressed in terms of number of WIMP events is shown in Figure 7.5 (right), placing an UL of ~ 3 WIMP events at $10\,\text{GeV}/c^2$ and

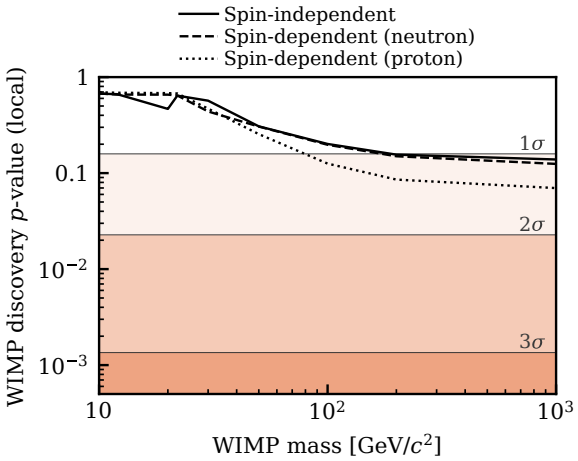

Figure 7.4.: Local WIMP discovery p-value versus WIMP mass for spin-independent and spin-dependent scattering.

$\sim$ 17 events at 1000 GeV/c^2. The results obtained for spin-dependent (SD) WIMP-nucleon interactions are shown in Figure 7.6. Given their similar distributions in cS1–cS2 space, the results are fairly similar compared to the SI result and in first order scaled by the relative rates at fixed cross section.

For reference and comparison with other experiments, we also report the ULs using the alternative statistical model with DEC charge yields as nuisance parameters. The sensitivity and ULs are shown in Figure 7.7 (left) relative to the nominal sensitivity. Here, unlike for the DEC hypothesis test, the DEC charge yield of the LM+LN peak relative to the β yield was constrained loosely to $q_{\mathrm{LM}} = 0.9 \pm 0.1$ (see Section 5.4) and a nominal value of $q_{\mathrm{LL}} = 0.8$ was used to compute the sensitivity. For low WIMP masses, the limits are essentially identical, while for high masses, the limit obtained with the alternative model is a factor of 1.3 more stringent. The sensitivity is comparable, which is attributed to the two effects of higher nominal background leakage and the added degrees of freedom to pick up excess events largely cancel. Similarly, Figure 7.7 (right) shows the result obtained using only SR1 data. Across all tested WIMP masses, the limit is above median sensitivity, indicating a slight over-fluctuation, which is strongest at high masses.

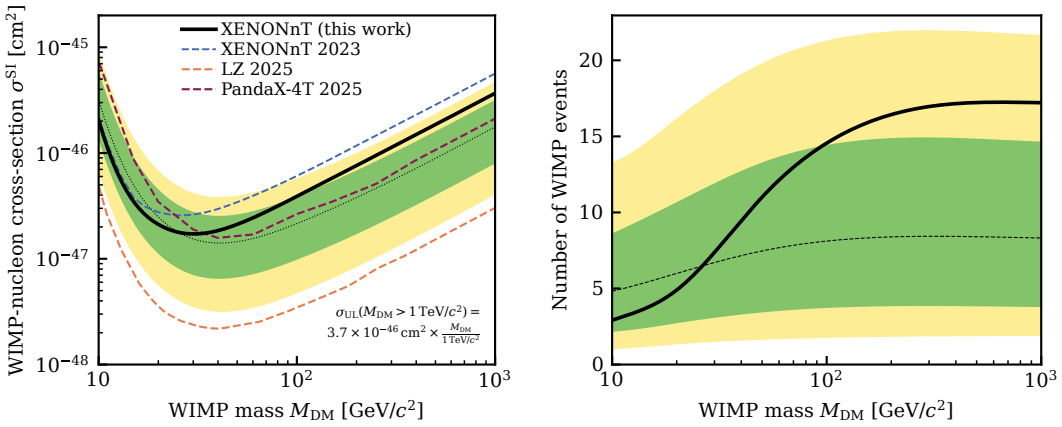

Figure 7.5.: *Left:* 90 % upper limits (ULs) on the SI WIMP-nucleon cross section as a function of WIMP mass (solid black line). The sensitivity band, representing the expected ULs under the background-only hypothesis, is shown as the regions containing 68 % (green) and 95 % (yellow) of ULs, with the median value indicated by a dotted line. Published results from XENONnT (SR0-only) [89], LUX-ZEPLIN (LZ) [58], and PandaX-4T [57] are also included for comparison; all limits are derived using the PCL method with a power threshold of 0.16 (the XENONnT SR0 result was recast accordingly). *Right:* Sensitivity band (yellow-green), median UL (dashed line), and observed UL (solid line) for the SI SR0 + SR1 WIMP search, all shown as a function of the number of WIMP events. Both reproduced from [Paper II].

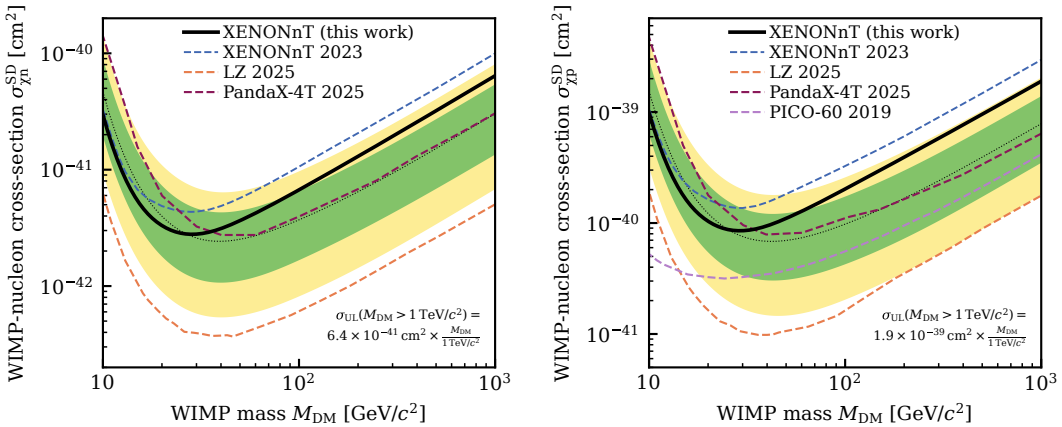

Figure 7.6.: Upper limits (ULs) on the cross section for SD WIMP-nucleon interactions for "neutron-only" (left) and "proton-only" (right) cases. As in Figure 7.5, the sensitivity of XENONnT is shown, and results from other searches are shown: XENONnT using only SR0 data (recast with a power threshold of 0.16) [89], LZ [58], PandaX-4T [57], and PICO-60 [250]. Reproduced from [Paper II].

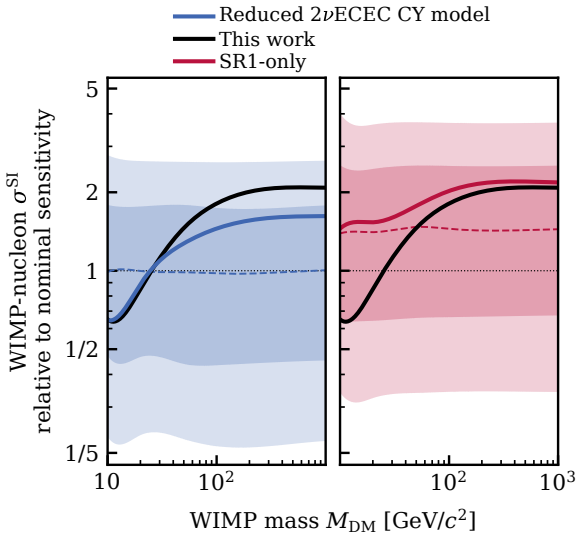

Figure 7.7.: Sensitivity and 90 % CL upper limits (ULs) for the model with reduced DEC (double electron capture, here 2νECEC) charge yield parameters (left) and for an SR1-only analysis (right), presented relative to the nominal model sensitivity for the combined SR0 + SR1 dataset. Dark and light shaded regions indicate the 68 % and 95 % containment regions of expected ULs under the background-only hypothesis, respectively, with dashed colored lines marking the medians. Solid colored lines show the observed ULs for each model, while black lines represent the observed limits from the nominal model (also shown in Figure 7.5). Reproduced from [Paper II].

7.2 First Measurement of ^{8}B CEνNS in Xenon

A search for NR signals with energies above 0.5 keV_{NR} from ^{8}B CEνNS was performed using the first two SRs of XENONnT [Paper III]. Approximately 90 % of NRs from CEνNS were expected in the energy range between 0.7 and 2.1 keV_{NR}, with the main contributions originating from the high-energy tail of ^{8}B neutrinos with energies between 8 and 15 MeV. The total livetime of this search after accounting for dead time from the DAQ and vetoes amounted to 316.5 d, comprising 108.0 d from SR0 and 208.5 d from SR1. With fiducial masses of (3.97 ± 0.20) t for SR0 and (4.10 ± 0.19) t for SR1 (see Section 6.3.3), this yielded a total exposure of 3.51 t yr.

Events in the ROI with R < 63 cm were blinded for this search. The WIMP search employing a 3-fold coincidence requirement using SR0 data [89] had previously unblinded a small fraction of three-hit events in the ROI, constituting less than 3 % of the total ^{8}B CEνNS rate. After unblinding, 37 events were observed (9 in SR0, 28 in SR1), compared to $26.4^{+1.4}_{-1.3}$ expected from backgrounds. The observed excess of 10.6 events is consistent with the nominal expectation of $11.9^{+4.5}_{-4.2}$ events from ^{8}B CEνNS.

7.2.1 Best-fit results

The nominal and best-fit expectation values from a fit including an unconstrained signal component are presented in Table 7.2. The background-only hypothesis was rejected with a p-value of 0.003, corresponding to a discovery significance of $2.73\,\sigma$. This result is consistent with the expected discovery potential (see Figure 6.6).

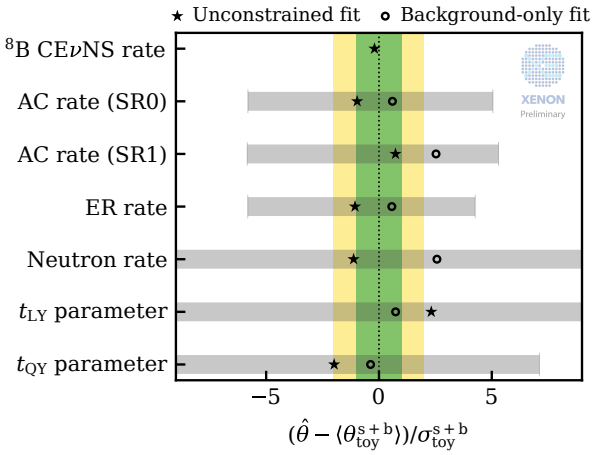

Figure 7.8.: Pull plot indicating the deviation of the best-fit values of the two fits from what is expected due to statistical fluctuations in the science dataset only. For reference, the $1\,\sigma$ intervals of the constraint terms are indicated as gray bands.

Parameter pulls were computed following the methodology described in Section 7.1 and are reported in Figure 7.8 for both the unconstrained signal-plus-background fit and the background-only fit. For the former, all background rate pulls fall within the $\pm 2\,\sigma$ band of expected variation due to statistical fluctuations of the science dataset. The light yield is pulled upward and the charge yield downward; however, both remain well within the ancillary constraints from YBe calibration. For the background-only fit, the best-fit background rate parameters are pulled toward larger values to account for the excess events, with the most extreme pulls beyond the $\pm 2\,\sigma$ band observed for the SR1 accidental coincidence (AC) and the neutron rate.

Table 7.2.: Nominal (pre-fit) and best-fit expectation values in the ROI. The uncertainties of background expectations correspond to the widths of Gaussian constraints in the fit. The uncertainty of the nominal signal expectation includes contributions from signal detection efficiency, light yield, and charge yield. It is unconstrained in the fit.

	Nominal	Best fit
AC (SR0)	7.5 ± 0.7	7.4 ± 0.7
AC (SR1)	17.8 ± 1.0	17.9 ± 1.0
ER	0.7 ± 0.7	$0.5^{+0.7}_{-0.6}$
Neutron	$0.5^{+0.2}_{-0.3}$	0.5 ± 0.3
Total background	$26.4^{+1.4}_{-1.3}$	26.3 ± 1.4
^{8}B CEνNS	$11.9^{+4.5}_{-4.2}$	$10.7^{+3.7}_{-4.2}$
Observed	37	

The distribution of events in projections of the analysis space together with the best-fit model is shown in Figure 7.9. The combination of four one-dimensional GOF tests was defined in Section 6.4, each with a p-value threshold of 0.013 to obtain an effective 95 % CL. The GOF tests for the unconstrained best-fit model show good agreement in cS2 and the two boosted decision tree (BDT) score parameters. In the projection to the $S2_{pre}/\Delta t_{pre}$ parameter, a p-value of 0.008 is observed, which indicates potential mismodeling. In both SRs, the bin of

lowest $S2_{pre}/\Delta t_{pre}$ shows a deficiency of events with respect to the best-fit model. Thorough post-unblinding checks of the events in various parameter spaces and of their waveforms were performed, finding no indication of mismodeling. No similar tendency was observed in any of the calibration data and sidebands used for validation of the AC model, further supporting that the observed deviation might be due to statistical fluctuations. Removing $S2_{pre}/\Delta t_{pre}$ as an analysis dimension would result in a $\sim 25\,\%$ larger best-fit ^{8}B CEνNS rate parameter and accordingly a higher discovery significance of $3.22\,\sigma$. Thus, we can conclude that the potential mismodeling induced by this parameter does not strongly bias estimates of parameters of interest beyond their intrinsic uncertainty, nor does it lead to an overly optimistic discovery significance. Moreover, the same XY asymmetry tests defined in Section 7.1 were performed, finding an unexpected overdensity in the densest half. Also here, possible sources that could introduce such an asymmetry were investigated, including the distribution of events in all discriminating variables used for selection criteria, but nothing suspicious was found. Since the distribution in XY does not enter the result of this analysis and the test was defined solely as a cross-check, this mismatch was deemed uncritical.

7.2.2 Confidence intervals

The signal rate is degenerately dependent on the ^{8}B solar neutrino flux and the cross section of the CEνNS process. Thus, confidence intervals were obtained separately, leaving one of the two parameters unconstrained at a time. With the cross section fixed to the Standard Model (SM) expectation, a ^{8}B solar neutrino flux of $(4.7^{+3.6}_{-2.3}) \times 10^6\,\mathrm{cm^{-2}\,s^{-1}}$ (68 % CL) is obtained, corresponding to the first measurement of the flux via this channel. It is consistent with the independent result of the Sudbury Neutrino Observatory (SNO) experiment [207]. Equivalently, the flux-weighted CEνNS cross section on xenon is measured to be $(1.1^{+0.8}_{-0.5}) \times 10^{-39}\,\mathrm{cm^2}$, using the flux measurement of SNO as a constraint. This result is consistent with the SM prediction of $1.2 \times 10^{-39}\,\mathrm{cm^2}$ and represents the first measurement of the CEνNS process in xenon. Figure 7.10 shows the two-sided 90 % and 68 % CL confidence intervals on the ^{8}B CEνNS neutrino flux (left) and the flux-averaged CEνNS cross section. An independent analysis of the PandaX-4T experiment recently also reported evidence for ^{8}B CEνNS with a significance of $2.64\,\sigma$ and a measured ^{8}B neutrino flux of $(8.4 \pm 3.1) \times 10^6\,\mathrm{cm^{-2}\,s^{-1}}$ [251].

7.2.3 Search for low-mass WIMP dark matter

The same dataset and analysis framework used for the solar neutrino analysis was also used to search for low-mass WIMPs probing a mass range between 3 and $12\,\mathrm{GeV}/c^2$ [59]. At a WIMP mass of $5.5\,\mathrm{GeV}/c^2$, the spectra from a potential dark matter signal and the ^{8}B CEνNS are nearly indistinguishable, giving rise to the "neutrino fog" (see Section 2.2).

The statistical model of this search is almost identical to the one described in Sections 6.1 and 6.2. Instead of being an unconstrained signal, however, the ^{8}B CEνNS component is now again treated as a background with the neutrino flux constrained by the measurement from SNO [207] and the CEνNS cross section fixed to the SM prediction. Various dark matter models can be probed. The sensitivity of this analysis for SI WIMP dark matter, shown in Figure 7.11, reached the neutrino fog for the first time between 5.5 and $8\,\mathrm{GeV}/c^2$.

As expected from the good agreement of the observed dataset with the signal-plus-background model of the ^{8}B CEνNS search, no significant excess of events was found, with a minimum

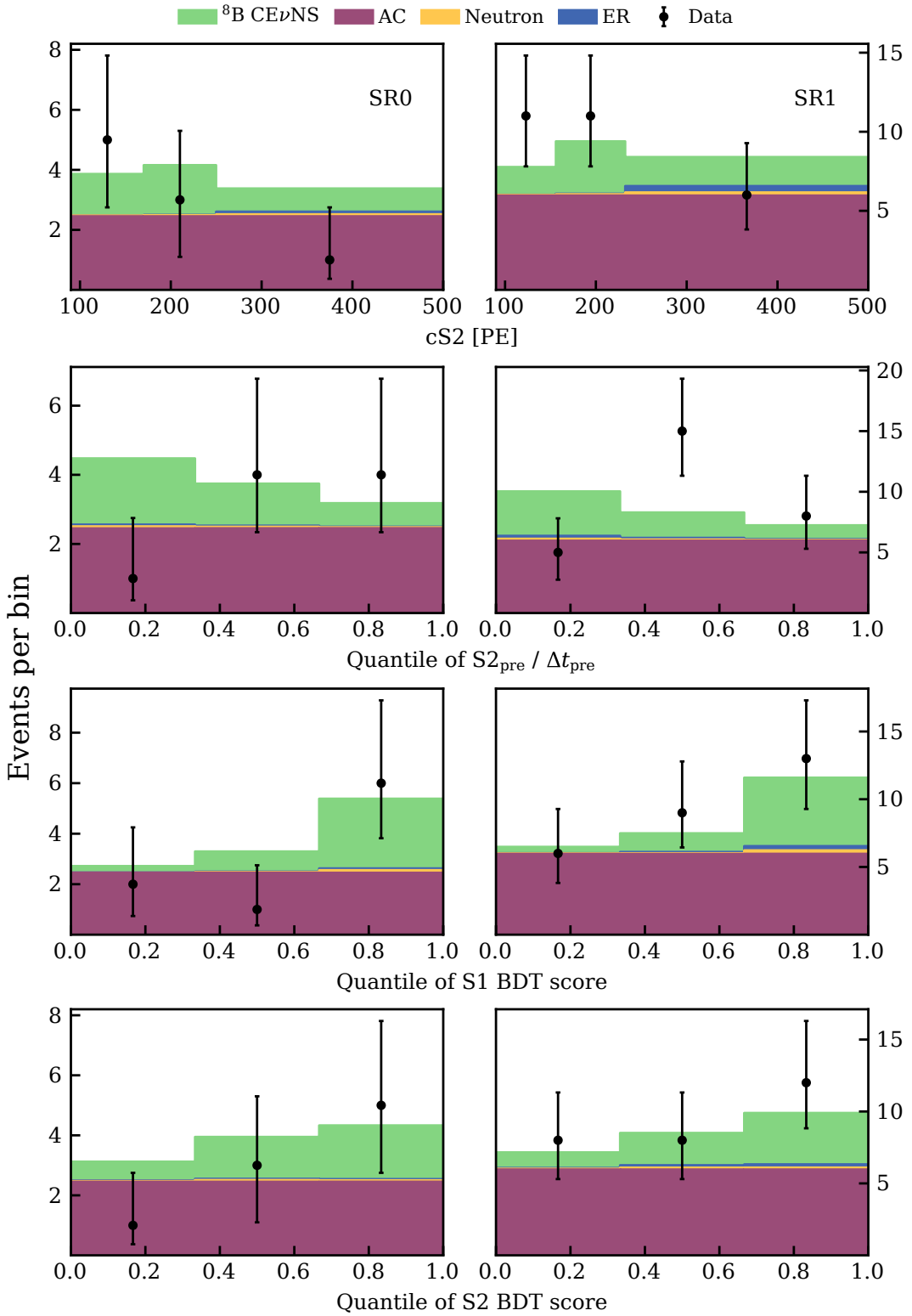

Figure 7.9.: Distributions of the best-fit signal and background, along with the data, are shown as stacked histograms for the projected analysis dimensions, with SR0 and SR1 displayed in the left and right columns, respectively. The neutron (yellow) and ER (blue) backgrounds shown between the accidental coincidence (AC) background (purple) and ^{8}B CEνNS signal (green) are only barely visible due to their subdominant contribution. Adapted from [Paper III].

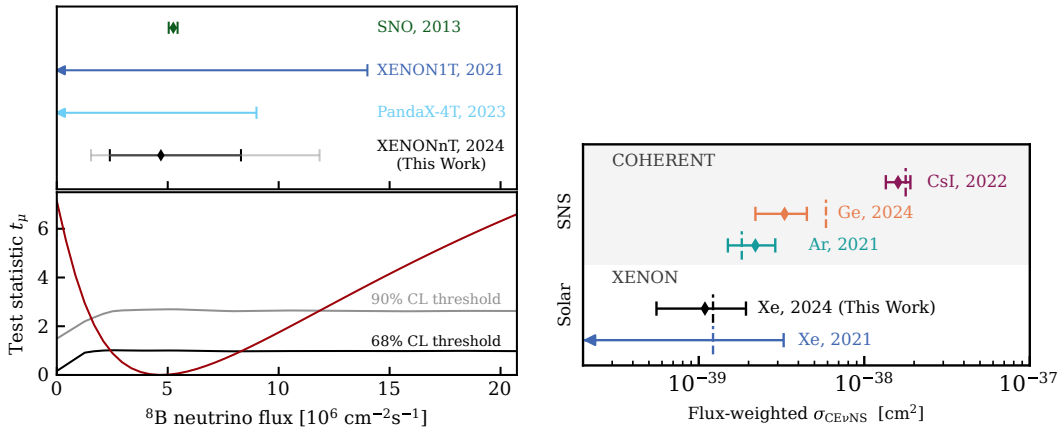

Figure 7.10.: Confidence intervals for the ^{8}B CEνNS search parameters of interest. *Left:* Solar ^{8}B neutrino flux confidence intervals at 68 % CL (black) and 90 % CL (gray) compared with results from SNO [207], XENON1T [252], and PandaX-4T [74] (top), and test statistic t_μ showing the interval construction (bottom). Adapted from [Paper III]. *Right:* Flux-weighted CEνNS cross section $\sigma_{\mathrm{CE}\nu\mathrm{NS}}$ comparing this work with measurements from COHERENT on Ar [71], Ge [72], and CsI [253], as well as the limit obtained with XENON1T [252]. Reproduced from [Paper III].

discovery p-value of 0.18 at 3 GeV/c^2. Consequently, world-leading ULs were placed on dark matter cross sections, shown in Figure 7.11 for SI WIMP-nucleon scattering. Below 5 GeV/c^2, an upward fluctuation is observed, and above a downward fluctuation. Above 8 GeV/c^2, the UL is clipped by the PCL requirement. In addition to SI and SD WIMP-nucleon interactions assuming a heavy mediator, limits were also placed assuming a light mediator [59].

7.3 Other Searches

In addition to NR event searches, we can also search for signals producing ER events on top of our low background. The first search carried out with XENONnT had the goal of clarifying the $> 3\,\sigma$-excess in the low-energy ER channel observed in XENON1T, which was best described by a signal from solar axions [169]. Using data from SR0 with an exposure similar to the total exposure of XENON1T, an approximately 5 times lower ER background rate in the ROI from 1 to 30 keV$_{\mathrm{ER}}$ allowed a sensitive analysis. No excess above background was observed, excluding new physics as an explanation for the XENON1T excess. Instead, it is now considered plausible that the excess originated from a trace contamination of β-decays from tritium. In absence of a signal, world-leading constraints were placed on various potential beyond-SM signals with an ER signature. Figure 7.12 shows the limits on bosonic dark matter candidates, in particular axion-like particles (left) and dark photons (right). For lower dark matter masses, limits on these candidates were additionally placed based on a dedicated analysis of single- and few-electron signals [186].

7.4 Conclusions and Outlook

This chapter presented two major results of the XENONnT experiment. The WIMP dark matter search using 3.1 t yr of exposure found no significant excess above background expectations, setting competitive constraints on SI and SD WIMP-nucleon cross sections with the most

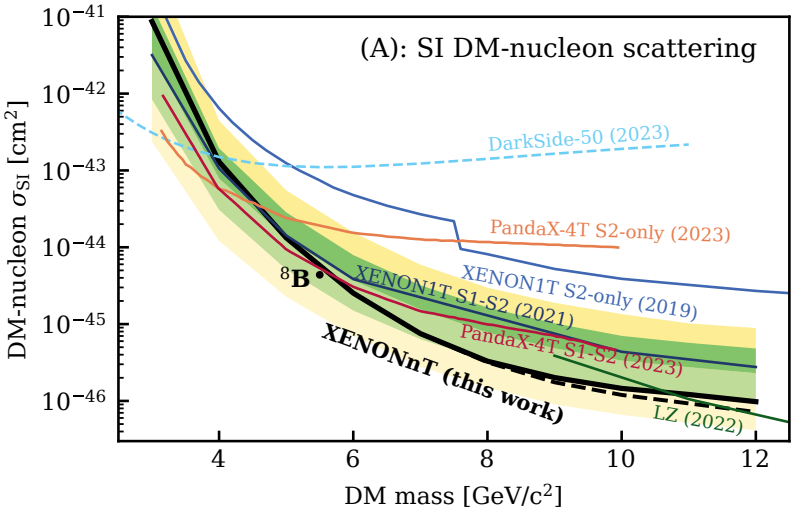

Figure 7.11.: Sensitivity band and 90 % CL upper limit on the spin-independent (SI) WIMP-nucleon cross section (black line) versus WIMP mass. The limits before applying the power-constrained limits (PCL) requirement are shown as a dashed black line. The xenon neutrino fog as defined in [49] is indicated in gray with the three shades corresponding to fog opacity indices $n = 2, 2.5$ and 3 (see Section 2.2). The mass and cross section of a WIMP signal nearly indistinguishable from ^{8}B neutrinos is indicated as a black dot. Other experimental limits are also shown; references to these can be found in [59], from where this plot was reproduced.

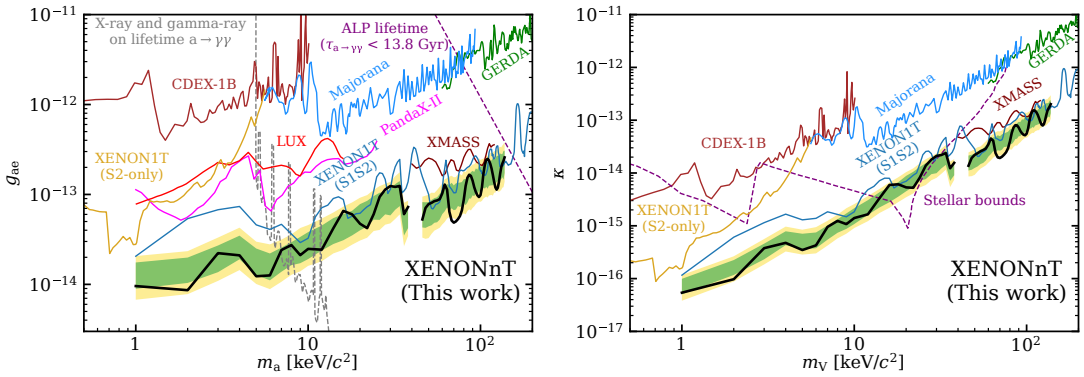

Figure 7.12.: Results from the XENONnT search for low-energy ER signals. The black line shows upper limits (90 %CL) on parameter spaces of axion-like particles (left; axion-electron coupling constant g_{ae} versus axion mass m_a) and dark photons (right; strength of the kinetic mixing between photon and dark photon κ versus rest mass of the vector boson m_V). Constraints between (39, 44) keV/c^2 are excluded due to the unconstrained ^{83m}Kr background. Other experimental limits and astrophysical bounds are also shown; references to these can be found in [146], from where the plot was reproduced.

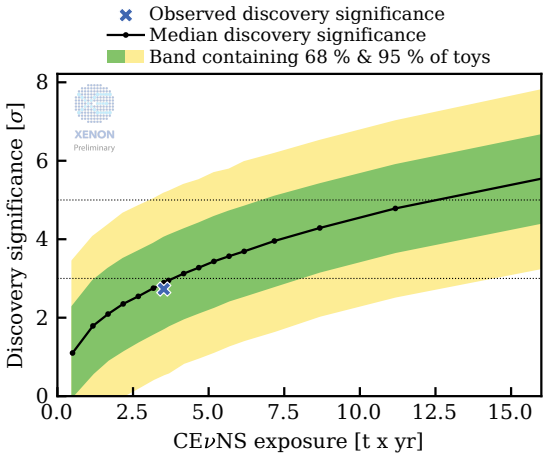

Figure 7.13.: Projected discovery potential for ^{8}B CEνNS with increasing exposure under the assumption of continuing SR1 conditions. The green (yellow) band and the black line indicate $1\,\sigma$ ($2\,\sigma$) containment region and median of expected discovery significances. The observed discovery significance with the SR0 + SR1 dataset is indicated as a blue cross.

stringent SI limit of $1.7 \times 10^{-47}\,\mathrm{cm}^2$ at $30\,\mathrm{GeV}/c^2$. A dedicated analysis optimized to lower the detection threshold achieved the first detection of solar neutrinos with a ton-scale detector, observing a $2.73\,\sigma$ excess consistent with SM predictions and independent flux measurements. Additionally, a complementary low-mass WIMP search reached the neutrino fog for the first time between 5.5 and $8\,\mathrm{GeV}/c^2$, setting world-leading constraints in this challenging regime where dark matter signals become nearly indistinguishable from neutrino interactions.

Since the end of SR1, more data has been acquired with XENONnT, which will further improve the sensitivity of the experiment for WIMP searches (see Section 5.5). More data will also improve the significance of the measured signal from ^{8}B neutrinos. The long-term projection of the ^{8}B CEνNS discovery significance assuming the same conditions as SR1 is shown in Figure 7.13. Under these assumptions, a median discovery significance of $5\,\sigma$ would be obtained at an exposure of approximately 12.5 t yr, which is in reach with the XENONnT experiment. In addition, we also aim to improve the precision of the rate measurement, which requires smaller uncertainties in the emission model, which can be achieved with a new high-statistics low-energy NR calibration campaign. The ^{8}B CEνNS results presented here have been phenomenologically reinterpreted to extract the weak mixing angle at low energies [254, 255], place constraints on models predicting new neutrino-matter interactions mediated by particles beyond the SM [255–260], and constrain neutrino electromagnetic properties [261] (see Section 2.3). These channels can be further probed in the future with a more precise rate measurement.

In the near future, the low-energy ER channel has the potential to measure solar neutrinos from the proton-proton fusion process (*pp* neutrinos) [262]. These sub-MeV neutrinos constitute the dominant component of the solar neutrino flux, but their low energies present significant detection challenges. To date, direct detection of *pp* neutrinos has only been achieved by the BOREXINO experiment [263], making any new measurement an important independent confirmation. The *pp* solar neutrino flux is of particular interest because it is tightly correlated with the Sun's luminosity, thereby providing a unique probe of the solar interior and enabling constraints on alternative energy production mechanisms [264, 265].

8

Experimental Setups for Infrared Scintillation Studies in Xenon

Xenon is a leading target material for rare event searches, primarily due to its excellent scintillation properties in the ultraviolet (UV) range. The UV scintillation response is well understood and widely utilized in xenon-based detectors. However, it has been known for over twenty years that xenon also emits scintillation light in the infrared (IR) regime. Harnessing this additional signal could enhance signal-background discrimination and energy resolution in future xenon detectors. Despite its potential, the properties of the long-wavelength component remain poorly characterized. To fully assess the benefits of multi-wavelength-sensitive xenon detectors, further dedicated studies are urgently needed.

This thesis presents measurements with two experimental setups, providing an initial step toward closing this knowledge gap. The following chapter introduces the two setups used for the measurements in Chapter 9: the room-temperature gas setup (Section 8.3) and a dual-phase setup (Section 8.4). Prior to this, an overview of xenon scintillation light is given in Section 8.1, and photosensors for detecting IR light are discussed in Section 8.2.

8.1 Xenon Scintillation Light

As introduced in Section 3.1.2, xenon scintillation arises from de-excitation of Xe_2^* excimers, producing two xenon atoms and UV light (Equation (3.1)). These excited bound states form in both liquid and gas phases through atomic excitation or electron-ion recombination. The population of radiative precursor states involves multiple steps, including collisional de-excitation and intermittent dissociative processes before rebinding (Equations (3.3) to (3.5)). Dominant mechanisms and thus scintillation outputs may differ between particle types, liquid and gas phases, and the gas density [266, 267].

Figure 8.1 shows a selection of energy potentials versus xenon-xenon internuclear radius for gaseous xenon (GXe) with key atomic and molecular states and transitions. This represents a

significant simplification: [268] reports nearly 120 molecular states, which is still an incomplete collection. Additionally, excited states of the dimer ion Xe_2^+ exist [269, 270].

Ground-state xenon atoms have the electronic configuration $[Kr]4d^{10}5s^25p^6$, described by the term symbol $^1S_0$ (common to all noble gases). Atomic excitation elevates a $5p$ electron to higher electronic states, the next being $6s$ states at ∼8.3 eV energy difference. Ionization occurs when the electron energy exceeds the first ionization energy of ∼12.1 eV [271]. Two ground-state xenon atoms cannot form bound states due to strong nucleus-electron binding, making the molecular ground state[1] 0_g^+ repulsive except for weak van-der-Waals binding (∼23 meV [273], not visible in Figure 8.1). Thus, no strongly bound Xe_2 dimers exist, and states decaying to the ground state dissociate into separate ground-state xenon atoms ($^1S_0$).

However, when one atom is excited or ionized, bound dimer states can form, shown as potential minima in Figure 8.1 for Xe_2^* (excimer) or Xe_2^+ (dimer ion). The lowest Xe_2^* excimer states at ∼8 eV minimum potential energy are the nearly degenerate $(1)1_u$ and $(1)0_u^-$ states (sometimes denoted $^3\Sigma_u^+$), and the slightly higher-lying $(1)0_u^+$ state (sometimes $^1\Sigma_u^+$). At large internuclear distances, these correlate to one ground-state atom and another atom with one electron excited to the $6s$ shell. The Xe_2^+ ground state is shown in Figure 8.1, which has a dissociation energy of ∼ 1 eV [270].

8.1.1 Ultraviolet scintillation in xenon

In thin GXe, excited xenon emits light from various atomic transitions. For denser GXe and in liquid xenon (LXe), the predominant part of scintillation comes from de-excitation of Xe_2^* excimers in dissociative bound-free transitions, i.e. $Xe_2^* \rightarrow Xe + Xe^{(*)}$. The transitions from bound states to repulsive states result in relatively broad continuous spectra as the photon energy strongly depends on the internuclear distance at which the transition occurs [274]. Four such continua are known. The spectra of the three present at approximately 1 bar in GXe are shown in Figure 8.2. The UV continua, which are the most thoroughly studied and widely established, are discussed below in order of ascending wavelength.

First continuum

The shortest-wavelength continuum peaks at ∼150 nm [267, 277] and contributes dominantly below ∼200 mbar in GXe [267, 278] though can be detected up to ∼1.3 bar [279]. As shown in Figure 8.1, it originates from vibrationally excited $(1)0_u^+$ states decaying to the dissociative ground state.[2] Collision-assisted vibrational relaxation competes with direct radiative decay from vibrationally excited levels. At low pressures, the collision rate is sufficiently low for radiative decay to predominate, resulting in the formation of the first continuum [266, 280]. The first continuum has not been observed in liquid but "reappears" in the solid phase, with increasing contribution at lower temperatures [281, 282].

[1] In Hund's case c notation for strong spin-orbit coupling, which is valid for xenon. The quantum numbers L and S for orbital angular momentum and spin, respectively, are no longer conserved. Instead, Ω (projection of total angular momentum $\vec{J}$ onto the internuclear axis) remains a good quantum number [272]. Electronic wavefunction symmetries include reflection in a plane containing the internuclear axis (+ symmetric, − antisymmetric) and coordinate inversion ("gerade" g symmetric, "ungerade" u antisymmetric), such that a molecular state is written as $\Omega_{g/u}^{(+/-)}$. Since term symbols are not unique, we add running index numbers before Xe_2^* state terms as in [268].

[2] Contributions from vibrationally excited $(1)1_u$, $(1)0_u^-$ states can be neglected as their decay constants are slower and thus collisional vibrational relaxation dominates [266].

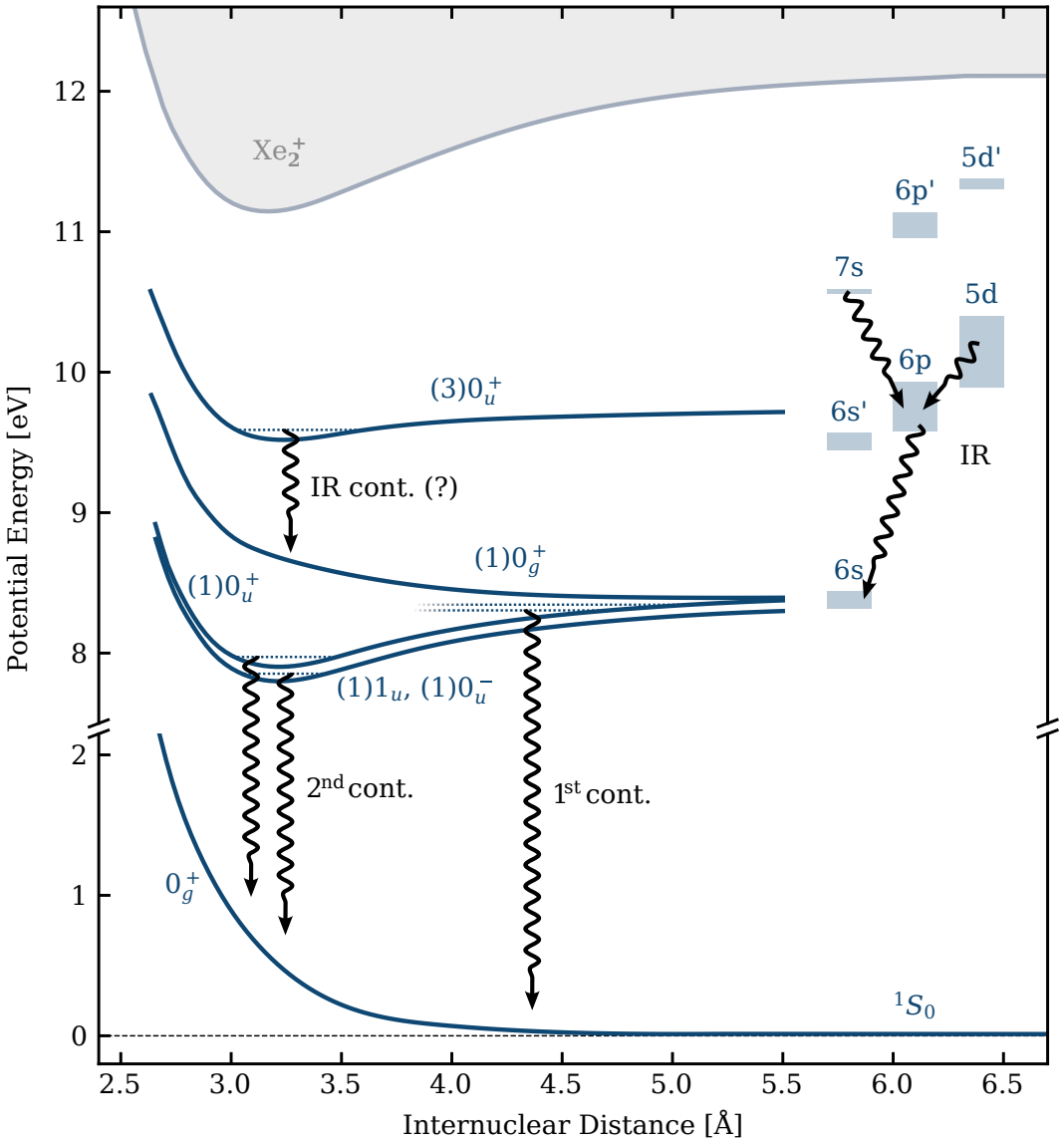

Figure 8.1.: Potential energy versus Xe–Xe internuclear distance showing the dimer ground state 0_g^+ [269] dissociating into two ground-state xenon atoms ($^1S_0$), four Xe_2^* curves [268], and the ground state of the dimer ion Xe_2^+ [270]. Atomic lines [271] appear as boxes at large radii (radial shifts for visual clarity only). Black arrows indicate radiative transitions.

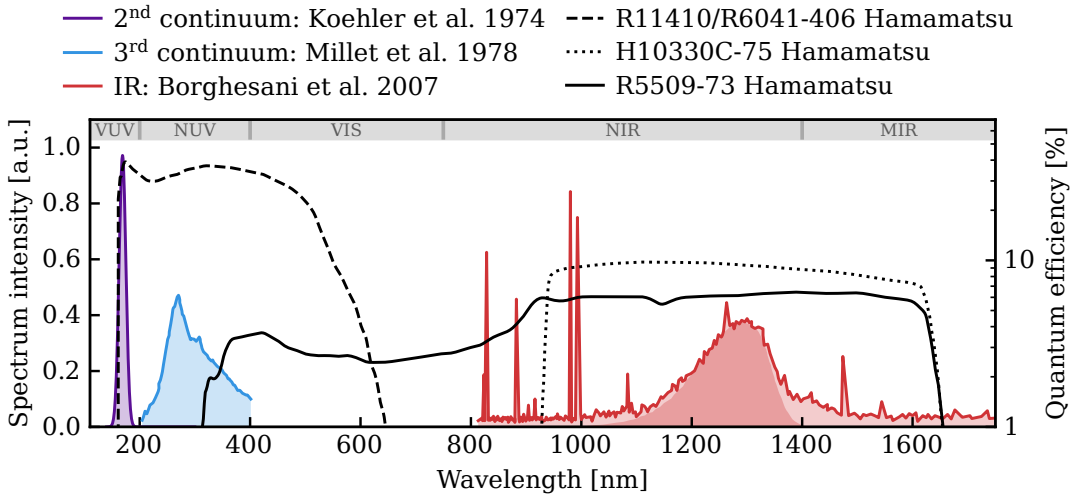

Figure 8.2.: Known emission spectra of GXe at 1 bar. Second continuum (purple) from [275], third continuum (blue) from [267]. IR emission (red, from [276]) features a dominant continuum centered at ∼1.3 µm (dark shaded) plus sharp atomic transition lines. Relative intensities are arbitrarily scaled. Overlaid quantum efficiency (QE) curves show photomultiplier tubes (PMTs) used in this work. Indicated wavelength bands: vacuum ultraviolet (VUV), near-ultraviolet (NUV), visible (VIS), near-infrared (NIR), and mid-infrared (MIR). Adapted from [Paper VI].

Second continuum

At higher pressures, frequent collisions facilitate vibrational relaxation prior to radiative de-excitation, producing the second continuum. At GXe pressures above a few hundred mbar and in liquid, dominant scintillation comes from vibrationally relaxed bound states $(1)0_u^+$ ("singlet") and $(1)1_u$, $(1)0_u^-$ ("triplet") [266, 283]. Peak emission occurs at ∼170 nm in GXe [121, 275] (see Figure 8.2, purple line) and ∼175 nm in LXe [120, 121], both with ∼10 nm full width at half maximum (FWHM).

In gas below ∼1 bar, the second continuum is dominated by triplet decay [267, 284]. Above ∼1.6 bar [266] and in LXe, the singlet component also contributes. Decay times differ between singlet and triplet precursors, with triplet states exhibiting longer lifetimes. In the absence of spin-orbit coupling, triplet-to-singlet ground state transitions are spin-forbidden. Xenon's strong spin-orbit coupling allows these transitions, though the triplet decay remains slower compared to the singlet. The fast and slow components of the second continuum have been measured to be ∼5 ns and ∼100 ns in GXe [121, 266, 285], and ∼4 ns and 20–40 ns in LXe [122–124].

Third continuum

First observed in [286], the third continuum emission has been measured in GXe for α-particles (up to 10 bar) and β-particles at 10 bar [284]. The spectrum peaks at ∼270 nm at 950 mbar [267] (see Figure 8.2, blue line). With a fast decay constant of ∼8 ns, this continuum constitutes the dominant fast UV component up to ∼1 bar [284]. No third continuum emission has been observed in LXe.

The underlying processes responsible for third continuum emission remain unclear. Proposed mechanisms include radiative decay from highly excited singly-charged molecular ions Xe_2^+ [287] and doubly-charged dimer ions $Xe_2^{2+} \rightarrow 2\,Xe^+ + h\nu$ [288]. Argon measurements suggest the third continuum comprises multiple peaks from at least four different precursors, all involving

highly excited ionic molecules [289]. While present in primary scintillation, electroluminescence contributions remain at sub-percent levels relative to second continuum signals, if present at all [284]. This is consistent with the process being associated with highly excited or ionized states.

8.1.2 Infrared scintillation in xenon

In 1970, Mulliken predicted previously unobserved IR bands based on estimated xenon energy potential curves [290]. The first systematic study of IR scintillation in noble gases was performed in 1988 by Lindblom and Solin [291], though measurements only extended to 930 nm, revealing just three atomic xenon transition lines. Far-IR scintillation (3–14 µm) was qualitatively observed in GXe [292].

Around 2000, Carugno, Borghesani, and collaborators began investigating the IR emission in xenon more quantitatively. Initial gas-phase studies found α-particle light yields exceeding 21 000 ph/MeV at 2 bar [293], comparable to established UV scintillation yields of approximately 25 000 ph/MeV [284, 294]. The strong scintillation was primarily attributed to a broad continuum centered around 1.3 µm [295] (see Figure 8.2), consistent with Mulliken's predictions [290]. At 1 bar gas pressure, narrow atomic transition lines accompany the continuum, with corresponding transitions indicated in Figure 8.1. For higher pressure, a red-shift and broadening of the IR continuum was observed and later modeled ($\sim$1.27 µm for $P \to 0$ to $\sim$1.47 µm at $P = 20$ bar) [276, 296, 297]. The proposed mechanism for the continuum involves a bound-free transition from the higher-lying $(3)0_u^+$ state (associated with an atomic $6p$-excited state) to the dissociative $(1)0_g^+$ state. This transition leads to dissociation into one ground state atom and one atom excited to the $6s[3/2]_1^0$ state (in Racah notation). The excited $6s[3/2]_1^0$ atom can subsequently form a $(1)0_u^+$ molecular state via a three-body process (Equation (3.2)). As a result, second continuum emission is expected to follow that of the IR continuum.[3] While pressure-dependent shifts and broadening are well understood, discrepancies remain: calculations using energy potentials from [268] predict the continuum to be centered around 1.41 µm, whereas measurements find it at 1.27 µm [276, 296]. In addition to the primary scintillation signal, evidence of IR emission from electroluminescence has been observed. For electric fields between 500 and 1300 V/cm, the IR signal increases approximately in proportion to the extracted ionization charge [293].

Measurements in LXe have also been performed, though only to a limited extent. The IR light yield from 80 keV electron beam irradiation has been estimated to be two orders of magnitude smaller than the IR yield in GXe [298]. Measurements with coarse bandpass filters indicated a significant blue-shift of the emission [298]. No strong dependence of the yield in LXe on impurity concentration was observed [299].

Most measurements employed InGaAs photodiodes with 0.7–1.6 µm wavelength sensitivity. Spectral resolution measurements required high-rate pulsed electron or proton beams; only the absolute yield measurement in GXe used an α-particle source.

[3] This includes emission from the slow component as an efficient collision-assisted process has been identified to eventually populate the $(1)1_u$ and $(1)0_u^-$ states from $(1)0_u^+$ states [266].

8.1.3 Infrared scintillation in argon and xenon-argon mixtures

Despite argon's much lighter atomic mass ($A \sim 40$ versus xenon's $A \sim 131$), it shares several comparable properties with xenon [103, 300]. Since argon is also used in rare-event searches, its scintillation properties and those of xenon-argon mixtures have been extensively studied.

Buzulutskov and colleagues first measured the IR scintillation yield and time response in liquid and gaseous argon in 2011 [301] using a pulsed X-ray tube. Measurements covered the visible to near-IR range: 690–1000 nm in gas and 400–1000 nm in liquid argon. The time response revealed a fast component (< 500 ns decay constant) and an unexplained slow component ($\sim 20 - 30$ µs decay constant) in both phases, each component contributing ∼50% of the total signal [302]. Fast component light yields were $(17\,000 \pm 3000)$ ph/MeV in gas and (510 ± 90) ph/MeV in liquid [303]. The ∼30-fold yield reduction in liquid remains unexplained. Electroluminescence produced 13 photons per drifting electron per kV, which is six times lower than in UV and occurred only at higher fields [303]. Both characteristics align with higher excitation energies required for IR scintillation [304].

However, these results are somewhat contradicted by later measurements from Neumeier and collaborators [305], who found no IR emission in pure liquid argon up to 3.5 µm, with signals appearing only when trace amounts of xenon were added. IR emission was strongest at a xenon concentration of 10 ppm, with the signal dominated by a continuum centered at 1.17 µm. Additionally, two weaker atomic lines were observed, with only one lying below 1 µm – within the sensitive range of earlier measurements. Total IR light yields with this xenon concentration reached $(13\,000 \pm 4000)$ ph/MeV. The dominant continuum emission exhibited an exponential time response with a decay constant of ~ 175 ns. Comparison with the timing of the second UV continuum indicates that IR scintillation precedes UV scintillation. In contrast, the atomic peaks displayed a much slower exponential decay of ~ 10 µs. For gas mixtures of 10 % xenon and 90 % argon, the primary source of IR emission was attributed to the xenon continuum [295].

8.2 Detection of Infrared Light

The two IR-sensitive detectors used in this work are PMTs with field-assisted InP/InGaAs photocathodes. These compound semiconductor photocathodes consist of an InP substrate onto which a layer of InGaAs is grown. The low band gap of 0.75 eV enables sensitivity to wavelengths as long as ∼1.65 µm [306]. Absorbed photons can elevate electrons from the valence band into the conduction band. Application of a bias voltage lowers the conduction band barrier between InGaAs and vacuum, allowing the electrons to be emitted as photoelectron (PE) into the PMT for amplification [307]. To limit dark count emission, these cathodes need to be cooled to −60 to −80 °C.

8.2.1 Hamamatsu H10330C-75 PMT

A Hamamatsu H10330C-75 PMT is employed in the room-temperature gas setup described in Section 8.3. The detector features an InP/InGaAs photocathode positioned behind a condenser lens to increase angular acceptance. It is housed inside a thermally insulated enclosure behind a fused silica window. An integrated thermoelectric cooler maintains an operating temperature of −60 °C. The PMT exhibits wavelength sensitivity from 950 nm to 1.65 µm (shown in Figure 8.2) with a quantum efficiency (QE) of approximately 9 %. The cutoff at 950 nm is

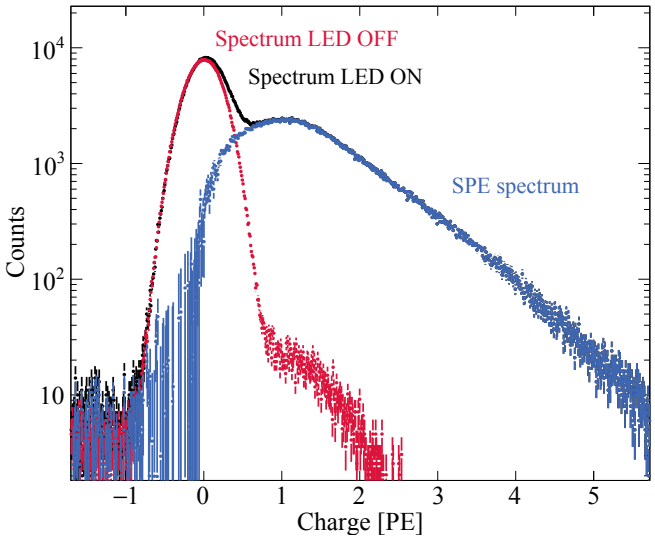

Figure 8.3.: Gain calibration results for the IR-sensitive Hamamatsu H10330C-75 PMT. The single photoelectron (SPE) spectrum (blue) was obtained by subtracting the LED-off spectrum (red) from the LED-on spectrum (black). Reproduced from [Paper IV].

characteristic of transmission-type InP/InGaAs photocathodes, as photons with shorter wavelengths are absorbed in the InP substrate. The substrate's band gap is 1.3 eV, equivalent to the photon energy at 950 nm [307, 308]. Single IR photons can be detected with fast time response (0.9 ns rise time and 0.4 ns transit time spread).

The PMT was calibrated in situ using a 950 nm light emitting diode (LED). Waveform integrals were recorded with the LED both on and off to generate the single photoelectron (SPE) spectrum illustrated in Figure 8.3. The PMT gain was determined using the model-independent approach described in [309], yielding a value of 3.5×10^6 at the operating voltage of −800 V. The dark count rate remained constant at 180 kHz throughout all measurements.

8.2.2 Hamamatsu R5509-73 PMT

The Heidelberg Xenon (HeXe) setup, which is described in Section 8.4, employs a 2-inch Hamamatsu R5509-73 PMT. This device features a borosilicate entrance window with an 8 mm diameter opening. A rectangular reflection-type InP/InGaAs photocathode measuring 3 mm × 8 mm is positioned 2 cm behind the window. The PMT is sensitive to wavelengths between 300 nm and 1.65 µm, as shown in Figure 8.2, with a nominal QE of 6 % at 1.3 µm. Similar to the H10330C-75 model, it offers good timing resolution, with a rise time of 3 ns and transit time spread of 1.5 ns. At the operation voltage of −1700 V, it features a gain of 3×10^6. Since it is operated directly in cold xenon at −95 °C, no external cooling system is required.

To overcome the conduction band barrier, a bias voltage of −4.75 V has to be applied to the photocathode[4] [307]. For this purpose, a base electronic was developed at Max-Planck-Institut für Kernphysik (MPIK), featuring a Zener diode in series with a potentiometer. Even though various tests at LXe temperatures were performed, the bias voltage during operation remained around −1 V with occasional jumps. The cause of this behavior is currently under investigation. Simulations indicate that reducing the bias voltage on an InP/InGaAs/InP photocathode from

[4]The precise value differs for every single device.

−5 to −1 V decreases the QE by roughly two orders of magnitude, with only a weak wavelength-dependence above 900 nm [308]. Based on this, we expect that our device likely exhibited a significantly reduced QE of unknown value during the measurements presented here, as the reduction should depend on the precise material specifications.

8.3 The Room-Temperature Gas Setup

A dedicated setup for studying IR scintillation in xenon gas was developed at MPIK and commissioned in [310]. Photographs and a schematic of the apparatus are shown in Figures 8.4 and 8.5. The apparatus consists of a cylindrical stainless steel tube (10 cm diameter) filled with GXe and instrumented with three PMTs: two UV-sensitive detectors (Hamamatsu R11410, identical to those used in XENON1T and XENONnT [311]) positioned opposite each other, referred to as 'right' and 'left' PMTs in Section 9.1, and one IR-sensitive detector (Hamamatsu H10330C-75) placed orthogonally, in the center of the two UV PMTs.

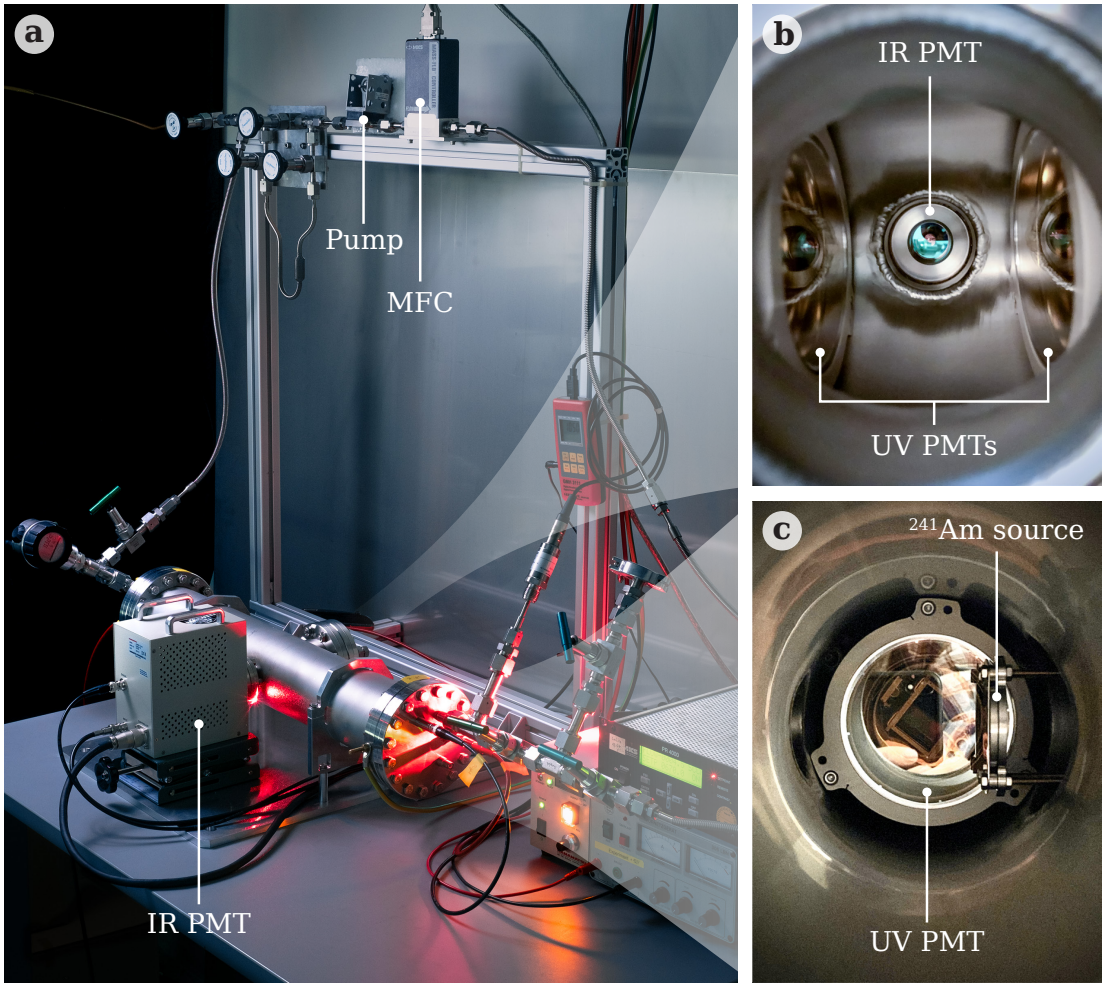

Figure 8.4.: Photographs of the room-temperature apparatus for measuring IR scintillation in GXe. *a*: Overview of the tabletop setup showing the IR PMT attached to the gas-filled tube and gas handling system, including recirculation pump and mass flow controller (MFC); *b*: View from the ^{241}Am α-particle source; *c*: View from the right UV-sensitive PMT.

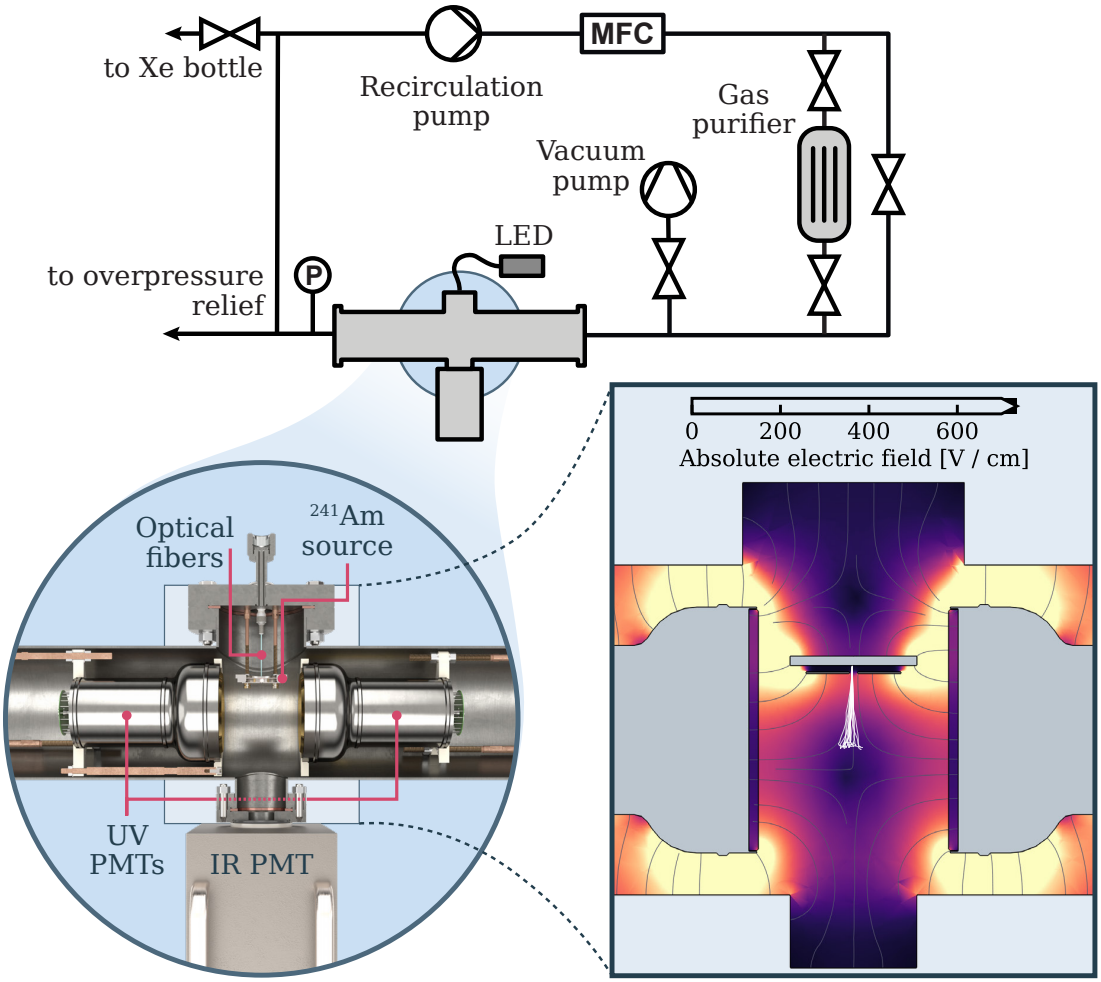

Figure 8.5.: Schematic of the gas purification system connected to the room-temperature apparatus used to study IR scintillation in GXe: The first magnified view (bottom left) shows a cutaway of the stainless steel tube, highlighting the PMT photo sensors and the ^{241}Am α-particle source. The second magnification (bottom right) presents a COMSOL [312] simulation of the electric field in the target region from [Paper IV], along with several typical α-particle trajectories (white) at a pressure of 1 bar, simulated using SRIM [313].

The GXe target is irradiated with a collimated ^{241}Am α-particle calibration source (3.7 kBq) positioned opposite the IR-sensitive PMT. The source, deposited on a metal substrate, is mounted behind a 2.5 mm diameter aperture at 3 mm distance to provide beam collimation. The ^{241}Am decay to ^{237}Np (half-life: 433 years) produces α-particles with energies of 5.486 MeV (85 %), 5.443 MeV (13 %), or 5.388 MeV (2 %) [314]. Accompanying γ-rays ($\sim$ 60 keV) are emitted in 36 % of decays, their contribution to the signal is small given their long mean free path ($\sim$20 cm in 1 bar GXe). Optical fibers, attached to the source holder, can guide light from external LEDs into the setup to enable PMT calibration.

The UV-sensitive PMTs are operated with negative high voltage applied to their photocathodes for the measurements presented here, unless stated otherwise. The resulting inhomogeneous electric field between the photocathodes and the grounded source holder varies from 0 V/cm to approximately 400 V/cm along a typical α-particle trajectory. Electric fields were simulated in three dimensions using COMSOL [312], and α-particle trajectories with SRIM [313]. The α-particles have a range of approximately 2.5 cm at 1 bar.

The pressure-dependent light collection efficiency (LCE) was determined through a simplified Monte Carlo (MC) simulation. In this simulation, photons were generated isotropically along central α-particle tracks, and their intersections with the UV PMT photocathodes or IR PMT condenser lens were recorded. Here, reflections were neglected, which represents a reasonable approximation for the IR photons given the experimental conditions, since the unpolished stainless steel chamber walls as well as the quartz windows of the UV PMTs exhibit low IR reflectivity [315]. The computed LCE decreases from 0.30 % at 500 mbar to 0.22 % at 1 bar for the IR-sensitive PMT, while each UV-sensitive PMT achieves approximately 15 % LCE across the pressure range. In addition, the fraction of the α-particle energy deposited in the active detector region behind the aperture was estimated. Based on the SRIM-simulated particle trajectories, this energy fraction ranges from approximately 97 % at 500 mbar to 92 % at 1 bar, reflecting the varying penetration depths of α-particles in xenon gas at different densities.

A gas purification system was commissioned for this work and attached to the stainless steel cylinder, as illustrated in Figure 8.5. The system employs a membrane recirculation pump to continuously circulate gas through a zirconium hot getter (SAES MonoTorr PS4) at a typical mass flow of 650 sccm, regulated by a mass flow controller (MFC). This configuration continuously removes impurities such as O_2 and water vapor released from material outgassing, which can affect the UV and IR signals. The system also enables gas filling from an attached xenon bottle and evacuation using a vacuum pump.

8.4 The Dual-Phase Setup

Measurements were performed with the HeXe setup – a small-scale time projection chamber (TPC) with an active volume of ∼350 g of LXe, corresponding to approximately one 12 000th of the fiducial mass of XENONnT. The detector is usually instrumented with two UV-sensitive PMTs. In previous studies, it has been employed to investigate the field dependence of LXe yields [156, 316], the prompt scintillation time response [124, 317], and electronic recoil (ER) yields at particularly low energies and drift fields [318]. Additionally, the polytetrafluoroethylene (PTFE) transmissivity for xenon scintillation light [156, 319] and the effects of PTFE cleaning procedures on LXe purity [320, 321] have been investigated. For the present study, the top PMT was replaced with one sensitive to IR wavelengths. Photographs of the HeXe detector and its auxiliary systems are shown in Figure 8.6.

8.4.1 The HeXe TPC

The general working principle of a dual-phase TPC is introduced in Chapter 3. Figure 8.7 illustrates the TPC configuration used in this work. Three grid electrodes establish the electric fields of the detector: the cathode at the bottom, and gate and anode at the top. During operation, LXe is filled such that the liquid-gas interphase is between gate and anode. Field-shaping rings connected via a resistor chain ensure a homogeneous electric field inside the active volume. As in XENONnT, the TPC wall is made of PTFE, which features a reflectivity above 99 % for wavelengths between approximately 350 nm and 1800 nm [145].

Scintillation light in the TPC is detected by two 2-inch PMTs, positioned at the top and bottom of the chamber. The bottom PMT is a Hamamatsu R6041-406, sensitive from the vacuum ultraviolet (VUV) to the visible spectrum, and features a QE comparable to the model

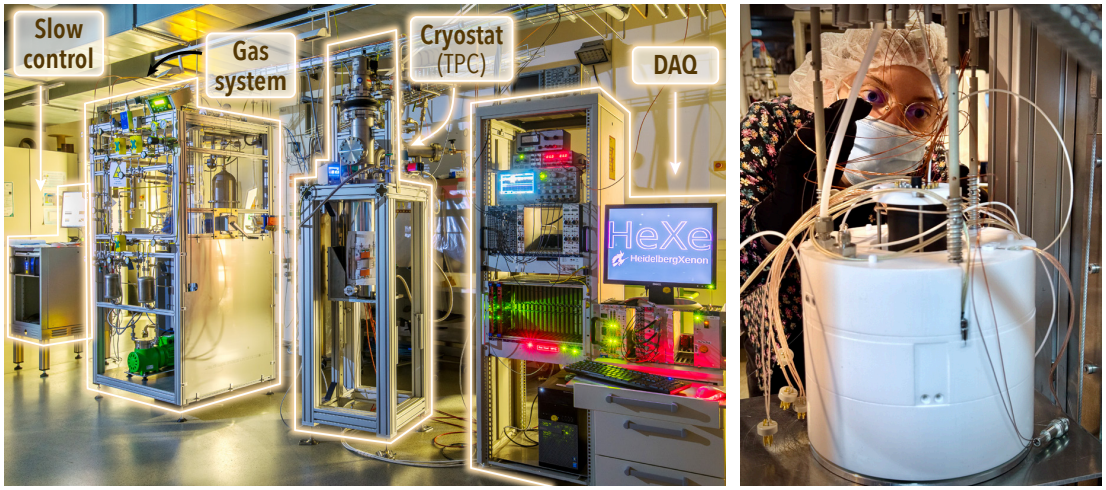

Figure 8.6.: *Left:* Photograph of the HeXe detector with its auxiliary systems. Photo credit: Ralph Lackner. *Right:* Installation of the IR-sensitive PMT in the HeXe time projection chamber (TPC). The photograph shows the detector after the PMT has been replaced, with cables being reconnected to the sockets visible along the top edge.

used in the room-temperature setup. In contrast to the standard HeXe configuration, the top PMT was replaced with an IR-sensitive Hamamatsu R5509-73 PMT, featuring wavelength sensitivity from 300 nm to 1.65 µm, as described in Section 8.2.2.

A drift field of 400 V/cm was established by setting the cathode to −1950 V and gate to −5 V, separated by 5 cm. The extraction and amplification fields depend on the liquid level between gate and anode, which are separated by 5 mm. While the liquid level is typically maintained at 2.5 mm – midway between the gate and anode – for the measurements presented here it was determined to be (4.1 ± 0.5) mm, based on a data-driven method described in Appendix B. The anode was set to 3750 V, yielding an amplification field in the gas phase of (12.1 ± 0.9) kV/cm. During the measurements presented here, the temperature was controlled at approximately −95 °C and the pressure in the gas phase was 2.5 bar.

Figure 8.7.: Schematic drawing of the HeXe time projection chamber (TPC) with the IR-sensitive PMT at the top. During operation, LXe is filled in the cylinder with a liquid level maintained between anode and gate (not shown here). Reproduced from [Paper VI].

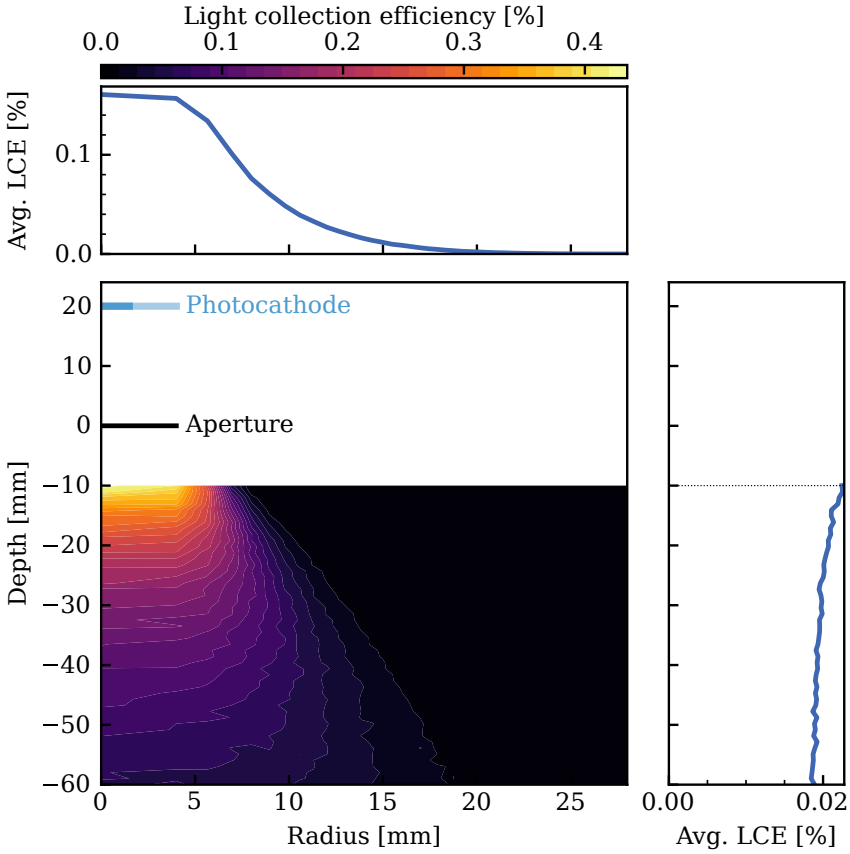

Figure 8.8.: Simulated light collection efficiency (LCE) map of the IR-sensitive PMT in HeXe, shown as a function of depth and radial position. The PMT's entrance window (aperture) is shown as a horizontal black line; the rectangular photocathode is indicated in light blue, with its two side lengths drawn in a lighter and darker shade.

A simplified MC simulation was performed to estimate the LCE of the IR PMT. The geometry included the cylindrical TPC and the IR PMT, with the photocathode located 2 cm behind an 8 mm diameter entrance window (aperture). Photons were generated isotropically in the LXe volume between cathode and gate electrodes. For this simplified estimate, photon reflections and absorptions were neglected. The resulting LCE map as a function of depth and radial position is shown in Figure 8.8. In the projection plots, one can see a strong radial dependence: directly beneath the aperture, the average LCE reaches approximately 0.15 %, but drops rapidly at larger radii, falling below 0.01 % for radii larger than 15 mm. When averaged over the radial coordinate, the LCE exhibits only a weak dependence on depth. The nearly constant value of 0.02 % results from a compensation between the decreasing solid angle at larger distances and the increasing angular acceptance of the aperture.

8.4.2 The HeXe gas handling system

The TPC is connected to a dedicated gas handling system that enables xenon storage, continuous purification, and the introduction of gaseous calibration sources, illustrated in Figure 8.9. During operation, xenon is continuously extracted from the liquid phase in the TPC, which resides in a cryostat. The evaporated xenon is circulated through a zirconium hot getter (SAES

MonoTorr PS4) using a double-membrane recirculation pump. The purified gas is re-condensed on the cold head and subsequently drips back into the liquid phase of the TPC.

The xenon purity is monitored via the "electron lifetime" (see Section 3.3.3), which quantifies the loss of drifting electrons due to attachments to electronegative impurities, such as O_2 or water. This parameter can be converted to an O_2-equivalent mole fraction of impurities x_{O_2} using the electron attachment rate constant at an electric field of 400 V/cm of $10^{11}\,\mathrm{mol}^{-1}\,\mathrm{s}^{-1}$ from [322] and a molar mass of xenon at the operating conditions of $21.5\,\mathrm{mol\,L}^{-1}$ to

$$x_{O_2} = \frac{465\,\mu\mathrm{s\,ppb}}{\tau_e}. \tag{8.1}$$

In the measurements presented here, the electron lifetime ranged between 40 to 50 µs, corresponding to an O_2-equivalent mole fraction of approximately 10 ppb. This lifetime is notably shorter than in previous runs where values of several hundred to above one thousand µs were achieved [318, 321]. The reduction was likely caused by outgassing from materials of the newly installed PMT and PTFE components of the TPC.

The flow path can be redirected through a gaseous calibration source. For the measurements presented here, a ^{222}Rn α-particle calibration source was used. The gaseous source was produced by placing a ^{226}Ra sample inside an emanation chamber filled with GXe, allowing ^{222}Rn to accumulate over a period of one to three days. The accumulated gas was then transferred into a U-tube and connected to the HeXe gas system, from which it was flushed into the TPC. Using this method yielded α-particle rates between 20 and 30 Hz, originating from the decays of ^{222}Rn (5.5 MeV), ^{218}Po (6.0 MeV), and ^{214}Po (7.7 MeV).

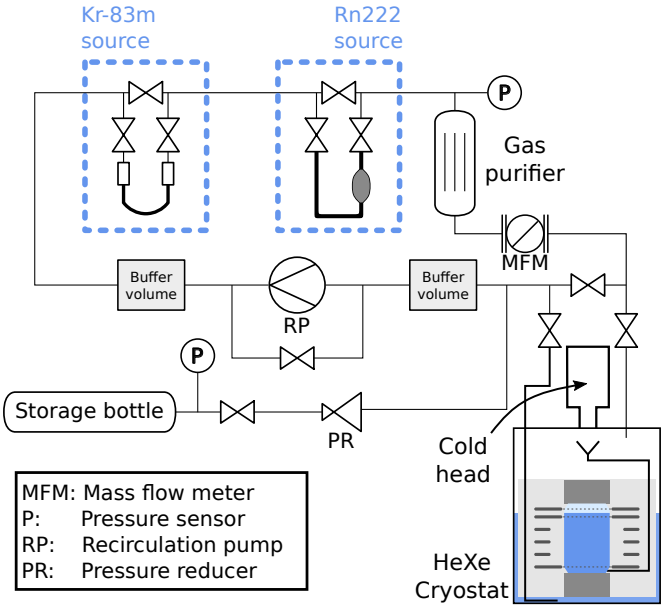

Figure 8.9.: Simplified schematic drawing of the HeXe gas handling system. Reproduced from [156].

9

Measurement of the Infrared Scintillation Response of Xenon

In Chapter 8, the current understanding of infrared (IR) scintillation in xenon is reviewed. Although the established lower limit on the light yield is encouraging, existing knowledge remains insufficient to determine whether IR scintillation could enhance future xenon detectors. In this thesis, the first measurements of the light yield in gaseous xenon (GXe) and the scintillation time response in both liquid and gaseous xenon are presented. These results represent important steps toward clarifying the underlying processes of IR scintillation and evaluating its potential for next-generation detectors.

Measurements in room-temperature GXe are described in Section 9.1, followed by results from a dual-phase setup in Section 9.2. The findings are interpreted in Section 9.3, with possible applications and future directions discussed in Section 9.4.

9.1 Measurements in Room-Temperature Xenon Gas

Several data-taking campaigns were performed with the setup described in Section 8.3 to study IR scintillation in GXe. The first campaign, reported in [Paper IV], was used to determine the light yield and characterize the time response for the first time, while investigating the dependence on pressure and gas purity. We found that the dominant component of the signal has a time constant of $\mathcal{O}(\mu s)$. This component was only partially measured up to $\sim 0.3\,\mu s$ due to digitizer constraints, resulting in the primary systematic uncertainty of the light yield measurement. A subsequent campaign, detailed in [Paper V], extended the acquisition window to $\sim 3\,\mu s$, revealing the exponential nature of the tail and thereby eliminating the associated systematic uncertainty. Additionally, a systematic study of electric field effects on the IR signal was conducted, ruling out light emission from drifting electrons or electron-ion recombination as dominant mechanisms for the observed signal.

9.1.1 Data acquisition and signal processing

The combination of low light collection efficiency (LCE) and quantum efficiency (QE) of the IR-sensitive photomultiplier tube (PMT) (see Chapter 8) results in individual IR photons being recorded for each α-particle event, while the ultraviolet (UV) channels simultaneously detect large signals of $\mathcal{O}(10^4)$ photons. This seemingly poor performance proves beneficial as it allows precise reconstruction of the IR time response via single-photon counting, described in Section 9.1.3.

Events were triggered on a coincident signal in both UV-sensitive PMTs and the waveforms of all three photosensors were recorded with the CAEN V1743 digitizer. This 12-bit switched-capacitor digitizer can achieve a sampling frequency of 3.2 GS/s (GigaSamples per second). Its architecture continuously samples the input signal into a circular analog memory buffer of 1024 cells, corresponding to a recording window of 320 ns at the maximum sampling frequency. Upon a trigger, the buffer's state is frozen, and its contents are subsequently digitized. To extend the effective recording duration in [Paper V], the digitizer's sampling frequency was lowered to 1.6 GS/s, providing a 640 ns time window per channel. The IR signal was passively split and fed into six separate digitizer channels with relative digital time delays of 500 ns. This technique resulted in an overlap of 140 ns between consecutive channels and extended the total effective time window to approximately 3 µs.

The recorded waveforms were processed using the `walpurgisnacht` framework [317], which identifies peaks and extracts key characteristics such as arrival time, pulse width, and area. The pulse area was then converted to units of photoelectrons (PE) using gain calibrations performed with light emitting diodes (LEDs) (see Section 8.2).

9.1.2 Data selection

Minimal selection criteria were applied to the IR signals. Peaks attributed to PMT electronic noise were rejected by requiring a pulse area exceeding 0.17 PE and a pulse width greater than 1.85 ns (2.2 ns for the measurements reported in [Paper V]). Selection criteria were applied to the UV signals to identify well-reconstructed α-particle events with trajectories passing through the central region of the detector volume. To quantify track centrality, an asymmetry parameter is defined as

$$\text{Area fraction left} = \frac{A_l}{A_r + A_l}, \tag{9.1}$$

where A_l and A_r represent the signal areas recorded by the left and right UV PMTs, respectively, as viewed from the perspective of the IR-sensitive detector. The event distribution for this parameter as a function of total UV signal area is presented in Figure 9.1. The distribution centers at a value slightly above 0.5, potentially indicating minor misalignment of the source holder or differences in PMT QEs. The width of the distribution reflects α-particle trajectories occurring at varying distances from each PMT. Most events cluster around a total UV area of approximately 10^4 PE. Events appearing at twice this value suggest pileup of two α-particle interactions. At lower energies, a tail of centrally distributed events is observed, likely from events experiencing energy loss within the ^{241}Am source or its holder. Below approximately 2000 PE, events exhibit a broad distribution across the area fraction left parameter, possibly arising from accompanying γ-rays depositing energy within the GXe volume.

Events within the central 40 % of the area fraction left distribution were selected. Additionally,

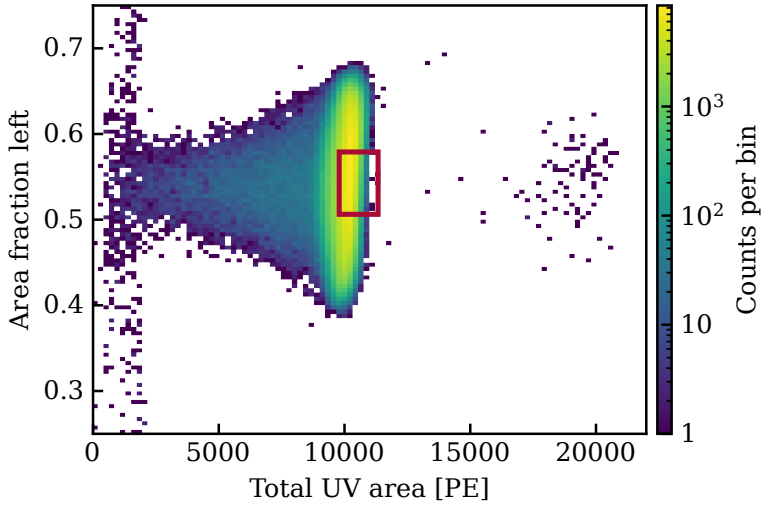

Figure 9.1.: Distribution of α-particle events as a function of the area fraction seen in the left PMT and total UV signal area. The rectangular selection region used for analysis is indicated in red. Reproduced from [Paper IV].

events were filtered based on their total UV area to exclude pileup events and low-energy interactions, resulting in the rectangular selection region shown in Figure 9.1.

9.1.3 Signal time response

The time response of the IR signal was reconstructed by calculating the time difference Δt between each identified IR photon in a waveform and the corresponding large UV signal. For both signals, the reference time was defined as the time of the sample immediately preceding the point where the signal reaches 10 % of its peak height. This procedure was repeated for 10^5 to 10^6 α-particle events, and the resulting relative arrival times were compiled into a histogram. This single-photon counting method, also utilized in [123, 124, 267, 301, 305] and other studies, offers the advantage of reduced susceptibility to signal distortions introduced by the electronics.

Effect of gas impurities

To investigate the impact of gas purity on the observed signals, signals were recorded with and without continuous purification. Initially, the freshly filled xenon gas ($P \simeq 1010$ mbar) was recirculated through the bypass of the gas purifier, starting at $t = 0$ min. Figure 9.2 shows the time evolution of signal sizes in both the IR (top panel) and UV (bottom panel) channels. For the IR-sensitive PMT, both a two-dimensional histogram of the number of observed photons within a 320 ns time window and the temporal evolution of the mean photon count (black solid line) are displayed.

During the initial unpurified phase, signal sizes in both IR and UV channels exhibited a gradual decline over time, likely due to continuous outgassing of impurities from materials within the detector setup. At $t = 185$ min (indicated by the dashed vertical line), purification was initiated by redirecting the gas flow from the bypass to the hot getter. Within minutes, both signal channels experienced dramatic enhancement, with the IR signal increasing by approximately a factor of 12 and the UV signal by a factor of 10, before reaching stable plateau values with

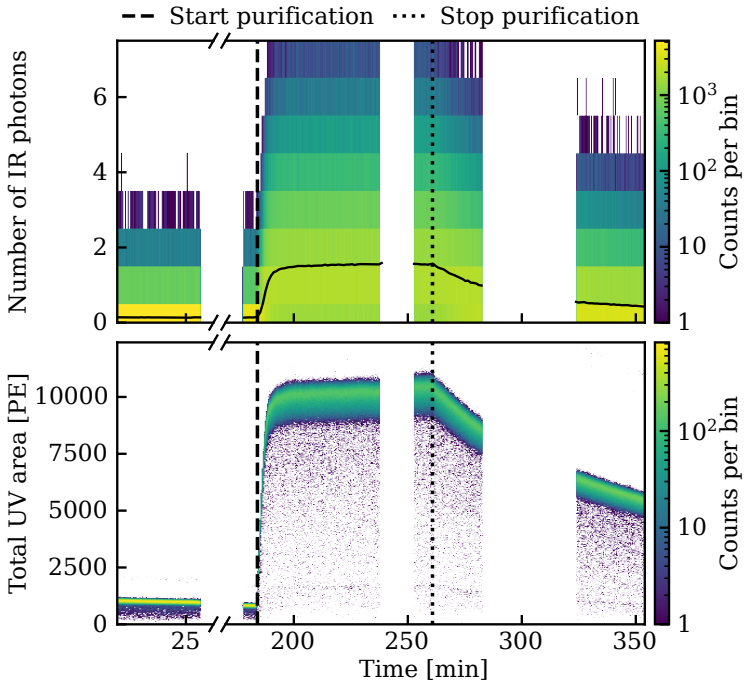

Figure 9.2.: Time evolution of signal sizes during the gas purity study. *Top:* Two-dimensional histogram showing the number of IR photons detected within a 320 ns time window, with the mean photon count overlaid (black solid line). *Bottom:* UV signal area over time. The dashed vertical line at $t = 185$ min indicates the start of purification, while the dotted line at $t = 260$ min marks its termination. Reproduced from [Paper IV].

a small remaining slope. At $t = 260$ min (dotted vertical line), the purification was stopped by returning the recirculation to bypass mode. Immediate signal degradation was observed in both wavelength regimes.

To further study how gas purity affects the IR and UV signals, time responses were analyzed for three distinct purity conditions: before purification ($t \in [0, 30]$ min), during stable purified operation ($t \in [193, 238]$ min), and after the purification was stopped ($t \in [324, 354]$ min). The results are presented in Figure 9.3. For the IR response (left panel), the photon counting method was employed, whereas for the UV signals (right panel), averaged waveforms from 500 events were used.

Under unpurified conditions, the IR signal is dominated by a fast component with a decay time of approximately 2 ns (red curve). During the purified phase, a pronounced slow component with a decay time of approximately 1 µs emerges (blue curve). After the purification is stopped, this slow component rapidly diminishes as impurities reaccumulate in the gas (purple curve), demonstrating the direct correlation between gas purity and the microsecond-scale IR emission. The observed shortening of the slow decay constant might be attributed to collisional quenching of the excited precursor states by impurities, analogous to the quenching mechanism observed for triplet state decays in argon [323]. Given that the amplitude of the fast component remains relatively unaffected by impurity levels, light absorption by impurities appears to play a subdominant role. The proposed transition for the dominant IR scintillation in xenon is expected to be followed by second continuum emission (see Section 8.1). However, this interpretation is challenged by the observation of a time constant that is slower than the well-established faster

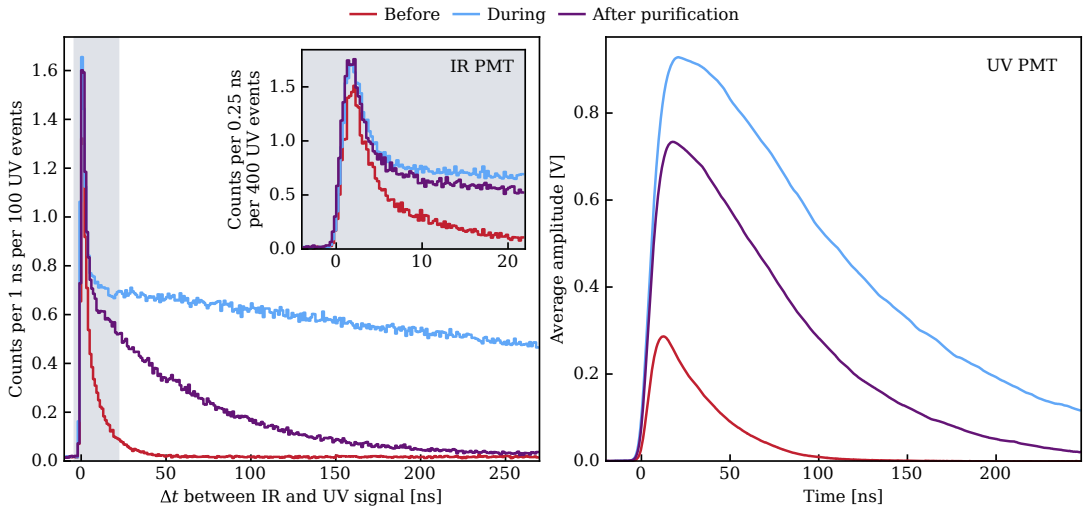

Figure 9.3.: Comparison of IR and UV time responses under different gas purity conditions. *Left:* IR time response obtained via photon counting for unpurified (red), purified (blue), and post-purification (purple) conditions. The inset shows a zoom to the first 20 ns of the signal. *Right:* Averaged UV waveforms from 500 events under the same three purity conditions. Reproduced from [Paper IV].

$\sim$ 100 ns time constant of the second continuum (see Section 8.1; also visible in Figure 9.2). Possible origins of this slow component are discussed in Section 9.3.

The UV signals exhibit significant amplitude reduction under impure gas conditions. Additionally, the temporal width of the UV signals decreases for higher levels of impurities, narrowing from approximately 110 ns full width at half maximum (FWHM) during purified operation (blue curve) to approximately 35 ns FWHM under unpurified conditions (red curve).

Given the strong dependence on gas purity observed in this study, all subsequent measurements were conducted at least 40 min after initiating recirculation through the gas purifier.

Characterization of the time response

Given the microsecond-scale time constant and substantial amplitude, the slow component dominates the total IR signal. Accurate quantification of this component requires extrapolation beyond the originally recorded time window, which requires knowledge of the functional form describing the signal tail. In [Paper IV], three different functional forms were tested: linear, exponential, and a model motivated by electron-ion recombination processes, proportional to $1/(1 + \Delta t/T_\mathrm{r})^2$ with the recombination time T_r motivated in [127]. While all three functions provided similarly good fits to the tail of the distribution, the extrapolated total integrals varied significantly between the models (resulting in corrections of $\times 2$ for linear, $\times 3.5$ for exponential, and $\times 6.5$ for extrapolation with the recombination model at 1 bar), constituting the dominant systematic uncertainty in the light yield measurement reported in that study.

Using the technique described previously, the effective recording window was extended to approximately 3 µs. The resulting time response for a pressure of (1077.0±1.0) mbar is presented in Figure 9.4. A constant baseline from PMT dark counts, estimated from pre-trigger samples, was subtracted. The relative peak detection efficiency at the reduced sampling rate of 1.6 GS/s (compared to 3.2 GS/s used earlier) was found to be (91.37 ± 0.25) %. This efficiency correction

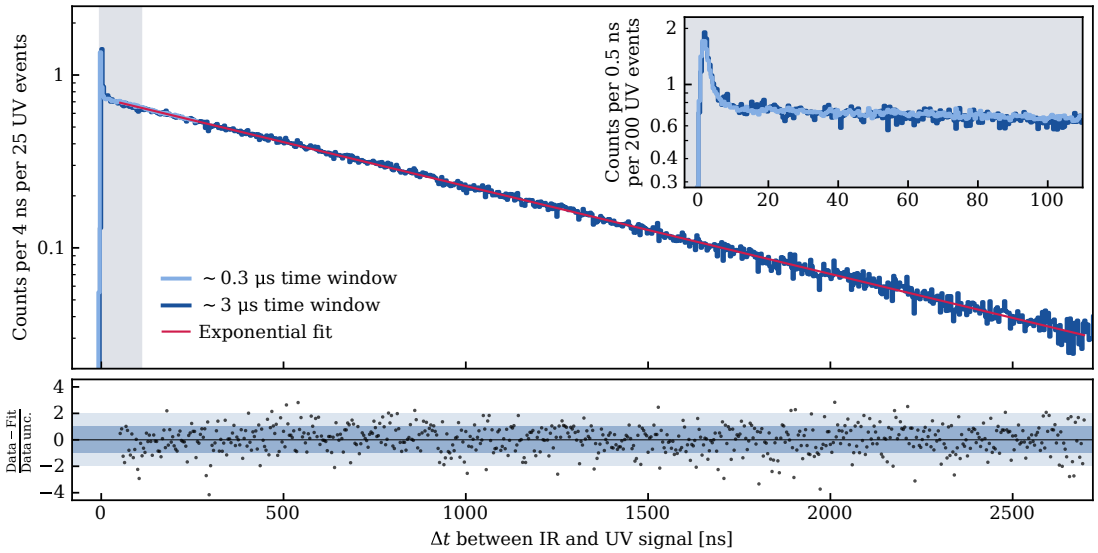

Figure 9.4.: Time response of IR scintillation in xenon gas at (1077.0 ± 1.0) mbar measured over an extended $\sim 3\,\mu s$ time window. *Top:* Photon arrival time histogram (blue) with exponential fit (red line). The inset shows a zoom to the first 110 ns of the signal. For reference, the result obtained in [Paper IV] with a time window of $\sim 0.3\,\mu s$ is overlaid in light blue. *Bottom:* Fit residuals showing good agreement with only isolated outliers. Reproduced from [Paper V].

was applied to the time response and was determined by comparing photon counts within the first 0.3 µs at approximately 740 mbar for both sampling rates. This reduction in efficiency is due to the decreased number of digitizer samples per IR photon pulse, from approximately 10 to 5.

To determine the functional form of the IR time response tail, least-squares fits were performed using the three models described previously over the time range from 50 ns to 2700 ns. Using Pearson's chi-squared test, it was assessed that only the exponential model provides an adequate description of the data, yielding $\chi^2/n_{\mathrm{dof}} = 726/660 = 1.1$, which corresponds to a p-value of 0.04. Although this p-value is slightly below the conventional 95 % confidence level (CL) threshold, the residuals displayed in the bottom panel of Figure 9.4 show no systematic deviations, with only a few isolated outliers below $-3\,\sigma$. The exponential fit yielded a decay time constant of $(854.0 \pm 1.8_{\,\mathrm{stat}}\,{}^{+26}_{-4\,\mathrm{syst}})$ ns, where the systematic uncertainty was estimated by varying the fit range boundaries. Based on the best-fit result for the tail and assuming the slow component follows an exponential distribution starting from $\Delta t = 0$, the fast component was estimated to contribute only 0.50 ± 0.19 % of the total signal.

Pressure dependence

To investigate the pressure dependence of the IR emission, the gas pressure was systematically varied between 500 and 1050 mbar [Paper IV]. The measurement was started at approximately 750 mbar, with the pressure increasing in three discrete steps to the maximum value. Subsequently, the same pressure points were revisited while decreasing the pressure to identify potential hysteresis or time-dependent effects. The only discernible difference between corresponding pressure datasets was observed for the initial measurement at 750 mbar, which started only 10 min after recirculation through the purifier began. Consequently, this dataset was excluded from the analysis to avoid contamination from residual impurities. The final pressure point at

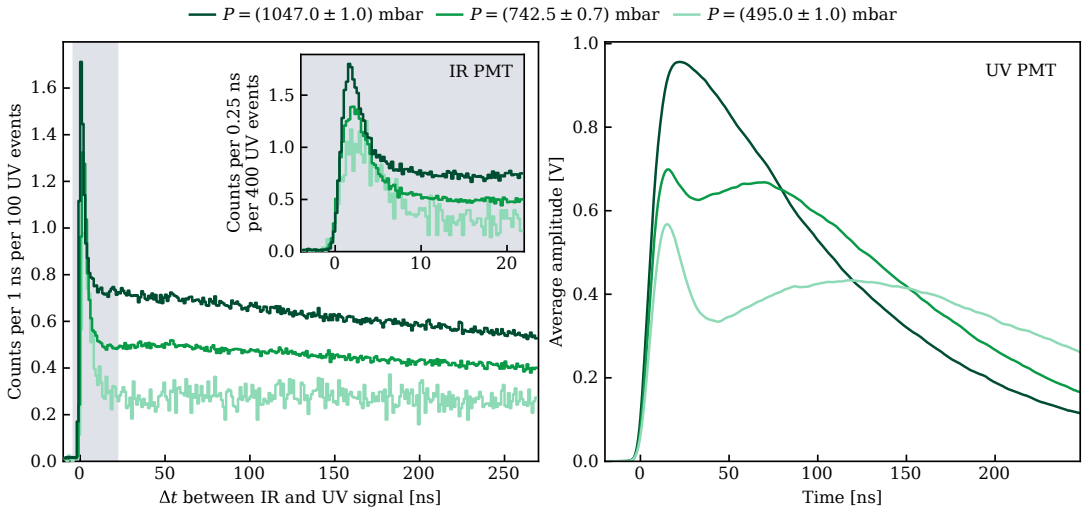

Figure 9.5.: Comparison of IR and UV time responses for different pressures. *Left:* IR time response obtained via photon counting for three characteristic pressures. The inset shows a zoom to the first 20 ns of the signal. *Right:* Averaged UV waveforms from 500 events for the same pressures. Reproduced from [Paper IV].

500 mbar yielded limited statistics, as one UV PMT experienced high-voltage breakdown after only 5 min of data acquisition, terminating the measurement campaign.

The IR time response exhibits clear pressure dependence, as shown in Figure 9.5 (left) for three representative pressure values. With decreasing pressure, two distinct phenomena emerge: the amplitude of the slow component diminishes, and its decay time constant increases. The pressure evolution of the decay constant is illustrated in Figure 9.6 (left). The data roughly follows a power-law trend; a precise characterization would require clarifying a small apparent offset between the results of the two campaigns and reducing the statistical uncertainties observed at low pressures. By extrapolating the slow component to $\Delta t = 0$, the relative contribution of the fast component to the total signal can be estimated, with results presented as a function of pressure in Figure 9.6 (right). Across all investigated pressures, the fast component fraction remains below 1 %, exhibiting a subtle trend toward decreased values at higher pressures. However, the precise form of the slow component should deviate from a purely exponential behavior at early arrival times, which would affect the estimation of the fast component. As shown in Figure 9.5 (right), the UV signal exhibits a distinctive double-peak structure at reduced pressures, consistent with third continuum emission (first peak) and second continuum emission (second peak) [267].[1]

Measurement at zero electric field

In all measurements presented so far, a small inhomogeneous electric field was present in the target volume (see Section 8.3). Although the reduced electric field in the experimental setup remained below the electroluminescence threshold of approximately 1 kV cm^{-1} bar [324], subthreshold emission via neutral bremsstrahlung could potentially contribute to the observed

[1] The reactions involved in precursor formation are pressure dependent; at ∼500 mbar, the time constant for second continuum precursor formation approaches the decay constant of ∼ 100 ns, while for third continuum emission, both time constants remain below 10 ns.

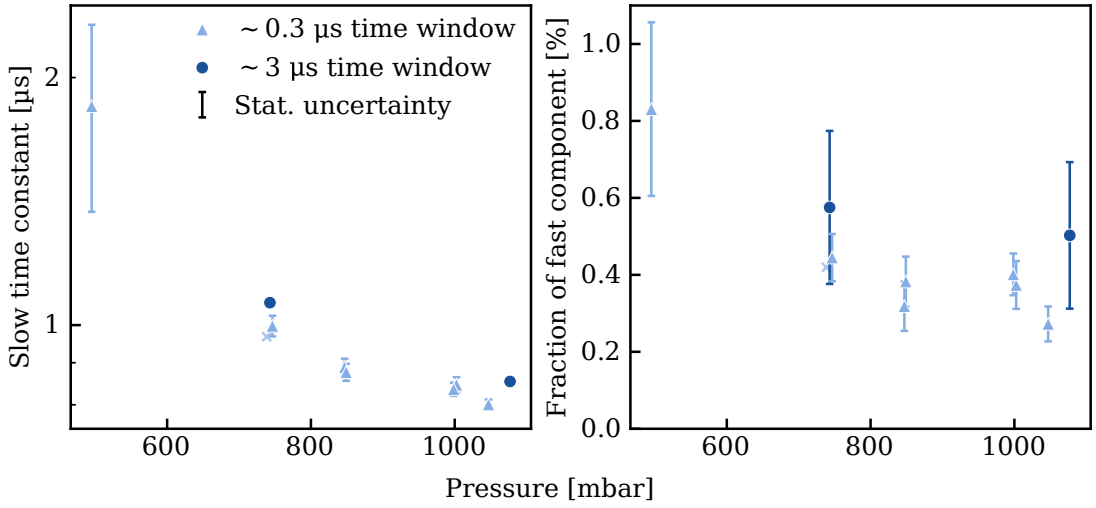

Figure 9.6.: Pressure dependence of IR emission characteristics. *Left:* Exponential decay constant of the IR signal tail as a function of pressure. *Right:* Fraction of the fast IR component relative to the total signal across different pressures. For visual clarity, only systematic uncertainties are shown.

signal [325]. In this process, the drifting electrons interact with the transient dipole moments they induce in neutral xenon atoms, rather than primarily with the Coulomb field of the nucleus. In contrast to ordinary electroluminescence, neutral bremsstrahlung does not exhibit an energy threshold and can occur even at very low electric fields. The emitted radiation spans a broad spectrum that extends into the IR wavelength range. Although neutral bremsstrahlung produces emission roughly two orders of magnitude weaker than electroluminescence at higher fields, it becomes the dominant source of light below approximately $650\,\mathrm{V\,cm^{-1}\,bar}$, where electroluminescence signals effectively vanish.

Another hypothesis proposed in [Paper IV] is that the microsecond-scale time constant is governed by recombination processes. To test both hypotheses, a dedicated measurement was conducted with zero electric field in the active detector region. This was accomplished by operating the UV PMT with the photocathodes at ground potential and the anodes at positive high voltage. Implementing this configuration required the addition of capacitors to the base electronics to decouple the high voltage supply from the low voltage signal. As a result, the rate of high voltage breakdowns increased, particularly affecting one of the two UV PMTs. Data acquisition was therefore limited to a single operational UV-sensitive channel, and the data quality selection criteria were adjusted accordingly.

The IR time response obtained under zero-field conditions at $(1057.0 \pm 1.0)\,\mathrm{mbar}$ is compared with the response measured in the original inhomogeneous field configuration in Figure 9.7. Both measurements exhibit consistent fast components, and the prominent slow component persists even in the absence of electric fields. While the slow component maintains similar amplitude, its decay constant of approximately 600 ns is faster compared to the previous configuration. As the setup was opened before the zero-field measurement to replace the base electronics, it cannot be excluded that the shorter observed decay time was caused by a slightly higher level of residual impurities in the gas.

Nevertheless, the persistence of a substantial slow component under zero-field conditions, without any increase in amplitude, allows us to rule out dominant contributions from drifting electrons or electron-ion recombination. The hypothesis of light emission associated with drift-

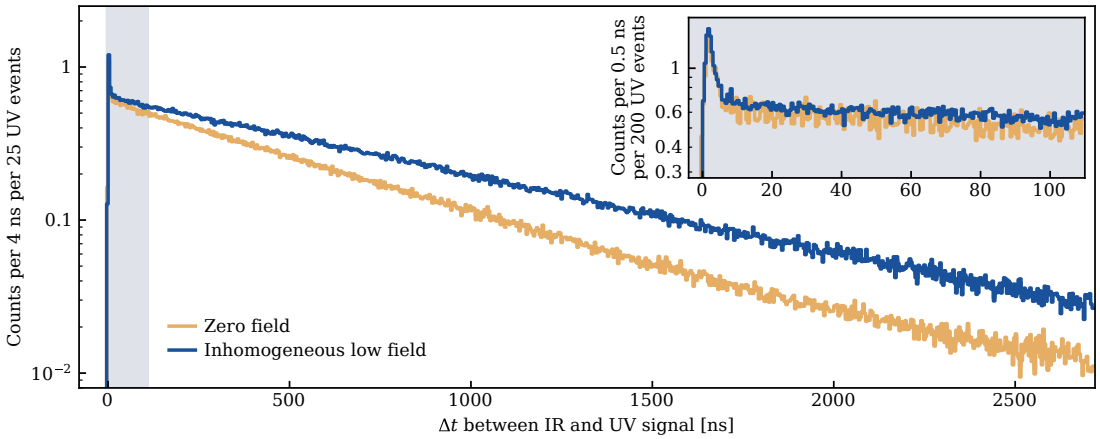

Figure 9.7.: Comparison of IR time responses under normal field conditions and zero electric field at approximately 1 bar. The inset magnifies the first 110 ns of the signals. Reproduced from [Paper V].

ing electrons can be excluded, since such contributions would vanish entirely in the absence of an electric field. This conclusion is further supported by kinematic considerations: the original electric field configuration should result in electron drift velocities below $2\,\mathrm{mm\,\mu s^{-1}}$ [326], which would in turn result in drift times exceeding 15 µs. This is approximately an order of magnitude longer than the observed time constant. Contributions from electron-ion recombination were already considered implausible, as the corresponding model failed to adequately describe the tail of the IR time response, as discussed above. Moreover, zero-field conditions should enhance the amplitude of the slow component due to increased recombination fractions, which is contrary to the experimental observations. A comprehensive discussion of alternative explanations for the IR time response is presented in Section 9.3.

9.1.4 Light yield measurement

A critical parameter for evaluating the practical utility of IR scintillation light in detector applications is the light yield LY_{IR}, defined as the number of photons emitted per unit deposited energy:

$$LY_{\mathrm{IR}} = \frac{\mu_{\mathrm{em}}}{E_\alpha} = \frac{\mu_{\mathrm{det}}}{E_\alpha\,\epsilon_{\mathrm{lce}}\,\epsilon_{\mathrm{tw}}\,\mathrm{QE}}, \tag{9.2}$$

where μ_{em} and μ_{det} represent the mean number of emitted and detected photons per α-particle event, respectively; E_α is the energy deposited in the active detector region; ϵ_{lce} is the PMT's LCE; and ϵ_{tw} is the fraction of the total signal within the acquired time window.

The mean number of detected photons was obtained by integrating the IR time response over the extended time window, accounting for temporal overlap between digitizer channels. The fraction of the signal outside the time window was estimated by extrapolating the exponential tail using the best-fit parameters, yielding ϵ_{tw}. The IR-sensitive PMT's QE of $(9.0 \pm 0.5)\,\%$ was taken from manufacturer specifications. Pressure-dependent parameters, including the LCE (0.22 % at 1 bar) for centrally located α-particle tracks and the fraction of α-particle energy deposited within the active region behind the aperture (92 % at 1 bar), were determined through simplified Monte Carlo (MC) simulations detailed in Section 8.3.

The measured IR light yield at $(1077.0 \pm 1.0)\,\mathrm{mbar}$ and room temperature is $LY_{\mathrm{IR}} = (6347 \pm 22_{\,\mathrm{stat}} \pm 400_{\,\mathrm{syst}})\,\mathrm{ph/MeV}$. The systematic uncertainty of approximately 6 % includes contribu-

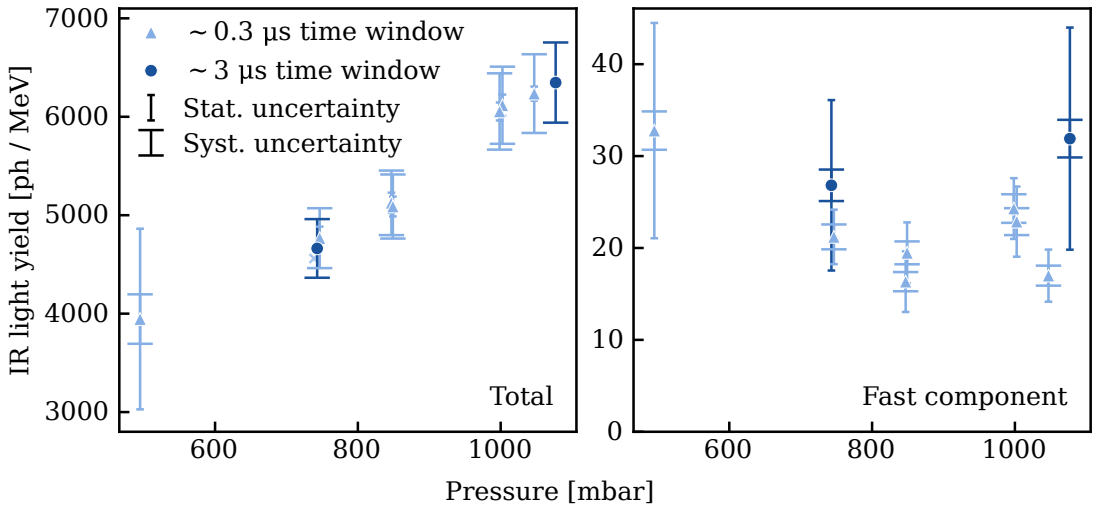

Figure 9.8.: Pressure dependence of the IR light yield in xenon gas at room temperature. *Left:* Total IR light yield. The measurement shows a linear relationship with pressure, yielding a slope of approximately 4 ph/MeV/mbar. The measurements with a long time window from [Paper V] shown in dark blue follow the same trend as the measurements previously measured with short time windows [Paper IV] shown in light blue. Note that error bars indicating the statistical uncertainty are not visible for the dark blue data points as they are smaller than the markers. *Right:* Light yield of the fast component.

tions from the deposited energy E_α, the LCE ϵ_{lce}, and the QE, with the latter providing the dominant contribution. This measured value corresponds to approximately one-third of the lower limit of 21 000 ph/MeV reported in [293] measured at 2 bar. Relative to the UV light yield of approximately 25 000 ph/MeV [284, 294], the IR emission is approximately four times lower. The pressure dependence of the IR light yield is illustrated in Figure 9.8 (left), revealing an approximately linear relationship with a slope of 4 ph/MeV/mbar. Extrapolating this trend to the 2 bar pressure used in [293] reduces the discrepancy to approximately a factor of two, suggesting that pressure-dependent effects could partially account for the observed differences between studies. The estimated light yield of the fast component as a function of pressure is presented in Figure 9.8 (right), and does not exhibit a strong pressure dependence.

9.2 Measurements in a Dual-Phase TPC

Data with an internal α-particle calibration source was acquired using the Heidelberg Xenon (HeXe) setup described in Section 8.4, which was modified to extend sensitivity across a broad wavelength range, from 170 nm to 1700 nm. This marks the first demonstration of such wide spectral sensitivity in a xenon time projection chamber (TPC), as reported in [Paper VI].

9.2.1 Data acquisition and signal processing

As in the measurements presented in Section 9.1, the combination of low QE and LCE (see Section 8.4.1) resulted in the measurement of individual photons in the IR-sensitive PMT, even for α-particle events, for which $\mathcal{O}(10^5)$ photons were detected in the UV channel. Events were triggered based on the UV signal, and all waveforms were recorded with a CAEN V1724 digitizer. The device features 14-bit resolution and a sampling rate of 100 MS/s, which is approximately

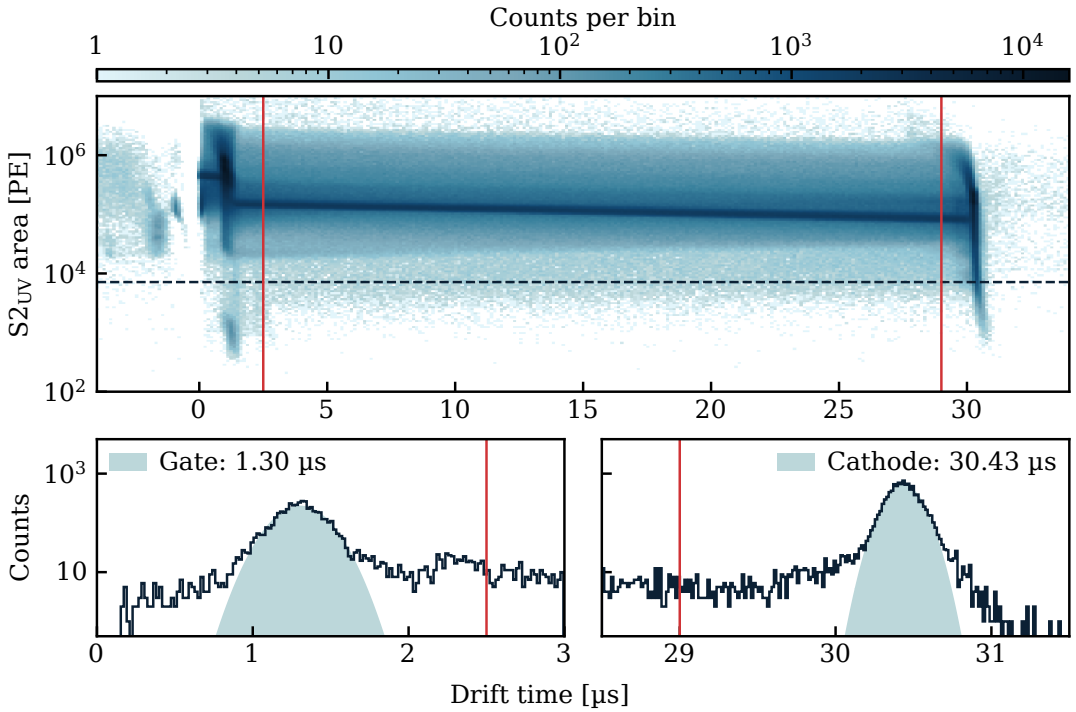

Figure 9.9.: Definition of the fiducial volume and determination of gate and cathode positions. The top panel shows events after minimal selection criteria in $S2_{UV}$ as a function of drift time. Small $S2_{UV}$ signals with areas below the dashed line are used to estimate the drift times for electrons from the gate and cathode electrodes. The corresponding histograms are presented in the bottom panels. Drift times between the two red vertical lines indicate the selected fiducial volume.

30 times slower compared to the digitizer used in Section 9.1. Given that individual IR photon signals have rise and fall times on the nanosecond scale, the IR signals were shaped using a timing filter amplifier prior to digitization.

Peaks were identified and key characteristics extracted using the `walpurgisnacht` framework, as in Section 9.1. In addition, peaks in the UV channel were classified into S1-like and S2-like signals based on their pulse shapes. For clarity, these are referred to as $S1_{UV}$ and $S2_{UV}$ in the following.

9.2.2 Data selection

For IR signals, only a minimal peak height threshold was applied to suppress electronic noise. Well-reconstructed α-particle events were selected based on their signals in the UV channel. Events in the liquid xenon (LXe) target region between gate and cathode were selected based on their drift time. The positions of the electrodes in drift time space were determined by identifying events with small $S2_{UV}$ area, attributed to photoemission from the electrodes following a bright $S1_{UV}$ signal. As illustrated in Figure 9.9, the gate and cathode were located at drift times of approximately 1.3 µs and 30.4 µs, respectively and events with drift times between 2.5 µs and 29 µs were selected.

Events with a single α-particle interaction were selected by requiring exactly one $S1_{UV}$ signal. Even for single-α events, a second $S2_{UV}$ signal was often reconstructed. Approximately 1.3 µs after the primary $S2_{UV}$ signal, a secondary signal – likely caused by photoionization of the gate

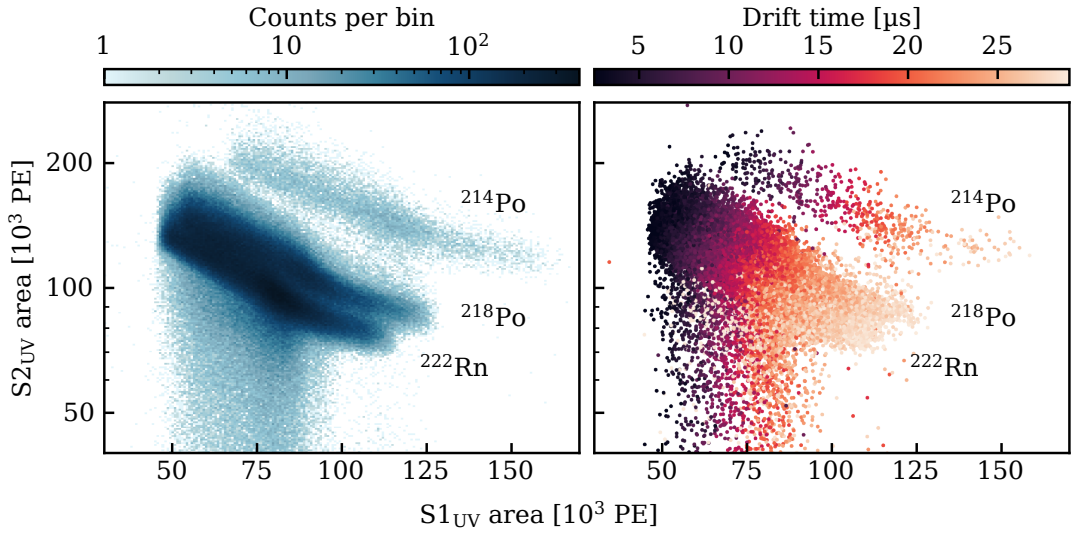

Figure 9.10.: Distribution of α-particle events in $S2_{UV}$ area versus $S1_{UV}$ area after all selection criteria. Both panels display the same dataset: the left panel presents a histogram, while the right panel shows a downsampled scatter plot with color indicating the corresponding drift time. Adapted from [Paper VI].

electrode – was observed and occasionally classified as an individual $S2_{UV}$ signal. Additionally, signals consistent with delayed electrons arriving at random times after the main $S2_{UV}$ signal were observed. Events exhibiting a second $S2_{UV}$ signal delayed by more than 2.3 µs after the primary signal were excluded to suppress any potential impact on the measured IR time response. Furthermore, $S2_{UV}$ signals with strongly asymmetric pulse shapes – indicative of merged pulses – were rejected based on the ratio of different width estimators. Muon events were effectively rejected by requiring $S2_{UV}$ signals with widths below 3.5 µs.

Finally, events were selected in $S1_{UV}$-$S2_{UV}$ space, as illustrated in Figure 9.10. Three populations with $S1_{UV}$ and $S2_{UV}$ areas of approximately 10^5 PE corresponding to α-decays of ^{222}Rn, ^{218}Po, and ^{214}Po, can be identified. Events originating from the top of the TPC exhibit larger $S2_{UV}$ areas compared to those from the bottom, due to electrons lost along the drift path, while the $S1_{UV}$ area increases toward the bottom of the TPC as a result of higher LCE.

9.2.3 Signal time response

The time structure of the IR signal following the $S1_{UV}$ and $S2_{UV}$ signals was investigated. For each IR pulse, the time differences with respect to the event's $S1_{UV}$ and $S2_{UV}$ signals were computed. Here, the pulse time of $S1_{UV}$ and IR signals was defined as the first sample preceding 10 % of the peak height, while for $S2_{UV}$ signals the time of the maximum pulse height was used.

Figure 9.11 displays the drift time of events with IR peaks as a function of the IR arrival time relative to the $S1_{UV}$ signal. A narrow vertical band aligned with the $S1_{UV}$ timing is visible, extending uniformly across the drift time. This observation is consistent with a uniformly distributed source and the weak depth dependence of the IR PMT's LCE (see Figure 8.8). In addition, a diagonal structure is observed, corresponding to IR peaks that occur in coincidence with, and subsequent to, the $S2_{UV}$ signals. The timing of the $S2_{UV}$ signal is indicated by a dashed red line in Figure 9.11. This pattern suggests that IR light is emitted during both the prompt scintillation and the delayed electroluminescence processes.

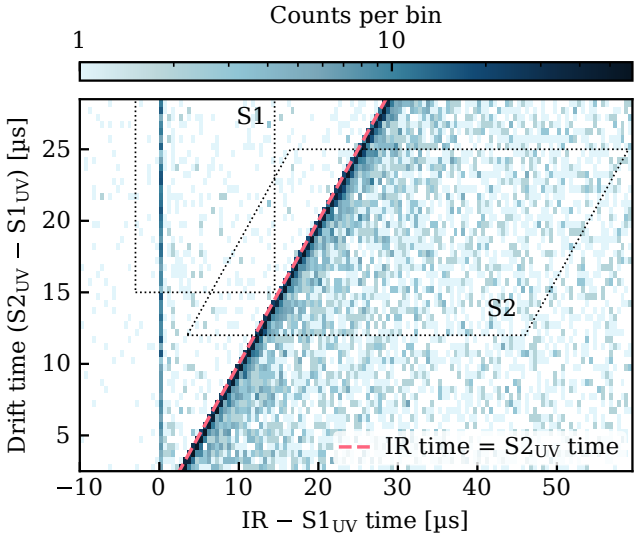

Figure 9.11.: Distribution of IR photon signals. The drift time of events with IR signals is shown as a function of their arrival time relative to the event's $S1_{UV}$ signal. The dashed red line indicates the time of the $S2_{UV}$ signal. Dotted regions show selections used to study the time structure of the IR emission following the $S1_{UV}$ and $S2_{UV}$ signals, as shown in Figure 9.12. Reproduced from [Paper VI].

To study the IR time response associated with the $S1_{UV}$ and $S2_{UV}$ signals, clean subsets of pulses were selected based on drift time and IR arrival time, as indicated by the dotted boxes in Figure 9.11. The selections were chosen to minimize overlap between them. Figure 9.12 shows the IR photon arrival time relative to the $S1_{UV}$ (left) and $S2_{UV}$ (right). Unbinned maximum likelihood fits were performed to extract the respective time responses.

The IR time response following $S1_{UV}$ signals consists of two main components. The first is a fast component modeled as an exponential decay with a time constant of $(28^{+2}_{-1.9})$ ns, convolved with a Gaussian of approximately 5 ns width to account for the timing resolution of the digitizer. This component contributes roughly half of the total IR signal following the $S1_{UV}$. The time constant is similar to the 26 ns component observed in UV light, which accounts for approximately 65 % of the signal [124]. The remaining half of the IR signal can be described by a slower exponential decay. Fitting the distribution tail, while accounting for a flat background from PMT dark counts, yields a time constant of (20^{+30}_{-6}) µs. Due to limited statistics, the time constant and underlying functional form cannot be determined with high precision.

The IR time response relative to the $S2_{UV}$ signals is modeled as the sum of three exponential components, each convolved with a Gaussian of ∼0.2 µs width to account for the spread in electron arrival times. In addition to the signal components, the model incorporates a flat background from PMT dark counts and an exponential background from the preceding S1 signal. Due to time smearing, the decay of the fastest component cannot be resolved and is therefore approximated by a Gaussian (i.e. $\tau_0 \to 0$). The second-fastest component has a time constant of $\tau_1 = (1.7 \pm 0.3)$ µs, similar to the slow component observed for α-particles in GXe (see Section 9.1). However, while the microsecond-scale component accounts for more than 99 % of the signal in gas, it contributes only about 13 % here. The third component, with a time constant of $\tau_2 = (31^{+5}_{-4})$ µs, dominates the signal, contributing more than half of the total. Such a slow component has not been previously reported in xenon. Interestingly, the

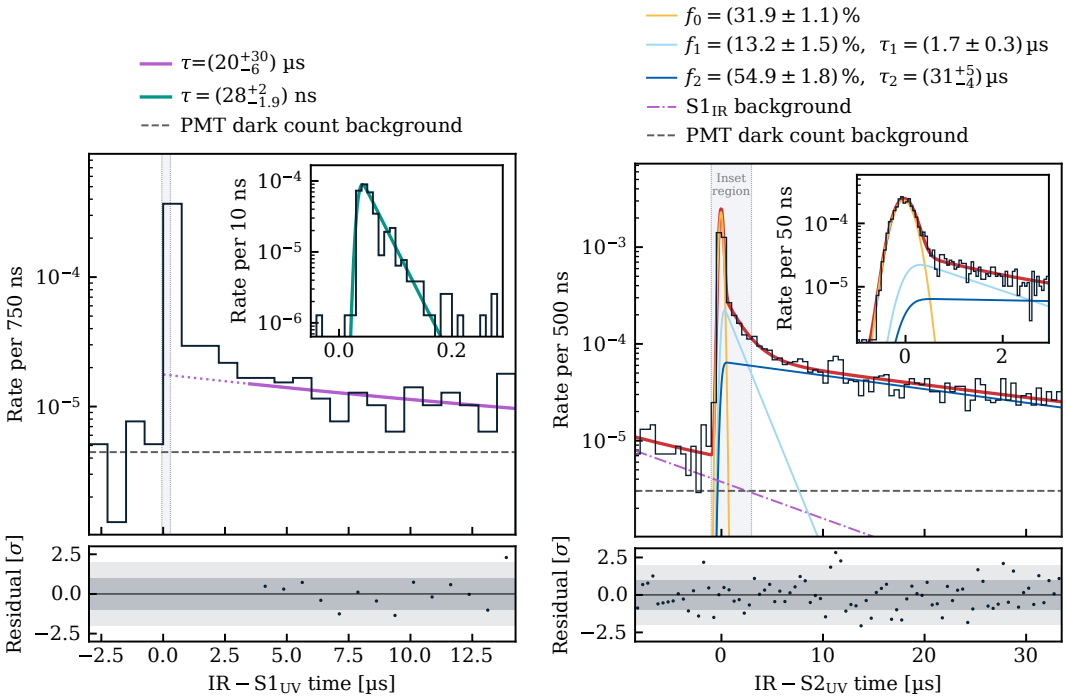

Figure 9.12.: Time response of IR signals relative to the $S1_{UV}$ (left) and $S2_{UV}$ (right) for a drift field of 400 V/cm and an amplification field of approximately 12 kV/cm. The insets magnify the regions indicated by the gray vertical bands. The best-fit results and individual components are overlaid. All fits were performed using unbinned likelihoods; the binning and residuals are for visual reference. Reproduced from [Paper VI].

slowest time constants observed following both the $S1_{UV}$ and $S2_{UV}$ signals are consistent within uncertainties, suggesting a potential common origin.

Electroluminescence signals observed in the UV and IR channels are compared in Figure 9.13. The plot overlays the average of 500 $S2_{UV}$ waveforms (black curve) with the background-subtracted best-fit IR model from Figure 9.12 (right). In both channels, the main feature is well-described by a Gaussian with a width of 0.2 µs. The $S2_{UV}$ signal exhibits a tail towards late time differences, likely arising from PMT afterpulses and delayed electrons due to incomplete extraction or photoionization of impurities in the liquid (see Section 4.4.3 for a detailed discussion of delayed UV signals). As noted in Section 9.2.2, a secondary peak is visible in the UV signal approximately 1.3 µs after the main pulse, with an amplitude roughly two orders of magnitude lower. This feature is consistent with photoemission of electrons from the gate electrode via $S2_{UV}$ light (see Appendix B). In contrast, the IR signal exhibits a much more pronounced tail – about an order of magnitude stronger than in the UV channel – and does not display a distinct photoemission peak. It is possible that this peak is masked by the dominant slow component in the IR response. Overall, the strong difference between the channels indicates that known delayed signals cannot fully account for the slow IR component.

9.3 Summary and Interpretation of the Measurements

The studies presented here independently confirm the emission of IR scintillation in xenon and extend limited earlier results with the first measurement of the emission's time response.

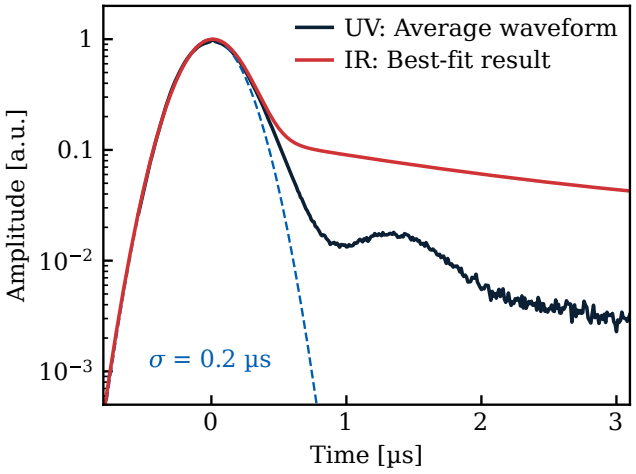

Figure 9.13.: Comparison of UV (black) and IR (red) electroluminescence time responses. The UV data show the average of 500 S2 waveforms, while the IR curve presents the background-subtracted best-fit model relative to the $S2_{UV}$ time from Figure 9.12 (right). A Gaussian with a width of 0.2 µs (dashed blue) is included for reference. Reproduced from [Paper VI].

Knowledge of the temporal response is crucial for detector applications and provides valuable constraints on potential de-excitation processes. This work thus represents an important step toward assessing the potential of IR scintillation for future xenon-based detectors. The IR scintillation response was investigated under two distinct experimental conditions. In room-temperature GXe, systematic pressure-dependent studies (500–1100 mbar) of light yield and time response were conducted using an α-particle calibration source. In a dual-phase TPC, signals were detected across a broad wavelength range consistent with primary scintillation in LXe and electroluminescence in GXe within the IR region, with subsequent analysis of their temporal characteristics.

9.3.1 Interpretation of the measurements in room-temperature gas

The measurements obtained from the room-temperature gas setup irradiated with α-particles can be summarized as follows:

- The time response exhibits two distinct components:
  - *Fast component:* ~2 ns decay time, contributing <1 % of the total signal.
  - *Slow component:* $\mathcal{O}$(µs) exponential decay, contributing >99 % of the total signal.
- Increased impurity levels significantly suppress the slow component.
- Higher pressure leads to a shorter slow decay constant with increased amplitude, which combined results in a slight linear increase of the light yield, while the fast component remains largely unaffected.
- The total light yield at approximately 1 bar is $LY_{IR} \simeq 6000$ ph/MeV.

This measurement was performed using a PMT with wavelength sensitivity centered around the expected dominant IR continuum emission (Figure 8.2). The observed light yield matches the order of magnitude of previous estimates [293]. We therefore attribute both temporal components to IR scintillation processes in GXe. Two alternative origins for the dominant slow

component have been evaluated and found to be subdominant: Contributions from light emission induced by drifting electrons via neutral bremsstrahlung were excluded via the zero-field measurement as well as kinematic considerations. Material fluorescence induced by intense UV scintillation cannot be entirely excluded, though such contributions would be expected to show neither pressure dependence nor sensitivity to gas purity variations. Similarly, gaseous contaminants are unlikely candidates, as any contributing species would need to exhibit exceptional scintillation yield while evading removal by the hot zirconium getter. Moreover, if the slow component was dominated by emission from another material, tension with previous yield measurements would increase to two orders of magnitude. Definitive confirmation, however, will require spectral resolution of the detected signals, which will be achievable with future instrumentation described in Section 9.4.

We gained insight into the origins of the fast and slow components by examining their qualitative dependencies on gas purity and pressure. In [297], the authors have reported that at high gas purity, continuum emission was much stronger than atomic line emission, whereas at low purity, atomic lines dominated. Drawing a parallel to our observations, we find that at high purity, the slow component dominates the IR signal and exhibits a strong purity dependence. This behavior suggests that the slow component may originate from continuum emission. Conversely, the fast component shows little dependence on purity, making its relative contribution larger at low purity; thus, it could be attributed to atomic transitions.

The observed time structure allows us to exclude the possibility that the slow IR decay is followed by UV emission; thus, it cannot efficiently populate the precursor state of the second UV continuum. If this were the case, the same slow time constant should also appear in the UV time response, which is not observed (see Section 8.1.2). The currently proposed transition responsible for the IR continuum, $(3)0_u^+ \rightarrow (1)0_g^+$, would, however, result in the subsequent formation of the second continuum precursor states. Consequently, the slow IR component is either unrelated to continuum emission – despite being the dominant IR feature and showing strong purity dependence – or another transition is responsible for the IR continuum. Such a transition would require a de-excitation pathway that bypasses the lowest-lying excimer states, potentially through collisional de-excitation of the IR transition products. In this scenario, each excited xenon atom may decay through either UV emission or the slow IR component. If these decay channels were mutually exclusive, it might be possible to exploit the anti-correlation between the UV and IR signals in order to enhance a detector's energy resolution.

A pressure dependence of the time profiles, as observed for the slow IR component, is not surprising since many reactions involved in the formation of radiative precursor states depend on gas density. Similar effects have been reported for the UV continua (e.g., [266, 267]). The pressure dependence suggests that the slow decay time might be related to the precursor formation process rather than its radiative decay. Comparison of time responses with and without an applied electric field showed that electron-ion recombination does not account for the observed slow process, implying that another slow mechanism may be involved in forming the precursor state of the slow IR emission. Alternatively, the observed pressure dependence may be an indirect consequence of changes in gas purity with pressure. In this setup, there was no means of quantifying the concentration of impurities directly. The observed relatively fast deterioration of the IR signal after stopping the purification (see Figure 9.2) as well as the difference in observed decay constant in the zero-field measurement (see 9.7) suggest a relatively high outgassing rate. If confirmed, this would imply that the true IR decay time constant may

be longer than observed, resulting in an underestimation of both the decay time and the light yield.

The measured IR light yield of approximately 6000 ph/MeV at 1 bar represents about one-third of the previously reported value. This discrepancy may arise from differences in detector configurations, wavelength sensitivities, and operating pressures between the studies. Additionally, impurity effects and unaccounted systematic uncertainties in either measurement could contribute to the observed difference. Nevertheless, even at 6000 ph/MeV, the IR light yield is substantial and offers potential for applications in particle detectors.

9.3.2 Interpretation of the measurements in a dual-phase TPC

The dual-phase TPC measurements with α-particle irradiation reveal several key features:

- Non-UV signals occur in coincidence with both prompt UV scintillation in LXe and electroluminescence in GXe.
- The prompt signal comprises at least two components:
  - *Fast component:* ~30 ns, contributing ~50 % of the total signal.
  - *Very slow component:* ~20 µs, contributing ~50 % of the total signal.
- The electroluminescence signal for an electric field in the gas of ~12 kV/cm consists of three components:
  - *Fast component:* <200 ns, contributing ~30 % of the total signal.
  - *Slow component:* ~2 µs exponential decay, contributing ~15 % of the total signal.
  - *Very slow component:* ~30 µs exponential decay, contributing ~55 % of the total signal.

The observed signals could originate fully or partly from IR scintillation in liquid and gaseous xenon. However, given the broad wavelength sensitivity of the IR PMT into the near-UV range (see Figure 8.2), several other effects need to be considered.

Several xenon-intrinsic processes could potentially contribute to the observed fast components. The third continuum emission, with a decay constant of approximately 8 ns [267], peaks at ~270 nm (see Figure 8.2). Although the IR PMT is not sensitive at this wavelength, the detector could still register part of the spectral tail. However, as discussed in Section 8.1, third continuum emission contributes at the sub-percent level relative to $S2_{UV}$ signals during electroluminescence, if at all. Due to the low relative QE at these wavelengths and the PMT's sensitivity being limited to the spectrum's tail, this contribution is likely subdominant. Another potential mechanism with broad-spectrum emission extending into the IR range involves neutral bremsstrahlung radiation from drifting electrons (see Section 9.1.3), which can even occur below the electroluminescence threshold [325]. Neither third continuum emission nor neutral bremsstrahlung has been reported in LXe so far.

The presence of a very slow component with a time constant of approximately 30 µs, observed in signals associated with both $S1_{UV}$ and $S2_{UV}$, and contributing roughly half of the total signal in both cases, suggests a common underlying mechanism. No such slow component has been reported so far in xenon, and this is the first time the time response was measured in this wavelength range in xenon. In the room-temperature measurements presented here, no such

slow component has been observed, although the measurement window in that configuration extended only to 3 µs, potentially missing similar contributions at lower amplitudes.

Several studies of IR scintillation in argon provide useful points of comparison (see Section 8.1.3). In signals from prompt scintillation in liquid argon and electroluminescence in gaseous argon, a fast component with decay time <500 ns and an unexplained slow component with 20–30 µs has been observed, both contributing approximately equally [301, 302]. While no explanation currently exists for the slow component, it might be attributed to a slow scintillation process that could similarly also be present in xenon. Furthermore, [305] reports the scintillation response of liquid argon containing 10 ppm xenon, exhibiting IR scintillation light from xenon. The dominant continuum emission in this case exhibited exponential decay with ∼175 ns, but atomic lines showed decay constants of ∼10 µs, similar to the very slow component observed here. The very low concentration of xenon results in kinematics that differ considerably from those in pure LXe, limiting the extent to which our results can be directly compared.

While it is possible that this very slow component arises from xenon scintillation, alternative origins must be considered. Delayed electron and photon signals are frequently reported in LXe with possible origins summarized in Section 4.4. Photoionization of impurities dissolved in the liquid following bright UV flashes can generate delayed electrons. This effect is particularly relevant for this measurement, given the moderate purity conditions. However, any delayed electron signal, regardless of the origin, would also generate signals in the UV channel and thus can only account for a small fraction of the tail. Material fluorescence from polytetrafluoroethylene (PTFE), residues attached to it, as well as quartz window materials used in the UV PMT represents another potential source of delayed IR photons. Depending on the fluorescence spectrum, the delayed signal can be very different in the UV and IR PMT. Finally, instrumental artifacts cannot be ruled out entirely, particularly given the suboptimal bias voltage applied to the IR PMT photocathode, which could result in delayed PE extraction from the photocathode material.

Due to the unknown QE of the IR PMT in this measurement, it is not possible to quantify the absolute IR light yield. Additionally, several contributions unrelated to IR scintillation may influence the observed signal and require further investigation. Nevertheless, the results can be interpreted under the assumption that the detected signal originates predominantly from IR scintillation. Following the same arguments made for the slow component observed in the room-temperature setup, components with decay times slower than ∼100 ns cannot be followed by UV emission, as the observed UV time constants are faster. This implies that an alternative de-excitation pathway, which bypasses the lowest-lying excimer states, would need to be present. The data support previous observations of IR signals from xenon electroluminescence [293], and the increase in signal with amplification field, also reported in [Paper VI], further reinforces this interpretation. If confirmed, this would indicate that the precursor for IR scintillation originates from relatively low-lying excited states. Under the applied amplification field, electrons reach mean energies of approximately 5 eV before colliding with xenon gas [304]. With maximum energies remaining just below xenon's first ionization energy of 12.1 eV, this excludes dominant contributions from potential precursor states associated with xenon ions (see Figure 8.1). Furthermore, the time response of electrons in gas can be compared to the prompt scintillation light produced by α-particles in the room-temperature setup. Both exhibit fast (sub-100-ns) and slow (microsecond-scale) components in their time profiles. However, the relative signal fractions differ significantly: while α-particle measurements show fast-to-slow ra-

tios below 1:100, electroluminescence exhibits a fast component that is approximately 2.4 times larger than the microsecond component. This discrepancy could be explained by differences in the populations of excited states resulting from different energies and ionization densities. If verified under more directly comparable conditions, this amplitude variation could potentially enable particle-type discrimination based on IR pulse shape analysis.

9.4 Possible Applications and Outlook

The measurements presented in this work mark a first step toward exploring the use of IR scintillation light to enhance future xenon-based detectors for rare event searches. These studies include the first time-resolved characterization of the IR scintillation time response in GXe, as well as the first successful demonstration of a dual-phase xenon TPC with broad wavelength sensitivity ranging from 170 to 1700 nm. While these results are promising, practical implementation of broad-spectrum sensitivity requires addressing several open questions, for which further measurements are already underway.

Applications of IR scintillation

The primary motivation for investigating IR scintillation in xenon lies in its potential use in next-generation dark matter observatories such as XLZD, described in Section 3.4. Possible applications depend critically on the IR light yield in LXe and the extent of particle-type discrimination capabilities. If the IR light yield in LXe is sufficiently high and exhibits particle-type dependence – whether in time response or absolute yield – the primary IR scintillation signal can significantly enhance signal-background discrimination. Conversely, even if the liquid-phase yield is low, IR detection can still provide valuable discrimination between small S1 signals and single- or few-electron S2 signals. The latter would remain visible in the IR channel given the substantial light yield observed for α-particles in GXe and the confirmed observation of IR emission associated with electroluminescence.

Suitable IR photosensors could be placed in free spaces between UV-sensitive PMTs or integrated along the TPC wall. Unlike UV light, IR signals can be transmitted efficiently through waveguides and optical fibers, making it possible to position the sensors remotely and thus significantly relaxing radiopurity requirements. This approach may even allow the sensors to be installed in dedicated, externally accessible compartments, so that maintenance and replacement can be carried out without needing to open the TPC itself.

High-pressure GXe detectors for neutrinoless double-beta decay searches [327, 328] could also benefit from employing sensitivity to IR scintillation light. The substantial IR light yield in GXe suggests that detecting this additional wavelength band could eventually enhance energy resolution, which is a critical parameter for sensitivity [112, 329]. Furthermore, if a particle-type dependence in the fast and slow IR components is confirmed, pulse shape analysis can offer a new method for background discrimination.

The photosensor technology employed in this study, while well-suited for precision measurements of the time response, is not suitable for large-scale detector applications. The combination of low QE, high cost, and significant radioactivity (see [Paper VI]) renders these devices impractical for detector integration. IR-sensitive avalanche photodiodes (APDs) could offer superior characteristics for practical applications [330, 331].

Next dual-phase measurements

Several follow-up measurements in the dual-phase TPC are planned to address key systematic uncertainties and build on the current results. The highest priority is to repeat the measurements using the nominal PMT bias voltage, in order to determine whether instrumental artifacts may have contributed to the observed very slow components. At the same time, this will allow for precise measurement of both the IR light yield in LXe and the IR electroluminescence yield in the gas phase. Xenon purity is another important source of systematic uncertainty, with impurities possibly related to part of the observed delayed signal. Extended purification campaigns are planned to achieve and maintain high purity levels throughout future experiments.

Advanced characterization of time responses can be achieved through dedicated measurements that separate prompt and delayed signal components. Measurements in zero-field configurations will allow for a detailed investigation of primary IR scintillation signals. The fast component can be studied in greater detail in the future by using the fast digitizer employed in the room-temperature measurements. Additional gas-only measurements will allow for a clear characterization of the electroluminescence signal and enable the study of its dependence on the electric field. These measurements will provide the IR electroluminescence yield, which is a relevant quantity for detector applications. Moreover, determining the electric field strength at which IR electroluminescence begins will offer valuable insight into the energy required to form the precursor state. Operating the HeXe setup in gas-only mode also offers opportunities for systematic verification of the results obtained in the room-temperature setup.

Finally, although studying the full wavelength range is valuable, it makes it more difficult to attribute observed temporal components to specific physical processes. To address this, sensitivity could be limited to wavelengths above 1 µm using appropriate filters. Alternatively, for a more comprehensive approach, light could be routed via optical fibers outside the TPC, allowing for simultaneous multi-band measurements.

Advanced room-temperature gas setup

To address the key questions raised by the GXe measurements, an improved room-temperature setup has been developed, shown schematically in Figure 9.14. The setup features a stainless steel CF-100 cube equipped with three MgF_2 windows, which are transparent to wavelengths from approximately 120 nm to 6 µm and capable of withstanding differential pressure up to 2.6 bar. This pressure tolerance enables light yield measurements under conditions that more closely resemble those in operational xenon detectors, and facilitates investigation of the linear pressure dependence observed between 500 mbar and 1.1 bar. Additionally, the design allows for the UV photosensors to be housed in separate evacuated or air-filled chambers, both of which offer higher breakdown voltages compared to GXe. In this way, PMTs can be operated with photocathodes at ground, eliminating unwanted electric fields in the active region, without suffering from high voltage breakdowns. Additionally, the physical separation removes plastic materials from the active volume, which should significantly reduce outgassing rates and thus enable improved control over gas purity. The IR-sensitive Hamamatsu H10330C-75 PMT is mounted behind one of the windows, opposite to the source holder, with the option of other mounting positions for systematic studies.

A primary goal of this new setup is to measure the IR light yield from electronic recoil (ER) interactions for the first time. Unlike α-articles, the interaction positions of ER sources are

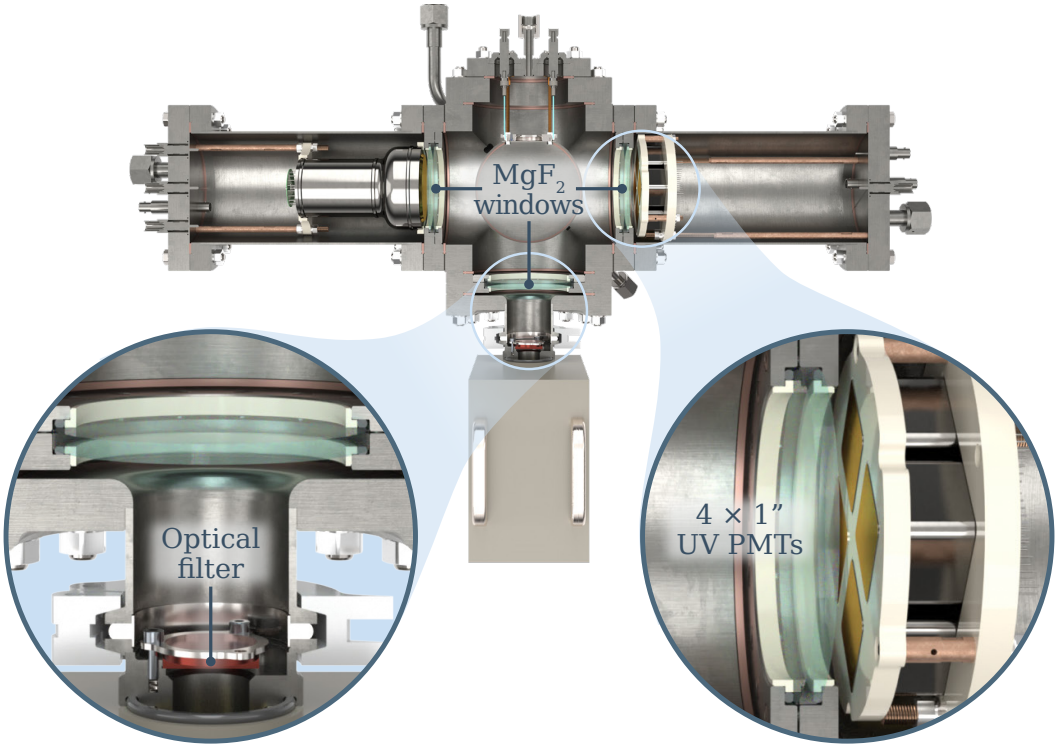

Figure 9.14.: Schematic of the enhanced room-temperature gas setup featuring improved pressure capability, position reconstruction, and wavelength-band-resolved measurements. Two magnifications highlight the quick-swap optical filter system in front of the IR PMT (left) and the four one-inch UV PMTs used for improved position reconstruction capabilities.

much less deterministic. Since the LCE of the IR PMT strongly depends on the event location within the target, achieving three-dimensional position reconstruction will greatly improve the precision of a light yield measurement. For this purpose, one 3-inch UV PMT is replaced with an array of four 1-inch Hamamatsu R8520-06-AL PMTs, enabling position reconstruction in the UV-detector plane.

Perhaps most importantly, the setup enables wavelength-resolved measurements through a modular filter system positioned in front of the IR PMT. Quick-release mounting allows rapid filter exchange, facilitating systematic scanning of narrow wavelength bands across the IR spectrum. This capability is expected to clarify the spectral characteristics of the various temporal components observed in previous measurements. Importantly, this will answer whether the dominant slow component originates from the broad IR continuum. Initial commissioning of this setup has been completed, with first physics measurements anticipated in the near future.

10

Conclusions and Outlook

Dark matter constitutes approximately 26 % of the Universe's total mass-energy content, with compelling evidence for its gravitational effects, yet its fundamental nature represents one of modern physics' most profound open questions. Liquid xenon (LXe) time projection chambers (TPCs) have emerged as the leading technology for direct dark matter searches, offering exceptional sensitivity to weakly interacting massive particle (WIMP) interactions. With its 5.9 t active LXe target, the currently running XENONnT experiment is one of the leading dark matter experiments. Striving for ever-better sensitivity, dark matter detectors also become sensitive to other rare processes, such as neutrino interactions via coherent elastic neutrino-nucleus scattering (CEνNS).

This work contributed significantly to both the latest search for WIMP dark matter and the first observation of ^{8}B solar neutrinos via CEνNS with the first two science runs (SRs) of XENONnT (presented in Chapter 7 and published in [Paper II] and [Paper III]). Additionally, this work laid important groundwork for assessing infrared (IR) scintillation in xenon as a potential enhancement for next-generation xenon detectors (discussed in Chapter 7 and published in [Paper IV], [Paper V], and [Paper VI]).

The combined analysis of the first two SRs of XENONnT, with a total exposure of 3.1 t yr, improved the experiment's sensitivity by a factor of up to 1.8 compared to the initial result. The analysis found no significant excess above background expectations, thus leading to competitive upper limits (ULs) on the WIMP-nucleon cross section as low as $1.7 \times 10^{-47}\,\mathrm{cm}^2$ for a WIMP mass of $30\,\mathrm{GeV}/c^2$, assuming spin-independent (SI) coupling. Through a dedicated analysis that pushed the energy threshold even further, the first measurement of ^{8}B solar neutrinos via CEνNS was achieved. The measurement observed 37 events with $26.4^{+1.4}_{-1.3}$ expected from backgrounds, yielding 10.6 excess events consistent with the predicted $11.9^{+4.5}_{-4.2}$ events from solar neutrinos. The background-only hypothesis was rejected with a statistical significance of $2.73\,\sigma$. This made XENONnT the first dark matter experiment to measure solar neutrinos, a feat previously achieved only with dedicated kiloton-scale detectors, and marked its entry into the "neutrino fog". While the neutrino fog eventually limits direct dark matter searches, it simultaneously opens exciting new opportunities to study astrophysical neutrino sources and test fundamental physics.

Central to these results were robust statistical models, extensive sensitivity studies, and thorough robustness assessments, all developed as part of this work to guide analysis decisions and ensure reliable results. To support these efforts, the `alea` statistical analysis framework was developed and implemented, which is now used for all major XENONnT analyses and for sensitivity projections for the next-generation LXe observatory XLZD.

For the WIMP search, several sensitivity studies were conducted that informed key analysis decisions (Chapter 5). Based on these studies, the first part of the second SR was excluded and the region of interest (ROI) and fiducial volume (FV) were slightly tightened – decisions that had minimal impact on sensitivity while enhancing the robustness of the results. This work placed particular focus on the possibility of double electron capture (DEC) background shifting into the signal region in the analysis space. The statistical implications of different treatments were studied, and a hypothesis test was devised to minimize unwanted statistical behavior, specifically excessive false WIMP discovery rates and overly optimistic exclusions of WIMP parameter space.

The first measurement of solar CEνNS required careful statistical modeling guided by sensitivity studies (Chapter 6). The dominant accidental coincidence (AC) background was modeled in a data-driven way, and this work identified that 15 % mismodeling of the AC rate could significantly impact results. This finding prompted additional validation using a high-statistics calibration dataset, which confirmed modelling reliability with systematic rate uncertainties below 5 %. Further studies demonstrated that the search's discovery significance was not susceptible to yield mismodeling, defined the FV based on obtained thresholds of tolerable unmodeled backgrounds, and selected a sensitive goodness of fit (GOF) test to identify potential mismodeling.

Following the first two SRs, XENONnT continued data-taking to increase the significance of the observed ^{8}B CEνNS signal and further explore the WIMP parameter space. At the time of writing, a major detector upgrade is underway, a decision that was driven by the sensitivity studies presented in Chapter 5. The upgrade will replace the TPC electrodes to enable higher drift fields, thereby improving background discrimination in future operations. The enhanced detector is expected to match the sensitivity that would have been achieved by continuing data-taking without the upgrade within months of resuming operations. It will then rapidly reach sensitivities that would only be achievable by the end of the decade in the non-upgrade scenario. Ultimately, this will enable probing parameter space that would otherwise remain inaccessible to XENONnT.

While current LXe detectors continue data-taking, the next-generation LXe detector for the XLZD experiment is under development to probe the WIMP parameter space down to the neutrino fog for all masses above a few GeV/c^2. In this context, the second major component of this thesis investigated IR scintillation in xenon as a potential enhancement for future xenon-based detectors. This work confirmed the presence of IR scintillation light in xenon and extended limited earlier studies by conducting the first time-resolved measurements in both gaseous and liquid phases, addressing an important gap in the understanding of xenon's scintillation properties.

Systematic measurements in room-temperature gaseous xenon (GXe) provided the first detailed characterization of IR scintillation temporal properties for α-particle irradiation across pressures from 500 to 1200 mbar. A sizeable light yield of approximately 6000 photons/MeV

was measured at 1 bar, representing approximately one-quarter of the ultraviolet (UV) yield and confirming the potential value of IR emission for detector applications. The time response revealed two distinct exponential components: a fast component ($\sim$2 ns decay time, $<$1 % of signal) and a dominant slow component (microsecond timescale, $>$99 % of signal). Crucially, the observation of this slow decay constant excludes the possibility that the dominant IR emission precedes UV scintillation, challenging previous understanding and suggesting alternative de-excitation pathways. The slow component exhibited strong pressure dependence – indicating density-dependent precursor formation mechanisms – as well as strong susceptibility to gas impurities.

A dual-phase xenon TPC was operated for the first time with broad wavelength sensitivity spanning from UV to IR wavelengths. This represents an important step toward evaluating the viability of IR detection in future LXe detectors. Signals consistent with IR scintillation were observed in coincidence with both primary UV scintillation in LXe and electroluminescence in GXe. However, several systematic effects require further investigation to determine their origin unequivocally. Confirmation of IR scintillation from electroluminescence through future measurements would strongly suggest that IR precursor states form at relatively low electron energies, below xenon's ionization threshold, thereby narrowing down potential precursor states. The temporal structure revealed multiple components, including a very slow component ($\sim$30 µs) that contributes approximately half of both primary and electroluminescence signals.

The results establish IR scintillation as a potentially valuable addition to future xenon detectors, offering several promising applications. The substantial light yield in GXe could enhance energy resolution, while indications of a particle-type dependence in the temporal components might enable improved background discrimination through pulse shape analysis. Importantly, IR photons can be transmitted through optical fibers, enabling remote sensor placement, reducing radioactivity requirements, and simplifying maintenance. Building on the results presented in this thesis, an enhanced room-temperature setup was developed featuring wavelength-resolved measurement capabilities and improved systematic control. This setup will address key remaining questions, including identifying the spectral origin of the observed temporal components and potential particle-type discrimination capabilities.

This work contributed to probing the invisible both through cutting-edge rare event searches with XENONnT and through foundational studies of IR scintillation for next-generation experiments.

Appendix

A

Impact of Background Variations on the Long-Term WIMP Sensitivity Projection

To assess the influence of individual background components, sensitivity projections for science run (SR)3 with new electrodes were performed by varying one background contribution at a time. Here, the most important background components, following the arguments in Section 5.5.3, were studied. The results are summarized in Figure A.1. Note that each background was varied in a different range according to what was considered plausible based on experimental considerations.

The accidental coincidence (AC) background rate was varied between 0.1 and 2.5 times its nominal value. The lower bound corresponds to a significant suppression beyond current expectations, while the upper bound reflects a scenario with only trivial improvement over the SR0 rate, accounting for the expected factor-of-two reduction from the doubled drift velocity. The sensitivity, particularly for the $10\,\mathrm{GeV}/c^2$ WIMP case, is visibly impacted by changes in the AC background, consistent with its dominant contribution estimated in Section 5.5.3.

The electronic recoil (ER) background, which can be more reliably predicted and mitigated (e.g., via cryogenic distillation, see Section 3.3), was varied between 0.6 and 1.5 times the nominal rate. The lower bound corresponds to the absence of the ^{3}H-like contribution seen in SR1, and the upper bound is motivated by variations observed in the past. This variation causes a modest change in sensitivity for the $50\,\mathrm{GeV}/c^2$ case, with negligible effect for $10\,\mathrm{GeV}/c^2$ WIMPs.

Neutron-induced backgrounds were varied from 0.1 to 4.7 times the nominal rate. The lower bound represents an optimistic scenario where detector components with major neutron emission can be replaced during the repair, while the upper bound reflects the case of no Gd loading in the water tank, leading to reduced neutron veto (NV) tagging efficiency (53 % instead of 90 %). As neutron background is already subdominant under nominal conditions, further reduction has little impact. However, a significant increase substantially degrades sensitivity, especially for the $50\,\mathrm{GeV}/c^2$ weakly interacting massive particle (WIMP) case.

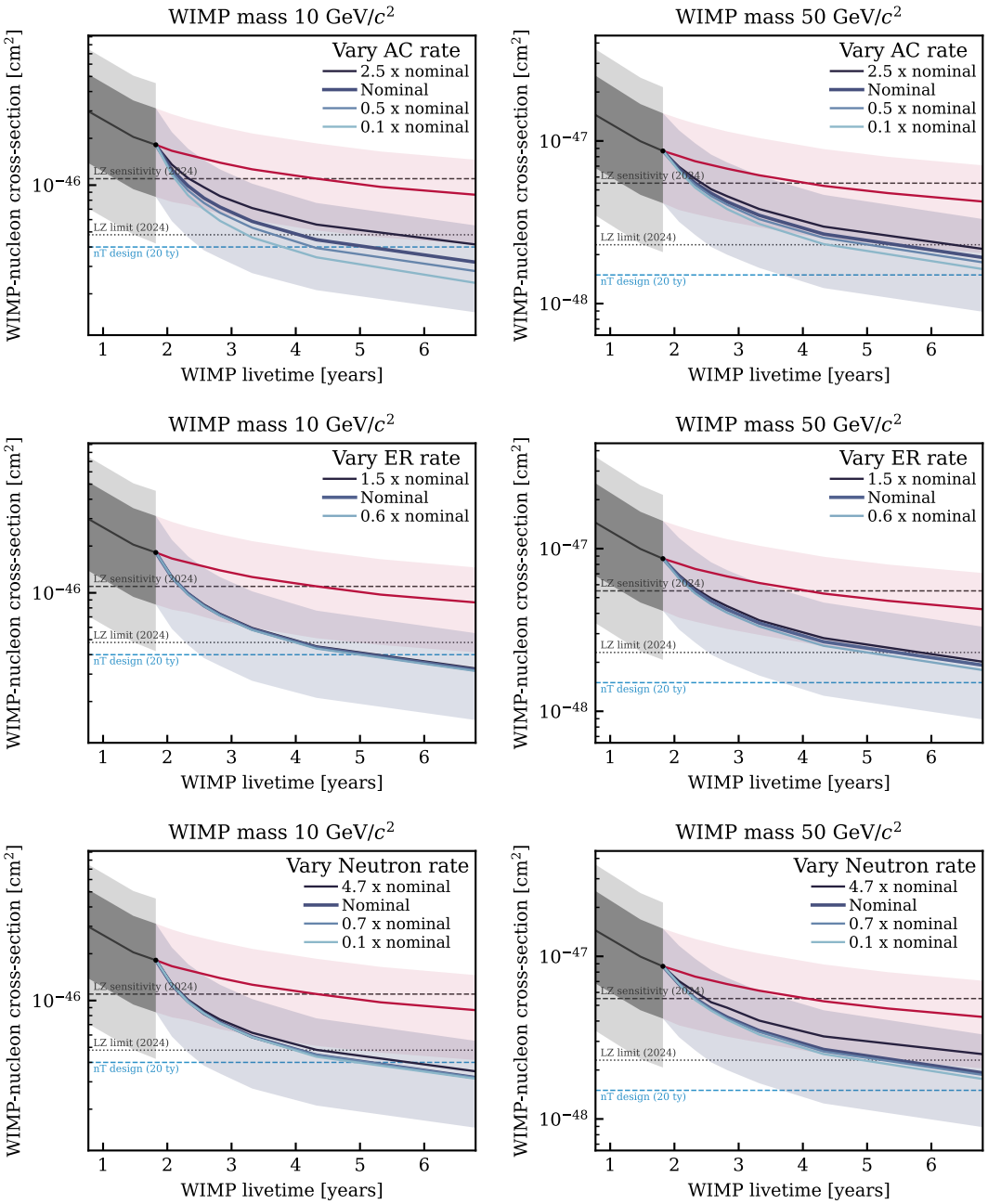

Figure A.1.: Impact of background rates on the long-tern WIMP sensitivity for 10 GeV/c^2 (left) and 50 GeV/c^2. The rate variations for accidental coincidence (AC), electronic recoil (ER), and neutron backgrounds differ. More details on the chosen values are provided in the text.

B

Estimation of the Liquid Level in HeXe

The electric field in the gas phase is a key parameter governing the electroluminescence process. Since the fields in both the liquid and gas between the gate and anode depend on the liquid level, an accurate determination of this level is necessary to interpret the Heidelberg Xenon (HeXe) data discussed in Section 9.2. Although the HeXe time projection chamber (TPC) is equipped with several capacitive level meters to monitor the liquid xenon (LXe) height, these provide only limited precision. To address this, a data-driven method was developed to infer the liquid level more reliably.

Approximating the gate and anode as an infinitely extended parallel-plate capacitor, the electric fields in the liquid E_l and gas E_g can be expressed as:

$$E_\mathrm{l} = \frac{\Delta V}{h_\mathrm{l} + \varepsilon_\mathrm{l}(d - h_\mathrm{l})} \qquad E_\mathrm{g} = \frac{\varepsilon_\mathrm{l}\Delta V}{h_\mathrm{l} + \varepsilon_\mathrm{l}(d - h_\mathrm{l})}. \tag{B.1}$$

Here, ΔV denotes the potential difference between anode and gate, $d = 5\,\mathrm{mm}$ is the total gap between anode and gate, $\varepsilon_\mathrm{l} = 1.85$ is the dielectric constant of LXe[332, 333], and h_l is the liquid level above the gate. For simplicity, the dielectric constant of the gas phase, $\varepsilon_\mathrm{g} \simeq 1$, is omitted in the equations. The resulting field strengths as functions of the liquid level are shown in Figure B.1 (left) for the operating voltages used in this work.

Electrons emitted from the gate electrode via photoionization by intense ultraviolet (UV) signals drift a distance h_l through the liquid before producing a light signal in the gas phase. In principle, the liquid level can be determined by dividing the measured gate drift time by the electron drift velocity. However, the electron drift velocity in LXe depends on the electric field (Figure B.1, right) – the very quantity we wish to determine. To address this, the liquid level was determined using an iterative procedure: for a given assumed ('input') liquid level, the electric field in the liquid is computed, for which we obtain the corresponding drift velocity. The 'output' liquid level is then computed by dividing the observed gate drift time by this velocity. This process is repeated until the input and output liquid levels converge, indicating the true liquid level. This matching procedure is illustrated in Figure B.2, using two methods for estimating the drift velocity, namely interpolation of the data from [334] and a power-law

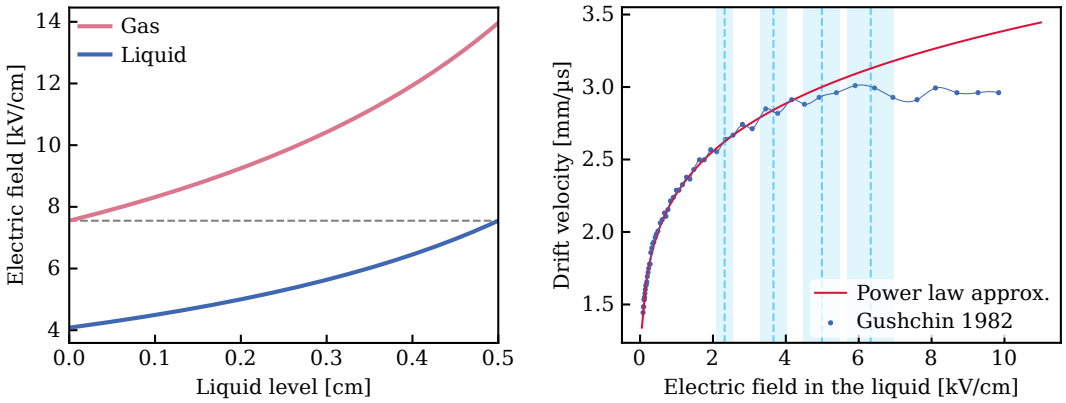

Figure B.1.: (Left) Dependence of the electric fields in liquid and gaseous xenon as a function of the liquid level above the gate. (Right) Dependence of the drift velocity of electrons on the electric field in the liquid from [334], interpolated for the liquid level matching illustrated in Figure B.2. Overlaid is a power-law approximation (red line).

approximation, as shown in Figure B.1 (right), and two approaches for estimating the $S2_{UV}$ time (rising edge and center time). During the measurement campaign, the anode voltage was varied temporarily, resulting in gate drift times measured at three different voltages. Averaging over these three voltages and four drift velocity estimation methods yields a liquid level of $h_l = (4.1 \pm 0.5)\,\mathrm{mm}$, which corresponds to approximately 82 % of the anode-gate distance. The resulting electric field in the gas phase is $(12.1 \pm 0.9)\,\mathrm{kV/cm}$.

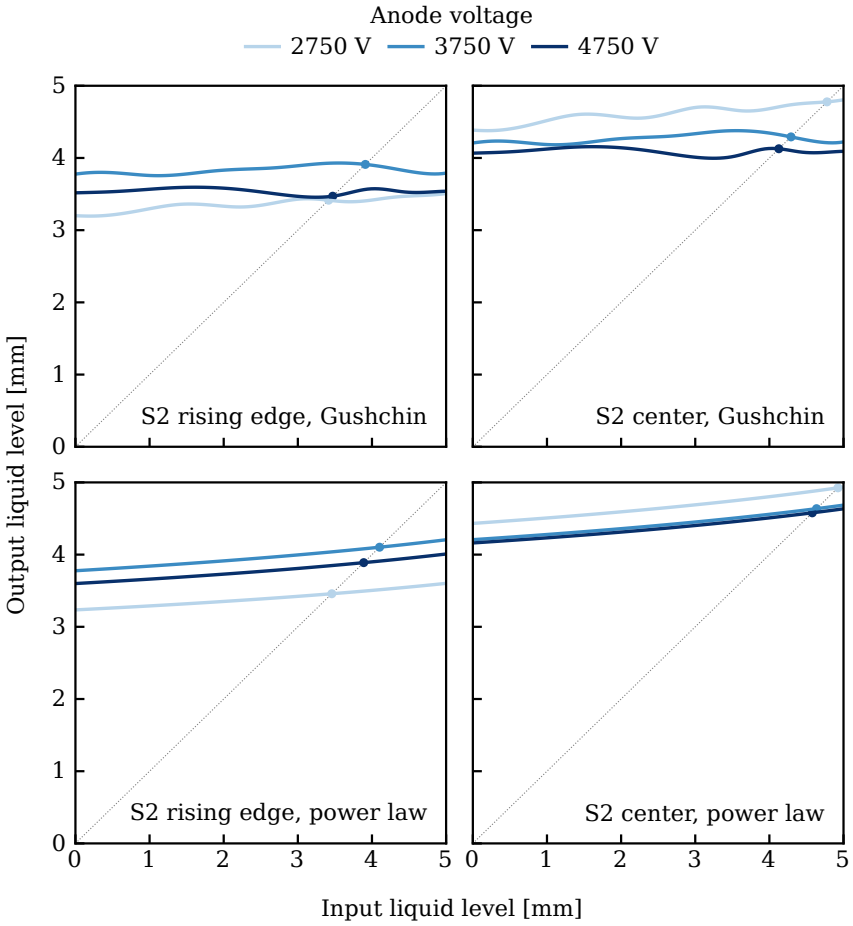

Figure B.2.: Illustration of the iterative liquid level matching approach. The output liquid level, obtained from observed gate drift time, is shown as a function of the input liquid level. The four panels correspond to combinations of two $S2_{UV}$ timing estimators and two approaches for determining the field-dependent drift velocity.

List of Figures

List of Tables

References

[1] Planck collaboration (N. Aghanim et al.), "Planck 2018 results: VI. cosmological parameters," *A&A*, vol. 641, A6, 2020. DOI: 10.1051/0004-6361/201833910.

[2] R. Bernabei et al., "Annual modulation results from DAMA/LIBRA," *Int. J. Mod. Phys. Conf. Ser.*, vol. 51, 2023. DOI: 10.1142/s2010194523610086.

[3] COSINE collaboration (G. H. Yu et al.), "Limits on WIMP dark matter with NaI(Tl) crystals in three years of COSINE-100 data," 2025. DOI: 10.48550/ARXIV.2501.13665.

[4] ANAIS collaboration (I. Coarasa et al.), "ANAIS-112 three years data: A sensitive model independent negative test of the DAMA/LIBRA dark matter signal," *Comm. Phys.*, vol. 7, no. 1, 2024. DOI: 10.1038/s42005-024-01827-y.

[5] Particle Data Group (S. Navas et al.), "Review of particle physics," *Phys. Rev. D*, vol. 110, no. 3, p. 030 001, 2024. DOI: 10.1103/PhysRevD.110.030001.

[6] H. Murayama et al., *Exploring the Quantum Universe: Pathways to Innovation and Discovery in Particle Physics (Report of the 2023 Particle Physics Project Prioritization Panel)*. 2023. DOI: 10.2172/2368847.

[7] M. Cirelli, A. Strumia, and J. Zupan, "Dark matter," 2024. DOI: 10.48550/ARXIV.2406.01705. arXiv: arXiv:2406.01705 [hep-ph].

[8] G. Bertone, D. Hooper, and J. Silk, "Particle dark matter: Evidence, candidates and constraints," *Phys. Rep.*, vol. 405, no. 5-6, p. 279, 2005. DOI: 10.1016/j.physrep.2004.08.031.

[9] L. Roszkowski, E. M. Sessolo, and S. Trojanowski, "WIMP dark matter candidates and searches—current status and future prospects," *Rep. Prog. Phys.*, vol. 81, no. 6, p. 066 201, 2018. DOI: 10.1088/1361-6633/aab913.

[10] E. Abdalla et al., "Cosmology intertwined: A review of the particle physics, astrophysics, and cosmology associated with the cosmological tensions and anomalies," *JHEAP*, vol. 34, pp. 49–211, 2022. DOI: 10.1016/j.jheap.2022.04.002.

[11] DESI collaboration (M. Abdul Karim et al.), "DESI DR2 results. II. measurements of baryon acoustic oscillations and cosmological constraints," *Phys. Rev. D*, vol. 112, no. 8, 2025. DOI: 10.1103/tr6y-kpc6.

[12] B. Famaey and S. S. McGaugh, "Modified newtonian dynamics (MOND): Observational phenomenology and relativistic extensions," *Living rev. relativ.*, vol. 15, no. 1, 2012. DOI: 10.12942/lrr-2012-10.

[13] V. C. Rubin and J. Ford W. Kent, "Rotation of the Andromeda nebula from a spectroscopic survey of emission regions," *ApJ*, vol. 159, p. 379, 1970. DOI: 10.1086/150317.

[14] V. C. Rubin, N. Thonnard, and J. Ford W. K., "Extended rotation curves of high-luminosity spiral galaxies. IV - systematic dynamical properties, sa through sc," *The Astrophysical Journal*, vol. 225, p. L107, 1978. DOI: 10.1086/182804.

[15] G. Bertone and D. Hooper, "History of dark matter," *Rev. Mod. Phys.*, vol. 90, p. 045 002, 4 2018. DOI: 10.1103/RevModPhys.90.045002.

[16] M. Persic, P. Salucci, and F. Stel, "The universal rotation curve of spiral galaxies — I. the dark matter connection," *Mon. Not. Roy. Astron. Soc.*, vol. 281, no. 1, pp. 27–47, 1996. DOI: 10.1093/mnras/278.1.27.

[17] F. Lelli, S. S. McGaugh, and J. M. Schombert, "SPARC: Mass models for 175 disk galaxies with Spitzer photometry and accurate rotation curves," *AJ*, vol. 152, no. 6, p. 157, 2016. DOI: 10.3847/0004-6256/152/6/157.

[18] X. Zhang, B. Chen, P. Chen, J. Sun, and Z. Tian, "The rotation curve and mass distribution of M31," *Mon. Not. Roy. Astron. Soc.*, vol. 528, no. 2, pp. 2653–2666, 2024. DOI: 10.1093/mnras/stae025.

[19] F. Zwicky, "Die Rotverschiebung von extragalaktischen Nebeln," *Helv. Phys. Acta*, vol. 6, pp. 110–127, 1933.

[20] R. Massey, T. Kitching, and J. Richard, "The dark matter of gravitational lensing," *Rep. Prog. Phys.*, vol. 73, no. 8, p. 086 901, 2010. DOI: 10.1088/0034-4885/73/8/086901.

[21] D. Clowe et al., "A direct empirical proof of the existence of dark matter," *AJO*, vol. 648, no. 2, pp. L109–L113, 2006. DOI: 10.1086/508162.

[22] S. W. Randall, M. Markevitch, D. Clowe, A. H. Gonzalez, and M. Bradač, "Constraints on the self-interaction cross section of dark matter from numerical simulations of the merging galaxy cluster 1e 0657-56," *ApJ*, vol. 679, no. 2, pp. 1173–1180, 2008. DOI: 10.1086/587859.

[23] D. Harvey, R. Massey, T. Kitching, A. Taylor, and E. Tittley, "The nongravitational interactions of dark matter in colliding galaxy clusters," *Science*, vol. 347, no. 6229, pp. 1462–1465, 2015. DOI: 10.1126/science.1261381.

[24] *Bullet cluster composite image*, https://chandra.harvard.edu/photo/2006/1e0657/, X-ray: NASA/CXC/CfA/M. Markevitch et al.; Optical: NASA/STScI; Magellan/U. Arizona/D. Clowe et al.; Lensing Map: NASA/STScI; ESO WFI; Magellan/U. Arizona/D. Clowe et al., 2006.

[25] R. Durrer, "The cosmic microwave background: The history of its experimental investigation and its significance for cosmology," *CQG*, vol. 32, no. 12, p. 124 007, 2015. DOI: 10.1088/0264-9381/32/12/124007.

[26] D. J. Fixsen, "The temperature of the cosmic microwave background," *ApJ*, vol. 707, no. 2, pp. 916–920, 2009. DOI: 10.1088/0004-637x/707/2/916.

[27] Planck collaboration (N. Aghanim et al.), "Planck 2018 results: I. overview and the cosmological legacy of Planck," *A&A*, vol. 641, A1, 2020. DOI: 10.1051/0004-6361/201833880.

[28] Planck collaboration (N. Aghanim, Y. Akrami, M. Ashdown, J. Aumont, C. Baccigalupi, M. Ballardini, et al.), "Planck 2018 results: V. CMB power spectra and likelihoods," *A&A*, vol. 641, A5, 2020. DOI: 10.1051/0004-6361/201936386.

[29] M. Schumann, "Direct detection of WIMP dark matter: Concepts and status," *J. Phys. G: Nucl. Part. Phys.*, vol. 46, no. 10, p. 103 003, 2019. DOI: 10.1088/1361-6471/ab2ea5.

[30] C. Frenk and S. White, "Dark matter and cosmic structure," *Ann. Phys. (Berlin)*, vol. 524, no. 9-10, pp. 507–534, 2012. DOI: 10.1002/andp.201200212.

[31] B. Carr and F. Kühnel, "Primordial black holes as dark matter: Recent developments," *Annu. Rev. Nucl. Part. Sci.*, vol. 70, no. 1, pp. 355–394, 2020. DOI: 10.1146/annurev-nucl-050520-125911.

[32] G. Arcadi et al., "The waning of the WIMP: Endgame?" *Eur. Phys. J. C*, vol. 85, no. 2, 2025. DOI: 10.1140/epjc/s10052-024-13672-y.

[33] S. Dodelson and L. M. Widrow, "Sterile neutrinos as dark matter," *Phys. Rev. Lett.*, vol. 72, no. 1, pp. 17–20, 1994. DOI: 10.1103/physrevlett.72.17.

[34] C. O'Hare, "Cosmology of axion dark matter," in *Proceedings of 1st General Meeting and 1st Training School of the COST Action COSMIC WSIPers — PoS(COSMICWISPers)*, ser. COSMICWISPers, Sissa Medialab, 2024, p. 040. DOI: 10.22323/1.454.0040.

[35] R. D. Peccei and H. R. Quinn, "CP conservation in the presence of pseudoparticles," *Phys. Rev. Lett.*, vol. 38, no. 25, pp. 1440–1443, 1977. DOI: 10.1103/physrevlett.38.1440.

[36] A. Boveia and C. Doglioni, "Dark matter searches at colliders," *Annu. Rev. Nucl. Part. Sci.*, vol. 68, no. 1, pp. 429–459, 2018. DOI: 10.1146/annurev-nucl-101917-021008.

[37] *Phys. Rep.*, vol. 1115, pp. 448–569, 2025. DOI: 10.1016/j.physrep.2024.09.013.

[38] J. Conrad and O. Reimer, "Indirect dark matter searches in gamma and cosmic rays," *Nat. Phys.*, vol. 13, no. 3, pp. 224–231, 2017. DOI: 10.1038/nphys4049.

[39] T. Marrodán Undagoitia and L. Rauch, "Dark matter direct-detection experiments," *J. Phys. G: Nucl. Part. Phys.*, vol. 43, no. 1, p. 013 001, 2015. DOI: 10.1088/0954-3899/43/1/013001.

[40] F. Queiroz, "Complementarity of direct detection, indirect detection and collider searches (LHC)," in *The 2nd DMNet International Symposium*, Heidelberg, Germany, 2022.

[41] J. Lewin and P. Smith, "Review of mathematics, numerical factors, and corrections for dark matter experiments based on elastic nuclear recoil," *Astropart. Phys.*, vol. 6, no. 1, p. 87, 1996. DOI: 10.1016/S0927-6505(96)00047-3.

[42] M. C. Smith et al., "The RAVE survey: Constraining the local galactic escape speed," *Mon. Not. Roy. Astron. Soc.*, vol. 379, pp. 755–772, 2007. DOI: 10.1111/j.1365-2966.2007.11964.x.

[43] D. Baxter et al., "Recommended conventions for reporting results from direct dark matter searches," *Eur. Phys. J. C*, vol. 81, no. 10, p. 907, 2021. DOI: 10.1140/epjc/s10052-021-09655-y.

[44] F. Iocco, M. Pato, and G. Bertone, "Evidence for dark matter in the inner Milky Way," *Nat. Phys.*, vol. 11, no. 3, pp. 245–248, 2015. DOI: 10.1038/nphys3237.

[45] M. Cautun et al., "The milky way total mass profile as inferred from Gaia DR2," *Mon. Not. Roy. Astron. Soc.*, vol. 494, no. 3, pp. 4291–4313, 2020. DOI: 10.1093/mnras/staa1017.

[46] X. Ou, A.-C. Eilers, L. Necib, and A. Frebel, "The dark matter profile of the Milky Way inferred from its circular velocity curve," *Mon. Not. Roy. Astron. Soc.*, vol. 528, no. 1, pp. 693–710, 2024. DOI: 10.1093/mnras/stae034.

[47] F. Froborg and A. R. Duffy, "Annual modulation in direct dark matter searches," *J. Phys. G: Nucl. Part. Phys.*, vol. 47, no. 9, p. 094 002, 2020. DOI: 10.1088/1361-6471/ab8e93.

[48] F. Mayet et al., "A review of the discovery reach of directional dark matter detection," *Phys. Rep.*, vol. 627, pp. 1–49, 2016. DOI: 10.1016/j.physrep.2016.02.007.

[49] C. A. J. O'Hare, "New definition of the neutrino floor for direct dark matter searches," *Phys. Rev. Lett.*, vol. 127, no. 25, 2021. DOI: 10.1103/physrevlett.127.251802.

[50] G. Bertone, Ed., *Particle Dark Matter: Observations, Models and Searches*. Cambridge University Press, 2010, ISBN: 9781107653924. DOI: 10.1017/cbo9780511770739.

[51] P. Klos, J. Menéndez, D. Gazit, and A. Schwenk, "Large-scale nuclear structure calculations for spin-dependent WIMP scattering with chiral effective field theory currents," *Phys. Rev. D*, vol. 88, no. 8, p. 083 516, 2013. DOI: 10.1103/PhysRevD.88.083516.

[52] CRESST collaboration (A. H. Abdelhameed et al.), "First results from the CRESST-III low-mass dark matter program," *Phys. Rev. D*, vol. 100, no. 10, 2019. DOI: 10.1103/physrevd.100.102002.

[53] SuperCDMS collaboration (R. Agnese et al.), "Search for low-mass dark matter with CDMSlite using a profile likelihood fit," *Phys. Rev. D*, vol. 99, no. 6, 2019. DOI: 10.1103/physrevd.99.062001.

[54] SuperCDMS collaboration (R. Agnese et al.), "Results from the Super Cryogenic Dark Matter Search experiment at Soudan," *Phys. Rev. Lett.*, vol. 120, no. 6, 2018. DOI: 10.1103/physrevlett.120.061802.

[55] DEAP collaboration (R. Ajaj et al.), "Search for dark matter with a 231-day exposure of liquid argon using DEAP-3600 at SNOLAB," *Phys. Rev. D*, vol. 100, no. 2, 2019. DOI: 10.1103/physrevd.100.022004.

[56] DarkSide-50 collaboration (P. Agnes et al.), "Search for low-mass dark matter wimps with 12 ton-day exposure of DarkSide-50," *Phys. Rev. D*, vol. 107, no. 6, 2023. DOI: 10.1103/physrevd.107.063001.

[57] PandaX collaboration (Z. Bo et al.), "Dark matter search results from 1.54 Tonne·Year exposure of PandaX-4T," *Phys. Rev. Lett.*, vol. 134, p. 011 805, 1 2025. DOI: 10.1103/PhysRevLett.134.011805.

[58] LUX-ZEPLIN collaboration (J. Aalbers, D. S. Akerib, A. K. A. Musalhi, F. Alder, C. S. Amarasinghe, A. Ames, et al.), "Dark matter search results from 4.2 tonne-years of exposure of the LUX-ZEPLIN (LZ) experiment," *Phys. Rev. Lett.*, vol. 135, no. 1, 2025. DOI: 10.1103/4dyc-z8zf.

[59] XENON collaboration (E. Aprile et al.), "First search for light dark matter in the neutrino fog with XENONnT," *Phys. Rev. Lett.*, vol. 134, no. 11, 2025. DOI: 10.1103/physrevlett.134.111802.

[60] XLZD collaboration (J. Aalbers et al.), "The XLZD design book: Towards the next-generation liquid xenon observatory for dark matter and neutrino physics," 2024. DOI: 10.48550/ARXIV.2410.17137.

[61] W. Pauli, *Letter to the group of radioactive people at the Gauverein meeting in Tübingen*, Pauli Archive, CERN, 1930.

[62] E. Fermi, "Tentativo di una teoria dei raggi ," *Nuovo Cim.*, vol. 11, no. 1, pp. 1–19, 1934. DOI: 10.1007/bf02959820.

[63] C. L. Cowan, F. Reines, F. B. Harrison, H. W. Kruse, and A. D. McGuire, "Detection of the free neutrino: A confirmation," *Science*, vol. 124, no. 3212, pp. 103–104, 1956. DOI: 10.1126/science.124.3212.103.

[64] Super-Kamiokande collaboration (Y. Fukuda et al.), "Evidence for oscillation of atmospheric neutrinos," *Phys. Rev. Lett.*, vol. 81, pp. 1562–1567, 1998. DOI: 10.1103/PhysRevLett.81.1562.

[65] E. Vitagliano, I. Tamborra, and G. Raffelt, "Grand unified neutrino spectrum at earth: Sources and spectral components," *Rev. Mod. Phys.*, vol. 92, no. 4, 2020. DOI: 10.1103/revmodphys.92.045006.

[66] D. Z. Freedman, "Coherent effects of a weak neutral current," *Phys. Rev. D*, vol. 9, no. 5, pp. 1389–1392, 1974. DOI: 10.1103/physrevd.9.1389.

[67] V. B. Kopeliovich and L. L. Frankfurt, "Isotopic and chiral structure of neutral current," *JETP Lett.*, vol. 19, pp. 145–147, 1974.

[68] M. Cadeddu, F. Dordei, and C. Giunti, "A view of coherent elastic neutrino-nucleus scattering," *Europhysics Letters*, vol. 143, no. 3, p. 34 001, 2023. DOI: 10.1209/0295-5075/ace7f0.

[69] P. Barbeau, Y. Efremenko, and K. Scholberg, "COHERENT at the Spallation Neutron Source," *Annu. Rev. Nucl. Part. Sci.*, vol. 73, no. 1, pp. 41–68, 2023. DOI: 10.1146/annurev-nucl-101918-023518.

[70] COHERENT collaboration (D. Akimov et al.), "Observation of coherent elastic neutrino-nucleus scattering," *Science*, vol. 357, no. 6356, pp. 1123–1126, 2017. DOI: 10.1126/science.aao0990.

[71] COHERENT collaboration (D. Akimov et al.), "First measurement of coherent elastic neutrino-nucleus scattering on argon," *Phys. Rev. Lett.*, vol. 126, no. 1, 2021. DOI: 10.1103/physrevlett.126.012002.

[72] COHERENT collaboration (S. Adamski et al.), "Evidence of coherent elastic neutrino-nucleus scattering with COHERENT's germanium array," *Phys. Rev. Lett.*, vol. 134, no. 23, 2025. DOI: 10.1103/physrevlett.134.231801.

[73] CONUS collaboration (N. Ackermann et al.), "Direct observation of coherent elastic antineutrino-nucleus scattering," *Nature*, vol. 643, no. 8074, pp. 1229–1233, 2025. DOI: 10.1038/s41586-025-09322-2.

[74] PandaX collaboration (W. Ma et al.), "Search for solar ^{8}B neutrinos in the PandaX-4T experiment using neutrino-nucleus coherent scattering," *Phys. Rev. Lett.*, vol. 130, no. 2, 2023. DOI: 10.1103/physrevlett.130.021802.

[75] J. Billard, E. Figueroa-Feliciano, and L. Strigari, "Implication of neutrino backgrounds on the reach of next generation dark matter direct detection experiments," *Phys. Rev. D*, vol. 89, no. 2, 2014. DOI: 10.1103/physrevd.89.023524.

[76] B. Dutta and L. E. Strigari, "Neutrino physics with dark matter detectors," *Annu. Rev. Nucl. Part. Sci.*, vol. 69, no. 1, pp. 137–161, 2019. DOI: 10.1146/annurev-nucl-101918-023450.

[77] J. Billard, L. E. Strigari, and E. Figueroa-Feliciano, "Solar neutrino physics with low-threshold dark matter detectors," *Phys. Rev. D*, vol. 91, no. 9, 2015. DOI: 10.1103/physrevd.91.095023.

[78] J. Aalbers et al., "A next-generation liquid xenon observatory for dark matter and neutrino physics," *J. Phys. G: Nucl. Part. Phys.*, vol. 50, no. 1, p. 013 001, 2022. DOI: 10.1088/1361-6471/ac841a.

[79] XENON collaboration (E. Aprile et al.), "Design and performance of the XENON10 dark matter experiment," *Astroparticle Physics*, vol. 34, no. 9, pp. 679–698, 2011. DOI: 10.1016/j.astropartphys.2011.01.006.

[80] XENON collaboration (J. Angle et al.), "First results from the XENON10 dark matter experiment at the gran sasso national laboratory," *Physical Review Letters*, vol. 100, no. 2, 2008. DOI: 10.1103/physrevlett.100.021303.

[81] XENON collaboration (E. Aprile et al.), "The XENON100 dark matter experiment," *Astropart. Phys.*, vol. 35, no. 9, pp. 573–590, 2012. DOI: 10.1016/j.astropartphys.2012.01.003.

[82] XENON collaboration (E. Aprile et al.), "The XENON1T dark matter experiment," *Eur. Phys. J. C*, vol. 77, no. 12, 2017. DOI: 10.1140/epjc/s10052-017-5326-3.

[83] XENON collaboration (E. Aprile et al.), "The XENONnT dark matter experiment," *Eur. Phys. J. C*, vol. 84, no. 8, p. 784, 2024. DOI: 10.1140/epjc/s10052-024-12982-5.

[84] XENON collaboration (E. Aprile et al.), "Dark matter results from 100 live days of XENON100 data," *Phys. Rev. Lett.*, vol. 107, no. 13, 2011. DOI: 10.1103/physrevlett.107.131302.

[85] XENON collaboration (E. Aprile et al.), "Dark matter results from 225 live days of XENON100 data," *Phys. Rev. Lett.*, vol. 109, no. 18, 2012. DOI: 10.1103/physrevlett.109.181301.

[86] XENON collaboration (E. Aprile et al.), "XENON100 dark matter results from a combination of 477 live days," *Phys. Rev. D*, vol. 94, no. 12, 2016. DOI: 10.1103/physrevd.94.122001.

[87] XENON collaboration (E. Aprile et al.), "First dark matter search results from the XENON1T experiment," *Phys. Rev. Lett.*, vol. 119, no. 18, 2017. DOI: 10.1103/physrevlett.119.181301.

[88] XENON collaboration (E. Aprile et al.), "Dark Matter Search Results from a One Tonne×Year Exposure of XENON1T," *Phys. Rev. Lett.*, vol. 121, no. 11, p. 111 302, 2018. DOI: 10.1103/PhysRevLett.121.111302.

[89] XENON collaboration (E. Aprile et al.), "First dark matter search with nuclear recoils from the XENONnT experiment," *Phys. Rev. Lett.*, vol. 131, p. 041 003, 4 2023. DOI: 10.1103/PhysRevLett.131.041003.

[90] XENON collaboration (E. Aprile et al.), "Projected WIMP sensitivity of the XENONnT dark matter experiment," *J. Cosmol. Astropart. Phys.*, vol. 11, P031, 2020. DOI: 10.1088/1475-7516/2020/11/031.

[91] LUX-ZEPLIN collaboration (D. Akerib et al.), "The LUX-ZEPLIN (LZ) experiment," *Nucl. Instrum. Meth. A*, vol. 953, p. 163 047, 2020. DOI: 10.1016/j.nima.2019.163047.

[92] PandaX collaboration (Y. Meng et al.), "Dark matter search results from the PandaX-4T commissioning run," *Phys. Rev. Lett.*, vol. 127, no. 26, 2021. DOI: 10.1103/physrevlett.127.261802.

[93] M. Auger et al., "The EXO-200 detector, part I: Detector design and construction," *JINST*, vol. 7, no. 05, P05010–P05010, 2012. DOI: 10.1088/1748-0221/7/05/p05010.

[94] G. Adhikari et al., "nEXO: Neutrinoless double beta decay search beyond 10^{28} year half-life sensitivity," *J. Phys. G*, vol. 49, no. 1, p. 015 104, 2021. DOI: 10.1088/1361-6471/ac3631.

[95] MEG II collaboration (A. M. Baldini et al.), "The design of the MEG II experiment," *Eur. Phys. J. C*, vol. 78, no. 5, 2018. DOI: 10.1140/epjc/s10052-018-5845-6.

[96] T. Iwamoto et al., "The liquid xenon detector for the MEG II experiment to detect 52.8 MeV γ with large area VUV-sensitive MPPCs," *Nucl. Instrum. Methods Phys. Res. A*, vol. 1046, p. 167 720, 2023. DOI: 10.1016/j.nima.2022.167720.

[97] RED collaboration (D. Akimov et al.), "The RED-100 experiment," *JINST*, vol. 17, no. 11, T11011, 2022. DOI: 10.1088/1748-0221/17/11/t11011.

[98] RELICS collaboration (C. Cai et al.), "Reactor neutrino liquid xenon coherent elastic scattering experiment," *Phys. Rev. D*, vol. 110, no. 7, 2024. DOI: 10.1103/physrevd.110.072011.

[99] PETALO collaboration (C. Romo-Luque), "PETALO: Time-of-flight PET with liquid xenon," *Nucl. Instrum. Methods Phys. Res. A*, vol. 958, p. 162 397, 2020. DOI: 10.1016/j.nima.2019.162397.

[100] PETALO collaboration (N. Salor-Iguiñiz et al.), "Evaluation of coincidence time resolution in a liquid xenon detector with silicon photomultipliers," *Phys. Rev. Res.*, vol. 7, no. 3, 2025. DOI: 10.1103/vy9h-twqf.

[101] A. Backues, J. Feng, M. Ni, and M. Zhong, "Design of a high-resolution liquid xenon detector for positron emission tomography," *Front. Detect. Sci. Technol.*, vol. 3, 2025. DOI: 10.3389/fdest.2025.1488822.

[102] L. Gallego Manzano et al., "XEMIS2: A liquid xenon detector for small animal medical imaging," *Nucl. Instrum. Methods Phys. Res. A*, vol. 912, pp. 329–332, 2018. DOI: 10.1016/j.nima.2017.12.022.

[103] E. Aprile and T. Doke, "Liquid Xenon Detectors for Particle Physics and Astrophysics," *Rev. Mod. Phys.*, vol. 82, p. 2053, 2010. DOI: 10.1103/RevModPhys.82.2053.

[104] V. Chepel and H. Araujo, "Liquid noble gas detectors for low energy particle physics," *JINST*, vol. 8, R04001, 2013. DOI: 10.1088/1748-0221/8/04/R04001.

[105] E. W. Lemmon, I. H. Bell, M. L. Huber, and M. O. McLinden, "Thermophysical properties of fluid systems," in *NIST Chemistry WebBook, NIST Standard Reference Database 69*, P. Linstrom, Ed., National Institute of Standards and Technology, 1997. DOI: 10.18434/T4D303.

[106] M. Berger, P. Bergstrom, J. Coursey, S. Seltzer, M. Zucker, and J. Chang, *Stopping-powers and range tables for electrons, protons, and helium ions, NIST standard reference database 124*, 2017. DOI: 10.18434/T4NC7P.

[107] M. Berger et al., *XCOM-photon cross sections database, NIST standard reference database 8*, en, 2010. DOI: 10.18434/T48G6X.

[108] Joint Evaluated Fission and Fusion Project, *JEFF-4.0 evaluated data: Neutron data*, 2025. DOI: 10.82555/E9AJN-A3P20.

[109] XENON collaboration (E. Aprile et al.), "Observation of two-neutrino double electron capture in ^{124}Xe with XENON1T," *Nature*, vol. 568, no. 7753, pp. 532–535, 2019. DOI: 10.1038/s41586-019-1124-4.

[110] XENON collaboration (E. Aprile, K. Abe, F. Agostini, S. Ahmed Maouloud, M. Alfonsi, L. Althueser, et al.), "Double-weak decays of ^{124}Xe and ^{136}Xe in the XENON1T and XENONnT experiments," *Phys. Rev. C*, vol. 106, no. 2, 2022. DOI: 10.1103/physrevc.106.024328.

[111] J. Aalbers et al., "Neutrinoless double beta decay sensitivity of the XLZD rare event observatory," *J. Phys. G: Nucl. Part. Phys.*, vol. 52, no. 4, p. 045 102, 2025. DOI: 10.1088/1361-6471/adb900.

[112] C. Adams et al., "Sensitivity of a tonne-scale NEXT detector for neutrinoless double-beta decay searches," *J. High Energy Phys.*, vol. 2021, no. 8, 2021. DOI: 10.1007/jhep08(2021)164.

[113] J. S. Coursey, D. J. Schwab, J. J. Tsai, and R. A. Dragoset, *NIST physical measurement laboratory*, 2015.

[114] XMASS collaboration (K. Abe et al.), "Improved search for two-neutrino double electron capture on ^{124}Xe and ^{126}Xe using particle identification in XMASS-I," *Prog. Theor. Exp. Phys.*, vol. 2018, no. 5, 2018. DOI: 10.1093/ptep/pty053.

[115] PandaX collaboration (X. Yan et al.), "Searching for two-neutrino and neutrinoless double beta decay of ^{134}Xe with the PandaX-4T experiment," *Phys. Rev. Lett.*, vol. 132, no. 15, 2024. DOI: 10.1103/physrevlett.132.152502.

[116] KamLAND-Zen collaboration (A. Gando et al.), "Precision analysis of the ^{136}Xe two-neutrino $\beta\beta$ spectrum in KamLAND-Zen and its impact on the quenching of nuclear matrix elements," *Phys. Rev. Lett.*, vol. 122, no. 19, 2019. DOI: 10.1103/physrevlett.122.192501.

[117] B. Lenardo, K. Kazkaz, A. Manalaysay, J. Mock, M. Szydagis, and M. Tripathi, "A global analysis of light and charge yields in liquid xenon," *IEEE Trans. Nucl. Sci.*, vol. 62, no. 6, pp. 3387–3396, 2015. DOI: 10.1109/tns.2015.2481322.

[118] XENON collaboration (P. Sorensen et al.), "The scintillation and ionization yield of liquid xenon for nuclear recoils," *Nucl. Instrum. Meth. A*, vol. 601, p. 339, 2009. DOI: 10.1016/j.nima.2008.12.197.

[119] P. Sorensen and C. E. Dahl, "Nuclear recoil energy scale in liquid xenon with application to the direct detection of dark matter," *Phys. Rev. D*, vol. 83, no. 6, 2011. DOI: 10.1103/physrevd.83.063501.

[120] K. Fujii et al., "High-accuracy measurement of the emission spectrum of liquid xenon in the vacuum ultraviolet region," *Nucl. Instrum. Meth.*, vol. A795, p. 293, 2015. DOI: 10.1016/j.nima.2015.05.065.

[121] I. Murayama and S. Nakamura, "Time profile of the scintillation from liquid and gaseous xenon," *Nucl. Instrum. Methods Phys. Res. A*, vol. 763, pp. 533–537, 2014. DOI: 10.1016/j.nima.2014.07.003.

[122] S. Kubota, M. Hishida, M. Suzuki, and J.-z. Ruan, "Liquid and solid argon, krypton and xenon scintillators," *Nucl. Instrum. Methods Phys. Res.*, vol. 196, no. 1, pp. 101–105, 1982. DOI: 10.1016/0029-554x(82)90623-1.

[123] A. Hitachi, T. Takahashi, N. Funayama, K. Masuda, J. Kikuchi, and T. Doke, "Effect of ionization density on the time dependence of luminescence from liquid argon and xenon," *Phys. Rev. B*, vol. 27, no. 9, pp. 5279–5285, 1983. DOI: 10.1103/physrevb.27.5279.

[124] D. Cichon, G. Eurin, F. Jörg, T. Marrodán Undagoitia, and N. Rupp, "Scintillation decay-time constants for alpha particles and electrons in liquid xenon," *Rev. Sci. Instrum.*, vol. 93, p. 113 302, 2022. DOI: 10.1063/5.0087216.

[125] S. Kubota, M. Hishida, M. Suzuki, and J.-z. Ruan(Gen), "Dynamical behavior of free electrons in the recombination process in liquid argon, krypton, and xenon," *Phys. Rev. B*, vol. 20, no. 8, pp. 3486–3496, 1979. DOI: 10.1103/physrevb.20.3486.

[126] U. Sowada, J. M. Warman, and M. P. de Haas, "Hot-electron thermalization in solid and liquid argon, krypton, and xenon," *Phys. Rev. B*, vol. 25, no. 5, pp. 3434–3437, 1982. DOI: 10.1103/physrevb.25.3434.

[127] M. Suzuki, J.-z. Ruan(Gen), and S. Kubota, "Time dependence of the recombination luminescence from high-pressure argon, krypton and xenon excited by alpha particles," *Nucl. Instrum. Methods Phys. Res.*, vol. 192, no. 2-3, pp. 565–574, 1982. DOI: 10.1016/0029-554x(82)90874-6.

[128] A. Mozumder, "Free-ion yield and electron-ion recombination rate in liquid xenon," *Chem. Phys. Lett.*, vol. 245, no. 4-5, pp. 359–363, 1995. DOI: 10.1016/0009-2614(95)01024-4.

[129] M. Szydagis et al., "NEST: A comprehensive model for scintillation yield in liquid xenon," *JINST*, vol. 6, no. 10, P10002, 2011. DOI: 10.1088/1748-0221/6/10/P10002.

[130] M. Szydagis et al., "A review of NEST models for liquid xenon and an exhaustive comparison with other approaches," *Front. Detect. Sci. Technol.*, vol. 2, 2025. DOI: 10.3389/fdest.2024.1480975.

[131] L. S. Miller, S. Howe, and W. E. Spear, "Charge transport in solid and liquid ar, kr, and xe," *Phys. Rev.*, vol. 166, no. 3, pp. 871–878, 1968. DOI: 10.1103/physrev.166.871.

[132] C. E. Dahl, "The physics of background discrimination in liquid xenon, and first results from XENON10 in the hunt for WIMP dark matter," Ph.D. dissertation, Princeton U., 2009.

[133] E. Conti et al., "Correlated fluctuations between luminescence and ionization in liquid xenon," *Phys. Rev. B*, vol. 68, no. 5, 2003. DOI: 10.1103/physrevb.68.054201.

[134] E. Aprile, K. L. Giboni, P. Majewski, K. Ni, and M. Yamashita, "Observation of anticorrelation between scintillation and ionization for MeV gamma rays in liquid xenon," *Phys. Rev. B*, vol. 76, no. 1, 2007. DOI: 10.1103/physrevb.76.014115.

[135] E. Aprile et al., "Simultaneous measurement of ionization and scintillation from nuclear recoils in liquid xenon for a dark matter experiment," *Phys. Rev. Lett.*, vol. 97, no. 8, 2006. DOI: 10.1103/physrevlett.97.081302.

[136] T. Doke, A. Hitachi, J. Kikuchi, K. Masuda, H. Okada, and E. Shibamura, "Absolute scintillation yields in liquid argon and xenon for various particles," *JJAP*, vol. 41, no. Part 1, No. 3A, pp. 1538–1545, 2002. DOI: 10.1143/jjap.41.1538.

[137] T. Takahashi et al., "Average energy expended per ion pair in liquid xenon," *Phys. Rev. A*, vol. 12, no. 5, pp. 1771–1775, 1975. DOI: 10.1103/physreva.12.1771.

[138] S. Farrell et al., *Nestcollaboration/nestpy: Update to v2.0.5*, 2025. DOI: 10.5281/ZENODO.15880627.

[139] XENON collaboration (E. Aprile et al.), "Radon removal in XENONnT down to the solar neutrino level," *Phys. Rev. X*, vol. 15, no. 3, 2025. DOI: 10.1103/zc1w-88p6.

[140] XENON collaboration (E. Aprile et al.), "Material radioassay and selection for the XENON1T dark matter experiment," *Eur. Phys. J. C*, vol. 77, no. 12, p. 890, 2017. DOI: 10.1140/epjc/s10052-017-5329-0.

[141] XENON collaboration (E. Aprile et al.), "Material radiopurity control in the XENONnT experiment," *Eur. Phys. J. C*, vol. 82, no. 7, p. 599, 2022. DOI: 10.1140/epjc/s10052-022-10345-6.

[142] L. Baudis et al., "Performance of the Hamamatsu R11410 photomultiplier tube in cryogenic xenon environments," *JINST*, vol. 8, no. 04, P04026–P04026, 2013. DOI: 10.1088/1748-0221/8/04/p04026.

[143] P. Barrow et al., "Qualification tests of the R11410-21 photomultiplier tubes for the XENON1T detector," *JINST*, vol. 12, no. 01, P01024–P01024, 2017. DOI: 10.1088/1748-0221/12/01/p01024.

[144] V. Antochi et al., "Improved quality tests of R11410-21 photomultiplier tubes for the XENONnT experiment," *JINST*, vol. 16, no. 08, P08033, 2021. DOI: 10.1088/1748-0221/16/08/p08033.

[145] V. R. Weidner and J. J. Hsia, "Reflection properties of pressed polytetrafluoroethylene powder," *J. Opt. Soc. Am.*, vol. 71, no. 7, pp. 856–861, 1981.

[146] XENON collaboration (E. Aprile et al.), "Search for new physics in electronic recoil data from XENONnT," *Phys. Rev. Lett.*, vol. 129, p. 161 805, 16 2022. DOI: 10.1103/PhysRevLett.129.161805.

[147] XENON collaboration (E. Aprile et al.), "Design and performance of the field cage for the XENONnT experiment," *Eur. Phys. J. C*, vol. 84, no. 2, p. 138, 2024. DOI: 10.1140/epjc/s10052-023-12296-y.

[148] XENON collaboration (E. Aprile et al.), "The neutron veto of the XENONnT experiment: Results with demineralized water," *Eur. Phys. J. C*, vol. 85, no. 6, 2025. DOI: 10.1140/epjc/s10052-025-14105-0.

[149] XENON collaboration (E. Aprile et al.), "Conceptual design and simulation of a water Cherenkov muon veto for the XENON1T experiment," *JINST*, vol. 9, no. 11, P11006–P11006, 2014. DOI: 10.1088/1748-0221/9/11/p11006.

[150] G. Plante, E. Aprile, J. Howlett, and Y. Zhang, "Liquid-phase purification for multi-tonne xenon detectors," *Eur. Phys. J. C*, vol. 82, no. 10, 2022. DOI: 10.1140/epjc/s10052-022-10832-w.

[151] XENON collaboration (E. Aprile et al.), "The liquid-phase xenon purification system of the XENONnT dark matter experiment," In preparation.

[152] XENON collaboration (E. Aprile et al.), "Removing krypton from xenon by cryogenic distillation to the ppq level," *Eur. Phys. J. C*, vol. 77, no. 5, 2017. DOI: 10.1140/epjc/s10052-017-4757-1.

[153] S. Lindemann and H. Simgen, "Krypton assay in xenon at the ppq level using a gas chromatographic system and mass spectrometer," *Eur. Phys. J. C*, vol. 74, no. 2, 2014. DOI: 10.1140/epjc/s10052-014-2746-1.

[154] M. Murra, D. Schulte, C. Huhmann, and C. Weinheimer, "Design, construction and commissioning of a high-flow radon removal system for XENONnT," *Eur. Phys. J. C*, vol. 82, no. 12, 2022. DOI: 10.1140/epjc/s10052-022-11001-9.

[155] M. Adrover et al., "Cosmogenic background simulations for neutrinoless double beta decay with the DARWIN observatory at various underground sites," *Eur. Phys. J. C*, vol. 84, no. 1, 2024. DOI: 10.1140/epjc/s10052-023-12298-w.

[156] F. Jörg, "From ^{222}Rn measurements in XENONnT and HeXe to radon mitigation in future liquid xenon experiments," Ph.D. dissertation, Ruprecht-Karls-Universität Heidelberg, 2022.

[157] S. Kravitz, H. Chen, R. Gibbons, S. J. Haselschwardt, Q. Xia, and P. Sorensen, "Operation and performance of a dual-phase crystalline/vapor xenon time projection chamber," *JINST*, vol. 17, no. 04, P04014, 2022. DOI: 10.1088/1748-0221/17/04/P04014.

[158] H. Chen, R. Gibbons, S. J. Haselschwardt, S. Kravitz, Q. Xia, and P. Sorensen, "Toward a neutrino-limited dark matter search with crystalline xenon," *Phys. Rev. D*, vol. 109, no. 7, 2024. DOI: 10.1103/physrevd.109.l071102.

[159] K. Sato et al., "Development of a dual-phase xenon TPC with a quartz chamber for direct dark matter searches," *Prog. Theor. Exp. Phys.*, vol. 2020, no. 11, 2020. DOI: 10.1093/ptep/ptaa141.

[160] Y. Wei, J. Long, F. Lombardi, Z. Jiang, J. Ye, and K. Ni, "Development and performance of a sealed liquid xenon time projection chamber," *JINST*, vol. 16, no. 01, P01018–P01018, 2021. DOI: 10.1088/1748-0221/16/01/p01018.

[161] J. Dierle et al., "Reduction of ^{222}Rn-induced backgrounds in a hermetic dual-phase xenon time projection chamber," *Eur. Phys. J. C*, vol. 83, no. 1, 2023. DOI: 10.1140/epjc/s10052-022-11151-w.

[162] T. Ye, K. Giboni, and X. Ji, "Initial evaluation of proportional scintillation in liquid xenon for direct dark matter detection," *JINST*, vol. 9, no. 12, P12007–P12007, 2014. DOI: 10.1088/1748-0221/9/12/p12007.

[163] J. Qi et al., "Low energy electronic recoils and single electron detection with a liquid xenon proportional scintillation counter," *JINST*, vol. 18, no. 07, P07027, 2023. DOI: 10.1088/1748-0221/18/07/p07027.

[164] F. Tönnies et al., "Proportional scintillation in liquid xenon: Demonstration in a single-phase liquid-only time projection chamber," *JINST*, vol. 19, no. 09, P09032, 2024. DOI: 10.1088/1748-0221/19/09/p09032.

[165] N. F. Bell, P. Cox, M. J. Dolan, J. L. Newstead, and A. C. Ritter, "Exploring light dark matter with the Migdal effect in hydrogen-doped liquid xenon," *Phys. Rev. D*, vol. 109, no. 9, 2024. DOI: 10.1103/physrevd.109.l091902.

[166] W. H. Lippincott et al., "HydroX, a light dark matter search with hydrogen-doped liquid xenon time projection chambers," *Comm. Phys.*, vol. 8, no. 1, 2025. DOI: 10.1038/s42005-025-02168-0.

[167] R. Itay et al., "DIREXENO — an apparatus for measuring correlated scintillation signatures in liquid xenon," *JINST*, vol. 15, no. 06, T06001–T06001, 2020. DOI: 10.1088/1748-0221/15/06/t06001.

[168] XENON collaboration (E. Aprile et al.), "XENONnT analysis: Signal reconstruction, calibration and event selection," *Phys. Rev. D*, vol. 111, no. 6, p. 062 006, 2025. DOI: 10.1103/PhysRevD.111.062006.

[169] XENON collaboration (E. Aprile et al.), "Excess electronic recoil events in XENON1T," *Phys. Rev. D*, vol. 102, no. 7, 2020. DOI: 10.1103/physrevd.102.072004.

[170] L. W. Kastens, S. B. Cahn, A. Manzur, and D. N. McKinsey, "Calibration of a liquid xenon detector with $^{83}Kr^{m}$," *Phys. Rev. C*, vol. 80, no. 4, 2009. DOI: 10.1103/physrevc.80.045809.

[171] LUX collaboration (D. S. Akerib et al.), "^{83m}Kr calibration of the 2013 LUX dark matter search," *Phys. Rev. D*, vol. 96, no. 11, 2017. DOI: 10.1103/physrevd.96.112009.

[172] A. Manalaysay et al., "Spatially uniform calibration of a liquid xenon detector at low energies using ^{83m}Kr," *Rev. Sci. Instrum.*, vol. 81, no. 7, 2010. DOI: 10.1063/1.3436636.

[173] R. Lang et al., "A ^{220}Rn source for the calibration of low-background experiments," *JINST*, vol. 11, no. 04, P04004–P04004, 2016. DOI: 10.1088/1748-0221/11/04/p04004.

[174] XENON collaboration (E. Aprile et al.), "Low-energy calibration of XENON1T with an internal ^{37}Ar source," *Eur. Phys. J. C*, vol. 83, no. 6, pp. 1–15, 2023. DOI: 10.1140/epjc/s10052-023-11512-z.

[175] D. Wenz, "Commissioning of the world's first water Cherenkov neutron veto and first WIMP dark matter search results of the XENONnT experiment," Ph.D. dissertation, Johannes Gutenberg-Universität Mainz, 2023. DOI: 10.25358/openscience-9654.

[176] J. I. Collar, "Applications of an ^{88}Y/Be photoneutron calibration source to dark matter and neutrino experiments," *Phys. Rev. Lett.*, vol. 110, no. 21, 2013. DOI: 10.1103/physrevlett.110.211101.

[177] XENON collaboration (E. Aprile et al.), "Low-energy nuclear recoil calibration of XENONnT with a ^{88}YBe photoneutron source," 2024. DOI: 10.48550/ARXIV.2412.10451.

[178] XENON collaboration (E. Aprile et al.), "The triggerless data acquisition system of the XENONnT experiment," *JINST*, vol. 18, no. 07, P07054, 2023. DOI: 10.1088/1748-0221/18/07/p07054.

[179] XENON collaboration (E. Aprile et al.), "XENON1T dark matter data analysis: Signal reconstruction, calibration, and event selection," *Phys. Rev. D*, vol. 100, p. 052 014, 5 2019. DOI: 10.1103/PhysRevD.100.052014.

[180] J. Aalbers et al., *AxFoundation/strax: v1.6.4*, 2024. DOI: 10.5281/ZENODO.11355772.

[181] XENON collaboration (J. R. Angevaare et al.), *XENONnT/straxen: v3.2.3*, 2025. DOI: 10.5281/ZENODO.16278327.

[182] L. Yuan, "First search for light dark matter in the neutrino fog with XENONnT," Ph.D. dissertation, The University of Chicago, 2025.

[183] XENON collaboration (J. Angle et al.), "Search for light dark matter in XENON10 data," *Phys. Rev. Lett.*, vol. 107, no. 5, 2011. DOI: 10.1103/physrevlett.107.051301.

[184] XENON collaboration (E. Aprile et al.), "Observation and applications of single-electron charge signals in the XENON100 experiment," *J. Phys. G*, vol. 41, p. 035 201, 2014. DOI: 10.1088/0954-3899/41/3/035201.

[185] XENON collaboration (E. Aprile et al.), "Emission of single and few electrons in XENON1T and limits on light dark matter," *Phys. Rev. D*, vol. 106, no. 2, 2022. DOI: 10.1103/physrevd.106.022001.

[186] XENON collaboration (E. Aprile et al.), "Search for light dark matter in low-energy ionization signals from XENONnT," *Phys. Rev. Lett.*, vol. 134, no. 16, 2025. DOI: 10.1103/physrevlett.134.161004.

[187] LUX collaboration (D. S. Akerib et al.), "Investigation of background electron emission in the LUX detector," *Phys. Rev. D*, vol. 102, no. 9, 2020. DOI: 10.1103/physrevd.102.092004.

[188] XENON collaboration (D. Xu et al.), *XENONnT/appletree: v0.5.4*, 2025. DOI: 10.5281/ZENODO.14794915.

[189] D. Foreman-Mackey, D. W. Hogg, D. Lang, and J. Goodman, "Emcee: The MCMC hammer," *PASP*, vol. 125, no. 925, p. 306, 2013. DOI: 10.1086/670067.

[190] XENON collaboration (R. Hammann et al.), *XENONnT/GOFevaluation: v0.1.5*, 2024. DOI: 10.5281/ZENODO.14562711.

[191] R. Hammann, "Investigation of a charge insensitive volume in XENONnT, analysis of goodness-of-fit techniques, and feasibility studies for an automated krypton assay system," Master's thesis, 2022. DOI: 10.5281/ZENODO.13946149.

[192] A. Manzur, A. Curioni, L. Kastens, D. N. McKinsey, K. Ni, and T. Wongjirad, "Scintillation efficiency and ionization yield of liquid xenon for mono-energetic nuclear recoils down to 4 keV," *Phys. Rev. C*, vol. 81, p. 025 808, 2010. DOI: 10.1103/PhysRevC.81.025808.

[193] G. Plante et al., "New measurement of the scintillation efficiency of low-energy nuclear recoils in liquid xenon," *Phys. Rev. C*, vol. 84, p. 045 805, 2011. DOI: 10.1103/PhysRevC.84.045805.

[194] LUX collaboration (D. S. Akerib et al.), "Low-energy (0.7-74 keV) nuclear recoil calibration of the LUX dark matter experiment using D-D neutron scattering kinematics," *preprint*, 2016. arXiv: 1608.05381 [physics.ins-det].

[195] LUX collaboration (D. S. Akerib et al.), "Nuclear recoil calibration at sub-keV energies in LUX and its impact on dark matter search sensitivity," *Phys. Rev. Lett.*, vol. 134, no. 6, 2025. DOI: 10.1103/physrevlett.134.061002.

[196] B. Lenardo et al., "Measurement of the ionization yield from nuclear recoils in liquid xenon between 0.3 – 6 kev with single-ionization-electron sensitivity," 2019. DOI: 10.48550/ARXIV.1908.00518.

[197] E. Aprile et al., "Scintillation response of liquid xenon to low energy nuclear recoils," *Phys. Rev. D*, vol. 72, p. 072 006, 2005. DOI: 10.1103/PhysRevD.72.072006.

[198] E. Aprile et al., "New measurement of the relative scintillation efficiency of xenon nuclear recoils below 10 kev," *Phys. Rev. C*, vol. 79, no. 4, 2009. DOI: 10.1103/physrevc.79.045807.

[199] XENON collaboration (E. Aprile et al.), "Response of the XENON100 Dark Matter Detector to Nuclear Recoils," *Phys. Rev. D*, vol. 88, p. 012 006, 2013. DOI: 10.1103/PhysRevD.88.012006.

[200] XENON collaboration (E. Aprile et al.), "XENON1T dark matter data analysis: Signal and background models and statistical inference," *Phys. Rev. D*, vol. 99, p. 112 009, 11 2019. DOI: 10.1103/PhysRevD.99.112009.

[201] C. McCabe, "The earth's velocity for direct detection experiments," *J. Cosmol. Astropart. Phys.*, vol. 02, p. 027, 2014. DOI: 10.1088/1475-7516/2014/02/027.

[202] R. Schoenrich, J. Binney, and W. Dehnen, "Local kinematics and the local standard of rest," *Mon. Not. Roy. Astron. Soc.*, vol. 403, p. 1829, 2010. DOI: 10.1111/j.1365-2966.2010.16253.x.

[203] J. Bland-Hawthorn and O. Gerhard, "The galaxy in context: Structural, kinematic, and integrated properties," *Annu. Rev. Astron. Astrophys.*, vol. 54, pp. 529–596, 2016. DOI: https://doi.org/10.1146/annurev-astro-081915-023441.

[204] GRAVITY collaboration (R. Abuter et al.), "Improved GRAVITY astrometric accuracy from modeling optical aberrations," *A&A*, vol. 647, A59, 2021. DOI: 10.1051/0004-6361/202040208.

[205] R. H. Helm, "Inelastic and elastic scattering of 187-MeV electrons from selected even-even nuclei," *Phys. Rev.*, vol. 104, no. 5, p. 1466, 1956. DOI: 10.1103/PhysRev.104.1466.

[206] XENON collaboration (E. Aprile, J. Aalbers, F. Agostini, M. Alfonsi, L. Althueser, et al.), "Constraining the spin-dependent WIMP-nucleon cross sections with XENON1T," *Phys. Rev. Lett.*, vol. 122, no. 14, 2019. DOI: 10.1103/physrevlett.122.141301.

[207] SNO collaboration (B. Aharmim et al.), "Combined analysis of all three phases of solar neutrino data from the Sudbury Neutrino Observatory," *Phys. Rev. C*, vol. 88, p. 025 501, 2013. DOI: 10.1103/PhysRevC.88.025501.

[208] J. N. Bahcall, E. Lisi, D. E. Alburger, L. De Braeckeleer, S. J. Freedman, and J. Napolitano, "Standard neutrino spectrum ^{8}B decay," *Phys. Rev. C*, vol. 54, no. 1, pp. 411–422, 1996. DOI: 10.1103/physrevc.54.411.

[209] J. Barranco, O. G. Miranda, and T. I. Rashba, "Probing new physics with coherent neutrino scattering off nuclei," *Journal of High Energy Physics*, vol. 2005, no. 12, pp. 021–021, 2005. DOI: 10.1088/1126-6708/2005/12/021.

[210] J. L. Newstead, R. F. Lang, and L. E. Strigari, "Atmospheric neutrinos in next-generation xenon and argon dark matter experiments," *Phys. Rev. D*, vol. 104, no. 11, 2021. DOI: 10.1103/physrevd.104.115022.

[211] D. G. Madland et al., *SOURCES 4A: A code for calculating (alpha,n), spontaneous fission, and delayed neutron sources and spectra*, 1999. DOI: 10.2172/15215.

[212] PandaX collaboration (A. Abdukerim et al.), "Study of background from accidental coincidence signalsin the PandaX-II experiment," *Chinese Physics C*, vol. 46, no. 10, p. 103 001, 2022. DOI: 10.1088/1674-1137/ac7cd8.

[213] D. Akimov et al., "Peculiarities of the Hamamatsu R11410-20 photomultiplier tubes," *Proc. Sci.*, vol. PhotoDet2015, p. 025, 2016. DOI: 10.22323/1.252.0025.

[214] P.-S. Shaw, Z. Li, U. Arp, and K. R. Lykke, "Ultraviolet characterization of integrating spheres," *Appl. Opt.*, vol. 46, no. 22, pp. 5119–5128, 2007. DOI: 10.1364/AO.46.005119.

[215] LUX collaboration (D. S. Akerib et al.), "Extending light WIMP searches to single scintillation photons in LUX," *Phys. Rev. D*, vol. 101, no. 4, 2020. DOI: 10.1103/physrevd.101.042001.

[216] T. Pollmann, private communication, 2025.

[217] P. Sorensen and R. Gibbons, "Quartz fluorescence backgrounds in xenon particle detectors," *Phys. Rev. D*, vol. 112, no. 5, 2025. DOI: 10.1103/lsmf-pm5g.

[218] PandaX collaboration (S. Li, M. Wu, A. Abdukerim, Z. Bo, W. Chen, X. Chen, et al.), "Search for light dark matter with ionization signals in the PandaX-4T experiment," *Phys. Rev. Lett.*, vol. 130, no. 26, 2023. DOI: 10.1103/physrevlett.130.261001.

[219] P. Sorensen, "Electron train backgrounds in liquid xenon dark matter search detectors are indeed due to thermalization and trapping," 2017. DOI: 10.48550/ARXIV.1702.04805. arXiv: 1702.04805.

[220] A. Kopec et al., "Correlated single- and few-electron backgrounds milliseconds after interactions in dual-phase liquid xenon time projection chambers," *JINST*, vol. 16, no. 07, P07014, 2021. DOI: 10.1088/1748-0221/16/07/p07014.

[221] P. Sorensen and K. Kamdin, "Two distinct components of the delayed single electron noise in liquid xenon emission detectors," *JINST*, vol. 13, no. 02, P02032–P02032, 2018. DOI: 10.1088/1748-0221/13/02/p02032.

[222] A. Buzulutskov, E. Frolov, E. Borisova, V. Nosov, V. Oleynikov, and A. Sokolov, "Unraveling the puzzle of slow components in gaseous argon of two-phase detectors for dark matter searches using thick gas electron multiplier," *Eur. Phys. J. C*, vol. 83, no. 9, 2023. DOI: 10.1140/epjc/s10052-023-12037-1.

[223] A. Buzulutskov, E. Frolov, E. Borisova, V. Nosov, V. Oleynikov, and A. Sokolov, "Possible evidence for the production of Ar_2^{*-} metastable negative molecular ions in gaseous argon of two-phase detectors for dark matter searches," *Eur. Phys. J. C*, vol. 83, no. 10, 2023. DOI: 10.1140/epjc/s10052-023-12088-4.

[224] XENON collaboration (D. Xu), *XENONnT/axidence: v0.4.0*, 2025. DOI: 10.5281/ZENODO.15459357.

[225] C. Ferrari, "Radon-induced lead isotopes in XENONnT: Studies on branching ratios and surface background," Ph.D. dissertation, Gran Sasso Science Institute, 2025.

[226] J. R. Klein and A. Roodman, "Blind analysis in nuclear and particle physics," *Annu. Rev. Nucl. Part. Sci.*, vol. 55, no. 1, p. 141, 2005. DOI: 10.1146/annurev.nucl.55.090704.151521.

[227] K. D. Morå, "Statistical modelling and inference for XENON1T," Ph.D. dissertation, Department of Physics, Stockholm University, 2019.

[228] G. J. Feldman and R. D. Cousins, "Unified approach to the classical statistical analysis of small signals," *Phys. Rev. D*, vol. 57, no. 7, p. 3873, 1998. DOI: 10.1103/PhysRevD.57.3873.

[229] S. S. Wilks, "The large-sample distribution of the likelihood ratio for testing composite hypotheses," *Ann. Math. Stat.*, vol. 9, no. 1, pp. 60–62, 1938. DOI: 10.1214/aoms/1177732360.

[230] S. Algeri, J. Aalbers, K. Morå, and J. Conrad, "Searching for new phenomena with profile likelihood ratio tests," English (US), *Nat. Rev. Phys.*, vol. 2, no. 5, pp. 245–252, 2020. DOI: 10.1038/s42254-020-0169-5.

[231] H. Chernoff, "On the Distribution of the Likelihood Ratio," *Ann. Math. Stat.*, vol. 25, pp. 573–578, 1954. DOI: 10.1214/aoms/1177728725.

[232] G. Cowan, K. Cranmer, E. Gross, and O. Vitells, "Asymptotic formulae for likelihood-based tests of new physics," *Eur. Phys. J. C*, vol. 71, no. 2, p. 1554, 2011. DOI: 10.1140/epjc/s10052-011-1554-0.

[233] XENON collaboration (D. Xu et al.), *XENONnT/alea: v0.3.4*, version v0.3.4, 2025. DOI: 10.5281/ZENODO.15724823.

[234] J. Aalbers, K. D. Morå, R. Hammann, B. Pelssers, D. Xu, and A. Brown, *JelleAalbers/blueice: v1.2.1*, 2024. DOI: 10.5281/ZENODO.14390807.

[235] A. L. Read, "Presentation of search results: The cls technique," *J. Phys. G: Nucl. Part. Phys.*, vol. 28, no. 10, p. 2693, 2002. DOI: 10.1088/0954-3899/28/10/313.

[236] V. L. Kashyap et al., "On computing upper limits to source intensities," *ApJ*, vol. 719, no. 1, p. 900, 2010. DOI: 10.1088/0004-637x/719/1/900.

[237] A. V. Lokhov and F. V. Tkachov, "Confidence intervals with a priori parameter bounds," *Phys. Part. Nucl.*, vol. 46, no. 3, pp. 347–365, 2015. DOI: 10.1134/S1063779615030089.

[238] G. Cowan, K. Cranmer, E. Gross, and O. Vitells, "Power-constrained limits," *preprint*, 2011. arXiv: 1105.3166 [physics.data-an].

[239] LUX-ZEPLIN collaboration (J. Aalbers et al.), "First dark matter search results from the LUX-ZEPLIN (LZ) experiment," *Phys. Rev. Lett.*, vol. 131, no. 4, 2023. DOI: 10.1103/physrevlett.131.041002.

[240] D. J. Temples et al., "Measurement of charge and light yields for ^{127}Xe L-shell electron captures in liquid xenon," *Phys. Rev. D*, vol. 104, no. 11, p. 112 001, 2021. DOI: 10.1103/PhysRevD.104.112001.

[241] LUX-ZEPLIN collaboration (J. Aalbers et al.), "Measurements and models of enhanced recombination following inner-shell vacancies in liquid xenon," *Phys. Rev. D*, vol. 112, no. 1, 2025. DOI: 10.1103/447w-94h3.

[242] E. Hogenbirk, M. Decowski, K. McEwan, and A. Colijn, "Field dependence of electronic recoil signals in a dual-phase liquid xenon time projection chamber," *JINST*, vol. 13, no. 10, P10031–P10031, 2018. DOI: 10.1088/1748-0221/13/10/p10031.

[243] J. B. Albert et al., "Measurement of the drift velocity and transverse diffusion of electrons in liquid xenon with the EXO-200 detector," *Phys. Rev. C*, vol. 95, no. 2, 2017. DOI: 10.1103/physrevc.95.025502.

[244] LUX-ZEPLIN collaboration (D. S. Akerib et al.), "Projected wimp sensitivity of the lux-zeplin dark matter experiment," *Phys. Rev. D*, vol. 101, p. 052 002, 5 2020. DOI: 10.1103/PhysRevD.101.052002.

[245] G. Cowan, *Statistical data analysis*. Oxford University Press, USA, 1998.

[246] L. Lista, *Statistical Methods for Data Analysis in Particle Physics*. Springer International Publishing, 2016, ISBN: 9783319201764. DOI: 10.1007/978-3-319-20176-4.

[247] S. Baker and R. D. Cousins, "Clarification of the use of chi-square and likelihood functions in fits to histograms," *Nucl. Instrum. Methods Phys. Res.*, vol. 221, no. 2, pp. 437–442, 1984. DOI: 10.1016/0167-5087(84)90016-4.

[248] J. G. Heinrich, "The log likelihood ratio of the poisson distribution for small mu," CDF Note 5718, Tech. Rep., 2001.

[249] T. W. Anderson and D. A. Darling, "Asymptotic theory of certain "goodness of fit" criteria based on stochastic processes," *The annals of mathematical statistics*, pp. 193–212, 1952.

[250] PICO collaboration (C. Amole et al.), "Dark Matter Search Results from the Complete Exposure of the PICO-60 C_3F_8 Bubble Chamber," *Phys. Rev. D*, vol. 100, no. 2, p. 022 001, 2019. DOI: 10.1103/PhysRevD.100.022001.

[251] PandaX collaboration (Z. Bo et al.), "First indication of solar ^{8}B neutrinos through coherent elastic neutrino-nucleus scattering in PandaX-4T," *Physical Review Letters*, vol. 133, no. 19, 2024. DOI: 10.1103/physrevlett.133.191001.

[252] XENON collaboration (E. Aprile et al.), "Search for Coherent Elastic Scattering of Solar B 8 Neutrinos in the XENON1T Dark Matter Experiment," en, *Phys. Rev. Lett.*, vol. 126, no. 9, p. 091 301, 2021. DOI: 10.1103/PhysRevLett.126.091301. Accessed: Apr. 12, 2022.

[253] COHERENT collaboration (D. Akimov et al.), "Measurement of the coherent elastic neutrino-nucleus scattering cross section on CsI by COHERENT," *Phys. Rev. Lett.*, vol. 129, no. 8, 2022. DOI: 10.1103/physrevlett.129.081801.

[254] T. N. Maity and C. Bœhm, "First constraint on the weak mixing angle using direct detection experiments," *Phys. Rev. D*, vol. 112, no. 5, 2025. DOI: 10.1103/1lgl-bx7v.

[255] V. De Romeri, D. K. Papoulias, and C. A. Ternes, "Bounds on new neutrino interactions from the first CEνNS data at direct detection experiments," *Journal of Cosmology and Astroparticle Physics*, vol. 2025, no. 05, p. 012, 2025. DOI: 10.1088/1475-7516/2025/05/012.

[256] G. Li, C.-Q. Song, F.-J. Tang, and J.-H. Yu, "Constraints on neutrino nonstandard interactions from COHERENT, PandaX-4T and XENONnT," *Phys. Rev. D*, vol. 111, no. 3, 2025. DOI: 10.1103/physrevd.111.035002.

[257] D. A. Sierra, N. Mishra, and L. Strigari, "Implications of first neutrino-induced nuclear recoil measurements in direct detection experiments: Probing nonstandard interaction via CEνNS," *Phys. Rev. D*, vol. 111, no. 5, 2025. DOI: 10.1103/physrevd.111.055007.

[258] A. Majumdar, D. K. Papoulias, H. Prajapati, and R. Srivastava, "Constraining low scale dark hypercharge symmetry at spallation, reactor, and dark matter direct detection experiments," *Phys. Rev. D*, vol. 111, no. 7, 2025. DOI: 10.1103/physrevd.111.073006.

[259] P. Blanco-Mas et al., "Clarity through the neutrino fog: Constraining new forces in dark matter detectors," *J. High Energy Phys.*, vol. 2025, no. 8, 2025. DOI: 10.1007/jhep08(2025)043.

[260] J. Liao, J. Tang, and B.-L. Zhang, "Tensor interaction in coherent elastic neutrino-nucleus scattering," *Phys. Rev. D*, vol. 112, no. 3, 2025. DOI: 10.1103/19yb-tstx.

[261] V. De Romeri, D. Papoulias, G. Sanchez Garcia, C. Ternes, and M. Tórtola, "Neutrino electromagnetic properties and sterile dipole portal in light of the first solar CEνNS data," *J. Cosmol. Astropart. Phys.*, vol. 2025, no. 05, p. 080, 2025. DOI: 10.1088/1475-7516/2025/05/080.

[262] XENON collaboration (J. Ye), "Progress of solar *pp* neutrino search with XENONnT," in *Topics in Astroparticle and Underground Physics (TAUP) conference*, 2025.

[263] BOREXINO collaboration (M. Agostini et al.), "Comprehensive measurement of *pp*-chain solar neutrinos," *Nature*, vol. 562, no. 7728, p. 505, 2018. DOI: 10.1038/s41586-018-0624-y.

[264] L. Baudis, A. Ferella, A. Kish, A. Manalaysay, T. M. Undagoitia, and M. Schumann, "Neutrino physics with multi-ton scale liquid xenon detectors," *J. Cosmol. Astropart. Phys.*, vol. 2014, no. 01, pp. 044–044, 2014. DOI: 10.1088/1475-7516/2014/01/044.

[265] J. L. Newstead, L. E. Strigari, and R. F. Lang, "Detecting CNO solar neutrinos in next-generation xenon dark matter experiments," *Phys. Rev. D*, vol. 99, no. 4, 2019. DOI: 10.1103/physrevd.99.043006.

[266] P. Moutard, P. Laporte, J.-L. Subtil, N. Damany, and H. Damany, "Pressure effects on kinetics and decay processes in xenon after selective photoexcitation," *J. Chem. Phys.*, vol. 88, no. 12, pp. 7485–7500, 1988. DOI: 10.1063/1.454313.

[267] P. Millet et al., "Time resolved study of the uv and near uv continuums of xenon," *J. Chem. Phys.*, vol. 69, p. 92, 1978. DOI: https://doi.org/10.1063/1.436349.

[268] C. Jonin and F. Spiegelmann, "Pseudopotential hole-particle formalism for excitations in xenon molecules and clusters. II. the electronic structure of Xe_2^*," *The Journal of Chemical Physics*, vol. 117, no. 7, pp. 3059–3073, 2002. DOI: 10.1063/1.1491400.

[269] W. C. Ermler, Y. S. Lee, K. S. Pitzer, and N. W. Winter, "Ab initio effective core potentials including relativistic effects. II. potential energy curves for Xe_2, Xe_2^+, and Xe_2^*," *J. Chem. Phys.*, vol. 69, no. 3, pp. 976–983, 1978. DOI: 10.1063/1.436650.

[270] C. Jonin, P. Laporte, and F. Spiegelmann, "Pseudopotential hole-particle formalism for excitations in xenon molecules and clusters. I. theory, atomic and molecular tests," *J. Chem. Phys.*, vol. 117, no. 7, pp. 3049–3058, 2002. DOI: 10.1063/1.1491399.

[271] J. Sansonetti, *Handbook of basic atomic spectroscopic data, NIST standard reference database 108*, 2003. DOI: 10.18434/T4FW23.

[272] P. F. Bernath, *Spectra of Atoms and Molecules*. Oxford University PressNew York, 2025, ISBN: 9780197754528. DOI: 10.1093/oso/9780197754498.001.0001.

[273] R. J. Munn, "Interaction potential of the inert gases. I," *J. Chem. Phys.*, vol. 40, no. 5, pp. 1439–1446, 1964. DOI: 10.1063/1.1725331.

[274] W. Demtröder, *Atoms, Molecules and Photons: An Introduction to Atomic-, Molecular- and Quantum Physics*. Springer Berlin Heidelberg, 2018, ISBN: 9783662555231. DOI: 10.1007/978-3-662-55523-1.

[275] H. A. Koehler, L. J. Ferderber, D. L. Redhead, and P. J. Ebert, "Vacuum-ultraviolet emission from high-pressure xenon and argon excited by high-current relativistic electron beams," *Phys. Rev. A*, vol. 9, pp. 768–781, 2 1974. DOI: 10.1103/PhysRevA.9.768.

[276] A. F. Borghesani, G. Carugno, and I. Mogentale, "Infrared emission spectrum and potentials of 0_u^+ and 0_g^+ states of Xe_2 excimers produced by electron impact," *J. Phys. B*, vol. 40, no. 24, p. 4551, 2007. DOI: 10.1088/0953-4075/40/24/001.

[277] P. K. Leichner, K. F. Palmer, J. Cook, and M. Thieneman, "Two-and three-body collision coefficients for $Xe(^3P_1)$ and $Xe(^3P_2)$ atoms and radiative lifetime of the $Xe_2(1_u)$ molecule," *Phys. Rev. A*, vol. 13, no. 5, p. 1787, 1976.

[278] Y. Salamero et al., "Multiphoton excitation near the $6s'(1/2)_1(^1P_1)$ resonant state of xenon. spectroscopic study and temporal analysis of the post-luminescence," *J. Phys. B: At. Mol. Opt. Phys.*, vol. 21, no. 11, pp. 2015–2025, 1988. DOI: 10.1088/0953-4075/21/11/016.

[279] R. Brodmann and G. Zimmerer, "Vacuum-ultraviolet fluorescence under monochromatic excitation and collision processes in gaseous Kr and Xe," *J. Phys. B: At. Mol. Phys.*, vol. 10, no. 17, pp. 3395–3408, 1977. DOI: 10.1088/0022-3700/10/17/014.

[280] T. D. Bonifield, F. H. K. Rambow, G. K. Walters, M. V. McCusker, D. C. Lorents, and R. A. Gutcheck, "Time resolved spectroscopy of xenon excimers excited by synchrotron radiation," *J. Chem. Phys.*, vol. 72, no. 5, pp. 2914–2924, 1980. DOI: 10.1063/1.439490.

[281] N. Basov et al., "Luminescence of condensed Xe, Kr, Ar and their mixtures in vacuum region of spectrum under excitation by fast electrons," *J. Lumin.*, vol. 1-2, pp. 834–841, 1970. DOI: 10.1016/0022-2313(70)90095-5.

[282] D. Varding, I. Reimand, and G. Zimmerer, "Time-resolved luminescence of exciton-polaritons in solid xenon," *Phys. Stat. Sol. (b)*, vol. 185, no. 1, pp. 301–318, 1994. DOI: 10.1002/pssb.2221850126.

[283] J. Jortner, L. Meyer, S. A. Rice, and E. G. Wilson, "Localized excitations in condensed Ne, Ar, Kr, and Xe," *J. Chem. Phys.*, vol. 42, no. 12, pp. 4250–4253, 1965. DOI: 10.1063/1.1695927.

[284] S. Leardini et al., "Time and band-resolved scintillation in time projection chambers based on gaseous xenon," *Eur. Phys. J. C*, vol. 82, no. 5, p. 425, 2022. DOI: 10.1140/epjc/s10052-022-10385-y.

[285] J. W. Keto, R. E. Gleason, and G. K. Walters, "Production mechanisms and radiative lifetimes of argon and xenon molecules emitting in the ultraviolet," *Phys. Rev. Lett.*, vol. 33, no. 23, pp. 1365–1368, 1974. DOI: 10.1103/physrevlett.33.1365.

[286] R. Henck and A. Coche, "Studies on noble gas scintillators," *IEEE Trans. Nucl. Sci.*, vol. 14, no. 1, pp. 478–486, 1967. DOI: 10.1109/tns.1967.4324458.

[287] A. M. Boĭchenko, V. F. Tarasenko, E. A. Fomin, and S. I. Yakovlenko, "Broadband emission continua in rare gases and in mixtures of rare gases with halides," *Quantum Electron.*, vol. 23, no. 1, pp. 3–25, 1993. DOI: 10.1070/qe1993v023n01abeh002929.

[288] H. Langhoff, "The origin of the third continua emitted by excited rare gases," *Opt. Commun.*, vol. 68, no. 1, pp. 31–34, 1988. DOI: 10.1016/0030-4018(88)90008-9.

[289] J. Wieser, A. Ulrich, A. Fedenev, and M. Salvermoser, "Novel pathways to the assignment of the third rare gas excimer continua," *Opt. Commun.*, vol. 173, no. 1-6, pp. 233–245, 2000. DOI: 10.1016/s0030-4018(99)00610-0.

[290] R. S. Mulliken, "Potential curves of diatomic rare-gas molecules and their ions, with particular reference to xe_2," *J. Chem. Phys.*, vol. 52, no. 10, p. 5170, 1970. DOI: 10.1063/1.1672756.

[291] P. Lindblom and O. Solin, "Atomic near-infrared noble gas scintillations I," *Nucl. Instrum. Methods Phys. Res. A*, vol. 268, no. 1, pp. 204–208, 1988. DOI: 10.1016/0168-9002(88)90607-9.

[292] G. Carugno, "Infrared emission in gaseous media induced by ionizing particles and by drifting electrons," *Nucl. Instrum. Meth.*, vol. 419, no. A2, p. 617, 1998. DOI: 10.1016/S0168-9002(98)00840-7.

[293] S. Belogurov, G. Bressi, G. Carugno, E. Conti, D. Iannuzzi, and A. Meneguzzo, "Measurement of the light yield of infrared scintillation in xenon gas," *Nucl. Instrum. Meth. A*, vol. 452, no. 1, p. 167, 2000. DOI: https://doi.org/10.1016/S0168-9002(00)00358-2.

[294] C. Henriques, J. Teixeira, P. Silva, R. Mano, J. dos Santos, and C. Monteiro, "Understanding the xenon primary scintillation yield for cutting-edge rare event experiments," *J. Cosmol. Astropart. Phys.*, vol. 2024, no. 06, p. 041, 2024. DOI: 10.1088/1475-7516/2024/06/041.

[295] A. F. Borghesani, G. Bressi, G. Carugno, E. Conti, and D. Iannuzzi, "Infrared fluorescence of Xe_2 molecules in electron/proton beam excited pure Xe gas and in an Ar/Xe gas mixture," *J. Chem. Phys.*, vol. 115, no. 13, p. 6042, 2001. DOI: 10.1063/1.1398307.

[296] A. F. Borghesani, G. Carugno, and I. Mogentale, "Low- and high-density features of IR luminescence of Xe_2 excimers produced by electron impact," *Physica Scripta*, vol. 76, no. 3, p. C84, 2007. DOI: 10.1088/0031-8949/76/3/N13.

[297] A. F. Borghesani, G. Carugno, and F. Chiossi, "Near-infrared cathodoluminescence of Xe_2 excimers in dense gaseous mixtures," *Front. Detect. Sci. Technol.*, vol. Volume 3 - 2025, 2025. DOI: 10.3389/fdest.2025.1580297.

[298] G. Bressi, G. Carugno, E. Conti, C. Noce, and D. Iannuzzi, "Infrared scintillation: A comparison between gaseous and liquid xenon," *Nucl. Instrum. Meth. A*, vol. 461, no. 1, p. 378, 2001, 8th Pisa Meeting on Advanced Detectors. DOI: https://doi.org/10.1016/S0168-9002(00)01249-3.

[299] G. Bressi, G. Carugno, E. Conti, D. Iannuzzi, and A. Meneguzzo, "Infrared scintillation in liquid Ar and Xe," *Nucl. Instrum. Meth.*, vol. A440, no. 1, p. 254, 2000. DOI: 10.1016/S0168-9002(99)01021-9.

[300] W. M. Bonivento and F. Terranova, "The science and technology of liquid argon detectors," *RMP*, vol. 96, no. 4, 2024. DOI: 10.1103/revmodphys.96.045001.

[301] A. Buzulutskov, A. Bondar, and A. Grebenuk, "Infrared scintillation yield in gaseous and liquid argon," *EPL*, vol. 94, no. 5, p. 52 001, 2011. DOI: 10.1209/0295-5075/94/52001.

[302] A. Bondar, A. Buzulutskov, A. Dolgov, A. Grebenuk, E. Shemyakina, and A. Sokolov, "Study of infrared scintillations in gaseous and liquid argon. part I: Methodology and time measurements," *JINST*, vol. 7, no. 06, P06015–P06015, 2012. DOI: 10.1088/1748-0221/7/06/p06015.

[303] A. Bondar et al., "Study of infrared scintillations in gaseous and liquid argon. part II: Light yield and possible applications," *JINST*, vol. 7, no. 06, P06014–P06014, 2012. DOI: 10.1088/1748-0221/7/06/p06014.

[304] C. Oliveira, P. Correia, A. Ferreira, S. Biagi, R. Veenhof, and J. Veloso, "Simulation of gaseous Ar and Xe electroluminescence in the near infra-red range," *Nucl. Instrum. Methods Phys. Res. A*, vol. 722, pp. 1–4, 2013. DOI: 10.1016/j.nima.2013.04.061.

[305] A. Neumeier et al., "Intense vacuum ultraviolet and infrared scintillation of liquid Ar-Xe mixtures," *EPL*, vol. 109, no. 1, p. 12 001, 2015. DOI: 10.1209/0295-5075/109/12001.

[306] J. Zhang, M. A. Itzler, H. Zbinden, and J.-W. Pan, "Advances in InGaAs/InP single-photon detector systems for quantum communication," *Light Sci. Appl.*, vol. 4, no. 5, e286–se286, 2015. DOI: 10.1038/lsa.2015.59.

[307] Hamamatsu Photonics K.K., *Photomultiplier Tubes - Basics and Applications - Fourth Edition*, Hamamatsu Photonics K.K., Ed., 2017.

[308] J. Xu, X. Xu, J. Tian, D. Luo, and D. Hui, "Numerical simulation study on quantum efficiency characteristics of InP/InGaAs/InP infrared photocathode," in *Infrared Technology and Applications, and Robot Sensing and Advanced Control*, vol. 10157, SPIE, 2016, p. 101573C. DOI: 10.1117/12.2247394.

[309] R. Saldanha, L. Grandi, Y. Guardincerri, and T. Wester, "Model independent approach to the single photoelectron calibration of photomultiplier tubes," *Nucl. Instrum. Methods Phys. Res. A*, vol. 863, pp. 35–46, 2017. DOI: 10.1016/j.nima.2017.02.086.

[310] M. Piotter, "Investigation of ^{83m}Kr decays and IR scintillation light in the noble gas xenon," Master's thesis, 2022.

[311] XENON collaboration (E. Aprile et al.), "Lowering the radioactivity of the photomultiplier tubes for the XENON1T dark matter experiment," *Eur. Phys. J. C*, vol. 75, no. 11, 2015. DOI: 10.1140/epjc/s10052-015-3657-5.

[312] COMSOL Inc., *Comsol multiphysics®user guide*, 2024.

[313] J. F. Ziegler, M. D. Ziegler, and J. P. Biersack, "SRIM - The stopping and range of ions in matter (2010)," *Nucl. Instrum. Meth. B*, vol. 268, p. 1818, 2010. DOI: 10.1016/j.nimb.2010.02.091.

[314] M. Basunia, "Nuclear data sheets for A = 237," *Nuclear Data Sheets*, vol. 107, no. 8, pp. 2323–2422, 2006. DOI: 10.1016/j.nds.2006.07.001.

[315] W. W. Coblentz, "Absorption, reflection, and dispersion constants of quartz," *Bull. NBS.*, vol. 11, no. 3, p. 471, 1915. DOI: 10.6028/bulletin.259.

[316] F. Jörg, D. Cichon, G. Eurin, L. Hötzsch, T. Marrodán Undagoitia, and N. Rupp, "Characterization of alpha and beta interactions in liquid xenon," *Eur. Phys. J. C*, vol. 82, no. 4, 2022. DOI: 10.1140/epjc/s10052-022-10259-3.

[317] D. Cichon, "Liquid xenon detector physics with XENON1T and HeXe: Electric noise stability, background discrimination studies and measurements of the scintillation pulse shape," Ph.D. dissertation, Ruprecht-Karls-Universität Heidelberg, 2021.

[318] L. M. Hötzsch, "Nuclear recoil modeling for the first XENONnT dark matter search results and electronic recoil yield measurements at low energies and fields," Ph.D. dissertation, Ruprecht-Karls-Universität Heidelberg, 2024.

[319] D. Cichon, G. Eurin, F. Jörg, T. M. Undagoitia, and N. Rupp, "Transmission of xenon scintillation light through PTFE," *JINST*, vol. 15, no. 09, P09010–P09010, 2020. DOI: 10.1088/1748-0221/15/09/p09010.

[320] S. Bruenner et al., "Radon daughter removal from PTFE surfaces and its application in liquid xenon detectors," *Europ. Phys. J. C*, vol. 81, no. 4, 2021. DOI: 10.1140/epjc/s10052-021-09047-2.

[321] N. M. R. E. Rupp, "Radon induced background in the XENON1T dark matter search experiment and studies on xenon purity in the HeXe system," Ph.D. dissertation, Ruprecht-Karls-Universität Heidelberg, 2020.

[322] G. Bakale, U. Sowada, and W. F. Schmidt, "Effect of an electric field on electron attachment to sulfur hexafluoride, nitrous oxide, and molecular oxygen in liquid argon and xenon," *J. Phys. Chem.*, vol. 80, no. 23, pp. 2556–2559, 1976. DOI: 10.1021/j100564a006.

[323] MiniCLEAN collaboration (M. Akashi-Ronquest et al.), "Triplet lifetime in gaseous argon," *Eur. Phys. J. A*, vol. 55, no. 10, 2019. DOI: 10.1140/epja/i2019-12867-2.

[324] M. A. Feio, A. J. P. L. Policarpo, and M. A. F. Alves, "Thresholds for secondary light emission by noble gases," *JJAP*, vol. 21, no. 8R, p. 1184, 1982. DOI: 10.1143/jjap.21.1184.

[325] C. Henriques et al., "Neutral bremsstrahlung emission in xenon unveiled," *Phys. Rev. X*, vol. 12, no. 2, p. 021 005, 2022.

[326] T. H. V. T. Dias, F. P. Santos, A. D. Stauffer, and C. A. N. Conde, "Monte carlo simulation of x-ray absorption and electron drift in gaseous xenon," *Phys. Rev. A*, vol. 48, no. 4, pp. 2887–2902, 1993. DOI: 10.1103/physreva.48.2887.

[327] NEXT collaboration (C. Adams et al.), "The NEXT-100 detector," *arXiv:2505.17848*, 2025. DOI: 10.48550/ARXIV.2505.17848.

[328] R. Bouet et al., "Simulation of a radial TPC for the detection of neutrinoless double beta decay," *Eur. Phys. J. C*, vol. 85, no. 7, 2025. DOI: 10.1140/epjc/s10052-025-14442-0.

[329] J. J. Gomez-Cadenas, F. Monrabal Capilla, and P. Ferrario, "High pressure gas xenon TPCs for double beta decay searches," *Front. Phys.*, vol. 7, 2019. DOI: 10.3389/fphy.2019.00051.

[330] C. Yu, Q. Xu, and J. Zhang, "Recent advances in InGaAs/InP single-photon detectors," *Meas. Sci. Technol.*, vol. 35, no. 12, p. 122 003, 2024. DOI: 10.1088/1361-6501/ad76ca.

[331] P. Martyniuk et al., "Infrared avalanche photodiodes from bulk to 2D materials," *Light Sci. Appl.*, vol. 12, no. 1, 2023. DOI: 10.1038/s41377-023-01259-3.

[332] R. L. Amey and R. H. Cole, "Dielectric constants of liquefied noble gases and methane," *J. Chem. Phys.*, vol. 40, no. 1, pp. 146–148, 1964. DOI: 10.1063/1.1724850.

[333] J. Marcoux, "Dielectric constants and indices of refraction of Xe, Kr, and Ar," *Can. J. Phys.*, vol. 48, no. 2, pp. 244–245, 1970. DOI: 10.1139/p70-033.

[334] E. Gushchin, A. Kruglov, and I. Obodovskii, "Electron dynamics in condensed argon and xenon," *Sov. Phys. JETP*, vol. 55, no. 55, p. 650, 1982.

Acknowledgements

Many people have supported, guided, and inspired me over the past three and a half years. These final lines are dedicated to all of you.

First, I would like to express my deepest gratitude to Prof. Dr. Teresa Marrodán Undagoitia for being the best supervisor I could have hoped for. Thank you for your unwavering guidance, for enabling me to grow scientifically while granting me the freedom to do so, and for always taking the time for inspiring discussions. I am also grateful to Prof. Dr. Dr. h.c. Manfred Lindner and Prof. Dr. Susanne Mertens for allowing me to work within the outstanding environment of the MPIK. My sincere thanks go to Prof. Dr. Belina von Krosigk for agreeing to referee this thesis and to Prof. Dr. Jörg Jäckel and Prof. Dr. Andreas Quirrenbach for their contributions as members of the thesis committee. A special thank-you goes to Prof. Dr. Stephanie Hansmann-Menzemer for her valuable advice as a member of my thesis advisory committee. I would also like to thank PD Dr. Loredana Gastaldo for an enjoyable semester tutoring the astroparticle physics lecture and for her continuous support and valuable advice throughout my scientific career.

My heartfelt thanks go to my wonderful colleagues at MPIK for making this journey so memorable. The fun discussions, Kicker sessions, and camaraderie made this journey truly special. A special mention to the entire HeXe team: Dr. Luisa Hötzsch, Dr. Florian Jörg, Dr. Dominick Cichon, Sophie Armbruster, Kai Böse, and Mona Piotter. I am especially grateful to Luisa, Florian, and Dominick for teaching me indispensable lab skills and making the time in the lab truly enjoyable – even when it is an emergency recuperation in the middle of the night. I also owe thanks to Dr. Tim Wolf for his guidance during the early stages of my PhD, and to Luisa, Florian, Matteo Guida, Dr. Giovanni Volta, Dr. Ying-Ting Lin, and Dr. Andrii Terliuk for the countless hours spent discussing XENON data analysis between the doors. I also want to thank Dr. Edgar Sánchez García for the great discussions on xenon and argon scintillation properties. A resounding "Hollaröhdulliöh" to Dr. Hardy Simgen for helpful input, especially everything related to the lab, and for organizing the most memorable group events. I owe immense gratitude to Steffen Form, Michael Reißfelder, Bettina Mörk, and the excellent electronic and mechanical workshops at MPIK. Their technical expertise ensured that I could measure the signals necessary for this work. I also want to thank Anja Berneiser and Britta Schwarz for their invaluable assistance in navigating bureaucratic hurdles.

A very big thank-you goes to the entire XENON family, whose support and collaboration greatly contributed to my development as a scientist. I am particularly grateful to Dr. Knut Dundas Morå, who patiently taught me much of what I know about statistics and provided invaluable guidance. I also want to thank Dr. Diego Ramírez García and Henning Schulze Eißing, with whom I had the pleasure of leading the Simulations, Modeling, and Statistics

team. Special thanks to the statistics enthusiasts – Dr. Pueh Leng Tan, Dr. Dominik Fuchs, Ananthu Ravindran, Dr. Knut Dundas Morå, Dr. Jelle Aalbers, Dr. Luisa Hötzsch, and Dr. Cecilia Ferrari – for their valuable input in countless meetings. I am particularly grateful to Zihao Xu and Dacheng Xu, with whom I worked closely on the two analyses forming the core of this thesis. I also want to thank Dr. Lanqing Yuan, Kexin Liu, and Shenyang Shi for many helpful discussions. My thanks further extend to the analysis coordinators, including Dr. Daniel Wenz, Dr. Giovanni Volta, Dr. Florian Jörg, Dr. Christian Wittweg, Dr. Maxime Pierre, and Prof. Dr. Jingqiang Ye. Their dedication was invaluable. I would like to thank Prof. Dr. Fei Gao, Prof. Dr. Laura Baudis, Prof. Dr. Masaki Yamashita, and Prof. Dr. Christian Weinheimer for their insightful input on the long-term sensitivity projections. A special thank-you goes to my fellow "plot police" partner, Dr. Michael Murra – I hope the plots in this thesis meet your standards.

Finally, I want to express my deepest gratitude to the most important people in my life – my family and friends. To my family: thank you for shaping me into who I am today and for your unconditional support and encouragement. A special thank-you to my mum, who has always been there for me, and of course to my grandma, who always crossed her fingers for me when it mattered most, including now as I finish this thesis. Most importantly, to my soon-to-be wife, Celine Karle: thank you for your unwavering support, for celebrating the highs, and for lifting me up during the lows. None of this would have been possible without you, and it certainly would not have been as enjoyable.

Thank you all for everything!